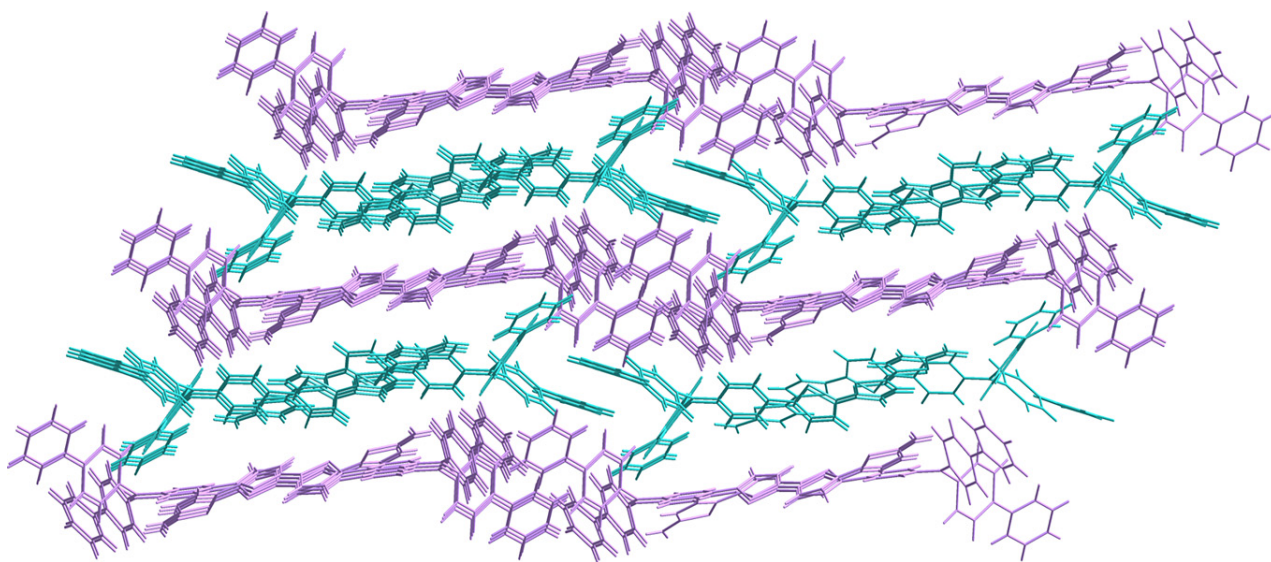




STUDIA UNIVERSITATIS
BABEȘ-BOLYAI



UNIVERSITATEA BABEȘ-BOLYAI
BABEȘ-BOLYAI TUDOMÁNYEGYETEM
BABEȘ-BOLYAI UNIVERSITÄT
BABEȘ-BOLYAI UNIVERSITY
TRADITIO ET EXCELLENTIA



CHEMIA

2/2025

STUDIA UNIVERSITATIS BABEȘ-BOLYAI CHEMIA

2/2025

ISSN (print): 1224-7154;
ISSN (online): 2065-9520; ISSN-L: 1224-7154
© STUDIA UBB CHEMIA

Published by Babeș-Bolyai University

EDITORIAL BOARD OF STUDIA UNIVERSITATIS BABEȘ-BOLYAI CHEMIA

ONORARY EDITOR:

IONEL HAIDUC – Member of the Romanian Academy

EDITOR-IN-CHIEF:

LUMINIȚA SILAGHI-DUMITRESCU

EXECUTIVE EDITOR:

ALEXANDRU LUPAN

ASSOCIATE EDITOR:

CASTELIA CRISTEA

EDITORIAL BOARD:

PAUL ȘERBAN AGACHI, Babeș-Bolyai University, Cluj-Napoca, Romania

LIVAIN BREAU, UQAM University of Quebec, Montreal, Canada

HANS JOACHIM BREUNIG, Institute of Inorganic and Physical Chemistry,
University of Bremen, Bremen, Germany

JEAN ESCUDIE, HFA, Paul Sabatier University, Toulouse, France

ION GROSU, Babeș-Bolyai University, Cluj-Napoca, Romania

EVAMARIE HEY-HAWKINS, University of Leipzig, Leipzig, Germany

FLORIN DAN IRIMIE, Babeș-Bolyai University, Cluj-Napoca, Romania

FERENC KILAR, University of Pecs, Pecs, Hungary

BRUCE KING, University of Georgia, Athens, Georgia, USA

ANTONIO LAGUNA, Department of Inorganic Chemistry, ICMA, University
of Zaragoza, Zaragoza, Spain

JURGEN LIEBSCHER, Humboldt University, Berlin, Germany

KIERAN MOLLOY, University of Bath, Bath, UK

IONEL CĂȚĂLIN POPESCU, Babeș-Bolyai University, Cluj-Napoca,
Romania

CRISTIAN SILVESTRU, Babeș-Bolyai University, Cluj-Napoca, Romania

YEAR
MONTH
ISSUE

Volume 70 (LXX) 2025
June
2

PUBLISHED ONLINE: 2025-06-20
PUBLISHED PRINT: 2024-07-30
ISSUE DOI: 10.24193/subbchem.2025.2

STUDIA UNIVERSITATIS BABEȘ-BOLYAI CHEMIA

2

CONTENT/ SOMMAIRE/ INHALT/ CUPRINS

- Daniel-Florin BOGOȘEL, Andreea Petronela CRIȘAN, Alexandra POP, Anamaria TERC, Ion GROSU, Investigation of Optical Properties and Solid-state Structure of Thiophene-containing Triarylamine Derivatives 7
- Iulia Maria CIOCOTIȘAN, Dana Maria MUNTEAN, Laurian VLASE, Kinetic Modeling Approach to *in vivo* Interactions of Curcumin and Curcuminoid-piperine Mixture with Quetiapine 19
- Ioana Lavinia LIXANDRU MATEI, Bogdan Alexandru SAVA, Andreea Iuliana IONESCU, Codruta SAROSI, Gabriel VASILIEVICI, Marian BAJAN, Daniela Luminița MOVILEANU, Daniela Roxana POPOVICI, Abeer BAIOUNF, Retinol Dispersion in the Form of Hydrogel for Dermal Delivery 37
- Anca BECZE, Dorina SIMEDRU, Liviu BÎLTEANU, Paul UIUIU, Chemical Characterization and Detergent Potential of *Chelidonium majus* Extracts 53
- Sultan PEKACAR, Ömer Furkan GÜVERTİ, Burçin ÖZÜPEK, Haticenur NEGİZ, Osman TUGAY, Didem DELİORMAN ORHAN, Phytochemical Characterization and Bioactivity Assessment of *Aethionema schistosum* with a Focus on Enzyme Inhibition and Antioxidant Potential 67

Nilgün GÜLER, Emine KILIÇKAYA SELVİ, Investigation of Anthraquinone Contents, DNA Cleavage, DNA Binding, Cytotoxic and Antioxidant Activities of <i>Xanthoria parietina</i> Samples'	81
Dejan PRVULOVIĆ, Radenka KOLAROV, Mirjana LJUBOJEVIĆ, Goran BARAĆ, Marijana PEIĆ TUKULJAC, Antioxidant Potential of Cherry Stalk Extracts	97
Aysun DİNÇEL, Nilüfer Burcu ER, Feyyaz ONUR, Chemometric-Assisted Spectrophotometric and HPLC Methods for the Simultaneous Analysis of Atorvastatin Calcium and Ezetimibe	111
Andreea Cătălina JOE, Ion ONUȚU, Dorin BOMBOȘ, Gabriel VASILIEVICI, Abeer BAIOUN, Laura SILAGHI-DUMITRESCU, Ioan PETEAN, The Influence of Some Powders on the Antimicrobial Activity of PLA Packaging with Oregano Oil Additives.....	129
Alexandra URDA, Diana LAZAR, Dragos COSMA, Ion GROSU, Crina SOCACI, Gold-decorated Titania Nanotubes with Graphene for Visible LIGHT-mediated amoxicillin Photodegradation	149
Santhosh VISWANATHAN, Siva PERIYASAMY, Senthilkumar KANDASAMY, Application of Banana Based Agro-waste as a Precursor of Heterogeneous Catalyst for Biodiesel Production	163
Marija VASIĆ JOVEV, Radomir LJUPKOVIĆ, Katarina STEPIĆ, Marjan RANĐELOVIĆ, Miloš MARINKOVIĆ, Aleksandra ZARUBICA, The Effect of Synthesis Process Parameters on the Physico-chemical Properties and Photocatalytic activity of Pristine and ZrO ₂ -doped TiO ₂ Catalysts	179
Haiting WANG, Haifeng XU, Pengfei HUO, Zhuangzhuang WANG, Jiqiang YUE, Zheng WANG, Di ZHANG, Tianzhi YU, Experimental Study on the Crystallization Formation Mechanism of Blind Pipe in Wujia Yuan Tunnel	191
Andra-Camelia PAVEL, Elena-Mihaela NAGY, Teodor Gabriel FODOREAN, Adina MICLĂUȘ, Behavior of Newtonian and Non-Newtonian Fluids in Pumping and Transport Processes.....	211

Studia Universitatis Babes-Bolyai Chemia has been selected for coverage in Thomson Reuters products and custom information services. Beginning with V. 53 (1) 2008, this publication is indexed and abstracted in the following:

- Science Citation Index Expanded (also known as SciSearch®)
- Chemistry Citation Index®
- Journal Citation Reports/Science Edition

INVESTIGATION OF OPTICAL PROPERTIES AND SOLID-STATE STRUCTURE OF THIOPHENE-CONTAINING TRIARYLAMINE DERIVATIVES

Daniel-Florin BOGOȘEL^a , Andreea Petronela CRIȘAN^a ,
Alexandra POP^a , Anamaria TERC^{a,*} , Ion GROSU^{a,*} 

ABSTRACT. The optoelectronic properties of some thiophene-containing triarylaminines derived formally from triphenyl amine by enlarging one, two, or all phenyl groups with phenyl, thiophene-phenyl, bithiophene, or terthiophene units, along with the molecular structure and the supramolecular arrangement of the molecules in the lattices, were revealed by spectroscopic and, in the case of two of the compounds, single crystal X-ray diffractometry investigations. This study confirms that solid-state interactions and conformations significantly influence the absorption and emission characteristics of these compounds, essential factors in designing efficient photovoltaic materials.

Keywords: *triarylamine, absorption and emission spectra, single crystal X-ray diffractometry, C-H... π and heteroatom... π contacts*

INTRODUCTION

Nowadays, our society faces significant challenges regarding the efficient use of current resources alongside the mindful exploitation of renewable energy sources, and finding new functional materials has become one of the most investigated lines of research over the last 25 years. Triphenylamine (TPA) or, more generally, triarylamine (TAA) derivatives distinguished themselves among the electroactive building blocks in functional materials, being used as hole transporters in numerous optoelectronic devices that convert solar light into

^a Babes-Bolyai University, Faculty of Chemistry and Chemical Engineering, Department of Chemistry and SOOMCC, Cluj-Napoca, 11 Arany Janos, 400028, Cluj-Napoca, Romania.

* Corresponding authors: anamaria.terec@ubbcluj.ro; ion.grosu@ubbcluj.ro



electricity,[1–3] such as organic solar cells (OSCs),[4–6] dye-sensitized solar cells (DSSCs),[7] and perovskite solar cells (PSCs).[8] Some TAA derivatives are luminescent and thus can be used in organic light emitting diodes (OLEDs)[9–11] and organic field effect transistors (OFETs)[12] or act as sensors[13, 14] and electrochromic systems.[15]

TAAAs have strong electron-donating capability that allows for the construction of extended π -systems toward acceptor moieties for hole-transporting properties, while the nonplanar propeller-shaped TPA unit restrains intermolecular aggregation via π - π stacking that usually leads to fluorescence quenching in the solid state. In most materials, the solid-state luminescent properties closely follow the intermolecular interactions that occur in aggregates or crystals.

In this context, our attention was directed toward two TAA derivatives containing thiophene units in the conjugated π -system (Chart 1). The supramolecular structure of smaller thiophene-containing TPA aldehydes (**TPA2TfCHO** and **TPA3TfCHO**) (Chart 2) was already reported in the literature [16–19] while the simplest brominated TPA derivative, *p*-bromotriphenylamine (**TPABr**) found application in various functional materials[20, 21] – for example, it was used as an additive in hybrid materials to enhance the fluorescence and phosphorescence of carbazole derivatives via halogen bonding.[22] Thus, we considered it of interest to investigate the luminescent properties of TAAAs **1** and **2** in correlation with their supramolecular association in crystals to account for the influence of the extended π -systems on their properties.

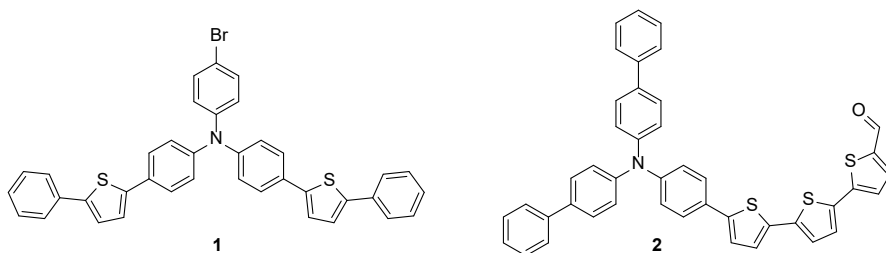


Chart 1

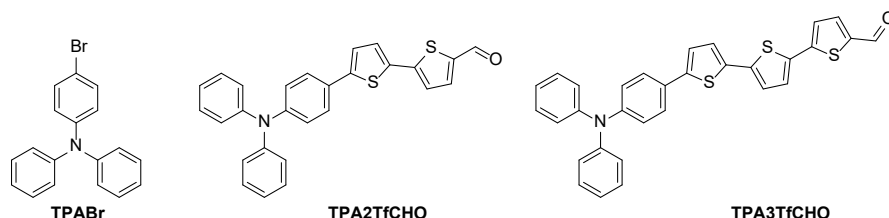


Chart 2

RESULTS AND DISCUSSIONS

We have accessed TAA derivatives **1** and **2** in our laboratory through multi-step synthesis from commercially available materials.[23] Additionally, we have synthesised the already-reported **TPABr**, **TPA2TfCHO**, and **TPA3TfCHO** as reference compounds.

First, the photophysical behaviour of the compounds in solution was examined to assess how structural changes in the extended TAA derivatives affect their optical properties.

The UV-VIS absorption spectra of the compounds were recorded in CH_2Cl_2 (10^{-5} M) and are presented in **Figure 1a**.

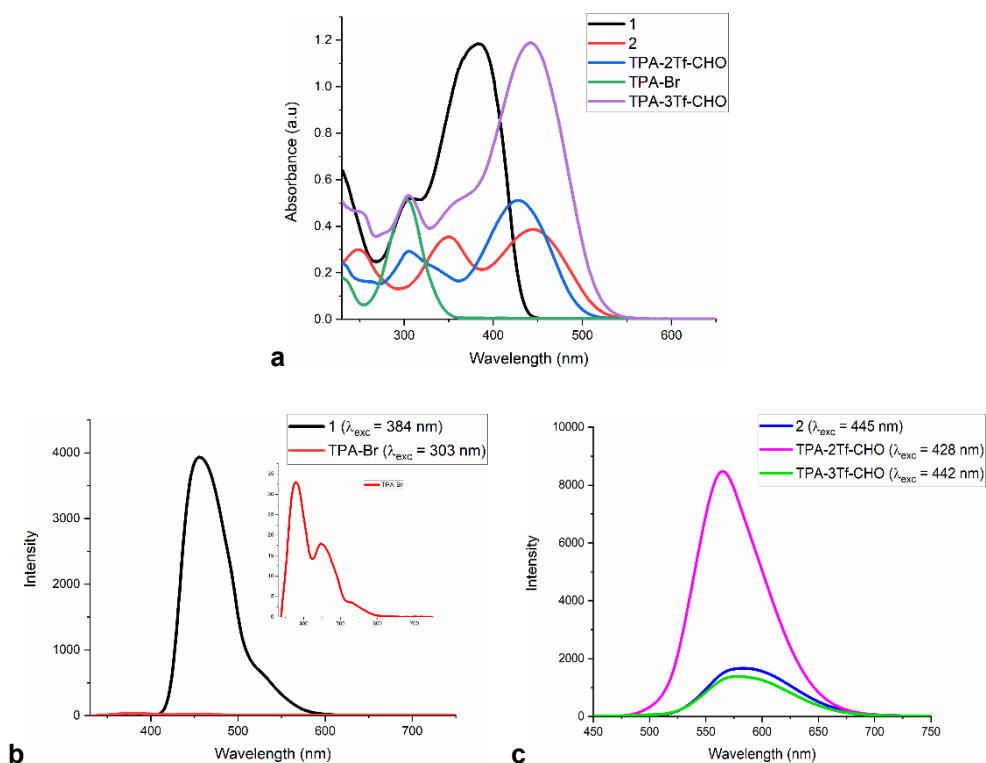


Figure 1. a) UV-vis absorption spectra of compounds **1**, **2**, **TPABr**, **TPA2TfCHO**, and **TPA3TfCHO** in 10^{-5} M CH_2Cl_2 solution; b) Emission spectra of brominated derivatives **1** and **TPABr** in 1.5×10^{-5} M CH_2Cl_2 solution; c) Emission spectra of aldehydes **2**, **TPA2TfCHO**, and **TPA3TfCHO** in 1.5×10^{-5} M CH_2Cl_2 solution.

Most of the compounds exhibit first absorption bands in the range of 300-305 nm, corresponding to π - π^* transitions in the molecules. Among the studied compounds, a noticeable red-shift of the π - π^* absorption band appears for compound **2** at 350 nm, which can be ascribed to the extended conjugation in the system. Additionally, all compounds, except for **TPABr**, exhibit a supplementary peak (at 385 nm for **1** and around 430-450 nm for the aldehydes) that can be associated with internal charge transfer (ICT) due to π - π stacking and transfer from the donor (TAA) to the acceptor (CHO) part of the molecule. The emission characteristics were investigated by recording the fluorescence spectra in 1.5×10^{-5} M CH_2Cl_2 solutions (Figure 1 b and c). All compounds, except for **TPABr**, display fluorescence exhibiting emission with maxima around 450 nm for **1** and red-shifted to 565-585 nm for the aldehydes due to ICT phenomena, confirming the extended π - π conjugation (**Figures 1b and 1c**).

Both our compounds showed only modest optical performances compared to some already reported compounds with similar functionalities used in photovoltaics, for which an increase in the intensities of ICT vs. π - π^* transitions was associated with a better conjugation favoured by the near-coplanarity of the extended π system.[24, 25]

To explain these observations, we have investigated their structure in solid state. Yellow crystals of **1** and orange crystals of **2** suitable for Single Crystal X-Ray Diffraction were obtained by slow evaporation of chloroform (**1**) and acetone/dichloromethane/pentane (1/1/1) solutions (**2**), respectively. Their molecular structures are presented in **Figure 2**. As a common feature, both compounds present a quasiplanar central triarylamine unit with (Ar)C-N-C(Ar) bond angles of approximately 120° and the propeller-like arrangement of the aryl groups around the N atom (torsion angles between 50° and 57° for **1** and between 24° and 65° for **2**, respectively).

Contrary to our expectations, the π -conjugated system in **1** strongly deviates from the desired coplanarity, with torsion angles in the range of 5.18° and 29.65° (depicted in blue in **Figure 3a**). This fact has poorer electron delocalization consequences. The unit cell consists of four molecules arranged in an antiparallel manner (**Figure 3a**), and the formation of catemeric chains connected *via* halogen bonds can also be noticed. The length between the bromine atom and C10 and C11 (Br-C10 and Br-C11 distances of 3.291 Å and 3.353 Å, respectively, depicted in red in **Figure 3**) is less than the sum of their Van der Waals radii (3.40 Å)[26], leading to above-the-bond C-Br \cdots π halogen bonding.[27, 28]

The three-dimensional crystal packing of **1** presented in **Figure 3b** shows the formation of antiparallely running catemers held together by multiple weak intermolecular C-H \cdots π contacts (H31 \cdots Cg1 [Cg1 = thiophene (S2) ring] distance of 2.785 Å and H35 \cdots Cg2 [Cg2 = C1-C6 phenyl ring]

INVESTIGATION OF OPTICAL PROPERTIES AND SOLID-STATE STRUCTURE
OF THIOPHENE-CONTAINING TRIARYLAMINE DERIVATIVES

distance of 3.102 Å) depicted in green. Similar C-H... π contacts were reported previously in some cyclophanes and supramolecular polymers containing fluorene or spirobifluorene units.[29–31]

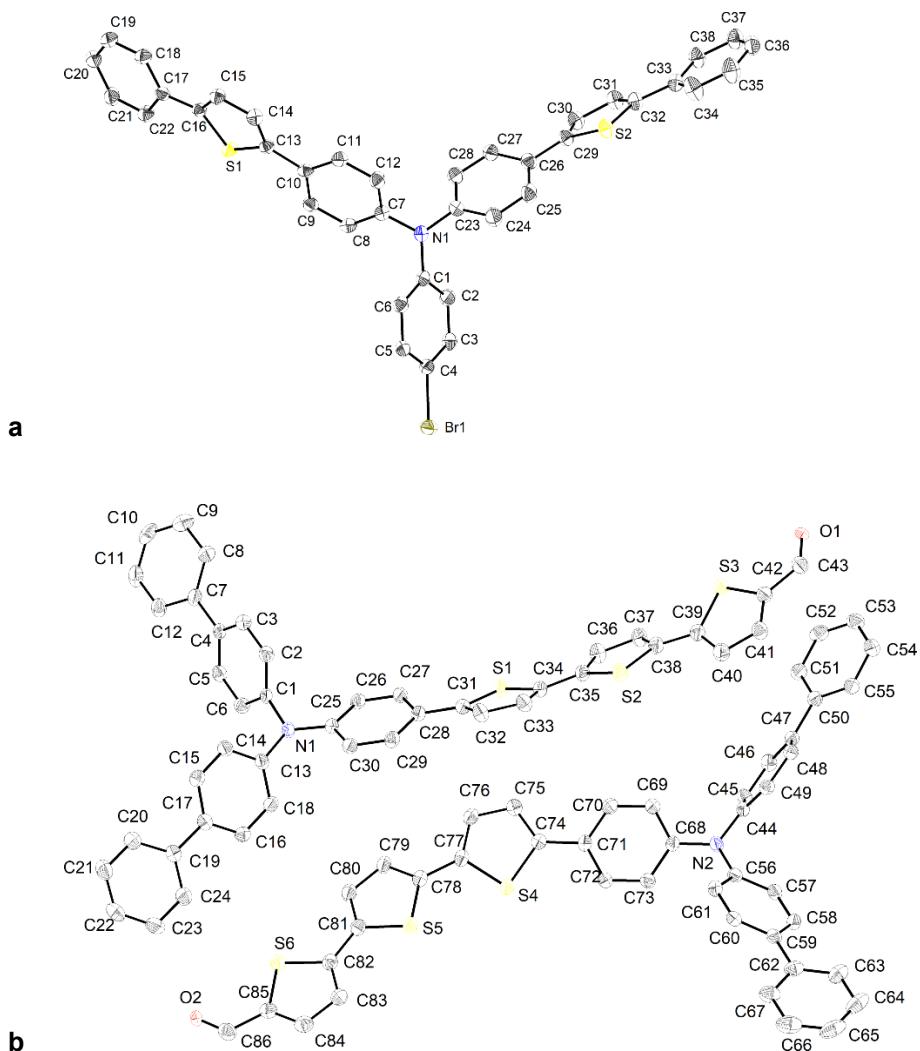


Figure 2. ORTEP representation (50% probability level of atomic displacement ellipsoids) of the molecular structure of compounds **1** (a) and **2** (b). Hydrogen atoms were omitted for clarity

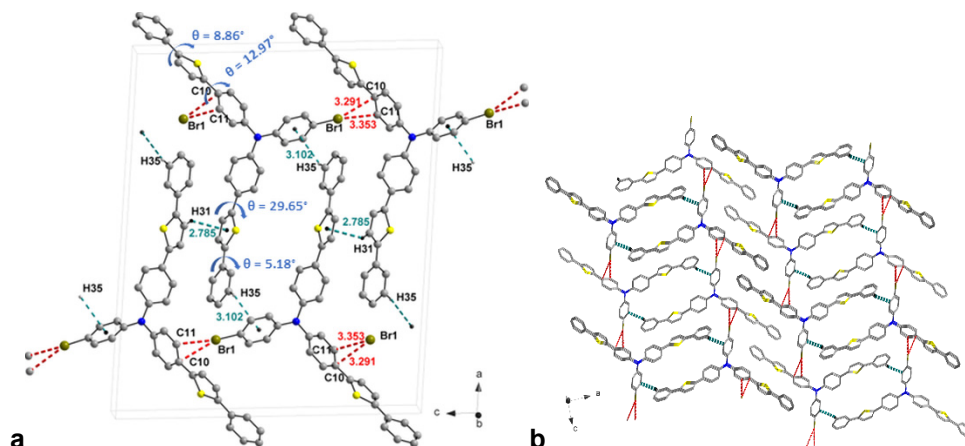


Figure 3. (a) Unit cell with detailed intermolecular interactions and significant torsion angles in the π system and (b) packing patterns of compound **1** crystal. Hydrogen atoms were omitted for clarity, except when involved in interactions.

The asymmetric unit of compound **2** contains two crystallographically independent molecules (**Figure 4b**) that differ in the relative arrangement of the three thiophene rings. In one of the molecules, there is a *syn-anti* disposal of the thiophene moieties (further named **2SA**), while in the other, the rings adopt an *anti-anti* conformation (further named **2AA**). Similar TAA-containing mono-, di- and terthiophene aldehydes, such as **TPA2TfCHO** and **TPA3TfCHO**, were reported to demonstrate polymorphism under different crystal growth conditions, and, in most reported cases, only same-conformer crystal was observed.[16, 19, 32–34]

Similarly to the above-described brominated triarylamine derivative **1**, there is a significant deviation from coplanarity in the π -conjugated system and, in this case, in the biphenyl terminal units as well. By contrast, in the case of simpler **TPA2TfCHO**, a quasiplanar arrangement of the oligothiophene moiety was observed.[16, 19, 32] In conformer **2AA**, only the middle thiophene units are coplanar with additional stabilization from C-H...S interactions (S2...H33 distance of 2.874 Å and S1...H27 distance of 2.815 Å, depicted in purple in **Figure 4a**). Meanwhile, the outer thiophene ring and the connecting phenyl ring jut out at significant angles ($\theta = 28.40^\circ$ and $\theta = 18.95^\circ$, respectively, shown in blue in **Figure 4a**). In **2SA** (**Figure 4b**), there is a notable torsion

angle of 20.39° between the two *syn* thiophene rings, while the other aromatic rings in the π system are stabilized in a local near planar conformation by additional C-H...S interactions (S6...H80 distance of 2.915 Å and S4...H72 distance of 2.719 Å, depicted in purple). In both conformers, the biphenyl rings attached to the N atom are twisted at torsion angles ranging from 13.12° to 32.59° (**Figures 4a** and **4b**). We have described similar supramolecular contacts involving the heterocyclic sulphur atoms in solid-state packing of some thiophene- or phenothiazine-containing heterocycles, too.[35, 36]

The conformer **2SA** associates in homomeric dimers (**Figure 4b**) connected in an antiparallel fashion by doubled C-H...O interactions (O2...H52 distance of 2.617 Å, shown in red). The thiophene units directly attached to the phenyl ring are above each other, slightly shifted in parallel planes (3.219 Å distance between planes), and strengthening reciprocal C-H... π interactions are observed (H76...Cg1 [Cg1 = thiophene (S4)] distance is 3.231 Å, depicted in green; Cg1...Cg1 distance 4.150 Å). A somewhat similar situation is encountered in **2AA**, in which dimeric head-to-head formations by C-H... π contacts in the biphenyl units (H11...Cg2 [Cg2 = C13-C18 phenyl] distance of 3.280 Å, depicted in green in **Figure 4a**) are observed, while a neighbouring **2AA** molecule is in an antiparallel arrangement, but more shifted than in **2SA** (2.325 Å distance between the parallel planes with 5.404 Å distance between thiophene (S1) rings centroids).

In turn, the different conformers are associated (**Figure 4c**) through C-H... π contacts (H76...C29 and H76...C28 distances are 2.759 Å and 2.780 Å, respectively, H75...Cg3 [Cg3 = thiophene (S1)] 2.716 Å), and π ... π interaction (distance between centroids of thiophene (S3) and phenyl ring is 3.856 Å, depicted in green) alongside C-H...S interactions (S6...H24 distance of 2.847 Å, shown in purple). A plethora of C-H... π intermolecular interactions ranging between 3.092 Å and 3.108 Å (in green in **Figure 4c**) and short C-H...O interactions (O1...H72 distance of 2.392 Å, shown in red) ensures further development of the supramolecular 2D network.

Inspection of the packing diagram of **2** revealed the alternation of homomolecular sheets of connected dimers, as shown in **Figure 4d**, with **2SA** molecules depicted in pink and the **2AA** conformers in green. The deviation from the planarity in both the extended π -system and in the biphenyl part disrupts the effective electron conjugation and constrains the molecules further from each other in the crystalline lattice.

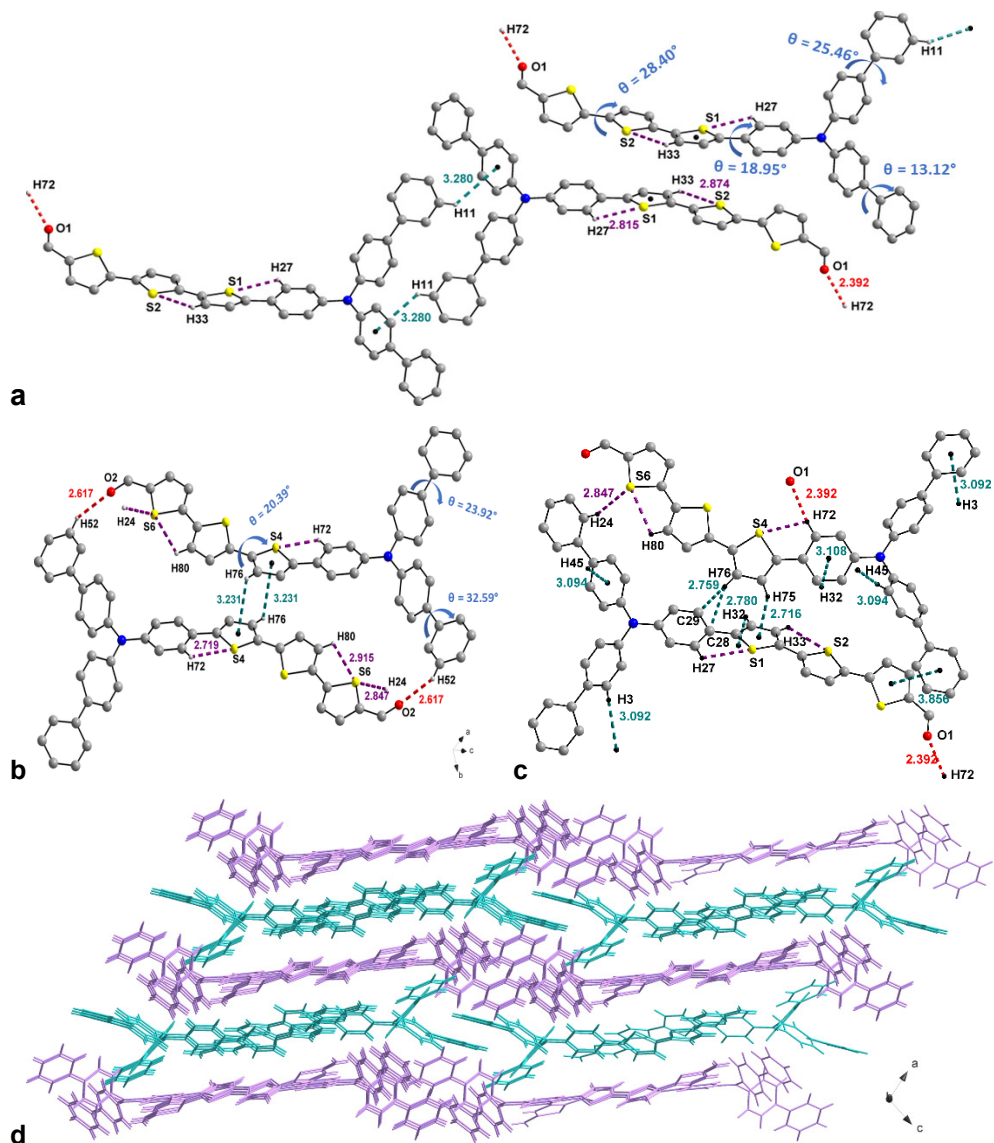


Figure 4. Views of (a) **2AA** conformer homomeric association, (b) one **2SA** homomeric dimer formation, (c) heteromeric association of **2SA** and **2AA** conformers, and (d) packing patterns of compound **2** in crystal showing homomeric (**2SA** conformers are presented in pink and **2AA** ones in green) sheet formation. C-H... π and π ... π (depicted in green), C-H...O (in red), and C-H...S (in purple) interactions are shown. Hydrogen atoms were omitted for clarity, except when involved in interactions.

CONCLUSIONS

The absorption spectra of compounds **1** and **2** revealed a bathochromic shift of absorption maxima comparatively to those of TPA compounds with less extended π - π structure. In both absorption and emission spectra, red-shifted peaks belonging to ICT (internal charge transfer) processes were observed. The single crystal X-ray diffractometry investigation of **1** and **2** highlighted the non-planar structure of the di-, ter- or quarter-aryl chains and the association of the molecules in the lattices via C-H $\cdots\pi$ and heteroatom $\cdots\pi$ contacts. In conclusion, in the depicted compounds **1** and **2**, the introduction of a more complex and extended π -system brings supplemental intermolecular interactions with detrimental effects on the solid-state packing, an essential feature for functional materials used in photovoltaics. This study underscores the importance of understanding the relationship between molecular structure, solid-state packing, and optical properties in the development of functional materials for electronic applications.

EXPERIMENTAL SECTION

UV-vis optical data in solution were recorded with an UV-vis 1900 Shimadzu spectrometer. Fluorescence spectra were recorded on a JASCO FP-8300 spectrofluorometer using quartz cuvettes (1 cm). Solutions for UV-vis and fluorescence measurements were prepared in HPLC grade dichloromethane.

Details about the crystal structure determination and refinement data are given in **Table S1**. The crystals of **1** and **2** were mounted on MiTeGen microMounts cryoloops, and data were collected on a Bruker D8 VENTURE diffractometer using Mo-K α radiation ($\lambda = 0.71073 \text{ \AA}$) from a I μ S 3.0 microfocus source with multilayer optics, at 100 K. The structures were refined with anisotropic thermal parameters for non-H atoms. Hydrogen atoms were placed in fixed, idealized positions and refined with a riding model and a mutual isotropic thermal parameter. For structure solving and refinement the Bruker APEX4 Software Package was used.[37] One solvent molecule in the structure of **1** was found to be disordered over several positions. The SQUEEZE procedure of the PLATON program was used for the removal of the contribution of the electron density from the intensity data corresponding to the disordered solvent. The solvent-free model was employed for the final refinement, and it was estimated that a volume of 274 \AA^3 corresponds to the pentane used for chromatographic purification.[23, 38] Drawings were created using the Diamond program.[39] The CCDC reference numbers are 2435059 (**1**) and

2435058 (2). The supplementary crystallographic data for this article can be obtained free of charge from The Cambridge Crystallographic Data Centre via <https://www.ccdc.cam.ac.uk/structures/>.

Table S1. Crystal data and structure refinement for **1** and **2**

Compound	1	2
Molecular formula	C ₃₈ H ₂₆ BrNS ₂	C ₄₃ H ₂₉ NOS ₃
Formula weight	640.63	671.85
Crystal size / mm ³	0.074 x 0.093 x 0.135	0.036 x 0.118 x 0.123
Crystal habit	yellow block	orange-yellow plate
$\lambda(\text{MoK}\alpha) / \text{\AA}$	0.71073	0.71073
T / K	100.(2)	99.(2)
Crystal system	monoclinic	triclinic
Space group	<i>P</i> 21/ <i>c</i>	<i>P</i> -1
$a / \text{\AA}$	26.0625(9)	10.4861(4)
$b / \text{\AA}$	5.5687(2)	13.5328(6)
$c / \text{\AA}$	21.6895(8)	23.9078(11)
$\alpha / ^\circ$	90	93.213(2)
$\beta / ^\circ$	94.1290(10)	102.3010(10)
$\gamma / ^\circ$	90	98.9090(10)
$V / \text{\AA}^3$	3139.72(19)	3260.8(2)
Z	4	4
$D_{\text{calc}} / \text{g cm}^{-3}$	1.355	1.369
μ / mm^{-1}	1.470	0.265
θ range for data collections ($^\circ$)	1.99 - 28.41	2.01 - 28.29
$F(000)$	1312	1400
$T_{\text{max}} / T_{\text{min}}$	0.83 / 0.90	0.96 / 0.99
Refl. collected / unique / R_{int}	95985 / 0.0776	100602 / 0.1021
Completeness to θ	99.8%	99.9%
Refinement method	Full-matrix least-squares on F^2	
Data / restraints / parameters	7875 / 0 / 379	16157 / 0 / 865
Goodness-of-fit, S	0.841	0.993
Final R indices [$I > 2\sigma(I)$]	$R_1 = 0.0472$	$R_1 = 0.0545$
	$wR_2 = 0.1743$	$wR_2 = 0.1380$
R indices (all data)	$R_1 = 0.0697$	$R_1 = 0.1051$
	$wR_2 = 0.2090$	$wR_2 = 0.1721$
$\Delta\rho_{\text{max}}, \Delta\rho_{\text{min}} / \text{e \AA}^{-3}$	0.552 / -0.903	0.330 / -0.433
CCDC No.	2435059	2435058

ACKNOWLEDGEMENTS

This work was supported by the Romanian Ministry of Research, Innovation and Digitization, CNCS – UEFISCDI, research projects PN-III-P4-ID-PCE-2020-1812 (ICOFOSC), PN-III-P2-2.1-PED-2019-2601 (REGRENPOS) and 312-COFFEE ERANET within PNCDI IV.

REFERENCES

1. R. Rybakiewicz; M. Zagorska; A. Pron; *Chem. Pap.* **2017**, *71* (2), 243–268
2. P. Blanchard; C. Malacrida; C. Cabanetos; J. Roncali; S. Ludwigs; *Polym. Int.* **2019**, *68* (4), 589–606
3. J. Wang; K. Liu; L. Ma; X. Zhan; *Chem. Rev.* **2016**, *116* (23), 14675–14725
4. J. Roncali; P. Leriche; P. Blanchard; *Adv. Mater.* **2014**, *26* (23), 3821–3838
5. A. Diac; D. Demeter; M. Allain; I. Grosu; J. Roncali; *Chem. – Eur. J.* **2015**, *21* (4), 1598–1608
6. D. Demeter; S. Mohamed; A. Diac; I. Grosu; J. Roncali; *ChemSusChem.* **2014**, *7* (4), 1046–1050
7. A. Mahmood; *Sol. Energy.* **2016**, *123*, 127–144
8. P. Agarwala; D. Kabra; *J. Mater. Chem. A.* **2017**, *5* (4), 1348–1373
9. J. Kwak; W. K. Bae; M. Zorn; H. Woo; H. Yoon; J. Lim; S. W. Kang; S. Weber; H.-J. Butt; R. Zentel; et al.; *Adv. Mater.* **2009**, *21* (48), 5022–5026
10. J.-X. Liang; Z.-H. Pan; K. Zhang; D. Yang; J.-W. Tai; C.-K. Wang; M.-K. Fung; D. Ma; J. Fan; *Chem. Eng. J.* **2023**, *457*, 141074
11. Q. Zhang; J. Jiang; Z. Xu; D. Song; B. Qiao; S. Zhao; S. Wageh; A. Al-Ghamdi; *RSC Adv.* **2021**, *11* (39), 24436–24442
12. L. M. Nhari; R. M. El-Shishtawy; A. M. Asiri; *Dyes Pigments.* **2021**, *193*, 109465
13. H. E. Okda; S. E. Sayed; R. C. M. Ferreira; R. C. R. Gonçalves; S. P. G. Costa; M. M. M. Raposo; R. Martínez-Máñez; F. Sancenón; *New J. Chem.* **2019**, *43* (19), 7393–7402
14. H. Chen; P. Yang; Y. Li; L. Zhang; F. Ding; X. He; J. Shen; *Spectrochim. Acta. A. Mol. Biomol. Spectrosc.* **2020**, *224*, 117384
15. T. Harimoto; Y. Ishigaki; *Chem. – Eur. J.* **2025**, *31* (3), e202403273
16. A. Benitz; M. B. Thomas; Y. Jang; V. Nesterov; F. D'Souza; *J. Chem. Sci.* **2021**, *133* (3), 71
17. B. Lv; Z. Wang; Y. Wu; Y. Zheng; Z. Cui; J. Li; W. Gu; *J. Hazard. Mater.* **2024**, *469*, 134105
18. V. Parthasarathy; S. Fery-Forgues; E. Campioli; G. Recher; F. Terenziani; M. Blanchard-Desce; *Small.* **2011**, *7* (22), 3219–3229
19. K. Amro; J. Daniel; G. Clermont; T. Bsaibess; M. Pucheault; E. Genin; M. Vaultier; M. Blanchard-Desce; *Tetrahedron.* **2014**, *70* (10), 1903–1909

20. A. J. Sindt; B. A. DeHaven; R. L. Goodlett; J. O. Hartel; P. J. Ayare; Y. Du; M. D. Smith; A. K. Mehta; A. M. Brugh; M. D. E. Forbes; C. R. Bowers; A. K. Vannucci; L. S. Shimizu; *J. Am. Chem. Soc.* **2020**, *142* (1), 502–511
21. J. Yang; X. Wu; J. Shi; B. Tong; Y. Lei; Z. Cai; Y. Dong; *Adv. Funct. Mater.* **2021**, *31* (52), 2108072
22. W. Dai; X. Niu; X. Wu; Y. Ren; Y. Zhang; G. Li; H. Su; Y. Lei; J. Xiao; J. Shi; B. Tong; Z. Cai; Y. Dong; *Angew. Chem. Int. Ed.* **2022**, *61* (13), e202200236
23. D.-F. Bogoșel; G.-I. Giurgi; A. Balan; A. Pop; I. Grosu; A. P. Crișan; A. Terec; *Org. Electron.* **2025**, *141*, 107212
24. S. Noureen; P. Devibala; P. M. Imran; S. Nagarajan; *Synth. Met.* **2024**, *302*, 117541
25. N. Terenti; G.-I. Giurgi; A. P. Crișan; C. Anghel; A. Bogdan; A. Pop; I. Stroia; A. Terec; L. Szolga; I. Grosu; J. Roncali; *J. Mater. Chem. C.* **2022**, *10* (14), 5716–5726
26. A. Bondi; *J. Phys. Chem.* **1964**, *68* (3), 441–451
27. F. C. Grozema; R. W. J. Zijlstra; M. Swart; P. Th. van Duijnen; *Int. J. Quantum Chem.* **1999**, *75* (4–5), 709–723
28. Q. J. Shen; X. Pang; X. R. Zhao; H. Y. Gao; H.-L. Sun; W. J. Jin; *CrystEngComm.* **2012**, *14* (15), 5027-5034
29. M. Balog; I. Grosu; G. Plé; Y. Ramondenc; E. Condamine; R. A. Varga; *J. Org. Chem.* **2004**, *69* (4), 1337–1345
30. I. G. Grosu; L. Pop; M. Miclăuș; N. D. Hădade; A. Terec; A. Bende; C. Socaci; M. Bărboiu; I. Grosu; *Cryst. Growth Des.* **2020**, *20* (5), 3429–3441
31. L. Pop; I. G. Grosu; M. Miclăuș; N. D. Hădade; A. Pop; A. Bende; A. Terec; M. Bărboiu; I. Grosu; *Cryst. Growth Des.* **2021**, *21* (2), 1045–1054
32. A. Vinod Kumar; P. Pattanayak; A. Khapre; A. Nandi; P. Purkayastha; R. Chandrasekar; *Angew. Chem. Int. Ed.* **2024**, *63* (40), e202411054
33. W. Xu; M. M. S. Lee; Z. Zhang; H. H. Y. Sung; I. D. Williams; R. T. K. Kwok; J. W. Y. Lam; D. Wang; B. Z. Tang; *Chem. Sci.* **2019**, *10* (12), 3494–3501
34. A. M. Raynor; A. Gupta; C. M. Plummer; S. L. Jackson; A. Bilic; H. Patil; P. Sonar; S. V. Bhosale; *Molecules.* **2015**, *20* (12), 21787–21801
35. A. Bende; I. Grosu; I. Turcu; *J. Phys. Chem. A.* **2010**, *114* (47), 12479–12489
36. M. Cîrcu; V. Pașcanu; A. Soran; B. Braun; A. Terec; C. Socaci; I. Grosu; *CrystEngComm.* **2012**, *14* (2), 632–639
37. G. M. Sheldrick; *Acta Crystallogr. Sect. C Struct. Chem.* **2015**, *71* (1), 3–8
38. A. L. Spek; *J. Appl. Crystallogr.* **2003**, *36* (1), 7–13
39. DIAMOND – Visual Crystal Structure Information System, **2001**

KINETIC MODELING APPROACH TO *IN VIVO* INTERACTIONS OF CURCUMIN AND CURCUMINOID-PIPERINE MIXTURE WITH QUETIAPINE

Iulia Maria CIOCOTIȘAN^a , Dana Maria MUNTEAN^{a*} ,
Laurian VLASE^a 

ABSTRACT. This study aimed to develop kinetic models that describe the preclinical drug interaction data between quetiapine, an atypical antipsychotic, and bioactive compounds derived from turmeric rhizome. The potential risk of interaction between these substances could alter the disposition of quetiapine and impact its efficacy. During the development of the kinetic models, first-order kinetic processes were assumed, and several hypotheses were evaluated, including the number of compartments for distribution, the presence of lag time in quetiapine absorption, the presystemic formation of its metabolite, and the relative bioavailability between the study groups. The most accurate models suggest that interactions between quetiapine and curcumin occur primarily at the intestinal level, as the systemic metabolism constant remained unaltered. Conversely, coadministration with curcuminoids and piperine markedly affected systemic metabolism, likely due to hepatic enzyme inhibition, resulting in a 59.6% increase in the relative bioavailability of quetiapine. The developed models successfully integrated data for quetiapine and norquetiapine, both as standalone administration and in combination with curcumin or curcuminoid-piperine bioactive compounds, capturing their disposition within the framework of pharmacokinetic interactions.

Keywords: *kinetic modeling, quetiapine, norquetiapine, curcumin, curcuminoids, drug interactions*

^a Department of Pharmaceutical Technology and Biopharmacy, Iuliu Hațieganu University of Medicine and Pharmacy, Cluj-Napoca, Romania

* Corresponding author: dana.muntean@umfcluj.ro



INTRODUCTION

Quetiapine (QUE), a dibenzothiazepine derivative is employed in treating psychotic disorders [1], primarily due to its moderate antagonism towards serotonin 5HT_{2A}, H₁ histamine and α_1 adrenergic receptors, alongside its low affinity for dopamine D2 receptors [2]. Immediate-release formulations exhibit rapid oral (p.o.) absorption, with a median time of 1–2 hours to reach maximum plasma concentration. QUE's moderate lipophilicity underpins its extensive volume of distribution (Vd) of 510–710 L and 83% plasma protein binding [2]. Metabolism predominantly occurs in the liver, with less than 1% excreted unchanged in urine. Phase I reactions, including oxidation, hydroxylation, and N-/O-dealkylation, followed by phase II conjugation, represent key metabolic pathways [3]. The cytochrome P450 (CYP) system—primarily the CYP3A4 isoenzyme, with minor contributions from CYP3A5 and CYP2D6—mediates QUE's clearance [4]. Intestinal CYP3A4 metabolism, occurring in enterocytes, further influences QUE's bioavailability – defined as the fraction of the administered dose that reaches systemic circulation and becomes available for therapeutic effect. CYP3A4 also converts QUE to its active metabolite, N-desalkylquetiapine (norquetiapine, NQ), which contributes to the overall antidepressant activity via noradrenaline reuptake inhibition, partial serotonin 5-HT_{1A} agonism, and presynaptic α_2 adrenergic and serotonin 5-HT_{2C}/5-HT₇ receptor antagonism. NQ undergoes subsequent CYP2D6-mediated metabolism, with limited involvement from CYP3A4 [5].

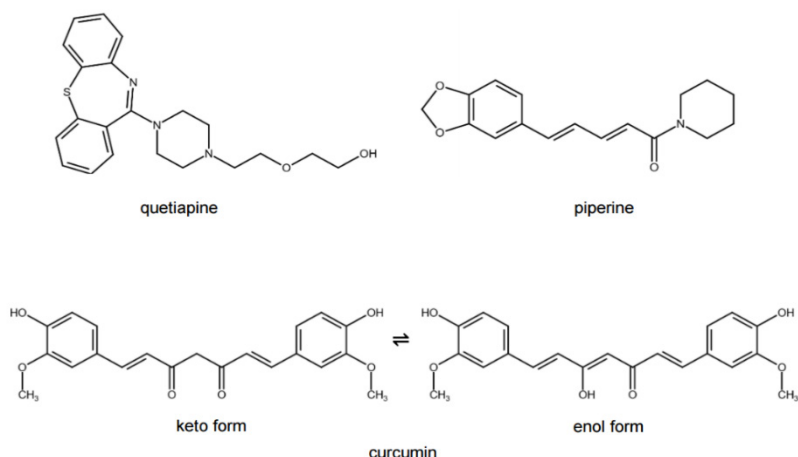
Curcumin, the principal bioactive compound of turmeric rhizome (*Curcuma longa* Linn.), has a diferuloylmethane structure, as depicted in Scheme 1, and belongs to the polyphenolic curcuminoid group, alongside demethoxycurcumin and bisdemethoxycurcumin.

Supplements containing turmeric rhizome extracts are recognized for their antioxidant, anti-inflammatory, and neuroprotective properties. However, curcumin alone demonstrated low oral bioavailability due to poor absorption and rapid metabolism at both pre- and systemic circulation [6]. One method to enhance curcumin's bioavailability involves the addition of piperine, an alkaloid with N-acyl pyridine structure. Piperine inhibits the rapid metabolism, including glucuronidation and potentially CYP enzymes, while increasing the intestinal permeability resulting in increased intestinal absorption. Both curcumin and piperine possess inhibitory activity towards a series of CYP enzymes, including CYP3A4 and CYP2D6 [7].

Patients prescribed antipsychotics often undergo polypharmacy due to coadministration of medications targeting the same condition or comorbidities. Curcumin and curcumin-derived formulations, with their anti-inflammatory and pro-cognitive effects, may complement psychiatric treatments and are likely to

KINETIC MODELING APPROACH TO *IN VIVO* INTERACTIONS OF CURCUMIN AND CURCUMINOID-PIPERINE MIXTURE WITH QUETIAPINE

be used alongside QUE [8]. Given their pharmacokinetic (PK) properties and shared interaction with CYP enzymes, a PK interaction between QUE and curcuminoids is plausible. Assessing this interaction is essential to ensure therapeutic efficacy and safety during concomitant administration.



Scheme 1. Structural formulas of quetiapine, piperine and curcumin (keto form – bottom left, enol form – bottom right)

PK modeling utilizes mathematical approaches to describe the absorption, distribution, metabolism, and excretion (ADME) of drugs, enabling predictions of their behavior across various physiological conditions [9]. Compartmental modeling simplifies ADME processes by grouping tissues and fluids with similar characteristics into compartments. These virtual spaces approximate drug movement and enhance predictions of PK behaviour. PK models primarily focus on temporal changes in drug concentration or amount within the body. Key steps in developing such models include identifying the structural framework, defining the number of compartments, and estimating relevant PK parameters [10].

The aim of this study was to develop kinetic models that comprehensively describe the absorption, distribution, metabolism, and elimination processes of QUE and its metabolite NQ, following the administration of a single dose of QUE after previous treatment with either crude curcumin or a combination of curcuminoids and piperine. This was achieved by comparing predicted data with the experimental results obtained from an *in vivo* rat study.

RESULTS AND DISCUSSION

Table 1 and Table 2 present the mean plasma concentration-time profiles and the standard deviation (S.D.) for QUE and its active metabolite, NQ, across the three study groups, which were used for kinetic modeling.

Table 1. The mean \pm S.D. plasma concentration-time values of quetiapine (85 mg/kg b.w., *p.o.*) single-dose across three study groups: quetiapine monotherapy (Reference, n=13), 6-day pre-treatment with curcumin (200 mg/kg b.w. *p.o.*, Test 1, n=13) and 6-day pre-treatment with curcuminoid (200 mg/kg b.w., *p.o.*)/piperine formulation (Test 2, n=13)

Time (h)	QUE Concentration (ng/mL)		
	Reference	Test 1	Test 2
0.16	126.7 \pm 50.9	70.6 \pm 47.7	74.5 \pm 24.8
0.33	323.1 \pm 187.3	121.6 \pm 73.0	229.6 \pm 82.4
0.5	383.7 \pm 240.9	158.5 \pm 96.7	316.4 \pm 168.8
0.75	364.4 \pm 297.7	192.3 \pm 87.7	350.7 \pm 158.9
1.0	349.8 \pm 307.6	210.1 \pm 88.0	439.2 \pm 269.5
1.5	308.5 \pm 194.3	227.1 \pm 102.0	471.1 \pm 311.3
2.0	272.3 \pm 151.3	224.5 \pm 122.9	482.2 \pm 274.1
2.5	252.6 \pm 148.5	215.5 \pm 144.4	415.2 \pm 236.4
3.0	226.0 \pm 140.1	186.2 \pm 110.0	364.6 \pm 192.1
4.0	152.2 \pm 90.7	155.1 \pm 117.8	253.1 \pm 122.1
6.0	76.4 \pm 42.4	101.7 \pm 77.1	153.2 \pm 79.0
8.0	53.6 \pm 38.5	50.5 \pm 47.8	83.5 \pm 44.0
10.0	39.0 \pm 24.9	25.9 \pm 22.4	63.7 \pm 46.5
12.0	20.4 \pm 12.9	19.5 \pm 14.6	33.4 \pm 18.4
16.0	9.9 \pm 7.4	16.5 \pm 10.9	26.0 \pm 15.5
20.0	7.7 \pm 4.5	12.2 \pm 6.1	17.2 \pm 7.7
24.0	6.3 \pm 5.4	7.6 \pm 4.3	14.2 \pm 9.3
30.0	6.5 \pm 3.9	4.5 \pm 2.8	5.9 \pm 2.9

KINETIC MODELING APPROACH TO *IN VIVO* INTERACTIONS OF CURCUMIN AND
CURCUMINOID-PIPERINE MIXTURE WITH QUETIAPINE

Table 2. The mean \pm S.D. plasma concentration-time values
of norquetiapine across three study groups

Time (h)	NQ Concentration (ng/mL)		
	Reference	Test 1	Test 2
0.16	120.9 \pm 69.8	149.7 \pm 108.4	123.7 \pm 54.8
0.33	192.9 \pm 98.0	212.9 \pm 130.4	219.8 \pm 70.3
0.5	239.8 \pm 97.9	262.1 \pm 127.8	255.3 \pm 86.8
0.75	237.1 \pm 96.4	303.3 \pm 156.0	297.5 \pm 146.9
1.0	230.0 \pm 69.6	338.1 \pm 161.2	331.9 \pm 177.9
1.5	229.1 \pm 72.9	356.6 \pm 169.2	358.1 \pm 168.9
2.0	226.9 \pm 71.5	358.7 \pm 182.6	361.4 \pm 173.4
2.5	224.4 \pm 72.0	352.2 \pm 175.9	330.3 \pm 145.8
3.0	209.2 \pm 65.6	343.0 \pm 166.0	320.1 \pm 146.4
4.0	178.8 \pm 58.4	298.7 \pm 166.6	289.1 \pm 138.1
6.0	135.1 \pm 52.2	234.4 \pm 143.2	236.0 \pm 130.1
8.0	102.8 \pm 56.4	181.2 \pm 150.9	177.2 \pm 125.0
10.0	70.6 \pm 55.6	116.0 \pm 124.5	137.4 \pm 109.0
12.0	41.2 \pm 34.3	61.3 \pm 41.2	68.5 \pm 40.1
16.0	18.2 \pm 15.9	44.3 \pm 50.0	38.9 \pm 14.2
20.0	17.0 \pm 11.2	23.3 \pm 36.4	33.3 \pm 55.2
24.0	5.7 \pm 3.5	22.9 \pm 29.9	30.9 \pm 45.1
30.0	3.8 \pm 1.3	12.0 \pm 21.2	7.1 \pm 6.5

The tested models assumed that the kinetic processes of absorption, elimination, metabolism follow first-order kinetics. In this initial series of kinetic models (M1-M4) developed solely using data related to QUE alone (Reference group), the hypotheses tested were the presence or absence of lag time and the distribution of QUE, either mono- or bicompartmental, as detailed in Table 3.

Table 3. Characteristics and tested hypotheses of kinetic models
for quetiapine (QUE) used in compartmental analysis

Model number	Lag time	Absorption process kinetic order	Number of compartments for QUE distribution
M1	No	1 st Order	1
M2	Yes		1
M3	No		2
M4	Yes		2

In this case, model M2, where QUE exhibited lag time during absorption into the bloodstream from the digestive system and followed a mono-compartmental distribution, yielded the lowest AIC value, as shown in Figure 1. Therefore, it was selected for the next modeling step. The one-compartment model assumes that the body functions as a single, uniform compartment, where the drug is distributed instantly and evenly throughout.

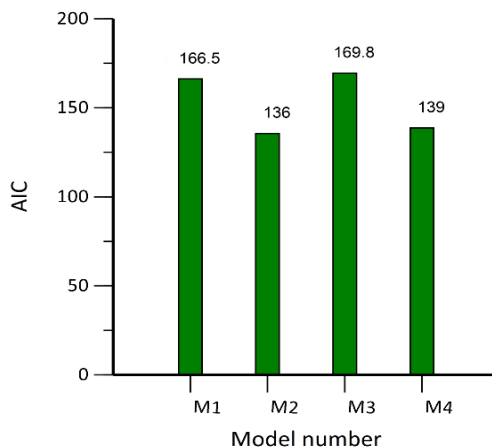


Figure 1. AIC values for kinetic models M1-M4 describing the disposition of quetiapine after a single 85 mg/kg oral dose

In the second step of kinetic modeling, the objective was to identify the most suitable kinetic model for the metabolite NQ while simultaneously integrating the characteristics of QUE disposition (systemic exposure of the drug) determined in the first step. Hypotheses tested included the number of compartments for NQ distribution and its presystemic formation. The characteristics and hypotheses for the NQ models (M21, M22, M23, M24) are detailed in Table 4.

Table 4. Characteristics and tested hypotheses of kinetic models for quetiapine and norquetiapine applied in the second step of compartmental analysis

Model number	Number of compartments for NQ distribution	Presystemic formation of NQ	Systemic metabolism	Other elimination routes for QUE from central compartment
M21	1	No	Yes	Yes
M22	1	Yes	Yes	Yes
M23	2	No	Yes	Yes
M24	2	Yes	Yes	Yes

By incorporating presystemic metabolism into model M22, as opposed to its absence in model M21, the AIC decreased by 30% for the dataset associated with the Reference group. Figure 2 presents the AIC values for the kinetic models tested for the metabolite, highlighting M22 as the most suitable model when including NQ data. This model accounts for the presence of presystemic metabolism in the formation of NQ and its monocompartmental distribution.

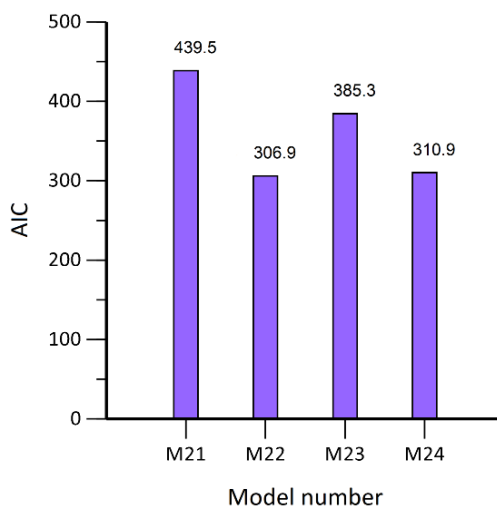


Figure 2. AIC values for kinetic models M21-24 describing the disposition of quetiapine, (administered as a single 85 mg/kg oral dose) and its metabolite, norquetiapine

In the third step, the kinetic model for QUE and NQ, developed in the previous two steps using Reference group data, was further refined by incorporating data from the two Test groups representing QUE's interactions with curcumin (Test 1) and curcuminoids/piperine (Test 2). Data from each Test group was modeled separately alongside the Reference data.

Initially, data from the Reference and Test 1 groups were modeled together. Assuming an identical V_d for both groups, we explored the possibility of differing relative bioavailability due to variations in the absorbed amount of QUE. Accordingly, the M221 and M222 models were developed under the assumption of identical V_d , aiming to test the hypothesis that the absorbed amount of QUE, equivalent to its relative bioavailability, varied between the groups, as shown in Table 5. For modeling the interaction between the Reference and Test 2, the characteristics from the previous

kinetic models and the same hypothesis regarding relative bioavailability were applied. The relative bioavailability was expressed as the ' f_{rel} ' parameter, displayed in Table 6. The following notations were also used for calculated parameters (see Table 6, Figure 6 and Figure 7): f_1 and f_2 represent the fraction of quetiapine converted into norquetiapine via presystemic metabolism for Reference and Tests, t_{lag} is the absorption lag time, k_{31} and k_{64} are the absorption rate constants of quetiapine for Reference and Tests, k_{12} and k_{45} are the systemic metabolism rate constants from quetiapine to norquetiapine for the Reference and Tests, k_{10} and k_{20} are the non-metabolic elimination rate constants of quetiapine and norquetiapine, for the Reference, and k_{40} and k_{50} are the elimination rate constants of quetiapine and norquetiapine for the Tests.

Table 5. Characteristics and tested hypothesis of kinetic models for quetiapine and norquetiapine in compartmental analysis, in the context of quetiapine's interactions with curcumin and the curcuminoid/piperine mixture

Model number	Number of compartments for QUE and NQ	Presystemic metabolism	Volume of distribution	Relative bioavailability
M221	1	Yes	Same	Same
M222	1	Yes	Same	Different

The lower AIC values for M222, as shown in Figure 3, justify the introduction of f_{rel} as a parameter into the kinetic model for both QUE interactions. These values support the inference that there is a different relative bioavailability of QUE between the Reference group and the two Test groups, indicating a difference in the amount of QUE absorbed across these groups.

Thus, M222 was chosen the optimal kinetic model for fitting the experimental data of QUE and NQ across all three experimental groups indicating: lag time for QUE absorption, NQ presystemic formation, monocompartmental distribution for both QUE and NQ, systemic formation of NQ from QUE, elimination of NQ and QUE from their central compartments, and distinct relative bioavailability between the Reference and both Test groups.

KINETIC MODELING APPROACH TO *IN VIVO* INTERACTIONS OF CURCUMIN AND CURCUMINOID-PIPERINE MIXTURE WITH QUETIAPINE

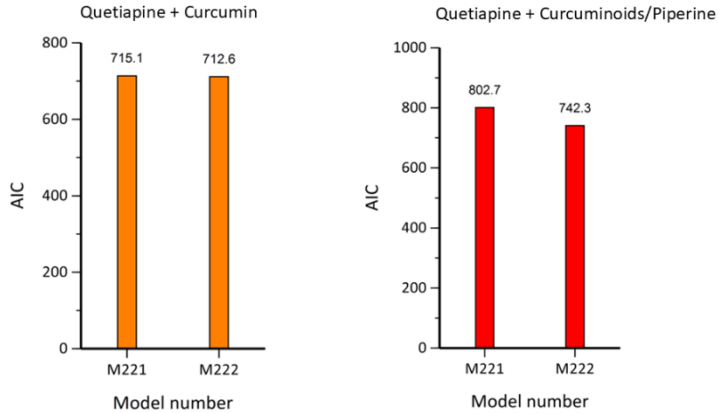


Figure 3. AIC results for compartmental modeling of quetiapine's pharmacokinetic interactions with curcumin (left) and with curcuminoids/piperine (right)

The R-squared values for the observed vs. predicted data of both interactions (Rsq = 0.9861 for Reference and Test 1, and Rsq = 0.9848 for Reference and Test 2), displayed in Figure 4 and Figure 5, respectively, demonstrate the model's predictive accuracy, showing strong agreement between predicted and experimental data.

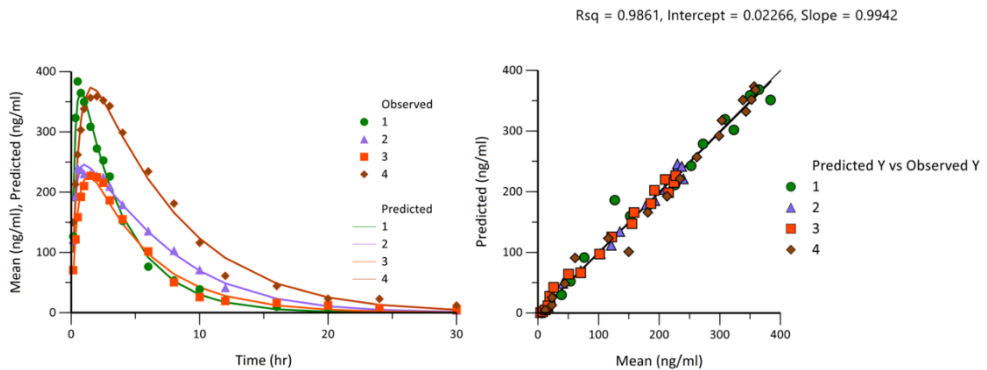


Figure 4. Fitting of M222 for the Reference and Test 1 groups (left) and correlation between experimental data and values predicted by the kinetic model for both groups (right). Legend: quetiapine in the central compartment for the Reference group (1) and Test 1 group (3); norquetiapine in the central compartment for the Reference group (2) and Test 1 group (4)

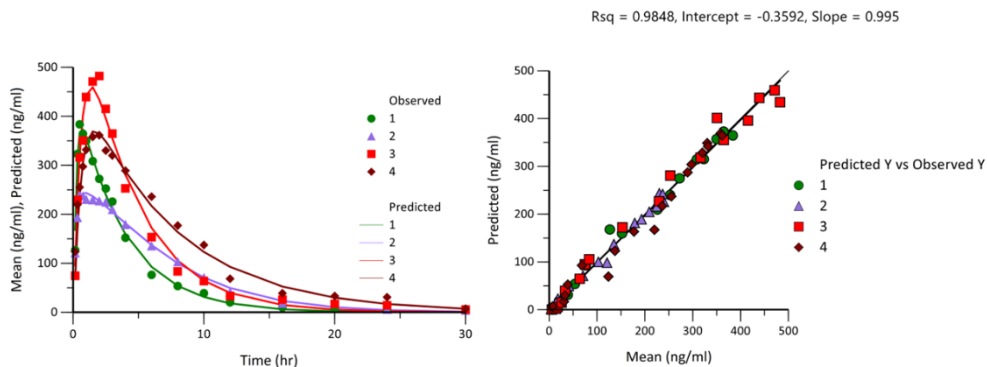


Figure 5. Fitting of M222 for the Reference and Test 2 groups (left) and correlation between experimental data and values predicted by the kinetic model for both groups (right). Legend: quetiapine in the central compartment for the Reference group (1) and Test 2 group (3); norquetiapine in the central compartment for the Reference group (2) and Test 2 group (4)

Table 6. Kinetic parameters of quetiapine and norquetiapine derived from the M222 model in the context of the studied pharmacokinetic interactions

Parameter	U.M.	Estimate for Reference and Test 1	S.E.	Estimate for Reference and Test 2	S.E.
f_1	-	0.4340	0.0125	0.4293	0.0154
f_2	-	0.6628	0.0109	0.4854	0.0106
f_{rel}	-	1.1194	0.0665	1.5967	0.0888
t_{lag}	hr	0.0219	0.0189	0.0663	0.0145
k_{31}	hr^{-1}	3.9700	0.5187	5.2099	0.7758
k_{10}	hr^{-1}	0.1680	0.0838	0.1307	0.0999
k_{12}	hr^{-1}	0.1106	0.0752	0.1408	0.0909
k_{20}	hr^{-1}	0.2105	0.0532	0.2234	0.0654
k_{64}	hr^{-1}	1.8379	0.2064	1.7535	0.1554
k_{40}	hr^{-1}	0.0887	0.2088	0.2434	0.0754
k_{45}	hr^{-1}	0.1200	0.1981	0.0016	0.0676
k_{50}	hr^{-1}	0.1823	0.0681	0.1423	0.0426
Vd	L	106.8405	4.0245	110.0745	4.5440

Modeling the processes underlying drug disposition is a key aspect of pharmacokinetics. Previous studies have employed a one-compartment kinetic model with first-order absorption and elimination for modeling QUE's disposition [11,12]. For instance, in a study involving healthy male adults, plasma QUE concentration–time profiles for immediate-release tablets were effectively

described by a one-compartment distribution model with first-order elimination, supplemented by four transit compartments with first-order transition rate constants to account for delayed absorption [13]. This aspect reinforces the appropriateness of selecting the models which employ a one-compartment distribution (M2 and M22), over M4 or M24, which incorporate a bicompartmental distribution (see Figures 1 and 2). Although the AIC values for the one-compartment models were lower—albeit closely comparable—this further supports their suitability for describing the data.

Comparing the Reference and Test 1 groups, the f_1 and f_2 parameters indicate enhanced presystemic formation of NQ or increased presystemic metabolism of QUE to NQ during Test 1 (43.40% vs. 66.28%). Additionally, k_{64} , the absorption rate constant for QUE during Test 1, was reduced to less than half compared to the reference group ($k_{64} = 1.8379 \text{ hr}^{-1}$ vs. $k_{31} = 3.9700 \text{ hr}^{-1}$). These findings suggest a presystemic interaction mechanism at the intestinal level. Given curcumin's low bioavailability in the absence of absorption enhancers or specialized formulations that increase its systemic availability, these interactions are likely localized at the intestinal presystemic phase. This is further supported by the fact that k_{12} and k_{45} (rate constants for QUE-to-NQ metabolism) remained unchanged between the two study groups, indicating that the systemic metabolism rate was unaffected by the coadministration of QUE and crude curcumin. This minimizes the likelihood of systemic-level interaction involving metabolic enzymes. Furthermore, the f_{rel} parameter reveals a 12% increase in the relative bioavailability of QUE for Test 1. While a lower absorption rate constant (k_a) reflects a less efficient absorption process, an extended duration of absorption may ultimately result in an increased total extent of absorption.

The M222 kinetic model successfully integrated the experimental data for the interaction between QUE and curcuminoids combined with piperine. Similarly, the schematic representation of kinetic processes in Figure 6 (right side) applies to both Test groups. In this case, the relative bioavailability of QUE in Test 2 was 59.6% higher than in the Reference group ($f_{\text{rel}} = 1.596$). The inhibition of hepatic metabolic enzymes, particularly CYP3A4, could explain the increased systemic presence of QUE. The marked reduction in k_{45} compared to k_{12} (0.0016 h^{-1} vs. 0.1408 h^{-1}) supports this hypothesis, suggesting that systemic metabolism might have been inhibited by curcuminoids, potentially with additional contribution from piperine. Furthermore, the reduction in k_{50} compared to k_{20} (0.1423 h^{-1} vs. 0.2234 h^{-1}) suggests that the elimination, specifically the metabolism of NQ, may have also been inhibited by curcuminoids and piperine.

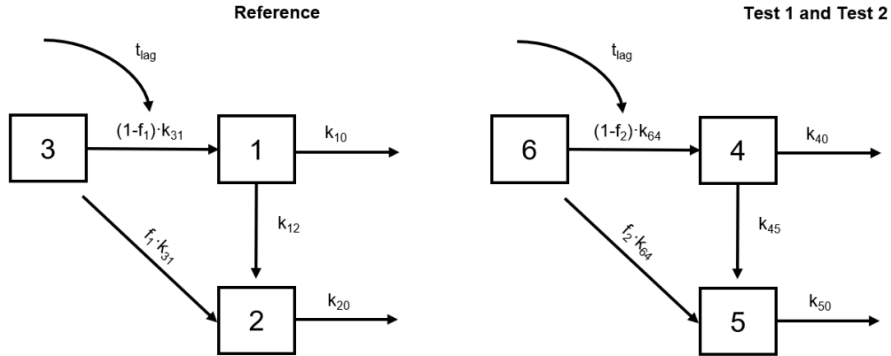


Figure 6. Schematic representation of kinetic processes in the M222 model. On the left is displayed the flowchart for the Reference group. On the right is shown the flowchart for both Test groups; Compartments: “3” and “6” are extravascular absorption sites, “1” and “2” are central compartments for quetiapine and norquetiapine in the Reference group, “4” and “5” are central compartments in the Tests groups

The kinetic models are described by partial differential equations that quantify changes in QUE and NQ concentrations and amounts within each compartment, capturing the processes of absorption, metabolism, and elimination.

$$\text{M222} \left\{ \begin{array}{l} \frac{\partial Q_{Qabs3}}{\partial t} = -k_{31} \times Q_{Qabs3} \\ \frac{\partial Q_{Qc1}}{\partial t} = k_{31} \times (1 - f_1) \times Q_{Qabs3} - k_{10} \times Q_{Qc1} - k_{12} \times Q_{Qc1} \\ \frac{\partial Q_{Nc2}}{\partial t} = k_{31} \times f_1 \times Q_{Qabs3} \times 0.77 + k_{12} \times Q_{Qc1} \times 0.77 - k_{20} \times Q_{Nc2} \\ \frac{\partial Q_{Qabs6}}{\partial t} = -k_{64} \times Q_{Qabs6} \\ \frac{\partial Q_{Qc4}}{\partial t} = k_{64} \times (1 - f_2) \times Q_{Qabs6} - k_{40} \times Q_{Qc4} - k_{45} \times Q_{Qc4} \\ \frac{\partial Q_{Nc5}}{\partial t} = k_{64} \times f_2 \times Q_{Qabs6} \times 0.77 + k_{45} \times Q_{Qc4} \times 0.77 - k_{50} \times Q_{Nc5} \end{array} \right.$$

Figure 7. Mathematical equations for the M222 kinetic model. Q_{Qabs3} and Q_{Qabs6} represent the amount of quetiapine remaining at the absorption sites for Reference and Test groups, respectively. Q_{Qc1} and Q_{Qc6} denote the amount of quetiapine, while Q_{Nc2} , Q_{Nc5} correspond to the amount of norquetiapine in the central compartments for Reference and Test groups. A molar ratio of 0.77 between quetiapine and norquetiapine was applied to convert moles to mass units from metabolic processes.

The rate constants determined previously (Table 6) provide the mathematical foundation for the equations depicted in Figure 7, enabling the time-dependent modeling of QUE and NQ kinetics across compartments. The metabolic conversion from QUE to NQ occurs on a molar basis, while the equations in Figure 7 use mass units. The molar ratio of 0.77 bridges difference, reflecting their molecular weight ratio.

Data for QUE with curcumin and QUE with curcuminoids/piperine resulted in a lower AIC value for the M222 model. The estimated kinetic parameters, together with their standard error (S.E.), for this model are noted in Table 6, while the flowchart in Figure 6 provides the schematic presentation of the model. Additionally, Figure 7 presents the equations that quantify the temporal changes in QUE and NQ amounts within the model's compartments.

CONCLUSIONS

A three-tier kinetic modeling approach was successfully developed to deepen the understanding of QUE disposition during concomitant administration with curcumin or a curcuminoid/piperine mixture found in food supplements. The distribution of both QUE and its active metabolite, NQ, was best described by a one-compartment model with first-order absorption, metabolism and elimination processes. Enhanced presystemic metabolism of QUE to NQ was observed when curcumin was administered alongside QUE. Varying relative bioavailability was determined between the reference group and each of the two test groups. Systemic metabolism of QUE was markedly influenced by curcuminoids and piperine, while the interaction with curcumin was attributed to a presystemic intestinal mechanism. These findings provide valuable insights into the PK interactions of QUE with herbal supplements, offering a foundation for optimizing therapeutic strategies. While specific dose adjustments for QUE cannot yet be recommended when co-administered with curcumin or curcuminoid derivatives, healthcare providers should remain vigilant about potential PK interactions between this antipsychotic and herbal extracts.

EXPERIMENTAL SECTION

Chemicals and reagents. Quetiapine fumarate substance was sourced from Menadiona (Barcelona, Spain). The norquetiapine analytical standard (97.0% purity), haloperidol pharmaceutical primary standard, methanol analytical reagent, and 98% formic acid were procured from Merck (Darmstadt, Germany). Crude curcumin (97% purity) was sourced from Apollo Scientific (Whitefield, UK),

while the curcuminoids and piperine mixture were taken from Curcumin C3 Complex® + piperine (95% curcuminoids, 380 mg, and 5% piperine, 20 mg/capsule) supplied by Herbagetica (Brașov, Romania).

Study design. The preclinical study protocol was approved by the local ethics committee and the Sanitary and Veterinary Directorate in compliance with the applicable regulations (approval number 322/02.08.2022). Experiments were conducted on healthy adult male Wistar albino rats (10-14 weeks old, 300 ± 50 g) under standard laboratory conditions: temperature (21-25°C), humidity (50 ± 30%) and ventilated cages. Housing spaces were cleaned daily and maintained with 12-hour light-dark cycles and noise reduction. Rats were fed a standard pellet diet and had *ad libitum* access to tap water. The *in vivo* experiment involved three groups of 13 healthy male Wistar albino rats: one reference group and two test groups. The reference group received a single oral dose of QUE (85 mg/kg body weight (b.w.)). The first test group was pretreated with daily oral doses of crude curcumin (200 mg/kg b.w.) for 6 days, followed by a single dose of QUE (85 mg/kg b.w.) administered 30 minutes after the last curcumin dose. The second test group received a 6-day pretreatment with an oral curcuminoid/piperine mixture, followed by a single oral dose of QUE (85 mg/kg). QUE fumarate was dissolved in a 3:1:1 (V/V/V) mixture of water, propylene glycol (cosolvent) and lactic acid (for pH adjustment). Curcumin powder and the curcuminoid/piperine mixture, were suspended in 1% carboxymethylcellulose and vortex-mixed for 5 minutes before each administration.

Sample collection and preparation. A total of 18 blood samples (100 µL each) per rat were collected from the femoral vein into heparinized Eppendorf tubes at intervals starting from 10 minutes to 30 hours after single-dose QUE administration. Blood collection was performed using the BASi Culex ABC® Automatic Blood Collector (BASi, Indiana, USA), which necessitates prior vein cannulation surgery under anesthesia. Samples were stored at -20 °C until analysis. Plasma proteins were precipitated by adding 300 µL of methanol to 100 µL blood. The mixtures were vortexed for 10 seconds (IKA Vortex 2, 1000 rpm) and centrifuged at 10.000 rpm (Sigma 3-30KS centrifuge, 9168× g) for 5 minutes. Supernatants were transferred to autosampler vials subsequently analyzed using a HPLC system.

Quantitative determination. Plasma concentrations of QUE and NQ were simultaneously measured using a validated LC-MS/MS method, developed in-house [14] and previously adapted for the quantitation of aripiprazole and dehydroaripiprazole [15]. Chromatographic separation was achieved using an Agilent 1100 series system equipped with a binary pump, autosampler, thermostat and a Zorbax SB-C18 column (100 x 3.0 mm, 3.5 µm) (Agilent Technologies, Santa Clara, CA, USA). Haloperidol, spiked into the blood samples,

served as the internal standard. The mobile phase consisted of 0.3% (m/v) formic acid (eluent A) and acetonitrile (eluent B), eluted in a linear gradient: starting with 10% acetonitrile, increasing to 33% acetonitrile over 3.5 minutes, maintained at 33% until 4.1 minutes, and then re-equilibrated to 10% acetonitrile for 2 minutes. The injection volume was 3 μ L, with a flow rate of 1 mL/min and the column temperature set at 40°C. Detection was conducted using a Bruker Ion Trap SL (Bruker Daltonics GmbH, Bremen, Germany) in multiple reaction monitoring mode, with ESI-MS spectra recorded in positive ion mode. Quantification involved the transitions m/z 253 from m/z 384 for QUE, m/z 253 from m/z 296 for NQ and m/z 165 from m/z 376 for haloperidol. Retention times were 3.0 minutes for NQ and 3.3 minutes for QUE. Calibration curves were linear over the 5–1000 ng/mL range, with correlation coefficients (*r*) of 0.9950 ± 0.0011 for QUE and 0.9935 ± 0.0014 for NQ (mean \pm S.D., *n* = 5).

Data analysis. Kinetic modeling was performed using Phoenix Win Nonlin 8.4 software (Pharsight Company, Mountain View, CA, USA).

The average measured concentration vs. time data for QUE and NQ presented in Table 1 and Table 2 were used to evaluate the disposition parameters of these drugs in the context of their interactions with curcumin derivatives.

A three-tier kinetic modeling approach was conducted to avoid giving rise to excessive number of potential model combinations, which would have rendered the analysis inefficient. To ultimately model QUE and its metabolite, NQ, within the context of their interactions with curcumin and curcuminoids/piperine, intermediate filtering steps were applied. Initially, kinetic models were developed solely for data related to QUE, deliberately omitting its metabolite and the influence of concomitantly administered substances which may interact with QUE disposition. This step provided a foundational framework for integrating additional data and variables in subsequent steps. The hypotheses tested during this initial step focused on the presence or absence of lag time for QUE absorption and its mono- or bicompartamental distribution, as detailed in Table 3. On the next step, the selected kinetic model for QUE was expanded to identify the optimal model for NQ, for its presystemic formation and distribution type (mono- or bicompartamental), as described in Table 4 alongside additional model characteristics. Finally, the best characteristics previously identified, along with testing the hypothesis of different relative bioavailability between the Reference and Test groups (as outlined in Table 5), were used to develop the final kinetic model that best describes the plasma levels of QUE and NQ across the Reference and the two Test groups.

The Akaike Information Criterion (AIC) was employed as the primary method for discrimination between competing models, enabling the determination of the kinetic model that best fit the experimental data. The AIC is a statistical

tool used to quantify the information content of parameter estimates by relating the weighted sum of squares of residuals (WRSS) to the number of parameters used in the model. When comparing two models with differing parameter counts under the same weighting scheme, AIC imposes a penalty on models with more parameters. The penalty ensures that the more complex model must achieve a sufficiently lower WRSS to justify its added complexity. The model deemed most appropriate is the one with the smallest AIC value [16]. The calculation of AIC was performed using Phoenix WinNonlin 8.4 software (Pharsight Company, Mountain View, CA, USA) with the following formula:

$$AIC = m \times \ln (WSSR) + 2 \times p,$$

where m is the number of observations, $WSSR$ is the weighted sum of squares of residuals and p represents the number of estimated parameters included in the model.

Some assumptions were made to simplify the complex interactions between drug molecules and body systems into a set of solvable equations. The one-compartment model with first-order absorption is based on three fundamental assumptions regarding ADME processes: first-order absorption, instantaneous distribution, and first-order elimination kinetics.

All PK models are derived by formulating the governing mass balance equations and solving them mathematically. Their general form can be expressed as:

$$\frac{\partial(\text{Amount of Drug})}{\partial t} = [\text{Rate of Drug In}] - [\text{Rate of Drug Out}]$$

The left side of the equation represents the rate of change in the amount of drug in each compartment, while the right side expresses the net difference between the rates of drug molecules entering and leaving the compartment. For multi-compartment models, a distinct mass balance equation is constructed for each compartment, capturing the specific dynamics of drug movement across the system [9].

ACKNOWLEDGMENTS

This work was supported by an internal research grant offered by “Iuliu Hațieganu” University of Medicine and Pharmacy, Cluj-Napoca, Romania. Research Project no. 882/17/12.01.2022.

REFERENCES

1. Maan JS, Ershadi M, Khan I, et al. Quetiapine. [Updated 2023 Aug 28]. In: StatPearls [Internet]. Treasure Island (FL): StatPearls Publishing; **2024** Jan-. Available online: <https://www.ncbi.nlm.nih.gov/books/NBK459145/> (accessed on 12 Feb 2024).
2. DeVane, C.L.; Nemeroff, C.B. Clinical pharmacokinetics of quetiapine: an atypical antipsychotic. *Clin Pharmacokinet* **2001**, *40*, 509-522, doi:10.2165/00003088-200140070-00003.
3. Mauri, M.C.; Paletta, S.; Di Pace, C.; Reggiori, A.; Cirnigliaro, G.; Valli, I.; Altamura, A.C. Clinical Pharmacokinetics of Atypical Antipsychotics: An Update. *Clinical Pharmacokinetics* **2018**, *57*, 1493-1528, doi:10.1007/s40262-018-0664-3
4. Bakken, G.V.; Molden, E.; Hermann, M. Impact of genetic variability in CYP2D6, CYP3A5, and ABCB1 on serum concentrations of quetiapine and N-desalkylquetiapine in psychiatric patients. *Ther Drug Monit* **2015**, *37*, 256-261, doi:10.1097/ftd.000000000000135.
5. López-Muñoz, F.; Alamo, C. Active metabolites as antidepressant drugs: the role of norquetiapine in the mechanism of action of quetiapine in the treatment of mood disorders. *Front Psychiatry* **2013**, *4*, 102, doi:10.3389/fpsyt.2013.00102.
6. Goswami, S.; Saxena, S.; Yadav, S.; Goswami, D.; Brahmachari, K.; Karmakar, S.; Pramanik, B.; Brahmachari, S. Review of Curcumin and Its Different Formulations: Pharmacokinetics, Pharmacodynamics and Pharmacokinetic-Pharmacodynamic Interactions. *OBM Integrative and Complementary Medicine* **2022**, *07*, 057, doi:10.21926/obm.icm.2204057.
7. Shamsi, S.; Tran, H.; Tan, R.S.J.; Tan, Z.J.; Lim, L.Y. Curcumin, Piperine, and Capsaicin: A Comparative Study of Spice-Mediated Inhibition of Human Cytochrome P450 Isozyme Activities. *Drug Metabolism and Disposition* **2017**, *45*, 49-55, doi:10.1124/dmd.116.073213.
8. Kucukgoncu, S.; Guloksuz, S.; Tek, C. Effects of Curcumin on Cognitive Functioning and Inflammatory State in Schizophrenia: A Double-Blind, Placebo-Controlled Pilot Trial. *J Clin Psychopharmacol* **2019**, *39*, 182-184, doi:10.1097/jcp.0000000000001012.
9. Byers, J.P.; Sarver, J.G. Chapter 10 - Pharmacokinetic Modeling. In *Pharmacology*, Hacker, M., Messer, W., Bachmann, K., Eds.; Academic Press: San Diego, 2009; pp. 201-277.
10. Ahmad, A.M. Recent advances in pharmacokinetic modeling. *Biopharmaceutics & Drug Disposition* **2007**, *28*, 135-143, doi:https://doi.org/10.1002/bdd.540.
11. Methaneethorn, J. Factors Influencing Quetiapine Pharmacokinetic Variability: A Review of Population Pharmacokinetics. *Current Psychiatry Research and Reviews Formerly: Current Psychiatry Reviews* **2024**, *20*, 94-105.
12. Elkomy, M.H. Changing the Drug Delivery System: Does it Add to Non-Compliance Ramifications Control? A Simulation Study on the Pharmacokinetics and Pharmacodynamics of Atypical Antipsychotic Drug. *Pharmaceutics* **2020**, *12*, doi:10.3390/pharmaceutics12040297.

13. Shilbayeh, S.A.; Sy, S.K.; Melhem, M.; Zmeili, R.; Derendorf, H. Quantitation of the impact of CYP3A5 A6986G polymorphism on quetiapine pharmacokinetics by simulation of target attainment. *Clin Pharmacol Drug Dev* **2015**, *4*, 387-394, doi:10.1002/cpdd.172.
14. Ciocotișan, I.-M.; Muntean, D.M.; Gherman, L.-M.; Vlase, L. The influence of multiple-dose oxcarbazepine on the metabolism of single-dose quetiapine. In vivo experiment in rats. *Acta Marisiensis - Seria Medica* **2025**, *71*, 53-59, doi:10.2478/amma-2025-0010.
15. Ciocotișan, I.-M.; Muntean, D.M.; Vlase, L. Bupropion Increased More than Five Times the Systemic Exposure to Aripiprazole: An In Vivo Study in Wistar albino Rats. *Metabolites* **2024**, *14*, doi:10.3390/metabo14110588.
16. Gabrielsson, J.; Weiner, D. Pharmacokinetic and pharmacodynamic data analysis: concepts and applications. 3rd ed. Stockholm: Swedish Pharmaceutical Press; **2001**.

RETINOL DISPERSION IN THE FORM OF HYDROGEL FOR DERMAL DELIVERY

Ioana Lavinia LIXANDRU MATEI^{a,b} ,
Bogdan Alexandru SAVA^{b,c,*} , Andreea Iuliana IONESCU^a,
Codruta SAROSI^d , Gabriel VASILIEVICI^e ,
Marian BĂJAN^f , Daniela Luminița MOVILEANU^f ,
Daniela Roxana POPOVICI^f , Abeer BAIOUNF^g

ABSTRACT. This study reports the development of a dermato-cosmetic hydrogel combining retinol (2% wt) and bioactive glass (1.25% wt) in a Carbopol-based matrix enriched with hyaluronic acid. The formulation was synthesized using high-shear dispersion and evaluated through TGA, DSC, FTIR, and XRD. Thermal analysis indicated strong water-polymer interactions, while FTIR and XRD confirmed amorphous structure favorable for controlled release. The hydrogel showed high conductivity (25000 $\mu\text{S}/\text{cm}$) and alkaline pH (12.4), attributed to its 85% water and triethanolamine content. Turbiscan and microscopy confirmed physical stability. Microbiological tests confirmed sterility. In vivo VISIA analysis on five volunteers over 45 days revealed visible improvements in wrinkles, pores, red areas, UV spots, and porphyrins, with notable changes as early as day 14. These results support the hydrogel's potential for effective and well-tolerated dermal delivery of retinol.

Keywords: *retinol, hydrogel, dermal delivery, stability, bioglass*

^a Botanical SRL, 7 Trandafirilor St., Tatarani, Prahova County, 107059 Romania.

^b University Politehnica Bucharest Splaiul Independenței, 060042 Bucharest, Romania.

^c National Institute of Laser, Plasma and Radiation Physics - INFLPR 409 Atomistilor St., Magurele, Jud. Ilfov, Romania.

^d Babes-Bolyai University, 1 Mihail Kogălniceanu St., 400084 Cluj-Napoca, Romania.

^e National Institute for Research Development for Chemistry and Petrochemistry-ICECHIM-Bucuresti, 202 Spl. Independentei, 060021 Bucharest, Romania.

^f Petroleum-Gas University of Ploiesti, Faculty of Petroleum Refining and Petrochemistry, 39 Bucharest Boulevard, 100515 Ploiesti, Romania.

^g Chemistry Department, Faculty of Science, University of Damascus, Damascus, Syria.

* Corresponding author: bogdan.sava2901@ubb.ro



INTRODUCTION

Retinol is an essential component in dermatological therapies due to its ability to stimulate skin renewal, increase collagen production, and improve the appearance of skin affected by photoaging and acne. However, its clinical use is often limited by side effects, including redness, dryness, and irritation, particularly in those with sensitive skin or weakened epidermal barriers.

To address these negative effects and improve the tolerability of retinoid treatments, new formulation techniques have been introduced. One innovative approach is the use of bioactive glass, a biocompatible substance recognized for its regenerative and anti-inflammatory properties. This material not only aids in skin regeneration but also allows for the controlled release of active ingredients, thereby minimizing irritation and enabling higher doses of retinoids to be used without damaging skin integrity [1- 6].

In a recent case series, Tran Thuy Len et al. assessed the effectiveness of herbal oil-based extracts from *Bambusa vulgaris* (bamboo) leaves as a topical remedy for atopic dermatitis. The findings demonstrated that bamboo leaf extract, when paired with appropriate carriers, significantly alleviated symptoms of atopic dermatitis, such as redness and itching, across various patient demographics. This underscores the potential of incorporating bioactive compounds into dermocosmetic products to enhance therapeutic effectiveness [7].

Another promising approach involves the development of silicone particles specifically designed for encapsulating and controlling the release of retinol. Research conducted by Nasrin Ghouchi Eskandar and colleagues demonstrated that silicone particles created through sol-gel polymerization can effectively encapsulate retinol, safeguarding it from degradation while facilitating its gradual release. This delivery system enhances retinol's stability and minimizes the potential for irritation, thereby offering a more user-friendly option for topical applications [8].

A study conducted by Cook et al. assessed a novel topical formulation that merges retinol with a natural peptide derived from peas and an antioxidant blend. In vitro tests demonstrated an increase in key skin biomarkers, including aquaporin-3, collagen, and elastin, while also reducing the expression of pigmentation-related genes. Clinically, this formulation significantly improved skin hydration, elasticity, and overall appearance without causing irritation [9].

The research conducted by Shields et al. investigated the encapsulation and controlled release of retinol using silicone particles for topical delivery. The authors introduced a novel category of silicone particles created through the sol-gel polymerization of silane monomers, enabling rapid and scalable production with a uniform size distribution (coefficient of variation <20%).

These particles demonstrated a high encapsulation efficiency of over 85% for retinol and significantly improved its stability, with a half-life nine times longer than that of unencapsulated retinol. The study also noted that these silicone particles could encapsulate other active ingredients, highlighting their versatility as a platform for topical drug delivery. This research underscores the potential of silicone particle-based systems in enhancing the stability, controlled release, and tolerability of retinol within dermocosmetic formulations [10].

Kim et al. developed low molecular weight, water-soluble chitosan nanoparticles to encapsulate retinol, achieving over a 1600-fold increase in solubility compared to free retinol. The nanoparticles were spherical in shape, with sizes ranging from 50 to 200 nm, and encapsulation was accomplished through ion complex formation between chitosan and retinol. This method enhanced the stability of retinol, as demonstrated by the absence of its characteristic peaks in Fourier-transform infrared (FT-IR) and nuclear magnetic resonance (NMR) spectroscopy. Moreover, X-ray diffraction (XRD) analysis revealed that the crystalline structure of retinol was modified during encapsulation, indicating a transition to an amorphous state that may improve both stability and bioavailability. These findings underscore the potential of chitosan nanoparticles as an effective delivery system to enhance the stability and solubility of retinol for dermocosmetic applications [11].

Laredj-Bourezga et al. investigated surfactant-free Pickering emulsions stabilized by biodegradable block copolymer micelles—specifically, poly(lactide)-block-poly(ethylene glycol) (PLA-b-PEG) and poly(caprolactone)-block-poly(ethylene glycol) (PCL-b-PEG)—for the targeted delivery of hydrophobic drugs such as all-trans retinol. The emulsions were formulated using two distinct approaches: one method involved encapsulating the drug within oil droplets, while the other incorporated the drug both within oil droplets and within non-adsorbed block copolymer nanoparticles. In vitro skin absorption tests utilizing pig skin biopsies and the Franz cell method, supplemented by confocal fluorescence microscopy, demonstrated that these Pickering emulsions resulted in significantly greater accumulation of retinol in the stratum corneum compared to traditional surfactant-based emulsions and oil solutions. Moreover, loading the drug within both oil droplets and block copolymer nanoparticles enhanced skin absorption, attributed to the additional effects of the free block copolymer nanoparticles containing the drug. This innovative approach facilitates customizable drug delivery to the skin, offering a promising strategy for improving the efficacy and stability of retinol in dermocosmetic formulations [12,13].

Mahmood and Shipman offer a historical perspective on acne vulgaris, emphasizing its persistent presence and the evolving understanding of the condition throughout medical history. The authors trace the acknowledgment

of acne back to ancient civilizations, citing its mention in the Ebers Papyrus from ancient Egypt and its connection to puberty in ancient Greek writings. The article delves into various theories surrounding the causes of acne, including hormonal factors, dietary influences, and hygiene practices, reflecting the changing viewpoints over time. A substantial portion of the discussion is devoted to the discovery and development of retinoids, particularly isotretinoin, highlighting their transformative impact on acne treatment and the pertinent considerations for women's health, especially in relation to pregnancy. The authors conclude by acknowledging the advancements made in acne treatment while also addressing ongoing challenges and the need for continued research in this area [14].

Im et al. conducted a randomized, double-blind, placebo-controlled split-face trial to evaluate the efficacy of a topical herbal cream based on Sasang constitutional medicine for reducing wrinkles in individuals with the So-eum (SE) type. This herbal formulation, which includes a blend of *Zingiber officinale*, *Atractylodes chinensis*, *Curcuma longa*, and *Cinnamomum cassia* (referred to as ZACC extract), was applied to the faces of 21 SE-type participants over a period of 12 weeks. The results revealed significant improvements in skin roughness (R1) and smoothness depth (R4) in the treated areas compared to the placebo, with no reported adverse dermatological reactions. These findings suggest that the ZACC herbal cream may effectively prevent or slow skin aging, including the development of wrinkles, in individuals of the SE type [15].

Building on these findings, the current study explores the effectiveness of a novel dermocosmetic formulation that combines retinol, infused in bioactive glass, to enhance skin appearance. This formulation aims to leverage the synergistic effects of retinol's skin-renewing properties alongside the regenerative capabilities of bioactive glass, providing a promising solution for those seeking effective and tolerable skin rejuvenation treatments. The novelty elements are given by the use of two competing mechanisms for the delayed release of retinol on the surface of the epidermis, namely the reduction of diffusion in the fluid phase by increasing the viscosity of the respective product and the adsorption of retinol in the pores of a powdered adsorbent. Thus, the increase in viscosity was achieved by transforming the retinol solution into a hydrogel based on hyaluronic acid and a copolymer of the Carbopol Aqua SF-1 OS type. The adsorbent used for the controlled release is powdered bioglass, a non-crystalline amorphous solid with various uses in the cosmetic and medical fields.

RESULTS AND DISCUSSION

Thermal Properties

The hydrogel demonstrated a pronounced mass loss during the initial portion of the TGA curve (Figure 1), specifically within the temperature range of 40 °C to 130 °C, with a peak mass loss observed on the differential thermogravimetric (DTG) curve around 125 °C. This significant mass loss is primarily attributed to the evaporation of water. In the subsequent heating phase, spanning from 130 °C to 230 °C, the rate of mass loss diminished, with the maximum loss recorded on the DTG curve at approximately 225 °C. This phenomenon is likely due to the evaporation of various volatile organic compounds, including triethanolamine (TEA). Beyond 230 °C, further mass losses were noted, albeit at a reduced rate, with no additional maxima detected in this temperature range. These losses can be ascribed to both the evaporation of organic compounds carried by the inert gas and the thermal degradation of non-volatile organic constituents such as hyaluronic acid, retinol, and the Carbopol Aqua SF-1 OS polymer, as was suggested by Altaieb [16].

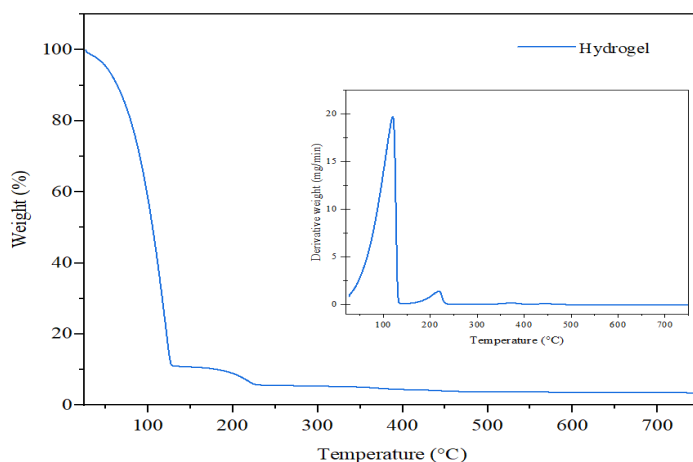


Figure 1. Thermogravimetric analysis of the hydrogel

The impact of the physicochemical characteristics of cosmetic hydrogel on thermal transitions is elucidated through the Differential Scanning Calorimetry (DSC) thermogram, as depicted in Figure 2. Notably, the initial segment of the curve reveals an endothermic peak, characterized by a maximum that occurs at temperatures of approximately 120 °C, attributed to the evaporation of water [17]. The endothermic inflexion point observed at 97 °C is probably indicating a transition within the amorphous matrix. The temperature at which this endothermic

peak is observed is influenced by the nature of the interactions between water molecules and other constituents present in the formulation. The hydrophilic polymer employed in the hydrogel formulation facilitates the retention of water molecules through hydrogen bonding and electrostatic interactions [18,19].

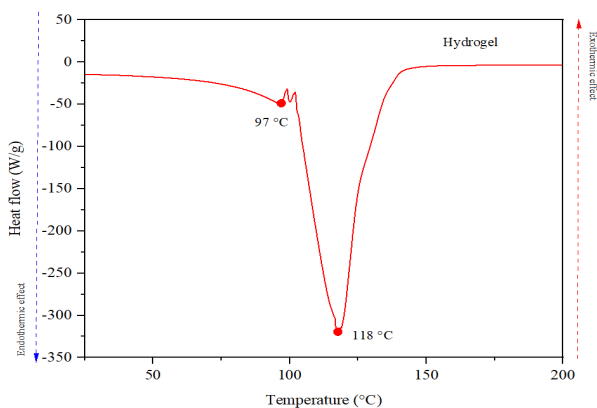


Figure 2. DSC thermogram of the hydrogel

FTIR Analysis

The results of the FTIR analysis, illustrated in Figure 3, reveal that the stretching vibrations observed at 3321 cm^{-1} are associated with the O-H bonds found in both water and triethanolamine (TEA). The presence of amine groups is indicated by the absorption peak at 1639 cm^{-1} , specific to the bending vibrations of the N-H bonds in these functional groups. The existence of carbon in paraffinic structures is indicated by a weak peak at 2085 cm^{-1} , specific to the stretching vibrations of the C-H bonds in methyl or methylene groups.

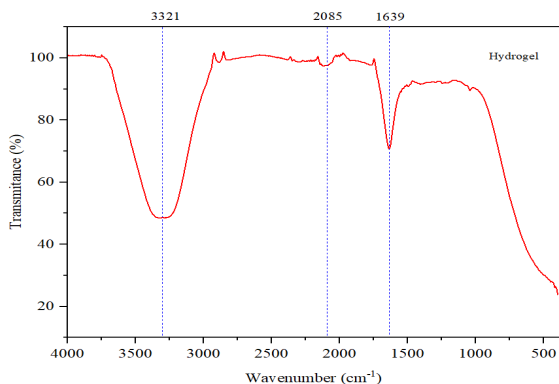


Figure 3. The FTIR spectra of the hydrogel

In the hydrogel, the shift of this band toward lower wavenumber values can be attributed to the incorporation of retinol [20].

XRD Analysis

The hydrogel (Figure 4) exhibits a predominantly amorphous structure, as indicated by X-ray diffraction (XRD) analysis. The XRD pattern reveals a broad and relatively weak peak in the range of 30° to 35° . This characteristic shape of the single broadened peak is consistent with the presence of bioglass, further supporting its classification as an amorphous material [1]. The lack of crystalline structures within the hydrogel is a critical attribute desired in the formulation of this material, as it facilitates the regulated release of nutrients. This characteristic enhances the hydrogel's efficacy in various applications, particularly in controlled delivery systems, by allowing for a more consistent and sustained liberation of active compounds.

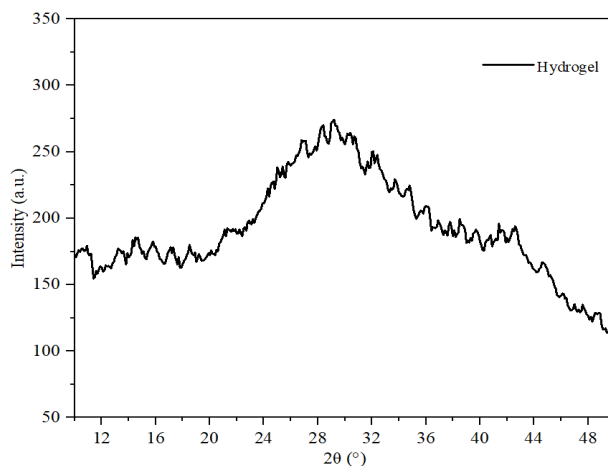


Figure 4. XRD spectra of the hydrogel

Electrical Conductivity and pH

The conductivity and pH values of the sample are the main physical characteristics of the hydrogel. It is evident that the hydrogel demonstrates a relatively high conductivity attributed to its high content of acrylic copolymer in ionized form ($25000 \mu\text{S}/\text{cm}$). That value sufficient mimicking electrical conductivity of some human tissues [21-23]. The hydrogel exhibits a higher pH value, which can be attributed to triethanolamine and acrylates content.

Stability Tests

We examined the variation in backscattering relative to the height of the container holding the analyzed sample, as well as the changes observed over a period of 6 hours with periodic measurements taken each hour. Across all samples, sedimentation was noted in the lower part of the container, with low backscattering values indicating the presence of sediment. At container heights exceeding 10%, backscattering exhibited a marked increase and tended to stabilize throughout the container's height. The maximum backscattering value for the hydrogel was approximately 23%, indicating a low concentration of particles within the sample (refer to Figure 5). For container heights greater than 10 mm, the backscattering curve showed variations within a narrow range of less than 2%, suggesting a relatively high stability of the hydrogel-based dispersion. Additionally, a modest decrease in backscattering over the 6-hour period was observed, amounting to less than 2%. This decline in signal indicates a degree of instability in the hydrogel-based dispersed system.

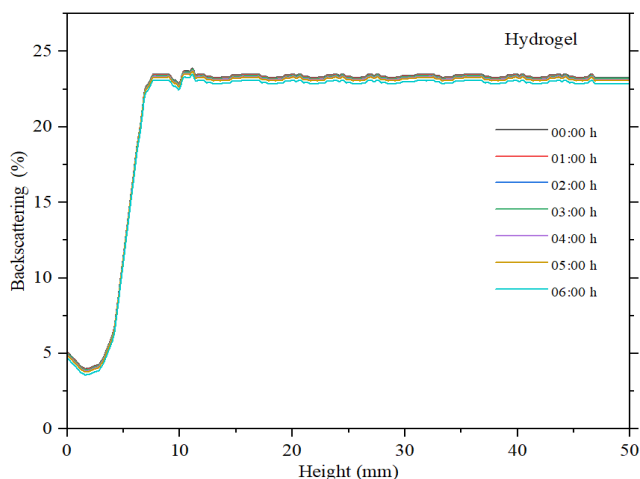


Figure 5. Backscattering curve for hydrogel

Hydrogel Droplet Size

Microscopic analyses performed at 160 \times magnification revealed visible hydrogel droplets predominantly in the size range of 300 to 900 μm . While finer details below this range cannot be resolved with optical microscopy at this magnification, the observed reduction in the apparent abundance of smaller droplets over time suggests coalescence or phase destabilization

phenomena at the microscale. Therefore, the “small droplets” abundance was assessed in a relative manner, based on droplet size appearance and distribution patterns observable under the given optical conditions. This interpretation has been updated accordingly in the discussion section to reflect the physical resolution limits of the employed optical system. (See Figure 6). The formulation was monitored for stability over a period of six hours after preparation, with an intermediate measurement taken at the three-hour mark. A slight trend toward droplet aggregation was observed over time, reflected by a gradual decrease in the proportion of small-sized droplets. The maximum estimation error was found to be 2.3%, based on sample analysis.

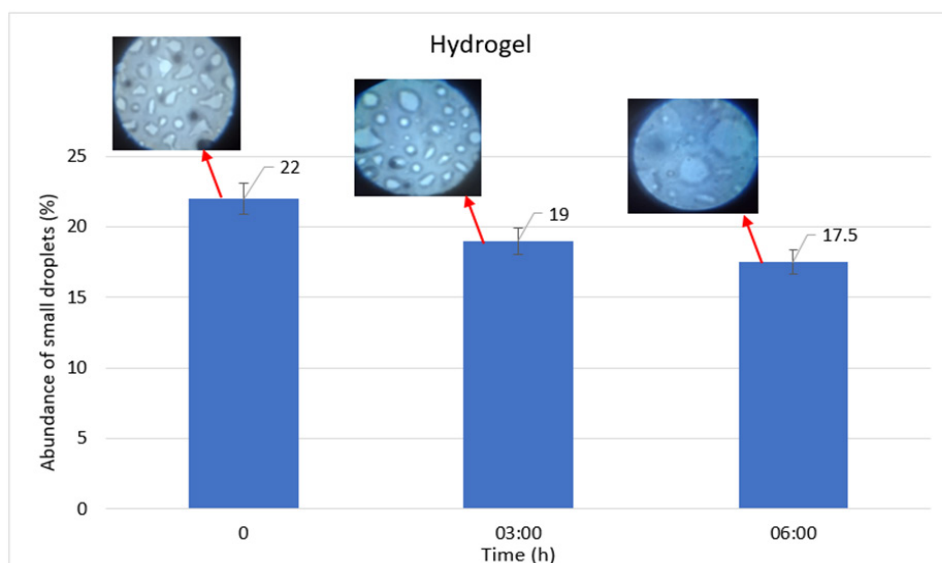


Figure 6. Evolution of the abundance of small droplets in the hydrogel formulation over a 6-hour period, measured at 0, 3, and 6 hours' post-preparation and their microscopically aspect at magnification of 160x.

Dermal Delivery Tests

The hydrogel prepared in the laboratory was applied by five volunteers (one male and four females) over a period of 45 days. The effectiveness of the hydrogel was evaluated using the advanced VISIA imaging system. Thus, a computerized dermal analysis of the skin was performed with the VISIA system.

The parameters obtained from this assessment included wrinkles, texture, pores, and the effects of sun exposure (UV spots, brown spots, and red areas). All tests were conducted in-house (at the Plush Bio laboratory).

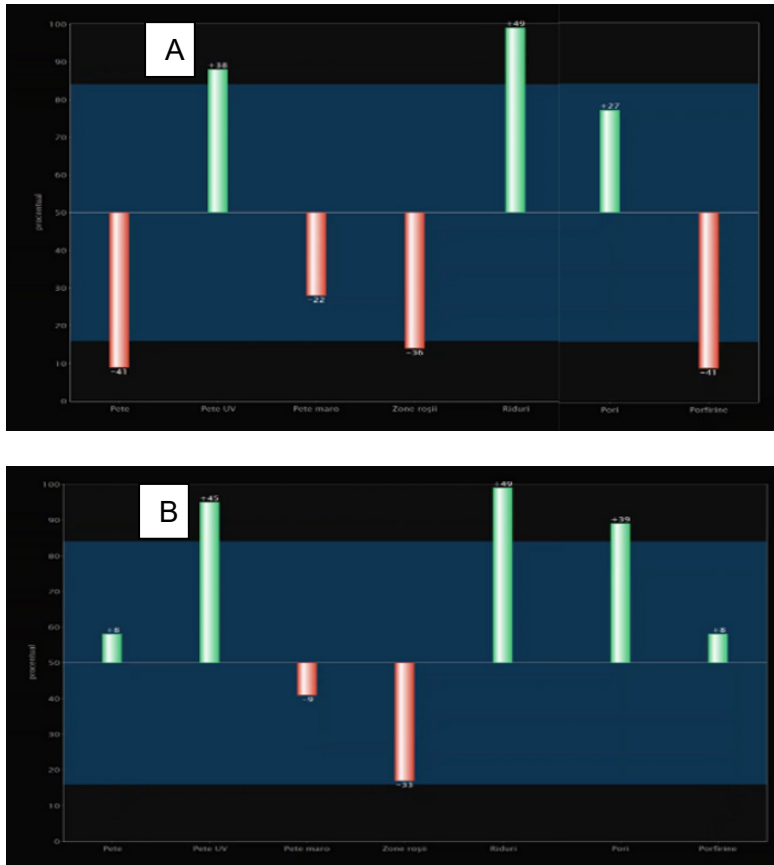


Figure 7. Comparative chart for relative scores: (A) start date – (B) end date

Figure 7 shows the skin evolution of one of the volunteers over a two-week period. The 3D scan captured by the VISIA system indicates a significant improvement in the red areas of the skin.

A comparative progression can thus be observed in terms of UV spots, brown spots, red areas, and porphyrins between the initial and final evaluations (Figure 8).

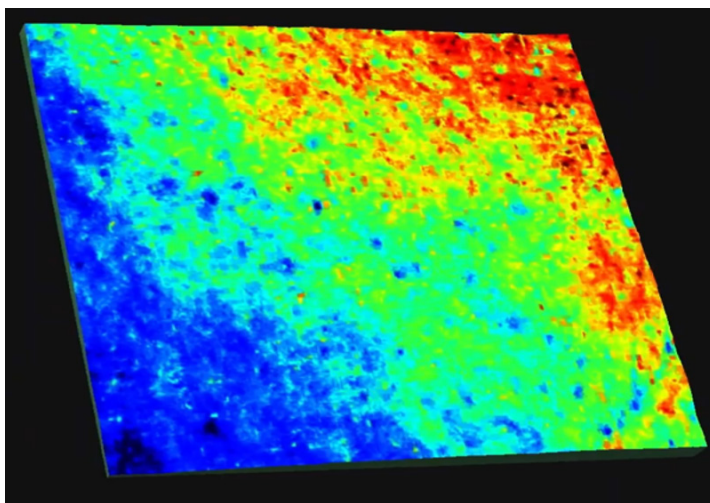


Figure 8. 3D VISIA scan illustrating skin parameter changes after two weeks of hydrogel application.

Discussion

The study investigates the characteristics of dermato-cosmetic formulation, specifically hydrogels, which synergistically incorporate bioglass and retinol. The objective is to mitigate the irritant potential of retinoids while prolonging their therapeutic efficacy for applications within the health and cosmetics industries. A multifaceted approach employing various characterization methods has been utilized to analyze these formulations comprehensively. Analytical techniques, including thermogravimetric analysis (TGA), differential scanning calorimetry (DSC), and X-ray diffraction (XRD), were employed alongside stability. The results indicate that the electrical conductivity of the formulation is influenced by the polarity of the polymer. Thus, the hydrogel exhibited markedly a higher conductivity. The pH values of the formulation were mainly determined by the content of triethanolamine (TEA) in the continuous phase. TGA and DSC analyses suggested a significant change in the temperature at which maximum water loss occurred, indicating strong interactions between water molecules and the polymer present in the hydrogel. Fourier-transform infrared (FTIR) spectroscopy confirmed the presence of Si-O-Ca and Si-O-Si bonds, at 1100 cm^{-1} , consistent with the incorporation of bioglass. XRD analysis was conducted to evaluate the crystallinity of the prepared materials, allowing for a quantitative assessment of any crystalline phases present, including those associated with the bioglass or organic

compounds with high melting points. The absence of diffraction peaks corresponding to oxide structures suggests a completely amorphous structure of the utilized bioglass. Stability analysis of the hydrogel, assessed by backscattering measurements, revealed a relatively low value of backscattering, indicating a low concentration of dispersed particles. The hydrogel demonstrated high stability over a period of six hours, evidenced by minimal variations in backscattering. The skin delivery test performed with the VISIA system to evaluate wrinkles, texture, pores and the effects of sun exposure, such as UV spots, brown spots and red areas, demonstrated a clear progress especially in terms of UV spots, brown spots, red areas and porphyrins compared to the initial evaluation.

CONCLUSIONS

The conditioning of retinol in the presence of bioglass in the form of a hydrogel represents a promising conditioning method for dermatological and cosmetic applications. Thermal and XRD analyses did not indicate the formation of crystalline structures that could hinder the controlled release of retinol. In addition, stability studies performed using the Turbiscan method and optical microscopy demonstrated that the hydrogel exhibits high stability over time. The proposed hydrogel composition showed high efficiency in treating wrinkles, UV spots, brown spots and red areas, where an obvious progress was noted.

EXPERIMENTAL SECTION

Materials and Reagents

Retinol (Merck, $\geq 95.0\%$), Bioglass® powder Schott (NovaMin USA), hyaluronic acid - HA (Oligo-HA4, Sigma-Aldrich), Carbopol Aqua SF-1 OS Polymer (Lubrizol) triethanolamine - TEA (Merck, reagent grade, 97%), and ultra-pure water, WIFI quality water (Pixico, Romania) were used for the synthesis of hydrogel.

Synthesis of Hydrogel

A hydrogel was prepared through mechanical stirring using an IKA 18 ULTRA-TURRAX digital disperser (IKA-Werke GmbH & Co. KG, Staufen,

Germany) at a speed of 9000 rpm and a temperature of 40 °C for a duration of 30 minutes. The composition and concentration of the components in the resulting hydrogel are outlined in Table 1.

Table 1. Recipes of the hydrogel

Component	Hydrogel (%wt.)
Distilled water	85.00
TEA	5.00
Retinol	2.00
Bioglass	1.25
Hyaluronic acid	0.50
Carbopol Aqua SF-1 OS	6.25

Characterization Methods

The following analyses were performed for the hydrogel obtained in the study: thermogravimetric analysis (TGA), differential scanning calorimetry (DSC), Fourier transform infrared spectroscopy (FTIR), X-ray diffraction (XRD), electrical conductivity, pH, stability analyses, and microbiological analyses.

Thermogravimetric analysis for DE, RE and hydrogel were performed with Thermal Analysis System TGA 2 apparatus from METTLER TOLEDO (Greifensee, Switzerland), in the 25–700 °C temperature range, in a nitrogen atmosphere, with a heating rate of 10 °C/min.

Differential scanning calorimetry was performed to investigate temperature induced transitions. The analysis was conducted using a Thermal Analysis System DSC 3+ from Mettler Toledo (Greifensee, Switzerland). The samples were heated from room temperature to 400 °C at a rate of 1 °C per minute in a nitrogen atmosphere.

For the qualitative analysis of the materials, Fourier Transform Infrared was used to identify the functional groups present in the structures. The analysis was conducted using a Shimadzu IRAffinity-1S spectrophotometer (Kyoto, Japan), which was equipped with the GladiATR-10 accessory. The measurements were taken within the wavelength range of 380 to 4000 cm^{-1} , with a spectral resolution of 4 cm^{-1} .

Determination of the conductivity and pH of the hydrogel was performed with the inoLab Multi 9630 IDS (Germany) multimeter. The electrode used for pH is SeTix 980 with glass rod and temperature sensor. The conductivity cell was WTW IDS TetraCon 925.

The degree of crystallinity of the prepared materials was determined by X-ray diffraction performed with a Bruker X-ray diffractometer (Bruker-AXS, Karlsruhe, Germany) equipped with a Cu-K α source at 40 kV and 5 mA, 2 θ range 10°– 50° at a rate of 1 °/ minute.

The stability of the hydrogel was evaluated using the Turbiscan Lab Expert Formulation (Toulouse, France). This provided insights into the tendencies of sedimentation, coalescence, or aggregation of the components in the hydrogel recipe. The colloidal stability of the studied systems was achieved by measuring the backscattering diffusion. Thus, by measuring the amount of light scattered back by the particles in emulsions or hydrogel, the tendency of their stability to change over time is evaluated.

Microscopic visualization of particle abundance was evaluated using a CELESTRON Microscope (Celestron, Torrance, CA, USA), model 4434, along with a Thoma Marienfeld counting chamber. Particles were visualized with green G53 and blue filters AE5202 within a magnification range of 40X to 160X, following an appropriated method [24,25]. Dermal analysis was performed computerized with the VISIA system.

Statistical Analysis

Both the pH and electrical conductance stability were evaluated through three consecutive measurements. The results were subsequently used to calculate experimental errors using the standard deviation statistical function, which provides insight into the dispersion of the data around the mean values. To assess whether the standard deviation is high or low, indicating that the values are either widely varied or closely clustered around the mean, the coefficient of variation was employed [26].

REFERENCES

1. I. L. Lixandru Matei; B. A. Sava; C. Sarosi; C. Duşescu-Vasile; D. R. Popovici; A. I. Ionescu; D. Bomboş; M. Băjan; R. Doukeh; *Nanomaterials*; **2024**, *14*, 1323.
2. M.M. Don; C. Y.San; J .Jeevanandam; Chapter 8 - Antimicrobial properties of nanobiomaterials and the mechanism, in *Nanobiomaterials in Antimicrobial Therapy Applications of Nanobiomaterials*; 1st Edition, Elsevier Inc. All, **2016**, *6*, 261-312.

3. J.R. Jones; D. S. Brauer; L. Hupa; D. C. Greenspan; *Inter.J. of Appl. G. Sci.*, **2016**, 7, 405-544.
4. L. L. Hench; *New Journal of Glass and Ceramics*; **2013**, 3, 67-73.
5. EP1272144A4/**2006**, New cosmetic body cleaning agent and food supplements containing bioactive glass and methods for the preparation and use there of; *European Patent Office*, <https://patents.google.com/patent/EP1272144A4/en>, accessed at 11.06.2025.
6. M. Matinfar; A. Elias ; J. A. Nychka; *Materials & Design*; **2025**, 253, 113919.
7. T.T. Len; H. N. Nhung; T. C.Thanh; *Phytomedicine Plus*, **2023**, 3, 100480.
8. N. G. Eskandar; S. Simovic; C. A. Prestidge; *Int. J. of Pharma*, **2009**, 376, 186-194.
9. B. Cook; M. Riggs; K.C. Holley; *Dermatol Ther (Heidelb)*, **2025**, 15, 189–200.
10. C. Wyatt Shields; J. P. White; E. G. Osta; J. Patel; S. Rajkumar; N. Kirby; J.-P. Therrien; S. Zauscher; *J. of Contr. Rel.*, **2018**, 278, 37-48.
11. D. G. Kim; Y.I. Jeong; C. Choi; S.H. Roh; S.K. Kang; M.K. Jang; J.W. Nah; *Inter. J. of Pharma*, **2006**, 319, 130-138.
12. F. Laredj-Bourezg; M.A.Bolzinger; J. Pelletier; J.P. Valour; M.R. Rovère; B. Smatti; Y. Chevalier; *Inter. J. of Pharma.*, **2015**, 496, 1034-1046.
13. F. Nicolescu; F. Lupu; O Pantea; C.G. Gheorghe; A. Bondarev; C. Calin; *Rev. Chim.*, **2015**, 66, 1181-1183.
14. N.F. Mahmood; A.R. Shipman; **2017**, 3, 71-76.
15. A.R. Im; K.Y. Ji; J. Nam; J. Yoon; S. Cha; Y. K. Seo; S. Chae; J. Y. Kim; *Integrative Medicine Research*, **2022**, 11, 100752.
16. H.A. Altaieb; *J.of Sau. Chem. Soc.*, **2024**, 28, 101852.
17. P. Ahmadi; A. Ahmadi; M. Tabibiazar; S. Hamidi; S. Ramezani; *Carbohydr Polym*, **2025**, 353, 12324.
18. E.Verni; F. Sabatini; C. Lee; G. Fiocco; M. L.Weththimuni; B.Vigani; H. Lange; M. Malagodi; F. Volpi; *Carbohydr. Polym. Tech.s and Appl.*, **2025**, 100875.
19. Y. Enomoto-Rogers; Y. Ohmomo; T. Iwata; *Carbohydr. Polym*, **2013**, 92, 1827–1834.
20. W.Chieng; N.A. Ibrahim; W. M. Z. W. Yunus; M. Z. Hussein; *Polym*, **2014**, 6, 93-104
21. H. Xu; J.M. Holzwarth; Y. Yan; P. Xu; H. Zheng; Y. Yin; S. Li; P.X. Ma; *Biomat*, **2014**, 35, 225–235
22. C. Ramon; P. Gargiulo; E.A. Fridgeirsson; J. Haeisen; *Front. Neuroeng*; **2014**, 7, 32
23. E. V. Parfenyuk; E.S. Dolinina; *Mat. Chem. and Phys.*, **2025**, 342, 130981
24. V. Gheorghe; C.G. Gheorghe; A. Bondarev; R. Somoghi; *Toxics*, **2023**, 11, 285
25. V. Gheorghe; C.G. Gheorghe; D.R. Popovici; S.Mihai; C. Calin; E.E. Sarbu; R. Doukeh; V. Matei; N. Grigoriu; C.N.Toader; C. Epure; *Toxics*, **2023**, 11, 672.
26. D.R. Popovici; C.G. Gheorghe; C.M. Duşescu-Vasile; *Bioengineering*, **2024**, 11, 1306.

CHEMICAL CHARACTERIZATION AND DETERGENT POTENTIAL OF *CHELIDONIUM MAJUS* EXTRACTS

Anca BECZE^{a*} , Dorina SIMEDRU^a ,
Liviu BÎLTEANU^b , Paul UIUIU^c 

ABSTRACT. The present study investigates the impact of different extraction methods—accelerated solvent extraction (ASE), ultrasound-assisted extraction (UAE), and maceration on the yield, phytochemical composition, antioxidant activity, and antimicrobial potential of *Chelidonium majus* extracts. ASE demonstrated the highest extraction yield (85.7%) and alkaloid content (5.4 mg AE/ml), correlating with enhanced antimicrobial activity against *Escherichia coli*, *Staphylococcus aureus*, and *Candida albicans* (lowest MIC values: 3.12%, 2.50%, and 6.25%, respectively). UAE resulted in the highest polyphenol content (15.2 mg GAE/ml) and antioxidant capacity (12.8 ± 1.5 $\mu\text{mol Trolox/ml}$), suggesting its effectiveness in preserving antioxidant compounds. Maceration produced the lowest bioactive compound yield and biological activity. These findings indicate that ASE is optimal for antimicrobial applications, while UAE is preferable for antioxidant-enriched extracts. The results provide valuable insights for optimizing *C. majus* extraction in pharmaceutical, food, and cosmetic formulations.

Keywords: *Chelidonium majus*, accelerated solvent extraction, ultrasound-assisted extraction, alkaloids, flavonoids, polyphenols, antimicrobial activity, antioxidant capacity, extraction efficiency

^a National Institute for Research and Development of Optoelectronics INOE 2000, Research Institute for Analytical Instrumentation, 67 Donath Str., RO-400293 Cluj-Napoca, Romania

^b BEST CLEAN EUROPE Ltd., located in Florești, Cluj County, Romania

^c Department of Fundamental Sciences, Faculty of Animal Science and Biotechnologies, University of Agricultural Sciences and Veterinary Medicine Cluj-Napoca, 3-5 Mănăștur Street, RO-400372 Cluj-Napoca, Romania

* Corresponding author: anca.naghiu@icia.ro



INTRODUCTION

Chelidonium majus L., commonly known as Greater Celandine, is a perennial herbaceous plant belonging to the Papaveraceae family. It has been traditionally used in herbal medicine due to its diverse pharmacological properties, including antimicrobial, anti-inflammatory, antioxidant, and antifungal activities. The plant is widely distributed across Europe and Asia, thriving in temperate climates and commonly found in meadows, forest edges, and near human settlements [1, 2].

The bioactive potential of *C. majus* is attributed to its rich phytochemical composition, predominantly consisting of alkaloids, flavonoids, saponins, and essential oils [1, 3]. The most notable compounds in *C. majus* are isoquinoline alkaloids, including chelidonine, sanguinarine, berberine, chelerythrine, and coptisine, which exhibit strong antimicrobial and antifungal effects [4, 5]. These alkaloids are responsible for the plant's characteristic yellow-orange latex, which has been historically used for its therapeutic benefits [6, 7].

In addition to alkaloids, *C. majus* contains significant amounts of flavonoids and polyphenolic compounds, which contribute to its antioxidant properties [1, 8, 9]. These bioactive molecules scavenge free radicals and provide stability to formulations that are prone to oxidative degradation. The presence of saponins further enhances the plant's detergent potential by acting as natural surfactants with foaming and emulsifying properties [10].

Given its unique chemical profile, *C. majus* presents a promising alternative to synthetic detergent additives. Its natural surfactant-like components, antimicrobial properties, and antioxidant capacity make it a viable candidate for eco-friendly detergent formulations [11]. However, a thorough chemical characterization and functional assessment are necessary to evaluate its suitability in detergent applications.

The growing demand for eco-friendly and sustainable cleaning products has led to increased research on plant-derived detergent ingredients [12,13]. Various plant-based compounds, such as saponins, flavonoids, and essential oils, have been explored for their surfactant, antimicrobial, and antioxidant properties, making them viable alternatives to synthetic detergent components [14]. Saponin-rich plants, such as *Sapindus mukorossi* (soapnut), *Quillaja saponaria* (soapbark tree), and *Glycyrrhiza glabra* (licorice), have been extensively studied for their natural foaming and emulsifying abilities, demonstrating their effectiveness in household and personal care formulations [15-18]. Studies have also highlighted the antimicrobial potential of plant extracts, particularly those containing alkaloids, tannins, and phenolics, which can enhance the hygienic properties of detergents by inhibiting bacterial and fungal growth [19, 20].

Several investigations have focused on the integration of essential oils from plants like *Eucalyptus globulus*, *Cymbopogon citratus* (lemongrass), and *Thymus vulgaris* (thyme) due to their broad-spectrum antimicrobial activity and pleasant aromatic properties [21, 22]. These essential oils have shown promising results in inhibiting common detergent contaminants such as *Escherichia coli*, *Staphylococcus aureus*, and *Candida albicans*, thus contributing to the formulation of natural disinfectant detergents [23, 24]. Additionally, polyphenolic-rich extracts from plants like *Camellia sinensis* (green tea) and *Punica granatum* (pomegranate) have been investigated for their antioxidant stability, preventing oxidative degradation of detergent formulations and enhancing product shelf life [25, 26].

While extensive research has been conducted on these plant-based surfactants and antimicrobial agents, fewer studies have explored the potential of alkaloid-containing plants such as *C. majus* for detergent applications. Given its rich composition of isoquinoline alkaloids, saponins, and flavonoids, *C. majus* represents a novel and underexplored candidate for natural detergent formulations. This study seeks to fill this research gap by evaluating its chemical composition, surfactant properties, and antimicrobial potential in detergent applications.

RESULTS AND DISCUSSION

Extraction Yield and Phytochemical Composition

The extraction efficiency and phytochemical composition of *C. majus* extracts varied depending on the method employed (Table 1). Accelerated Solvent Extraction (ASE) demonstrated the highest extraction yield (85.7%), significantly surpassing Ultrasound-Assisted Extraction (UAE) (72.3%) and Maceration (68.5%). This trend indicates that high pressure and controlled temperature in ASE enhance solvent penetration, leading to a more efficient recovery of bioactive compounds.

ASE produced the highest alkaloid concentration (5.4 mg AE/ml), followed by UAE (4.1 mg AE/ml) and maceration (3.2 mg AE/ml). Given that alkaloids such as chelidonine, sanguinarine, and chelerythrine contribute to antimicrobial activity, the higher yield in ASE correlates with the stronger antimicrobial properties observed in MIC testing. The total flavonoid concentration was highest in ASE (9.3 mg QE/ml), indicating that high-pressure extraction preserves and extracts a broader range of flavonoids. UAE was slightly lower (8.8 mg QE/ml), while maceration resulted in the lowest yield (8.5 mg QE/ml). Flavonoids are potent antioxidants, making these results relevant for applications

in detergent formulations requiring oxidative stability. UAE extracts had the highest total polyphenol content (15.2 mg GAE/ml), followed by ASE (14.1 mg GAE/ml) and maceration (12.5 mg GAE/ml). The superior performance of UAE in polyphenol recovery is attributed to ultrasound-induced cell wall disruption, allowing a more efficient release of these bioactive compounds. The pH of all extracts remained in a narrow range (5.5–5.8), which is considered suitable for detergent formulations. Maintaining a balanced pH is essential to ensure product stability and compatibility with surfactants, as extreme pH variations could affect the performance and shelf-life of the formulation (Figure 1).

Table 1. Extraction Yield and Phytochemical Composition of *C. majus* Extracts

Extraction Method	Polyphenol Yield (%)	Total Alkaloids (mg AE/ml)	Total Flavonoids (mg QE/ ml)	Total Polyphenols (mg GAE/ ml)	pH
Maceration (5 h, 22–25°C)	68.5 ± 10.2	3.2 ± 0.4	8.5 ± 0.8	12.5 ± 1.0	5.8 ± 0.2
UAE (1 h, 45°C)	72.3 ± 8.5	4.1 ± 0.5	8.8 ± 0.9	15.2 ± 1.2	5.6 ± 0.1
ASE (35°C, 10.3 MPa)	85.7 ± 9.8	5.4 ± 0.6	9.3 ± 0.7	14.1 ± 1.3	5.5 ± 0.1

Extraction Yield and Phytochemical Composition of *Chelidonium majus* Extracts

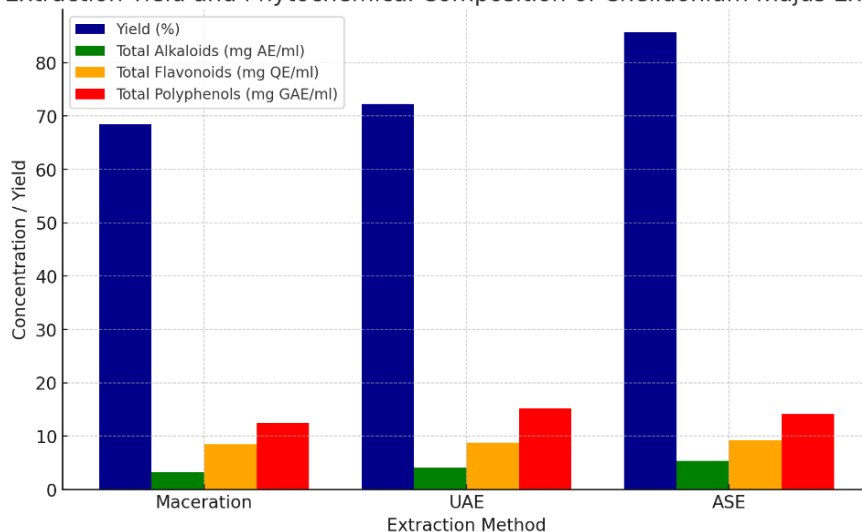


Figure 1. Extraction yield and phytochemical composition of *C. majus* extracts

CHEMICAL CHARACTERIZATION AND DETERGENT POTENTIAL OF
CHELIDONIUM MAJUS EXTRACTS

The higher yield and alkaloid content in ASE extracts suggest that high-pressure conditions enhance the extraction of bioactive compounds with antimicrobial properties, supporting their application in eco-friendly detergent formulations. Meanwhile, UAE appears to be the most effective in polyphenol extraction, making it a preferable method for producing antioxidant-rich extracts.

In comparison, a study by Boia et al. identified 74 phytochemicals in Romanian wild-grown *C. majus*, including alkaloids, amino acids, phenolic acids, flavonoids, carotenoids, fatty acids, sterols, and others. However, this study did not specify extraction yields or compare different extraction methods [2].

Another study evaluated various extraction techniques—aqueous and alcoholic extraction, supercritical fluid extraction, pressing-centrifugation, and microwave extraction—but did not provide specific yields or phytochemical concentrations for comparison [27].

Antimicrobial Activity (MIC Values)

The antimicrobial potential of *C. majus* extracts obtained through maceration, ultrasonic-assisted extraction (UAE), and accelerated solvent extraction (ASE) was evaluated against *Escherichia coli* (Gram-negative), *Staphylococcus aureus* (Gram-positive), and *Candida albicans* (fungal species). The results of the minimum inhibitory concentration (MIC) assay are summarized in Table 2. The MIC values are expressed as % (v/v), representing the volume of extract per volume of testing solution (e.g., 6.25% extract means 6.25 μ L extract in 100 μ L total solution).

Table 2. Minimum Inhibitory Concentration (MIC) of *C. majus* Extracts (v/v %)

Microorganism	Maceration	UAE	ASE	Positive Control
<i>E. coli</i>	12.5% \pm 1.2	6.25% \pm 0.8	3.12% \pm 0.6	Ampicillin (2 μ g/ml)
<i>S. aureus</i>	10.0% \pm 1.0	5.00% \pm 0.7	2.50% \pm 0.5	Vancomycin (1 μ g/ml)
<i>C. albicans</i>	25.0% \pm 1.5	12.5% \pm 1.0	6.25% \pm 0.8	Fluconazole (1 μ g/ml)

The data demonstrate that the antimicrobial efficacy of *C. majus* extracts was strongly influenced by the extraction method used. ASE consistently exhibited the lowest MIC values across all tested microorganisms, indicating the highest antimicrobial potency, followed by UAE, while maceration resulted in the weakest inhibitory effect (Figure 2).

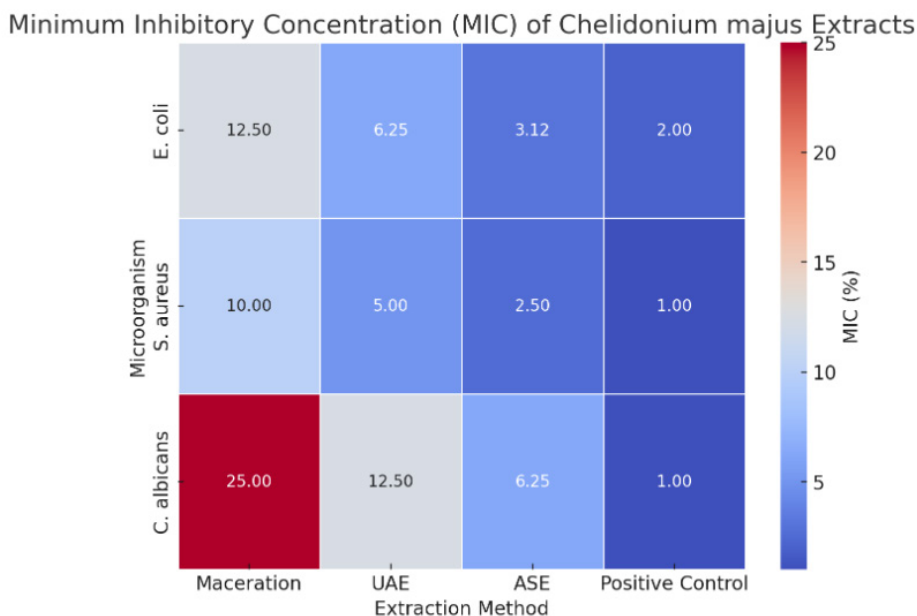


Figure 2. Minimum Inhibitory Concentration (MIC) of *C. majus* extracts

The ASE extract displayed the strongest inhibition of *E. coli* (MIC = $3.12\% \pm 0.6$), while UAE showed moderate efficacy (MIC = $6.25\% \pm 0.8$), and maceration exhibited the highest MIC ($12.5\% \pm 1.2\%$). The Gram-negative bacterial cell wall, which contains an outer membrane rich in lipopolysaccharides, is known to limit the penetration of antimicrobial compounds, which may account for the relatively higher MIC values compared to *S. aureus*. However, ASE-extracted bioactive compounds approached the inhibitory strength of the positive control (ampicillin, $2 \mu\text{g/ml}$), suggesting its potential as a natural antibacterial agent.

The extracts demonstrated higher inhibition against *S. aureus* compared to *E. coli*, with ASE again yielding the lowest MIC ($2.50\% \pm 0.5\%$), followed by UAE ($5.00\% \pm 0.7\%$) and maceration ($10.0\% \pm 1.0\%$). The increased sensitivity of *S. aureus* is likely due to the lack of an outer membrane, making it more susceptible to plant-derived alkaloids and polyphenols. The MIC of ASE was relatively close to vancomycin ($1 \mu\text{g/ml}$), suggesting the extract's strong antibacterial potential against Gram-positive pathogens.

The antifungal activity of the extracts followed the same trend as antibacterial efficacy, with ASE showing the lowest MIC ($6.25\% \pm 0.8\%$), UAE demonstrating moderate inhibition ($12.5\% \pm 1.0\%$), and maceration being the least effective ($25.0\% \pm 1.5\%$). These results indicate that higher

extract concentrations were required for fungal inhibition compared to bacteria, possibly due to the thicker fungal cell wall composed of chitin and glucans, which provides structural resistance. Despite showing promising antifungal activity, the extracts did not reach the potency of the positive control fluconazole (1 µg/ml).

One-way ANOVA followed by Tukey's post-hoc test confirmed statistically significant differences ($p < 0.05$) among extraction methods, with ASE extracts exhibiting significantly lower MIC values compared to UAE and maceration. These findings highlight the superior efficiency of ASE in extracting antimicrobial bioactives from *C. majus*.

Similarly, a study by Krzyżek et al. (2021) found that *C. majus* extracts demonstrated antimicrobial activity against *Helicobacter pylori*, with MIC value of 128 µg/ml for root extracts [28]. This aligns with our findings that *C. majus* extracts possess significant antimicrobial properties [1].

Antioxidant Activity

Table 3 shows the antioxidant capacity in Trolox equivalents. The antioxidant capacity of *C. majus* extracts varied significantly depending on the extraction method employed, as measured in µmol Trolox/ml extract. Among the three methods tested, ultrasound-assisted extraction (UAE) exhibited the highest antioxidant capacity (12.8 ± 1.5 µmol Trolox/ml), followed by accelerated solvent extraction (ASE) (10.9 ± 1.3 µmol Trolox/ml), while maceration resulted in the lowest antioxidant yield (8.5 ± 1.2 µmol Trolox/ml). These findings highlight the crucial role of extraction technique in maximizing the recovery of bioactive compounds with antioxidant properties.

Table 3. Antioxidant Capacity of *C. majus* Extracts

Extraction Method	Antioxidant Capacity (µmol Trolox/ml extract)
Maceration	8.5 ± 1.2
UAE	12.8 ± 1.5
ASE	10.9 ± 1.3

A study by Dumitru and Gănescu assessed the antioxidant activity of alcoholic extracts of *C. majus* flowers using the DPPH method and found notable antioxidant activity, though specific values were not provided [2].

CONCLUSIONS

The extraction method significantly influenced the yield, phytochemical composition, antioxidant capacity, and antimicrobial activity of *C. majus* extracts. Accelerated solvent extraction (ASE) demonstrated the highest overall yield (85.7%) and alkaloid content (5.4 mg AE/ml), correlating with its superior antimicrobial activity (lowest MIC values). Ultrasound-assisted extraction (UAE) was the most effective for polyphenol recovery (15.2 mg GAE/ml) and exhibited the highest antioxidant capacity (12.8 ± 1.5 μ mol Trolox/ml).

ASE extracts showed the strongest antimicrobial activity, particularly against *E. coli*, *S. aureus*, and *C. albicans*, likely due to their higher alkaloid and flavonoid content. In contrast, UAE produced extracts with enhanced antioxidant properties, suggesting its suitability for applications where oxidative stability is critical. Maceration yielded the lowest bioactive compound recovery and biological activity.

Overall, ASE is optimal for antimicrobial-rich extracts, while UAE is preferable for antioxidant applications. These findings provide a basis for selecting appropriate extraction techniques depending on the intended application of *C. majus* bioactive. Future studies should explore the stability and bioavailability of these extracts in formulated products.

EXPERIMENTAL SECTION

Plant Material and Extraction

Collection and Preparation of *C. majus* Samples

The aerial parts of *C. majus* were collected from the Cluj County area during the optimal harvesting period, which typically falls between May and July when the plant reaches peak biosynthesis of bioactive compounds such as alkaloids, flavonoids, and saponins. Fresh plant material was air-dried in a well-ventilated, shaded area to prevent degradation of thermolabile compounds. The dried samples were then ground into a fine powder to facilitate efficient extraction.

Reagents

All solvents were sourced from VWR (Darmstadt, Germany), while ultra-pure water was obtained using the ULTRACLEAR UV UF EVOQUA Purification System (Pittsburgh, PA, USA). The ACL Kit was supplied by Analytik Jena (Jena, Germany). All other standards used in the analysis were purchased from Sigma-Aldrich (Saint Louis, MO, USA).

Extraction Methods

To assess the efficiency of different extraction techniques, three distinct methods were employed: maceration, ultrasonic-assisted extraction (UAE), and accelerated solvent extraction (ASE). The same extraction solvent mixture of ethanol-water (2:3, v/v) was used for all extractions to ensure consistency in solvent polarity and compound solubility. 10 g of dry powdered plant material was extracted with 100 mL of solvent in each method.

Maceration was conducted at ambient temperature (~22–25°C) for 5 hours under continuous stirring to allow passive diffusion of bioactive compounds into the solvent. The extract was then filtered and stored at 4°C until further analysis.

Ultrasonic-Assisted Extraction (UAE) was performed at 45°C for 1 hour using an ultrasonic bath at 59 kHz. The ultrasonic waves facilitated cell wall disruption, enhancing the release of phytochemicals into the extraction medium. The extract was then filtered and stored at 4°C until further analysis.

Accelerated Solvent Extraction (ASE) was carried out using a Thermo Scientific™ Dionex™ ASE 350 Accelerated Solvent Extractor at high pressure (10.3 MPa) and 35°C, ensuring rapid and efficient extraction while minimizing thermal degradation of sensitive compounds. The extracts were stored at 4°C until further analysis.

Phytochemical Composition Analysis

Total Alkaloids - The quantification of total alkaloids in *C. majus* extracts was performed using UV-Vis spectrophotometry. The alkaloid content was determined based on complex formation with a chromogenic reagent, followed by absorbance measurement at a specific wavelength. The results were expressed as milligrams of alkaloid equivalents per ml of extract (mg AE/ml). 1 ml of extract was diluted with 10 ml methanol (MeOH). The solution was then mixed with the 1 ml Dragendorff's reagent and 1.5 ml Bromocresol Green (BCG) buffer solutions and allowed to react for 30 minutes at room temperature to develop the color. The absorbance of the alkaloid-dye complex was measured at 470 nm. A standard calibration curve was constructed using berberine as reference alkaloids (5–50 µg/ml).

Total Polyphenols - The polyphenol content was determined using the Folin-Ciocalteu method, a widely used spectrophotometric assay for phenolic compounds. The reaction of polyphenols with the Folin-Ciocalteu reagent resulted in a blue complex, whose absorbance was measured at 765 nm. The total polyphenol content was expressed as mg gallic acid equivalents per ml of extract (mg GAE/ml).

Polyphenol Yield Calculation - The extraction yield for polyphenols was calculated based on the total amount of polyphenols recovered in the extract relative to the total polyphenol content measured in the raw plant material. The following formula was used:

$$\text{Polyphenol Yield (\%)} = \left(\frac{\text{Total polyphenols in extract}}{\text{Total polyphenols in plant material}} \right) \times 100$$

The total polyphenol content of the unextracted plant material was determined separately using methanol as solvent and the same Folin-Ciocalteu method.

Total Flavonoids - The total flavonoid content was assessed using UV-Vis spectrophotometry, employing a colorimetric method based on the reaction with aluminum chloride (AlCl_3). 1 ml of extract was diluted with 10 ml methanol (MeOH). To each extract solution, 1 ml 2% AlCl_3 was added and mixed thoroughly. The reaction mixture was allowed to incubate for 30 minutes at room temperature in the dark to prevent degradation. Absorbance was measured at 415 nm. The calibration curve was prepared using quercetin (standard solutions at different concentrations (5–50 $\mu\text{g/ml}$), ensuring $R^2 \geq 0.99$ for accuracy. The total flavonoids content was expressed as mg quercetin equivalents per ml of extract (mg QE/ml).

pH Measurement - The pH of the extracts was measured using a calibrated pH meter to assess their suitability for detergent formulations. Maintaining an optimal pH is crucial for ensuring the stability and performance of the detergent, as well as its compatibility with other formulation components.

Antimicrobial and Antioxidant Properties

Antimicrobial Activity – Minimum Inhibitory Concentration (MIC) Testing
The antimicrobial activity of *C. majus* extracts was evaluated using the Minimum Inhibitory Concentration (MIC) assay, which determines the lowest extract concentration required to inhibit the visible growth of microbial contaminants commonly found in detergent formulations. The test was performed against Gram-negative bacteria (*Escherichia coli*), Gram-positive bacteria (*Staphylococcus aureus*), and fungal species (*Candida albicans*), which are representative of potential spoilage microorganisms and human pathogens in detergent environments. Bacterial strains used were *Escherichia coli* (ATCC 25922) and *Staphylococcus aureus* (ATCC 29213) and fungal strain was *Candida albicans* (ATCC 10231). The culture medium used was Mueller-Hinton

CHEMICAL CHARACTERIZATION AND DETERGENT POTENTIAL OF
CHELIDONIUM MAJUS EXTRACTS

broth (MHB) for bacteria and Sabouraud dextrose broth (SDB) for *C. albicans*. Incubation was done at 37°C for 18–24 hours for bacteria and 30°C for 24–48 hours for fungi. The liquid extracts were diluted in sterile distilled water or Mueller-Hinton broth (for bacteria) and Sabouraud broth (for fungi) to prepare serial two-fold dilutions ranging from 100% (undiluted) to 0.1% (v/v) to determine the lowest effective concentration. Controls included: negative control (growth control) were microorganisms in broth without the extract to ensure normal growth; positive control: were standard antibiotics (ampicillin for *E. coli*, vancomycin for *S. aureus*, and fluconazole for *C. albicans*) and solvent control: control wells containing only the extraction solvent (ethanol-water 2:3, v/v) were included to verify the solvent did not inhibit microbial growth. The MIC was determined using the broth microdilution method in a 96-well microplate, a standard method for assessing antimicrobial activity of liquid samples.

The microbial inoculum was prepared from fresh bacterial cultures that were standardized to 0.5 McFarland standard ($\sim 1.5 \times 10^8$ CFU/ml) using a spectrophotometer at 600 nm. The suspension was diluted 1:100 in broth to reach a final concentration of 5×10^5 CFU/ml per well. 100 μ L of liquid extract at the highest concentration (100% v/v) was added to the first row of wells. Two-fold serial dilutions were performed by transferring 100 μ L to the next well, ensuring concentrations from 100% down to 0.1% (v/v) were tested. 100 μ L of standardized microbial suspension was added to each well, resulting in a final volume of 200 μ L per well. The plate was incubated at 37°C for 18–24 hours for bacteria and 30°C for 24–48 hours for fungi under aerobic conditions. The MIC was recorded as the lowest concentration of the extract where no visible microbial growth (turbidity) was observed. Optical density (OD) was measured at 600 nm using a microplate reader to confirm microbial inhibition. A 0.015% resazurin solution was added to the wells and incubated for an additional 2 hours to confirm viability (live cells reduce resazurin to a pink color, while inhibited cells remain blue). The MIC was expressed as the lowest concentration of *C. majus* extract (v/v) that completely inhibited microbial growth. The antimicrobial effectiveness was compared across different extraction methods (maceration, UAE, ASE) to determine the most potent extract.

Antioxidant capacity - 1 ml of extract was diluted with 10 ml MeOH and then directly injected in to PHOTOCHEM, Analytik Jena, Germany and the antioxidant capacity was measured using the ACL kit and expressed in equivalent Trolox. The samples were done in triplicate.

Statistical evaluation - The results were expressed as mean \pm standard deviation, and statistical analysis was performed using one-way analysis of variance (ANOVA) in Minitab for Windows, version 17.0 (Minitab, LLC, State College, PA, USA).

ACKNOWLEDGMENTS

This work was carried out through the financing contract no. 105/07.08.2024 SMIS 304140 financed from the European Union budget, through the North-West Regional Program 2021-2027, Policy Objective 1: A more competitive and smarter Europe, by promoting an innovative and intelligent economic transformation and regional ICT connectivity Priority 1: A competitive region through innovation.

REFERENCES

1. X.L. Li, Y.P. Sun, M. Wang, Z.B. Wang, H.X. Kuang; *Front. pharmacol.*, **2024**, 15, p.1440979.
2. A. E. Segneanu, G. Vlase, T. Vlase, M. V. Ciocalteu, C. Bejenaru, G. Buema & S. Boia; *Plants*, **2024**, 13(5), 734.
3. M. Terzic, S. Fayez, N. M. Fahmy, O. A. Eldahshan, A. I. Uba, S. K. M. Ponniya, S. Selvi, I. Koyuncu, Ö. Yüksesdağ, G. Zengin; *Fitoterapia*, **2024**, 174, p.105835.
4. M. Strzemski, S. Dresler, B. Podkościelna, K. Skic, I. Sowa, D. Załuski, R. Verpoorte, S. Zielińska, P. Krawczyk, M. Wójciak; *Molecules*, **2022**, 27(9), p.2815.
5. T. Tuzimski, A. Petruczynik, T. Plech, B. Kaproń, A. Makuch-Kocka, M. Szultka-Młyńska, J. Misiurek, B. Buszewski, M. Waksmundzka-Hajnos; *Int. J. Mol. Sci.* **2023**, 24(7), p.6360.
6. M. Zwerger, L. Boeck, J. Manzl, S. Schwaiger, M. Ganzera; *Planta Med.*, **2024**, 90(07/08), pp.523-533.
7. G. Göger; *Chelidonium majus* L.. In: *Novel Drug Targets With Traditional Herbal Medicines: Scientific and Clinical Evidence 2022*, Cham: Springer International Publishing, **2022**, pp. 121-129.
8. N. Stefanowski, H. Tkachenko, N. Kurhaluk; *Medicinal Herbs: from Past Experience to New Technologies: Proceedings of Ninth International Scientific and Practical Conference*, **2021**, pp. 154-160.
9. T. Bilušić, I. Šola, V. Čikeš Čulić; *Food Technol. Biotechnol.*, **2024**, 62(1), pp.49-58.
10. A. Danila, M. Costea, L. Profire, C.M. Rimbu, M. Baican, F. Lupascu, S. M. Tatarusanu, B. S. Profire, E. I. Muresan; *Polymers*, **2022**, 14(15), p.3194.
11. D. Yue, D. Zheng, Y. Bai, L. Yang, J. Yong, Y. Li; *Phytother. Res.*, **2024**, 38(5), pp.2518-2538.
12. E. Gayathiri, P. Prakash, N. Karmegam, S. Varjani, M. K. Awasthi, B. Ravindran; *Agronomy*, **2022**, 12(3), p.662.
13. M. Ayub, M. H. D. Othman, I. U. Khan, S. K. Hubadillah, T. A. Kurniawan, A. F. Ismail, M. A. Rahman, J. Jaafar; *J. Clean. Prod.*, **2021**, 295, p.126296.
14. A. K. Chaudhari, V. K. Singh, A. Kedia, S. Das, N. K. Dubey; *Environ. Sci. Pollut. Res.*, **2021**, 28, pp.18918-18940.

CHEMICAL CHARACTERIZATION AND DETERGENT POTENTIAL OF
CHELIDONIUM MAJUS EXTRACTS

15. Y. Kunatsa, D. R. Katerere; *Plants*, **2021**, 10(5), p.842.
16. M. E. A. Benarbia, P. Gaignon, C. Manoli, P. Chicoteau; *Front. Vet. Sci.*, **2022**, 9, p.946576.
17. J. Lv, S. Liu, C. Hu, L. Ding, H. Wang, X. Li, F. Yang, Q. Shen, H. Zhang, G. Ma, S. Zhang; *Front. Plant Sci.*, **2025**, 16, p.1535170.
18. S. Rai, E. Acharya-Siwakoti, A. Kafle, H. P. Devkota, A. Bhattarai; *Sci*, **2021**, 3(4), p.44.
19. M. R. Wylie, D. S. Merrell; *Front. Pharmacol.*, **2022**, 13, p.891535.
20. K. D. Rakholiya, M. J. Kaneria, A. M. Shaikh, S. S. Wandhekar, S. V. Chanda; Medicinal plants as alternative sources of therapeutics against multidrug resistant pathogenic microorganisms based on their antimicrobial potential and synergistic properties. In: *Fighting multidrug resistance with herbal extracts, essential oils and their components*, (Second Edition), Academic Press, **2025**, Chapter 12, pp.271-289.
21. E. Guzmán, A. Lucia; *Cosmetics*, **2021**, 8(4), p.114.
22. P. Bolouri, R. Salami, S. Kouhi, M. Kordi, B. Asgari Lajayer, J. Hadian, T. Astatkie; *Molecules*, **2022**, 27(24), p.8999.
23. M. Angane, S. Swift, K. Huang, C. A. Butts, S. Y. Quek; *Foods*, **2022**, 11(3), p.464.
24. A. Mutlu-Ingok, G. Catalkaya, E. Capanoglu, F. Karbancioglu-Guler; *Food front.*, **2021**, 2(4), pp.508-518.
25. S. Kyoung-Sun, W. Y. Kyeong; *Res Crops.*, **2023**, 24(2), pp.378-383.
26. C. Gosset-Erard, M. Zhao, S. Lordel-Madeleine, S. Ennahar; *Food Chem.*, **2021**, 352, p.129396.
27. K. Szentmihályi, I. Szöllősi-Varga, M. Then; *Eur. Chem. Bull.*, **2021**, 10(1), 58-66.
28. P. Krzyżek, A. Junka, W. Słupski, A. Dołowacka-Jóźwiak, B. J. Płachno, A. Sobiecka, A. Matkowski, G. Chodaczek, T. Płusa, G. Gościński, et al.; *Pathogens*, **2021**, 10, 1033.
29. A. E. Segneanu, G. Vlase, T. Vlase, M. V. Ciocalteu, C. Bejenaru, G. Buema, L. E. Bejenaru, E. R. Boia, A. Dumitru, S. Boia, **2024**. Romanian Wild-Growing *Chelidonium majus*—An emerging approach to a potential antimicrobial engineering carrier system based on AuNPs: In Vitro investigation and evaluation. *Plants*, 13(5), p.734.

PHYTOCHEMICAL CHARACTERIZATION AND BIOACTIVITY ASSESSMENT OF *AETHIONEMA SCHISTOSUM* WITH A FOCUS ON ENZYME INHIBITION AND ANTIOXIDANT POTENTIAL

Sultan PEKACAR^a, Ömer Furkan GÜVERTİ^{a,*},
Burçin ÖZÜPEK^a, Hatice Nur NEGİZ^a, Osman TUGAY^b,
Didem DELİORMAN ORHAN^a

ABSTRACT. The study examines the antioxidant, antidiabetic, antihyperlipidemic, and antiobesity properties of the 80% methanol extract prepared from the aerial parts of *Aethionema schistosum*, a plant widely distributed in certain regions. The extract was evaluated *in vitro* for its inhibitory effects on α -glucosidase (antidiabetic), α -amylase (antidiabetic), pancreatic lipase (antiobesity), and pancreatic cholesterol esterase (antihyperlipidemic) enzymes. It exhibited moderate α -glucosidase inhibition ($99.15 \pm 0.04\%$) compared to acarbose ($56.94 \pm 3.88\%$). The DPPH radical scavenging activity of the extract at a concentration of 2 mg/ml was measured at $80.50 \pm 1.23\%$. This value is considered close to the inhibitory effect of ascorbic acid, which was recorded at $90.60 \pm 0.29\%$ at the same concentration. The extract's total phenol (74.73 ± 4.76 mg GAE/g) and flavonoid (42.80 ± 2.25 mg QE/g) contents were measured, and chlorogenic acid was identified as a major compound via HPLC. This is the first study to analyze the phytochemical composition and enzyme inhibitory effects of *A. schistosum*. Further research is needed to isolate its bioactive compounds and assess its therapeutic potential through diverse *in vitro* and *in vivo* models, highlighting its potential in drug discovery efforts.

Keywords: Antidiabetic, Antioxidant, *Aethionema schistosum*, Reverse phase-HPLC

^a Gazi University, Faculty of Pharmacy, Department of Pharmacognosy, Ankara, Turkey.

^b Selçuk University, Faculty of Pharmacy, Department of Pharmaceutical Botany, Konya, Turkey.

* Corresponding author: furkanguvertiomer@gmail.com



INTRODUCTION

The Brassicaceae family comprises over 340 genera and approximately 3350 species distributed predominantly in the temperate regions of the Northern Hemisphere. Anatolia is not only the main gene center but also the main diversification center for the genus *Aethionema*, represented by 57 taxa. *A. schistosum* Boiss. & Kotschy, commonly known as Göksun Kayagülü in Turkey, is an endemic perennial herb exhibiting unique morphological and chemical characteristics [1,2].

Studies on the biological activity and phytochemical properties of *Aethionema* species are relatively rare. These studies have focused on the phytochemical analysis of volatile compounds, fatty acids, alkaloids, flavonoids, and phenolic acids of the plant and on the investigation of their antioxidant and antimicrobial activities. On the other hand, literature survey findings also showed that no activity or phytochemical studies have been carried out on *A. schistosum* so far [3].

Diabetes is an endocrine system disease that is defined as an excessive increase in blood glucose levels caused by a combination of hereditary and environmental factors. Diabetes is a chronic metabolic disorder and also has an increased oxidative stress state. Increased free radicals can interact with lipids, proteins, and nucleic acids, leading to loss of membrane integrity and structural or functional changes in proteins. Therefore, internal and external antioxidant pools and supplements are important in diabetes. Coronary artery disease is the most common cause of death in diabetic patients, and hyperlipidemia, which manifests itself with hypertriglyceridemia and low high-density lipoprotein cholesterol levels, is very common, especially in type 2 diabetics. Considering that experts estimate that this disease will affect 693 million adults by 2045, the discovery of new molecules for its treatment is very important. In order to discover new drug molecules from medicinal plants, firstly, folk remedies and secondly, randomly selected plants are used in research [4,5].

In this study, the antidiabetic, antiobesity, and antihyperlipidemic effects of the extract prepared with 80% methanol from the aerial parts of *A. schistosum* were investigated. For this purpose, α -glucosidase, α -amylase, pancreatic lipase, and pancreatic cholesterol esterase enzymes were used. The antioxidant activity of the methanol extract was evaluated by DPPH (1,1-diphenyl-2-picrylhydrazyl) radical scavenging activity, ferric reducing power, and metal chelating capacity methods. In addition, the total flavonoid and total phenol contents of the extract were measured by UV spectroscopy, and the Reverse phase-HPLC technique was used to define the phenolic compounds.

RESULTS AND DISCUSSION

The *A. schistosum* MeOH extract exhibited the highest antioxidant activity by effectively scavenging the DPPH radical, as assessed by three different methods. Activity of the extract ($80.50 \pm 1.23\%$) was comparable to that of the reference compound, ascorbic acid ($90.60 \pm 0.29\%$), at an equivalent concentration (2 mg/ml). The ability of the MeOH extract to reduce ferric ions at a concentration of 2 mg/ml (1.56 ± 0.03) was weaker than that of the reference compound quercetin (3.65 ± 0.11), which was also tested at the same concentration. Table 1 presents the results of ferric reducing power, metal chelating capacity, and DPPH radical scavenging activity.

The ferric-reducing power of MeOH extract at 2 mg/ml concentration (1.56 ± 0.03) was found to be weak compared to the reference compound quercetin (3.65 ± 0.11) also at 2 mg/ml concentration. Ferric reducing power, metal chelating capacity and DPPH radical scavenging activity results are given in Table 1.

Table 1. Metal binding capacity, DPPH radical scavenging, and ferric-reducing power activity results of *A. schistosum* MeOH extract

Sample/References	Concentration (mg/ml)	DPPH radical scavenging activity % \pm SD	Metal chelating capacity % \pm SD	Ferric reducing power Absorbance \pm SD
MeOH extract	0.01	$79.79 \pm 0.01^{***a}$	-	$0.42 \pm 0.01^{***c}$
	1	$80.14 \pm 0.35^{***a}$	-	$0.82 \pm 0.03^{***c}$
	2	$80.50 \pm 1.23^{***a}$	-	$1.56 \pm 0.03^{***c}$
^a AA/ ^b EDTA/ ^c QE	0.01	$89.71 \pm 0.21^{***a}$	$99.73 \pm 0.91^{***b}$	$1.91 \pm 0.13^{***c}$
	1	$90.35 \pm 0.20^{***a}$	$100.00 \pm 0.03^{***b}$	$3.14 \pm 0.04^{***c}$
	2	$90.60 \pm 0.29^{***a}$	$100.00 \pm 0.02^{***b}$	$3.65 \pm 0.11^{***c}$

∴ No activity, SD: Standard Deviation, * $p < 0.05$, ** $p < 0.01$, *** $p < 0.001$ AA: ^aAscorbic acid, ^bEDTA: Ethylenediamine tetraacetic acid, ^cQE: Quercetin

In order to evaluate the antidiabetic effect, the effects of the MeOH extract against α -glucosidase and α -amylase enzymes were investigated. The inhibition values for these two enzymes were calculated as $56.94 \pm 3.88\%$ and $40.55 \pm 3.65\%$, respectively. It was determined that the MeOH extract was ineffective on pancreatic lipase enzyme. Inhibition of pancreatic cholesterol esterase enzyme was calculated as $24.36 \pm 3.64\%$ for 200 $\mu\text{g/ml}$ concentration. All percent inhibition results obtained were found to be statistically significant. Enzyme inhibition results are given in Table 2.

Table 2. Inhibitory activities of *A. schistosum* MeOH extract on α -glucosidase, α -amylase, pancreatic lipase, and pancreatic cholesterol esterase enzymes

Sample/ References	200 μ g/mL inhibition % \pm SD (IC ₅₀ : μ g/mL \pm SD)			
	α -Amylase	α -Glucosidase	Pancreatic lipase	Pancreatic cholesterol esterase
MeOH extract	40.55 \pm 3.65 ^{***a} (IC ₅₀ :> 200)	56.94 \pm 3.88 ^{***a} (IC ₅₀ : 155.43 \pm 2.50)	- (IC ₅₀ : -)	24.36 \pm 3.64 ^{***c} (IC ₅₀ :> 200)
AKA^a/ ORL^b/SIM^c	91.62 \pm 1.33 ^{***a} (IC ₅₀ : 15.38 \pm 1.81)	99.15 \pm 0.04 ^{***a} (IC ₅₀ : 0.03 \pm 0.01)	74.93 \pm 3.71 ^{***b} (IC ₅₀ : 0.96 \pm 0.82)	66.33 \pm 2.12 ^{***c} (IC ₅₀ : 81.71 \pm 1.36)

-: No activity, SD: Standard Deviation, *p<0.05, **p<0.01, ***p<0.001 AKA: ^aAcarbose, ^bORL: Orlistat, ^cSIM: Simvastatin

In order to examine the phytochemical profile of the MeOH extract, total phenol and flavonoid contents were determined. The total phenol and total flavonoid contents of the extract were found to be 74.73 \pm 4.76 GAE mg/g extract and 42.80 \pm 2.25 QE mg/g extract, respectively. In addition, qualitative and quantitative analyses of chlorogenic acid, hesperidin, rutin, and quercetin 3-O-glucoside were performed by the Reverse phase-HPLC (Table 3). Chromatograms of rutin, quercetin 3-O-glucoside, chlorogenic acid, hesperidin, and the extract are given in Figures 1-3.

Table 3. Amounts of chlorogenic acid, quercetin 3-O-glucoside, rutin, and hesperidin in *A. schistosum* MeOH extract

Compounds	Rt (Min.)	g/ 100 g dry extract	Calibration curve	Linearity	LOD (ppm)	LOQ (ppm)
Rutin	30.181	0.100 \pm 0.002	y=95.462x +27.260	r ² =0.9973	0.036	0.119
Chlorogenic acid	15.533	1.420 \pm 0.001	y=24.523x +9.432	r ² =0.9981	0.059	0.176
Quercetin 3-O-glucoside	30.812	0.610 \pm 0.003	y=66.434x -95.636	r ² =0.9993	0.011	0.041
Hesperidin	31.123	0.020 \pm 0.003	y=36.112x -6.254	r ² =0.9998	0.021	0.063

PHYTOCHEMICAL CHARACTERIZATION AND BIOACTIVITY ASSESSMENT OF *AETHIONEMA SCHISTOSUM* WITH A FOCUS ON ENZYME INHIBITION AND ANTIOXIDANT POTENTIAL

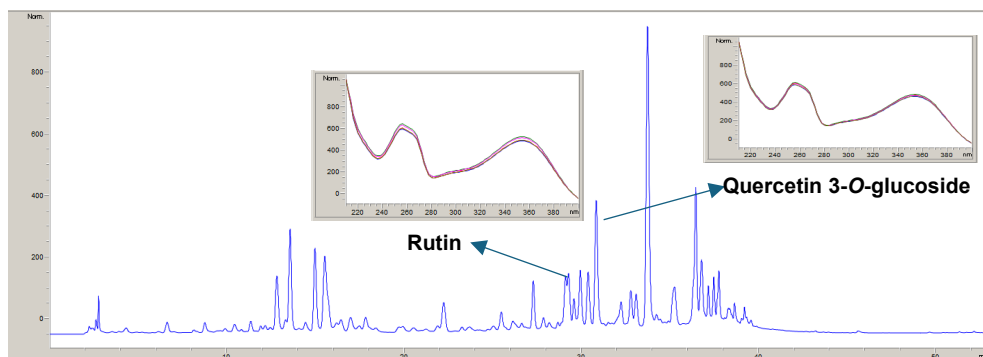


Figure 1. Chromatogram of *A. schistosum* MeOH extract at 260 nm

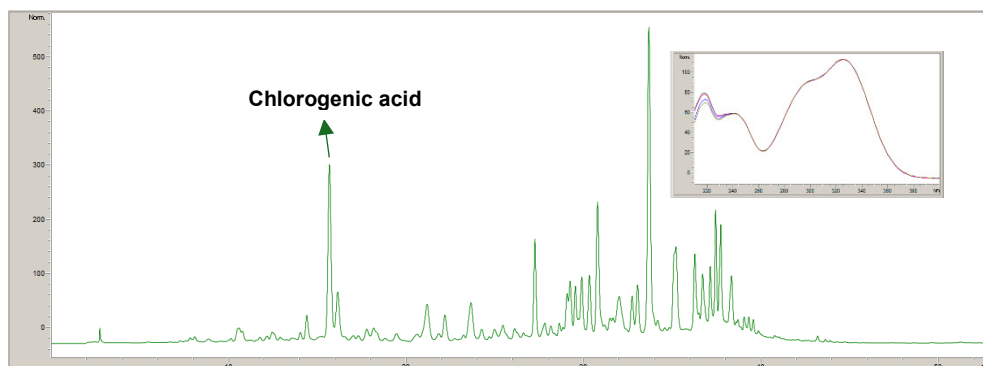


Figure 2. Chromatogram of *A. schistosum* MeOH extract at 320 nm

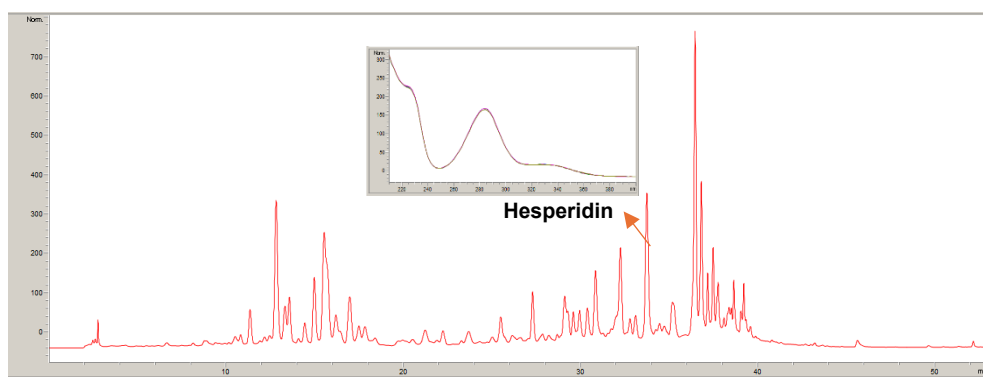


Figure 3. Chromatogram of *A. schistosum* MeOH extract at 280 nm

It was determined that the MeOH extract contained high amounts of chlorogenic acid (1.420 ± 0.001 g/100 g dry extract) and low amounts of hesperidin (0.020 ± 0.003 g/100 g dry extract). Among the phenolic compounds and flavonoids analyzed by HPLC, the highest amount of chlorogenic acid and the lowest amount of hesperidin were determined in the extract. The *Aethionema* genus is a taxon that is widely found in Turkey but has not been studied much. To date, scientific studies based on antioxidant activity studies and isolation and qualitative and quantitative determination of some phytochemical compounds have been conducted on these species belonging to this taxon. Scientific study findings on *Aethionema* species other than *A. schistosum*, which is our plant species, are presented below.

Goffman et al. (1999) reported that *A. grandiflora* Boiss. & Hohen. contained 63.60%, 10.9%, and 11.80% linolenic, oleic, and linoleic acid, respectively, by the GC-MS technique [6].

In a study conducted by Molan et al. in 2012, the antioxidant activities and phenolic contents of 14 plants traditionally used in Northern Iraq, including *A. grandiflorum*, were evaluated. Total phenolic contents, iron-reducing powers, and DPPH radical scavenging effects of the aqueous and ethanolic extracts of the plants were investigated. The total phenolic content of *A. grandiflorum* was determined as 32.7 ± 0.13 and 33.20 ± 0.05 mg GAE/100 ml in aqueous and ethanolic extracts, respectively. Ferric-reducing power was calculated as 12.80 ± 0.06 and 13.60 ± 0.03 in aqueous and ethanolic extracts, respectively. DPPH radical scavenging effect was found to be 22.70 ± 1.1 and 34.03 ± 0.90 in aqueous and ethanolic extracts, respectively [7].

In a study conducted by Duran et al. (2015), the total phenolic contents and antioxidant activities of thirty different plants, including *A. oppositifolium* (Pers.) Hedge and *A. dumanii* Vural & Adigüzel, were investigated. The plants were extracted in 90% methanol, 9% water, and 1% acetic acid mixtures. The total phenolic content of the extracts was determined by the Folin-Ciocalteu method. The antioxidant activities of the plants were determined by the DPPH radical scavenging activity method. The total phenolic contents of *A. oppositifolium* and *A. dumanii* were determined as 3.337 and 3.267 (mg GAE/100 ml), respectively. Again, the antioxidant activities of the plants were calculated as 81.158% and 78.941%, respectively [8].

Aliyazicioglu et al. (2017) investigated the volatile components, phenolic composition, and antioxidant properties of *A. diastrophis* Bunge and its antibacterial and antifungal activities. Qualitative and quantitative analyses of protocatechuic aldehyde (29.4%), chlorogenic acid (14.3%), and benzoic acid (56.3%) were carried out in the methanol extract, and it was found that the DPPH radical scavenging activity of methanol and aqueous extracts was weaker than butylhydroxytoluene, and the cupric-reducing power of the

aqueous extract (508.00 ± 2.02 $\mu\text{mol Trolox/g}$ extract) was higher than that of the methanol extract (160.00 ± 1.15 $\mu\text{mol Trolox/ g}$ extract). The volatile component mixture obtained from the plant by SPME method was found to be rich in α -humulene and viridiflorene [9].

Demirpolat (2022) identified the essential oil and fatty acid compositions of the aerial parts of *A. sancakense* Yild. & Kılıç using the GC/GC-MS technique and determined the presence and amount of linoleic acid (23.1%), α -humulene (19.8%), camphene (13.9%), and heptanal (9.7%) [9, 10].

A study by Oboh et al. (2014) found that rutin (diluted to 500 μl) inhibited α -amylase ($\text{IC}_{50} = 0.043$ μM) and α -glucosidase ($\text{IC}_{50} = 0.037$ μM) activities more potently than quercetin. In this study, the researchers demonstrated the inhibitory effect of quercetin (diluted to 500 μl) and rutin on α -amylase and α -glucosidase activity *in vitro*. They also demonstrated that this effect has synergistic inhibition abilities, suggesting that a combination of food sources rich in these flavonoids could be very effective in the management/prevention of Type 2 diabetes [11].

Zheng et al. (2020) reported that chlorogenic acid (0.1-2.0 mg/ml), a phenolic acid commonly found in potatoes, honeysuckle, and other plants, showed a significant inhibitory effect on α -amylase [12].

Panda et al. (2007) investigated the potential of quercetin-3-O-glucoside isolated from *Annona squamosa* leaves to regulate alloxan-induced hyperglycemia and lipid peroxidation (LPO) in rats. An increase in serum glucose concentration and a decrease in insulin levels were observed in animals with alloxan-induced diabetes. Following administration of 15 mg/kg quercetin-3-O-glucoside daily for 10 days, the animals' blood glucose levels decreased, insulin levels increased, and hepatic glucose-6-phosphatase activities were simultaneously inhibited. These findings indicate that quercetin-3-O-glucoside is effective in diabetes mellitus and has the potential to reduce tissue LPO levels [13].

In a study conducted by Aja et al., in which the binding affinities of bisphenol A (BPA) and hesperidin to fibroblast growth factor 21, α -amylase, and α -glucosidase enzymes were evaluated by the molecular docking method, it was proven that hesperidin (-5.80, -9.60, and -9.60 kcal., respectively) binds to these proteins with a greater affinity than BPA (-4.40, -7.20, and -7.10 kcal.). As a result, it was predicted that hesperidin could be a promising natural compound for metabolic and endocrine disorders [14].

Our study identified and quantified the presence of four compounds in the MeOH extract: rutin, chlorogenic acid, quercetin-3-O-glucoside, and hesperidin. Based on the above-mentioned literature, it was considered that rutin, chlorogenic acid, quercetin-3-O-glucoside, and hesperidin may contribute to the glucosidase inhibitory effect of *A. schistosum* MeOH extract.

CONCLUSIONS

In conclusion, *A. schistosum* MeOH extract was found to have a relatively moderate effect on α -glucosidase enzymes at a concentration of 200 μ g/ml. This suggests that this plant may have a therapeutic or supportive effect in diseases associated with these enzymes. However, it is not possible to reach this conclusion directly from these experiments alone. Therefore, these results can be further justified by *in vivo* studies. The aim of our study is to contribute to the realization of this by shedding light on future studies. Since the number of studies of this type is quite limited, it is thought that our study will help other studies to be conducted on this subject. As can be seen, there are no studies evaluating the effects of other *Aethionema* species against these enzymes, which play an important role in metabolic diseases. In this study, both the antioxidant activity and *in vitro* enzyme inhibitory effect potential of *A. schistosum* were investigated for the first time. In this study, the antidiabetic, antihyperlipidemic, and antiobesity effects of *A. schistosum*, a plant commonly grown in Anatolia, were investigated by *in vitro* methods. However, they found that the methanol extract of the aerial part of the plant did not significantly inhibit other enzymes except the α -glucosidase enzyme. In terms of phytochemical studies, it is the first study conducted on the species. As a result, it is recommended that future studies be designed as projects in which various *in vitro* and *in vivo* experimental models will be used and different enzyme activities will be examined in order to better determine the antidiabetic properties of the plant. Additionally, to utilize *Aethionema* species, which are widely distributed in our country and typically regarded as ornamental plants, for medical purposes, activity screening and isolation studies of bioactive compounds should be conducted using *in vitro* enzyme systems.

EXPERIMENTAL SECTION

Plant material

A. schistosum was collected in June 2023 from Ankara, Turkey. The collected plant was identified by Prof. Dr. Osman Tugay (Selçuk University, Faculty of Pharmacy, Department of Pharmaceutical Botany, Konya, Turkey). The specimens of the plant are preserved in the Herbarium of Gazi University Faculty of Pharmacy (Herbarium Number: GUE 3885). The aerial parts of the plant were selected for use. These parts were left to dry in a shaded area at room temperature. The dried plant material was ground into a powder using a mechanical grinder.

Chemicals used

All solvents and chemicals used in the activity evaluation studies, enzyme inhibition assays, and High-Performance Liquid Chromatography (HPLC) methods were of high purity. These chemicals were obtained from Sigma-Aldrich.

Extraction

The powdered aerial parts of *A. schistosum* (10 g) were extracted with 80% methanol (200 ml) at room temperature for 24 hours. A mechanical stirrer (RW20, IKA Janke Kunkel Labortechnik, IKA®-Werke GmbH & Co. KG, Germany) was used during the extraction process. The extraction procedure was repeated three times, and each time, the extracts were filtered using 0.45 µm filter papers. The methanol (MeOH) extract obtained from each extraction was combined and concentrated to dryness under reduced pressure at 45 °C using a rotary evaporator (Heidolph, Germany). (MeOH extract yield: 26.14% w/w dry plant material).

Antioxidant activity assays

DPPH radical scavenging activity

To evaluate the DPPH radical scavenging activity of the extract, a 1 mM DPPH (1,1-diphenyl-2-picrylhydrazyl) solution was added to the extracts (0.01, 1, and 2 mg/ml). The mixture was then incubated for 30 minutes. Absorbance was measured at 520 nm using an ELISA microplate reader. Ascorbic acid (AA) was used as the reference compound [15].

Ferric reducing power

The extracts (0.01, 1, and 2 mg/ml) and the reference compound QE were mixed with 0.1 mol/L sodium phosphate buffer at pH 7.2. Subsequently, a 1% (w/v) $K_3Fe(CN)_6$ solution was added, and the mixture was incubated at 37°C in an incubator. After the incubation, a 10% trichloroacetic acid solution was added to the mixture. The absorbance values were measured at 700 nm using an ELISA microplate reader. Following the first measurement, a 0.1% (w/v) $FeCl_3$ solution was added, and a second absorbance measurement was performed. The difference between the two absorbance values was then calculated. The experiments were conducted in triplicate [16].

Metal chelating capacity

A 2 mM $FeCl_2$ solution was added to the extracts (0.01, 1, 2 mg/ml) and incubated at room temperature for 5 minutes. Subsequently, a 5 mM

ferrozine solution was added, and the mixture was allowed to stand at room temperature for an additional 10 minutes. The absorbance of the extract and the reference compound (Ethylenediaminetetraacetic acid (EDTA)) was measured at 562 nm using an ELISA microplate reader. The experiments were performed in triplicate [17].

Enzyme inhibitory activity tests

α -Glucosidase enzyme inhibition activity

In this study, α -glucosidase type IV enzyme (from *Bacillus stearothermophilus*) (EC 232-604-7 Sigma Co., St. Louis, USA) was used. The enzyme was dissolved in 0.5 M phosphate buffer solution at pH 6.5. *p*-Nitrophenyl- α -D-glucopyranoside (PNG) was used as the substrate, which was dissolved in phosphate buffer and adjusted to a concentration of 20 mM. The 80% MeOH extract was prepared at concentrations of 0.01, 1, and 2 mg/ml. The enzyme solution and extract mixture were pre-incubated at 37°C for 15 minutes in a microplate. Subsequently, 20 mM PNG substrate was added to the wells, and the mixture was incubated again at 37°C for 35 minutes. Acarbose (Bayer, Turkey) was used as the reference compound. Absorbance values were measured at 405 nm using an ELISA microplate reader. The experiment was performed in triplicate [18].

α -Amylase enzyme inhibition activity

In this study, α -amylase type I-A (EC 3.2.1.1, Sigma) enzyme obtained from porcine pancreas was used. The enzyme was dissolved in sodium phosphate buffer (pH 6.9). Potato starch (2.5% w/v) prepared in a phosphate buffer solution was used as the substrate. The 80% MeOH extract was prepared at concentrations of 0.01, 1, and 2 mg/ml. 3,5-dinitrosalicylic acid (DNS) solution was used as the color reagent. The DNS solution was prepared using 96 mM DNS, 2 M NaOH, and 5.31 M sodium potassium tartrate. Acarbose was used as the reference compound. The α -amylase enzyme and sodium phosphate buffer (20 mM NaH₂PO₄ and 6.7 mM NaCl) (pH 6.9) were added to the samples, followed by incubation at room temperature for 5 minutes. The substrate was then added to the mixture, and it was incubated again at 37°C for 15 minutes. Subsequently, DNS was added, and the mixture was incubated at 80°C for 40 minutes in an oven. Absorbance values were measured at 540 nm using an ELISA microplate reader. The amount of maltose produced was found using the standard maltose calibration graph ($y=0.7615x-0.1246$ and $r^2=0.9839$) [19].

Pancreatic lipase enzyme inhibition activity

In this study, the pancreatic lipase type II enzyme (from porcine pancreas) was used. The enzyme buffer solution (pH 6.8) was prepared using 1 mM EDTA and 10 mM 4-morpholinepropanesulfonic acid. The extract was prepared at concentrations of 0.01, 1, and 2 mg/ml. Tris buffer (100 mM Tris-HCl and 5 mM CaCl₂, pH 7.0) was added to the extract and the reference compound orlistat, followed by pre-incubation at 37°C for 15 minutes. Subsequently, 5 mM 4-nitrophenyl butyrate was added to the wells, and the mixture was incubated at 37°C for 30 minutes. Absorbance values were measured at 405 nm using an ELISA microplate reader [20].

Pancreatic cholesterol esterase enzyme inhibition activity

In this study, the porcine pancreatic cholesterol esterase enzyme was utilized. The enzyme buffer solution (pH 7) was prepared using 100 mM NaCl and 100 mM. 80% MeOH extract was prepared at concentrations of 0.01, 1, and 2 mg/ml, and 50 µL of phosphate buffer was added to the extract. Following this step, taurocholic acid (12 mM) and 5 mM *p*-NPB (*p*-nitrophenyl butyrate) substrate were added. After incubation at 25°C for 5 minutes, porcine pancreatic cholesterol esterase enzyme was added to the mixture at a concentration of 0.1 µg/ml. Absorbance values were determined kinetically at 405 nm over 15 minutes using an ELISA microplate reader. Simvastatin was used as the reference compound [21].

Chemical composition of the MeOH extract

Total phenolic content

The Folin-Ciocalteu reagent (10% w/v) was added to the extract (1 mg/ml). Following this, a 7.5% (w/v) sodium carbonate solution was added, and the mixture was incubated in the dark at room temperature for 30 minutes. After the incubation, the absorbance value was measured at 735 nm using an ELISA microplate reader (SpectraMax i3x, Molecular Devices, USA). The total phenolic content was calculated as gallic acid equivalents (GAE) in mg/g of extract. The calibration equation was determined to be $y=6.6511x-0.025$ and $r^2=0.9998$ [22].

Total flavonoid content

Aluminum chloride, sodium acetate, and ethanol solutions were added to the MeOH extract (1 mg/ml), followed by incubation at room temperature for 30 minutes. Absorbance values were measured at 415 nm using an ELISA microplate reader. The total flavonoid content was expressed as quercetin equivalents (QE) in mg/g of extract. The calibration curve equation was found as $y=1.8346x-0.004$ and $r^2=0.9988$ [23].

Reverse-Phase HPLC

The HPLC system used in this study was an HP Agilent 1260 Series LC System equipped with an ACE 5 C18 column (5 μm , 150 mm x 4.6 mm). The column temperature was maintained at 25°C throughout the analysis. For the qualitative and quantitative determination of phenolic compounds and flavonoids in the infusion, standard mixtures of the following compounds were used. Phenolic compound mixture: gallic acid, protocatechic acid, chlorogenic acid, vanillic acid, syringic acid, p-coumaric acid, ferulic acid, sinapic acid, ellagic acid, caffeic acid, trans-cinnamic acid, rosmarinic acid, epicatechin, catechin. Flavonoid mixture: umbelliferone, rutin, naringenin, hesperidin, quercetin-3-O-glucoside, apigenin-7-O-glucoside, myricetin, quercetin, luteolin, apigenin. Standard compounds were sourced from Sigma-Aldrich. A gradient elution system was applied using a mobile phase consisting of 5% solvent A (acetonitrile: water: formic acid, 50:50:0.5) and 95% solvent D (water: formic acid, 100:0.5). The total analysis time was set to 55 minutes, and 20 μL of the sample was injected. Analyses were performed using a DAD detector at five wavelengths: 220, 260, 280, 320, and 366 nm. The extract was prepared at a concentration of 10 mg/ml using a 25% acetonitrile solution. A membrane filter with a pore size of 0.22 μm was used for filtration. Calibration curves were prepared for rutin, quercetin-3-O-glucoside, chlorogenic acid, and hesperidin. Standard solutions of these compounds were prepared by diluting their stock solutions in 25% acetonitrile-water solution to achieve concentrations of 1, 10, 20, 50, and 100 mg/L. Calibration curves were constructed by plotting the mg/L values (x) against the peak areas (y) [3].

Statistical analysis

All analyses were performed in triplicate. All values were calculated as mean \pm standard deviation (SD). Linear regression analyses and calculations were conducted using Microsoft Excel, while IC_{50} values were statistically evaluated using GraphPad ANOVA. (* $p < 0.05$, ** $p < 0.01$, *** $p < 0.001$)

ACKNOWLEDGMENTS

We would like to thank Gazi University Faculty of Pharmacy where we carried out the studies.

REFERENCES

- [1] A. Franzke; M. A. Lysak; I. A. Al-Shehbaz; M. A. Koch; K. Mummenhoff, *Trends Plant Sci.*, **2011**, 16(2), 108-116.
- [2] M. C. Karaismailođlu, *Caryologia*, **2018**, 71(2), 128-132.
- [3] H.N. Gök; N. Orhan; B. Özüpek; S. Pekacar; Ş.N. Selvi; D.D. Orhan, *Iran. J. Pharm. Res.*, **2021**, 20 (3): 441-455.
- [4] H. Akkaya; S. Çelik, *FÜ Sağ. Bil. Vet. Derg.*, **2010**, 24(1), 5-10.
- [5] J. B. Cole; J. C. Florez, *Nat. Rev. Nephrol.*, **2020**, 16(7), 377-390.
- [6] F.D. Goffman; W. Thies; L. Velasco, *Phytochem.*, **1999**, 50, 793-798.
- [7] A. L. Molan; A. M. Faraj A. S.; Mahdy, *J Phytopharmacol*, **2012**, 2(2), 224-233.
- [8] A. Duran; N. Uslu; B. Dogan; M. Ozcan; M. Çelik, *J. Agroaliment. Processes Technol.*, **2015**, 21(2), 136-141.
- [9] R. Aliyazicioglu; O. E. Eyupoglu; U. Ozgen; S. A. Karaoglu, *Chem. Nat. Compd.*, **2017**, 53, 379-380.
- [10] A. Demirpolat, *EJOSAT*, **2022**, 37, pp. 1-7.
- [11] G. Oboh; A. O. Ademosun; P. O. Ayeni; O. S. Omojokun; F. Bello, *Comp Clin Path*, **2015**, 24, 1103-1110.
- [12] Y. Zheng; W. Yang; W. Sun; S. Chen; D. Liu; X. Kong; J. Tian; X. Ye, **2020**, *J. Funct. Foods*, 64, 103587.
- [13] S. Panda; A. Kar, 2007, *Biofactors*, 31(3-4), 201-210.
- [14] P. M. Aja; J. N. Awoke; P. C. Agu; A. E. Adegboyega; E. M. Ezeh; I. O. Igwenyi; O. U. Orji; O. G. Ani; B. A. Ale; U. A. Ibiam, **2022**, *JGEB*, 20(1), 84.
- [15] İ. Gulcin; S. H. Alwasel, *Process*, **2023**, 11(8), 2248.
- [16] Z. Menekşe; B. Marangoz; S. Kahraman, *KFBD*, **2021**, 11(2), 340-354.
- [17] B. Özüpek; S. Pekacar; D. D. Orhan, *KSÜ Tar Doga Derg.*, **2024**, 27(1), 26-37.
- [18] M. Çavuşođlu; M. Akdeniz; İ. Yener; H. Alkan; A. Ertaş, *DOFEBD*, **2024**, 6(2), 24-37.
- [19] K. Özcan; T. Acet, *KFBD*, **2024**, 14(2), 982-996.
- [20] H. N. Gök; S. Bulut; D. D. Orhan, *J. Fac. Pharm. Ankara*, **2023**, 47(2), 349-359.
- [21] B. Özüpek; S. Pekacar; D. D. Orhan, *FABAD J. Pharm. Sci.*, **2023**, 48(1), 125-138. doi:10.55262/fabadeccacilik.1175781.
- [22] M. Zor; S. Pekacar; D. D. Orhan, *J. Fac. Pharm. Ankara*, **2022**, 46(1), 114-128. doi:10.33483/jfpau.1018949.
- [23] Y. Çelik, *Anadolu Tıbbı Dergisi*, **2023**, 2(2), 13-17.

INVESTIGATION OF ANTHRAQUINONE CONTENTS, DNA CLEAVAGE, DNA BINDING, CYTOTOXIC AND ANTIOXIDANT ACTIVITIES OF *XANTHORIA PARIETINA* SAMPLES

Nilgün GÜLER^a , Emine KILIÇKAYA SELVİ^{a*} 

ABSTRACT. In this study, *Xanthoria parietina* samples were collected from different regions of Türkiye like Yozgat (Xp3), Izmit (Xp14), and Kütahya (Xp20). Anthracenedione, anthraquinone (parietin) contents of the lichens were determined quantitatively by GC-MS and spectrophotometric methods. The interaction of lichen extracts with pBR322 DNA and CT-DNA was examined by performing an agarose gel electrophoresis method. The cell proliferative activities of *Xanthoria parietina* samples were tested against the colon cancer cell line (DLD-1) by MTT assay. As a results of the GC-MS and spectrophotometric analysis, the highest and the lowest parietin contents were found for Xp20 and Xp14 extracts, respectively. These results were supported by those of the DNA cleavage, binding, and toxicity studies. The Xp14 sample can be considered as a drug that could be a new approach to cancer treatment, as it has the lowest polyaromatic hydrocarbon content and is not toxic for the cell.

Keywords: *Xanthoria parietina*; parietin; DNA cleavage; cytotoxicity; colon cancer, GC/MS

INTRODUCTION

New pharmacologically effective synthetic drugs are usually accompanied by the emergence of new side effects. Hence, the discovery and use of phytochemicals as the savior of this situation has become widespread. Also, new lichens including a richer and different content from plants have been discovered as drug raw materials and DNA binding agents.

^a Department of Chemistry Technology, Mustafa Cıkrıkçıoğlu Vocational School, Kayseri University, Kayseri, Turkey

* Corresponding author: emineselvi@kayseri.edu.tr



Herbal medicines have been used for a long time in the treatment of diseases such as cancer [1-6]. They are vital owing to the production of unique substances including more than 800 aliphatic, cycloaliphatic, aromatic, polyaromatic and terpenic compounds [7]. Some studies report that these compounds possess antibiotic, antimicrobial, antiviral, anti-inflammatory, analgesic, and antipyretic qualities. A number of unique chemical agents of lichens have also been proven to be effective against various cancer models. In addition, lichens have been widely used as food, feed, perfume, spice, dye, and traditional medicine all over the world. Besides, many types of lichens have been utilized for the treatment of diseases and cancer in recent years. There are more studies on the anticancer activity of secondary metabolites found in lichens. The most common secondary metabolite found in lichen species is usnic acid. There are at least 40 articles about it. Especially the *Evernia prunastri* species contains a lot of it. In the study conducted by [8], it was found that Atranorin secondary metabolite showed strong cytotoxic activity against brain cancer, breast cancer, cervical cancer, colorectal cancer, lung cancer, ovarian cancer, prostate cancer, melanoma cancer types (IC_{50} between 12.5 and 26.5 $\mu\text{g/ml}$) (except leukemia cell lines ($IC_{50} = 93.5 \mu\text{g/ml}$)). In the study conducted by [9] the cytotoxic effects of metabolites isolated from the lichen species *Flavocetraria cucullata*, such as usnic acid, salazinic acid, squamatic acid, baeomysesic acid, d-protolichesterinic acid and lichesterinic acid, on several human cancer cells were evaluated by the MTT method. The cells in which the determined IC_{50} value for usnic acid was obtained activated the specific apoptotic signaling pathway and an increase in the apoptotic cell population was observed. In the study conducted by Singh et al.; the anticancer effect of usnic acid in human lung carcinoma A549 cells and possible molecular changes were evaluated. Usnic acid secondary metabolite significantly suppressed the proliferative effect of A549 cell line. Cell growth inhibition was associated with cell cycle arrest in G0 and G1 phase. Usnic acid decreased the expression of cyclin-dependent kinase (CDK)4, CDK6 and cyclin D1 and increased the expression of CDK inhibitor (CDKI) p21/cip1 protein. Thus, usnic acid caused an increase in apoptotic cells more than two-fold. The apoptotic effect of usnic acid was realized by increased poly(ADP-ribose) polymerase cleavage [10-15].

Xanthoria parietina is a leafy lichen in the Teloschistaceae family. *Xanthoria* species have been traditionally used for various purposes, including medicinal utilities (antipyretic and jaundice) in Anatolia. Due to the anthraquinone dyestuff, which is abundant in its structures [16-20], they can be used for colouring purposes. Parietin-containing anthraquinones are well-known as one of the common bioactive compounds of lichens. Numerous scientific studies have presented the chemical composition, enzyme inhibition activities of *Xanthoria* lichens cultivated worldwide, and biopharmacological properties

of their parent compound "parietin" [21-23]. However, only a few studies have investigated the biologically active species and potential biological activities of *Xanthoria* lichens grown in Turkey [24].

Parietin is an anthraquinone pigment usually isolated from some plants such as *Rheum ribes* and *Xanthoria parietina* (lichen species). This secondary metabolite is localized as a small extracellular crystal in the uppermost level of the upper cortex of lichens and plays a protective role owing to its strong orange-brownish coloration against sunlight [25-27]. Parietin was considered responsible for the antiproliferative, antibacterial, antifungal, antioxidant [28,29], In this literature study, it was shown that parietin showed cytotoxic effect but not genotoxic effect at low concentration in HepG2 cells. As a result, it is predicted that parietin may be a useful agent in combination with other drugs in the treatment of hepatocellular carcinoma and should be supported by more detailed studies [30]. In the study conducted by Dodurga et al., the effects of parietin on cytotoxicity, gene expression, migration, invasion and colony formation in neuroblastoma cells treated with parietin were investigated. As a result, it was stated that parietin could be used as an alternative, complementary and supportive agent together with other drugs in the treatment of neuroblastoma [31,32]. There are many studies showing that parietin is an anthraquinone that has promising effects in preventing the proliferation of cancer cells and tumor growth [33-35].

In this study, the chemical profile of *Xanthoria parietina* (Xp) belonging to the family of Teloschistaceae was analyzed. The examined *Xanthoria parietina* was collected from three cities that are placed in different regions of Türkiye like Yozgat (Xp3), Izmit (Xp14), and Kütahya (Xp20). Since the DNA cleavage and DNA binding properties of the Xp lichen species, which were collected from different regions of Turkey, have not been reported in the literature, this original study can fill this empty in the literature. Total phenolic and total flavonoid content of Xp samples assessed spectroscopically. Besides, the in vitro antiproliferative effects of the Xp compounds were tested using the (3-(4,5-dimethylthiazol-2-yl)-2,5-diphenyltetrazolium bromide (MTT) test.

RESULTS AND DISCUSSION

GC-MS Analyses

The GC-MS results are listed in Tables (1-3). As a result, parietin, which has a flavonoid structure, was obtained 65.23% for Xp3, 58.03% for Xp14, and 71.75% for Xp20. The related spectra are showed in Figure 1 Parietin (anthraquinone derivative) was the main component determined by GC-MS in three Xp extracts.

Table 1. GC-MS results of sample Xp3

No	RT (min)	Formula	Area%	Molecular	Name
1	5.444	C ₆ H ₁₂ O ₂	4.35	116.158	4-hydroxy-4-methylpentan-2-one
2	46.597	C ₁₈ H ₂₂	0.59	238.367	(2,3-dimethyl-3-phenylbutan-2-yl)benzene
3	49.035	C ₁₈ H ₂₀	0.97	236.351	[(E)-2-methyl-4-phenylpent-3-en-2-yl]benzene
4	81.264	C ₂₄ H ₃₈ O ₄	25.09	390.556	bis(2-ethylhexyl) benzene-1,2-dicarboxylate
5	86.202	C ₁₆ H ₁₂ O ₅	65.23	284.268	1,8-Dihydroxy-3-methoxy-6-methyl-9,10-
6	90.575	C ₂₀ H ₄₀ O	2.33	296.540	(E)-3,7,11,15-tetramethylhexadec-2-en-1-ol
7	91.994	C ₁₉ H ₃₃ Br	1.44	373.400	3-bromoprop-2-ynyl hexadecanoate

Table 1 shows that the Xp3 sample contained 1,8-Dihydroxy-3-methoxy-6-methyl-9,10-anthraquinone at the highest value of 65.23%. This is consistent with the spectrum result.

Table 2. GC-MS results of sample Xp14

No	RT (min)	Formula	Area%	Molecular	Name
1	5.501	C ₆ H ₁₂ O ₂	4.05	116.158	4-hydroxy-4-methylpentan-2-one
2	45.591	C ₁₈ H ₂₂	0.45	238.367	(2,3-dimethyl-3-phenylbutan-2-yl)benzene
3	47.035	C ₁₈ H ₂₀	0.82	236.351	[(E)-2-methyl-4-phenylpent-3-en-2-yl]benzene
4	80.244	C ₂₄ H ₃₈ O ₄	24.03	390.556	bis(2-ethylhexyl) benzene-1,2-dicarboxylate
5	85.212	C ₁₆ H ₁₂ O ₅	58.03	284.268	1,8-Dihydroxy-3-methoxy-6-methyl-9,10-
6	89.504	C ₂₀ H ₄₀ O	1.23	296.540	(E)-3,7,11,15-tetramethylhexadec-2-en-1-ol
7	90.871	C ₁₉ H ₃₃ Br	0.94	373.400	3-bromoprop-2-ynyl hexadecanoate

Table 2 shows that the Xp14 sample contained 1,8-Dihydroxy-3-methoxy-6-methyl-9,10-anthraquinone at the highest value of 58.03%. This is consistent with the spectrum result.

Table 3. GC-MS results of sample Xp20

No	RT	Formula	Area%	Molecular	Name
1	5.323	C ₆ H ₁₂ O ₂	3.96	116.158	4-hydroxy-4-methylpentan-2-one
2	49.074	C ₁₈ H ₂₀	0.44	236.351	[(E)-2-methyl-4-phenylpent-3-en-2-yl]benzene
3	66,419	C ₁₄ H ₂₈ O	0.81	212.370	1-ethenoxy-2,6,8-trimethylnonane
4	81.146	C ₂₄ H ₃₈ O ₄	18.93	390.556	bis(2-ethylhexyl) benzene-1,2-dicarboxylate
5	85.930	C ₁₆ H ₁₂	71.75	284.268	1,8-Dihydroxy-3-methoxy-6-methyl-9,10-
6	98.101	C ₁₈ H ₃₄ O ₂	4.11	282.461	Ethenyl hexadecanoate

*: RT: Retention time, min: minute, Area %: Peak area %

Table 3 shows that the Xp20 sample contained 1,8-Dihydroxy-3-methoxy-6-methyl-9,10-anthraquinone at the highest value of 71.25% than other samples. This is consistent with the spectrum result.

INVESTIGATION OF ANTHRAQUINONE CONTENTS, DNA CLEAVAGE, DNA BINDING, CYTOTOXIC AND ANTIOXIDANT ACTIVITIES OF *XANTHORIA PARIETINA* SAMPLES

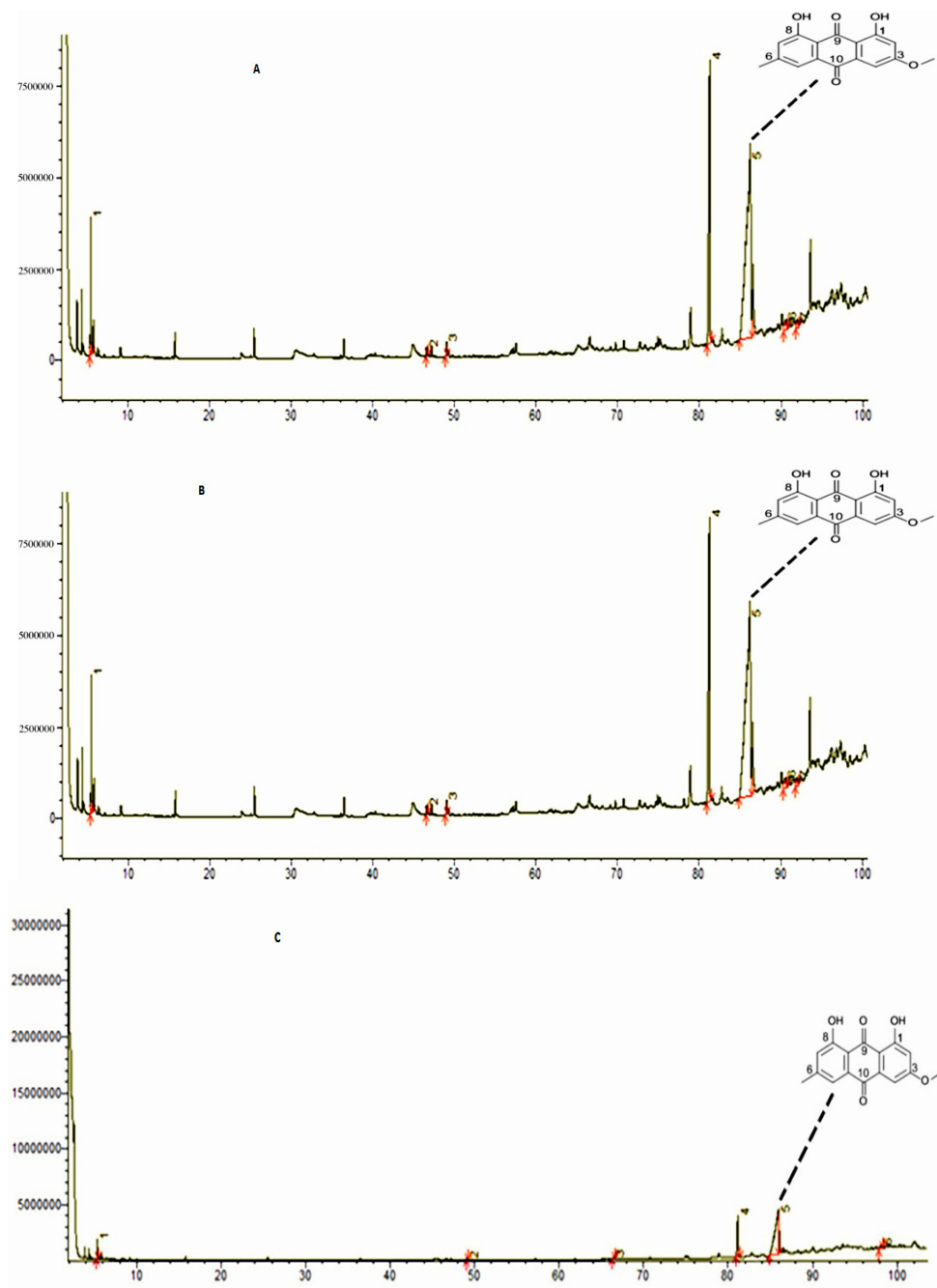


Figure 1. GC-MS spectrum of lichen samples; A: Xp3, B: Xp14, C: Xp20

Figure 1 shows the spectra containing the GC-Mass analysis results of three different lichen samples. The highest peak in each of these shows that the common anthraquinone structures are at the highest rate in each of them.

Total phenolic and flavonoid content results

TPC and TFC of the three extracts had assessed spectroscopically (Table 4). TPC of the extracts ranged between 17.07 and 25.30 mg GAE g⁻¹, (R²=0.999). The highest TPC was obtained for extract Xp20 while the lowest TPC was obtained for extract Xp14. Quercetin was standard for TFC. The results are summarized in Table 4. The highest TFC was obtained for extract Xp20 (51.42±0.15 mg QE. g⁻¹) while the lowest TFC was obtained for extract Xp14 (23.73±0.18 mg QE. g⁻¹).

Table 4. The total phenolic and total flavonoid contents of the Xp extracts

Extracts	Total Phenolic Content mg GAE/g	Total Flavonoid Content mg QE/g
Xp3	18.27±0.10	28.35±0.25
Xp14	17.07±0.11	23.73±0.18
Xp 20	25.30±0.05	51.42±0.15

DNA Binding results

The DNA binding properties of the studied extracts are showed in Figure 2. Lanes 1-3 contained different concentrations of CT-DNA in the absence of the extracts. In the presence of the extracts (lanes 4-12), as the CT-DNA concentration decreased the smear light intensity increased. The highest CT-DNA intercalation activity was obtained for sample Xp20 (lanes 10 and 11).

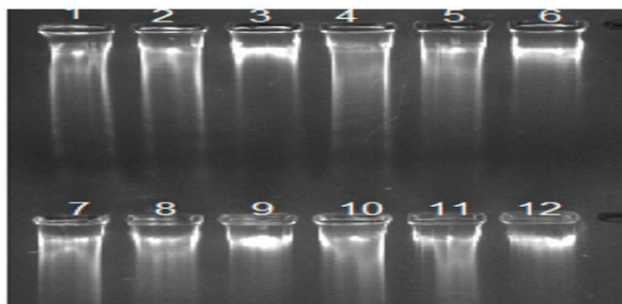


Figure 2. DNA Binding activity of Xp3, Xp14, and Xp20 extracts. Lane (1) CT-DNA (2 mg/ mL) + Buffer. Lane (2) CT-DNA (1 mg/mL) + Buffer. Lane (3) CT-DNA (0.5 mg/ mL) + Buffer. Lane (4) CT-DNA (2mg/ mL) + Buffer + 1.0 % Xp3. Lane (5) CT-DNA (1 mg/ mL) + 1.0 % Xp3+ Buffer. Lane (6) CT-DNA (0.5 mg/ mL) + 1.0 % Xp3+ Buffer. Lane (7) CT-DNA (2mg/ mL) + Buffer + 1.0 % Xp14. Lane (8) CT-DNA (1 mg/ mL) + Buffer + 1.0 % Xp14. Lane (9) CT-DNA (0.5 mg/ mL) + Buffer + 1.0 % Xp14. Lane (10) CT-DNA (2 mg/mL) + Buffer + 1.0 % Xp20. Lane (11) CT-DNA (1 mg/mL) + Buffer + 1.0 % Xp20. Lane (12) CT-DNA (0.5mg/mL) + Buffer + 1.0 % Xp20 (Ladder dye was put into every lane).

DNA Cleavage results

DNA cleavage properties of the studied extract are shown in Figure 3. The same results were obtained as there was no cleavage in lanes 1 and 7. Lanes 2, 8 and 11 did not contain DNA, so the samples did not emit with UV light. Acetone did not affect polar DNA (lane 5), whereas methanol, being a polar solvent, affected DNA (lane 6). There was no significant cleavage in lanes 3 and 4 containing sample Xp3 compared to lane 1. However, weak cleavage was seen in lane 9 in the presence of sample Xp14. Furthermore, thicker Form II and thinner Form I occurred in lanes 12 and 13 containing Xp20, resulting in DNA cleavage (over 50 percent).

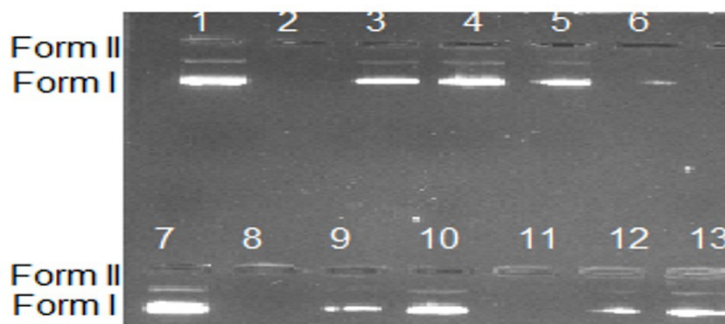


Figure 3. DNA Cleavage activity in 1% agarose gel of Xp3, Xp14, Xp20 extracts. Lane (1) pBR322DNA + ddw. Lane (2) Xp3+ ddw. Lane (3) pBR 322DNA + 1% Xp3+ddw. Lane (4) pBR 322DNA + 0.5% Xp3+ddw. Lane (5) pBR 322DNA + Aceton. Lane (6) pBR 322DNA + Methanol. Lane (7) pBR 322DNA + ddw. Lane (8) Xp14+ ddw. Lane (9) pBR 322DNA + 1% Xp14+ddw. Lane (10) pBR 322DNA + 0.5% Xp14+ddw. Lane (11) Xp20+ ddw. Lane (12) pBR 322DNA + 1% Xp20 +ddw. Lane (13) pBR 322DNA + 0.5% Xp20 +ddw (Ladder dye was put into the every lane).

Cytotoxicity results

The control group is the negative control group. In other words, it is the microscopic observation of the culture medium containing only the cells without any added substance. Therefore, since there is no additional substance medium that will disrupt the structure of the cells in this group, the cells are seen in the main form with the highest column in maximum viability numbers in Figure 4. During cultivation, the cells that incubated with Xp14 extract had abnormal morphology, cells were demonstrated shrinkage structure. For this study, it was tested by using MTT cell proliferation test *in vitro* cytotoxic effects of compounds on DLD-1 cell line. The obtained results of cytotoxic effects were presented Figure 4.

Some concentrations of lichen samples continued to show cell proliferation without causing cell toxicity. According to Figure 4, Xp14 extract reduced cell proliferation with the increasing concentration. On the other hand, cell proliferation decreased as the concentration of Xp20 and Xp3 extracts.

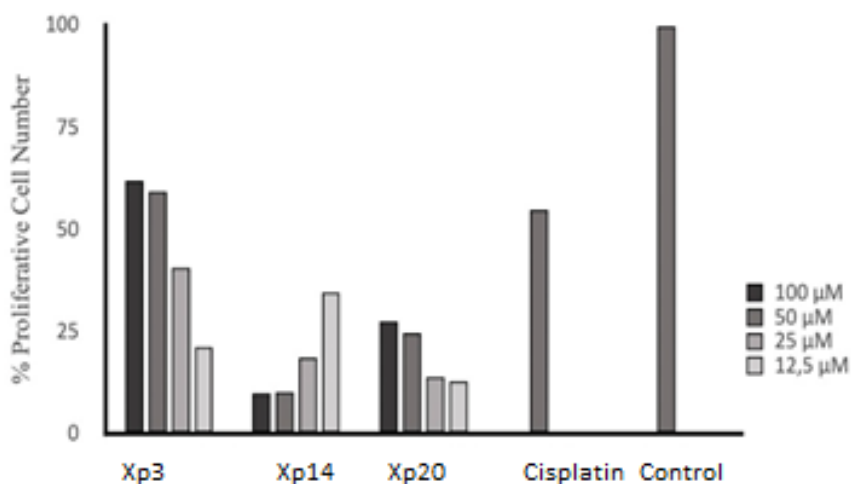


Figure 4. Cell proliferation at different concentrations of lichen extract (12.5 µM, 25 µM, 50 µM, and 100 µM), positive control (cisplatin, 10 µM), and negative control (without extract)" on the DLD-1 cell line experiments

DISCUSSION

Xp samples were taken from different cities located in different regions of Turkey and their chemicals were quantitatively analyzed. This study indicated that sample Xp20 collected from the province of Kütahya, located in the Central West Anatolian part of the Aegean region, contained more phenolic, flavonoid, and anthraquinone derivatives. In Tables 1-3, which were created according to the GC-MS results performed on the *Xanthoria parietina* (Xp) contents used in this study, it was seen that 1,8-dihydroxy-3-methoxy-6-methyl-9,10-anthraquinone structure was more prevalent in the 50-71% range. This achievement can originate from the fact that the Aegean region has maquis vegetation and a Mediterranean climate [36]. Anthracene (Parietin) is a carcinogenic organic substance since it contains polycyclic aromatic hydrocarbons [37-39]. However, this compound and its derivatives are used as a dyestuff source in the food, medicine, and textile industries [40-42]. Since Xp 20 contains the highest amount of anthraquinone group at 71.75%, it can be used as a dye source in

the textile and food industries. The study of the DNA cleavage and DNA binding activities of materials is a suitable method to examine their anticancer properties [43-44]. Therefore, the DNA properties and toxicity of the parietin structures were investigated in this study. In the cytotoxicity evaluation of three Xp extracts at 100 μ M concentration, that is, in their most concentrated state, the closest cell proliferation to control and cisplatin was Xp 3, then Xp 20. In the study conducted by diluting these, cell proliferation continued to increase as Xp 14 did not show a toxic effect. However, since Xp 3 and Xp 20 reduce the number of cancer cells with a toxic effect, they are seen to have anticancer potential.

Marian Temina et al carried out GC-MS and HPLC analysis for the determination of acids and esters in the lichen-type structures of *Collema* [45]. The phenolic-flavonoid phytochemical content of *Xanthoria* species growing in Türkiye is higher than other *Rocella* lichen species.[46]. Torres et al. studied the surface alkanes and fatty acids content of *Xanthoria parietina* lichen collected from the Jerusalem hills using the GC-MS method [47]. Basile et al. reported the parietin content of *Xanthoria parietina* by performing the HPLC method. The results proved that the pure parietin extracts as secondary metabolites exhibited effective antimicrobial and anticancer properties [34,35;47]. Also, phytochemical features of *Xanthoria parietina* lichen obtained from Australia were studied only using spectroscopic methods. In this study, the phenolic-flavonoid content of *Rocella* lichen species was studied by applying the same spectrophotometric method [48,49]. No DNA cleavage or DNA binding studies have been found for the *Xanthoria parietina* species in the literature. In this study, DNA cleavage was significant only in Xp 20, while it was very weak in the others. More biological activities such as cytotoxicity and significant DNA cleavage were observed in Xp samples with high anthraquinone content. Solutions of Xp3 and Xp20 Lichen samples were prepared as 100 μ M. However, it is seen in Figure 4 that the samples showed a cytotoxic effect in the cytotoxicity test applied at a lower concentration of 12.5 μ M and reduced cancer cell proliferation. On the other hand, the Xp14 lichen sample showed the opposite activity at all concentrations, i.e., it did not show a cytotoxic effect. It has been determined that cytotoxicity is also lowest in Xp 14 sample with low flavonoid, phenolic or anthraquinone content.

CONCLUSION

This study presents new *Xanthoria parietina* samples, which include mostly parietin/flavonoid/phenolic content and were obtained from different regions of Turkey for the first time. Due to 71.75% anthracene (parietin) and high

flavonoid-phenolic contents, the *Xanthoria parietina* lichen (Xp20) collected from Kütahya city of Turkey can be used as a natural dyestuff source. Since Xp3 (from Yozgat) and Xp 20 (from Kütahya) Lichen samples show cytotoxic effects at low concentrations such as 12.5 μ M, they can be evaluated as anticancer drugs and chemotherapy agents when supported by additional studies.

MATERIALS AND METHODS

Lichen Samples

Samples of *Xanthoria parietina* species (Figure 5) were harvested properly from the wild as described below and transferred to the laboratory within 6 hours. Lichenological identities of lichen materials were carried out at Biology Department Herbarium (ERC), Science Faculty, Erciyes University, Kayseri, Turkey. The voucher specimens were deposited at ERC. The herbarium information of the samples is detailed as follows:

Xanthoria parietina (Xp3) Th.Fr.; Yozgat, Çamlık; on *Fagus orientalis*, GPS coordinates 39°48'52.98" N, 34°48'48.81"E, 1375 m, Turkey, February 2011, Herbarium code: ERC-Xp3; Collector: Mehmet Gökhan Halıcı, Emre Kılıç.

Xanthoria parietina (Xp14) Th. Fr.; İzmit, Kandıra; east of Cebeci, frutices in litore. GPS coordinates 41°12' 04" N, 30°15'46"E, 10 m, Turkey, May 2012, Herbarium code: ERC-Xp14; Collector: Mehmet Gökhan Halıcı, Emre Kılıç.

Xanthoria parietina (Xp20) Th. Fr.; Kütahya, between Kütahya and Afyon, northeast of Körs village, *Salix* communities. GPS coordinates 39°19'10" N, 30°17'16"E, 1095 m, Turkey, June 2012, Herbarium code: ERC-Xp20; Collector: Mehmet Gökhan Halıcı, Emre Kılıç.



Figure 5. Images of the collected *Xanthoria parietina*:
(a) Xp3, (b) Xp14, (c) Xp20

Chemicals and Other Materials

Methanol, Ethanol, acetone, DMSO, TAE and Folin Ciocalteu, sodium carbonate, aluminium nitrate, potassium acetate, sodium hydroxide, ethidium bromide, Tris HCl were supplied by Merck (Darmstadt, Germany). CT-DNA, 1% Agarose, glycerol, FBS, penicilline-streptomycin got from Sigma-Aldrich (St. Louis, MO, USA). pBR322 plasmid DNA was used DNA model for cleavage activity by Thermo Fisher Scientific (Baltics UAB | V.A. Graiciuno 8, LT-02241 Vilnius, Lithuania).

Preparation of the extracts from *Xanthoria parietina* samples

Soxhalation was used for the preparation of solvent extracts. A 1.00 g of shade-dried Xp samples were taken separately in a thimble and the extracts were collected using 20 ml acetone. Then, the filtrates were concentrated by a rotary evaporator (BuchiR200 Rota vapor). The extracts resuspended in DMSO and kept at 4 °C in a refrigerator for further use [48-49].

Gas Chromatography-Mass Analysis Procedure

GC-MS analysis of the extracts was performed on a SHIMADZU QP2010 ULTRA GC System fitted with a Rtx-5MS capillary column (30 m 0.25 mm inner diameter, 0.25 µm film thickness, max. temperature, 350 °C) coupled to a SHIMADZU GC-MS. Pure, ultra-high helium (99.99%) was used at a sustained flow rate of 1.0 mL/ min. Ion source temperatures and transfer line injection were all 290 °C. The ionizing energy was 70 eV. The electron multiplier voltage was obtained from an auto-tuning. The oven temperature was programmed from 60 °C (hold for 2 minutes) to 280 °C at a rate of 3 °C/min. The samples were diluted with a convenient solution (1/100, v/v) and filtered. The particle-free diluted extracts (1 µL) were aspirated into a syringe and injected into the injector at a split ratio of 50:1. All data were obtained from the full-scan mass spectra within the scan range of 40-850 amu. The percentage composition of the sample extracts was expressed as a percentage by peak area. The characterization and identification of the chemical compounds in various sample extracts were based on the GC retention time. The mass spectra were computer-matched with those of standards available in mass spectrum libraries.

Determination of Total Phenolic Content (TPC)

Total phenolic content was determined using the Folin–Ciocalteu colorimetric method. Gallic was used as standards. Briefly, 20 µL of the filtered extracts were mixed with 400 µL of 0.5 N Folin-Ciocalteu reagent and 680 µL distilled water. This mixture was incubated for 3 min at room temperature before adding 400 µL Na₂CO₃ (10%). After incubation of the samples for 2 hours,

their absorbances were measured at 760 nm with the UV-Vis machine (Thermo Multiskan Go). The concentration of total phenolic compounds was calculated as mg gallic acid equivalents (GAE) per g dried extract [50].

Determination of Total Flavonoid Content (TFC)

The aluminum complexation method was used to determine the total flavonoid content. 0.5 mL of plant extract, 0.1 mL of 10% aluminum nitrate, 0.1 mL of 1 M potassium acetate, and 4.3 mL of 80% ethyl alcohol were combined using this method. The samples were incubated at room temperature for 40 minutes, and then their absorbance at 415 nm was measured using a UV-Vis device (Labomed Inc., Culver City, USA). Using quercetin as the standard, a curve for calibration in the range of 0.00195 to 0.5 mg.mL⁻¹ ($r^2 = 0.999$) was created. Based on the average of three measurements, the total flavonoid concentration was expressed as mg of quercetin equivalent (QE) per g of dry weight (dw) [51].

DNA Cleavage Test

The DNA cleavage properties of the Xp3, Xp14, Xp20 extracts that the process was carried out in 1% agarose gel electrophoresis device. No light was used for interaction prior to sample and DNA incubation. Supercoiled pBR322 plasmid DNA had used with a decreasing percentage of the extracts (1%, 0.5%) in ddw and Tris HCl buffer (pH=7). Gel electrophoresis process was applied in the referenced study with a few changes [52].

DNA Binding Test

The samples were prepared by the dissolution of Xp3, Xp14, and Xp20 extracts in ddw. The different concentrations of Calf Thymus DNA (CT-DNA) (2-0.5mg/ml) in Tris HCl buffer and a constant concentration of the extracts (1%). The mixtures were adjusted to a final volume of 25µL with buffer and incubated at 37°C for 24 hours. Then, the mixtures were loaded on 1% agarose gel with ethidium bromide staining in Tris Acetate Edta (TAE). The electrophoresis was carried out at 80 V for 45 minutes. The results were visualized using the BioRad Gel Doc XR system [53].

Cytotoxicity Test

Human colon cancer cell line (DLD-1) for this study was obtained from American Type Culture Collection CCL-221™, ATCC, USA). DLD-1 cells in nitrogen tank were dissolved at 37°C for one minute. Dissolved cells were placed in a falcon tube, FBS was added to remove DMSO, and pipetting was done several times. Then, RPMI-1640 (Sigma) cell medium containing 10% Fetal bovine serum (FBS) and 1% penicillin-streptomycin was used.

Cells were cultured in 75 cm³ flasks with RPMI-1640 medium. 5 % CO₂ and 37 °C humidified incubator was used. Cells were seeded as 5x10³ cells per well in 96 well plate for MTT assay. The extracts were added separately to the cells as 100 (1%), 50 (0.5%), 25 (0.25%), 12.5µM final concentrations after 24 hours after seeding. 10 µM Cisplatin was used as a positive control. There is no lichen extract in the positive control, but the anticancer drug cisplatin is present. There is no lichen extract in the negative control. All groups were incubated at 5 % CO₂ and 37 °C humidified incubator for 24 hours. After the medium liquids of the incubated cells were withdrawn. The remaining process was completed as in the reference. [54-55].

ACKNOWLEDGMENTS

The author thanks Prof. Dr. M. Gökhan Halıcı, Prof. Dr. Fatma Öztürk Kıp and Dr. Mithat Güllü (Department of Biology, Turkey Erciyes University, Kayseri) for their valuable scientific supports and collection of the *Xanthoria parietina* lichens.

AUTHORS CONTRIBUTIONS

NG: Conception, design, data collection and analysis, manuscript writing and editing, and supervision. EKS: Material preparation, data collection and analysis, manuscript writing and editing.

FUNDING

The author did not receive support from any organization for the submitted work.

CONFLICT OF INTEREST

The authors declare no conflict of interest.

REFERENCES

1. M. Bačkorová; R. Jendželovský; M. Kello; M. Bačkor; J. Mikeš; P. Fedoročko; *In Vitro Toxicol.*, **2014**, 26(3), 462-468. <https://doi.org/10.1016/j.tiv.2012.01.017>
2. F. Chavant; A. Boucher; R. Boisselier; S. Deheul; D. Debruyne; *Thérapie*, **2015**, 70(2), 179-89. [10.2515/therapie/2015001](https://doi.org/10.2515/therapie/2015001)
3. D. Koche; R. Shirsat; M. Kawale; *Hislopia Journal*, **2016**, 9(1/2), 1-11.

4. J. Plsíková; J. Stepankova; J. Kasparkova; V. Brabec; M. Backor; M. Kozurkova; *In Vitro Toxicol.*, **2014**, 28(2),182-186. <https://doi.org/10.1016/j.tiv.2013.11.003>
5. M. Sxena; S. Jyoti; R. Nema; S. Dharmendra; G. Abhishek; *JPP.*, **2013**, 1(6),168-182.
6. T.H. Nash; Cambridge, UK: Cambridge University Press, **2008**, 301-316.
7. V. Cardile; A.C.E. Graziano; R. Avola; M. Piovano; A. Russo; *Chem. Biol. Interact.*, **2017**, 263, 36-45. <https://doi.org/10.1016/j.cbi.2016.12.007>
8. A. Shcherbakova; A. A. Strömstedt; U. Göransson; O. Gnezdilov; A. Turanov; D. Boldbaatar; D. Kochkin; G. U. Merzenich; A. Koptina; *World J Microbiol Biotechnol.*,**2021**, 37,129.
9. T.T. Nguyen; S.Yoon; Y. Yang; H.B. Lee; S. Oh; M.H. Jeong; et al. *PLoS One*, **2014**, 31,9 (10),e111575.
10. A. Dinçsoy; D. Cansaran-Duman; (2017). *Turk. J. Biol.*. **2017**, 41. 10.3906/biy-1609-40.
11. K. Ingolfsdottir; *Phytochem*, **2002**, 61, 729-36.
12. M. Sekerli; K. Nil; C.D. Demet; *Turk. Hij. Den. Biyol. Derg.*, **2017**, 74, 95-102. 10.5505/TurkHijyen.2016.24650.
13. N. Singh; D. Nambiar; R.K. Kale; R.P. Singh; *Nutr. Cancer.*, **2013**, 65, 36-43.
14. M. Bačkorová; R. Jendželovský; M. Kello; *Toxicol. in Vitro.*, **2012**, 26, 462-8.
15. E.R. Correche; M. Carrasco; F. Giannini; *Acta Farm. Bonaerense.*, **2002**, 21, 273-78.
16. M.M. Kosani'c; B.R. Rankovi'c; T. P. Stanojkovi'c; *J. Sci. Food Agric.*, **2012**, 92(9), 1909-1916. <http://dx.doi.org/10.1002/jsfa.5559>
17. L. Nybakken; K.A. Solhaug; W. Bilger; Y. Gauslaa; *Oecologia*, **2004**, 140, 211–216. <https://doi.org/10.1007/s00442-004-1583-6>
18. B. Rankovi'c; M. Kosani'c; T. Stanojkovi'c; P. Vasiljevi'c; N. Manojlovi'c; *Int. J. Mol. Sci.*, **2012**, 13, 14707–14722. <http://dx.doi.org/10.3390/ijms131114707>
19. A. Sweidan; M. Chollet-Krugler; A. Sauvager; P. van de Weghe; A. Chokr; M. Bonnaure-Mallet, et al., *Fitoterapia*, **2017**, 121,164–9. <https://doi.org/10.1016/j.fitote.2017.07.011>
20. V.M. Thadhani; V. Karunaratne; *Oxid. Med. Cell. Longev.*, **2017**, 1-10. <https://doi.org/10.1155/2017/2079697>
21. S. Ali; H.N. Hameed; *JAPS*, **2019**, 29 (3), 881-888.
22. A. Cornejo; F. Salgado; J. Caballero; R. Vargas; M. Simirgiotis; C. Areche; *Int. J. Mol. Sci.*, **2016**, 17(8), 1303. <https://doi.org/10.3390/ijms17081303>
23. J. Kumar; P. Dhar; A.B. Tayade; D. Gupta; O.P. Chaurasia; D.K. Upreti et al., *Plos One*, **2014**, 9(6),98696. <https://doi.org/10.1371/journal.pone.0098696>
24. M. Mükemre; G. Zengin; R.S. Türker; A. Aslan; A. Dalar; *IJSM*, **2021**, 8(4),376-388. <https://doi.org/10.21448/ijsm.994427>
25. L. Comini; F.E.M. Vieyra; R.A. Mignone; P.L. Paez; M.L. Mugas; B.S. Konigheim et al., *PPS*, **2017**, 16, 201-210. <https://doi.org/10.1039/c6pp00334f>
26. Y. Gauslaa; E.M. Ustvedt; *PPS*, **2003**, 2,424-432. <https://doi.org/10.1039/b212532c>
27. K. Solhaug; Y. Gauslaa; *Oecologia*, **1996**, 108,412-418. <https://doi.org/10.1007/BF00333715>
28. Lawrey, J.D. Biological role of lichen substances. *Byrologist*, **1986**, 89, 111–122. <http://dx.doi.org/10.2307/3242751>.

29. A. Basile; D. Rigano; S. Loppi; A. Di Santi; A. Nebbioso; S. Sorbo; et al., *Int. J. Mol. Sci.*, **2015**, *16*(4), 7861-7875. <https://doi.org/10.3390/ijms16047861>
30. A.K. Demirkaya; G. Gündoğdu; Y. Dodurga; M. Seçme; K. Gündoğdu; *J. Vet. Sci.*, **2019**, *14*(1), 29-37. <https://doi.org/10.17094/ataunivbd.387311>
31. Y. Dodurga; M. Seçme; L. Elmas; G. Gündoğdu; A. Çekin; N.S. Günel; *Pam.Tıp Derg.*, **2024**, *17*, 243-253.
32. T. Varol; M. Ertuğrul; *Fresenius Environ. Bull.*, **2015**, *24*, 3436-3444.
33. A.M. Abdallah; U.A. Muhammed; A. Ghazala; D. Alice Abu; M. A. Ahmed, S. Ahmed; E. Konrad; W. Matthias; S. Jens; B. Udo; *Biomater Adv.*, **2022**, *134*, 112543. <https://doi.org/10.1016/j.msec.2021.112543>.
34. S. Chopra *et al*; Breast cancer Medicine, 2020
35. M. Bačkorová; M. Bačkor; J. Mikeš; R. Jendželovský; P. Fedoročko; *Toxicol. in Vitro*, **2011**, *25*(1), 37-44. doi: 10.1016/j.tiv.2010.09.004.
36. C.A.H. Bigger; I. Pontén; J.E. Page; A. Dipple; *Mutat. Res. Fund. Mol. M.*, **2000**, *450*(1-2), 75-93. [https://doi.org/10.1016/S0027-5107\(00\)00017-8](https://doi.org/10.1016/S0027-5107(00)00017-8)
37. B.M. Sahoo; B.V.V. Ravi Kumar; B.K. Banik; P. Borah; *Curr. Org. Synth.*, **2020**, *17*(8), 625-640. <https://doi.org/10.2174/1570179417666200713182441>
38. A.A. Stec; K.E. Dickens; M. Salden; F.E. Hewitt; D.P. Watts; P.E. Houldsworth; et al., *Sci. Rep.*, **2018**, *8*, 2476. <https://doi.org/10.1038/s41598-018-20616-6>
39. C. Boyles; S.J.S. Sobeck; *Food Chem.*, **2020**, *315*, 126249.
40. Y. Ito; N. Harikai; K. Ishizuki; K. Shinomiya; N. Sugimoto; H. Akiyama; *Chem. Pharm. Bull.*, **2017**, *65*(9), 883-887. <https://doi.org/10.1248/cpb.c17-00404>
41. L. Malinauskiene; M. Bruze; K. Ryberg; E. Zimerson; M. Isaksson; *Contact Dermatitis*, **2013**, *68*(2), 65-75. <https://doi.org/10.1111/cod.12001>
42. A. Narayanankutty; A. Nair; S.P. Illam; A. Upananlawar; A.C. Raghavamenon; *Nutr. Cancer*, **2021**, *73*(5), 809-816. <https://doi.org/10.1080/01635581.2020.1778745>
43. Z. Bıyıklıoğlu; H. Baş; Y. Altun; C.Ö. Yalçın; B. Barut; *Appl. Organomet. Chem.*, **2022**, *32*, 1-10.
44. Z.E. Hillman; J.M. Tanski; A. Roberts; *Acta crystallogr., C Struct. Chem.*, **2020**, *76*, 639-646. <https://doi.org/10.1107/S2053229620008128>
45. M. Temina; D.O. Levitsky; V.M. Dembitsky; *Rec. Nat. Prod.*, **2010**, *4*(1), 79-86.
46. M. Ben Salah; C. Aouadhi; A. Khadhri; *Bioprocess Biosyst. Eng.*, **2021**, *44*, 2257-2268.
47. A. Torres; I. Dor; J. Rotem; M. Srebnik; V.M. Dembitsky; *Eur. J. Biochem.*, **2003**, *270*(10), 2120-2125. <https://doi.org/10.1046/j.1432-1033.2003.03556.x>
48. D. Dias; S. Urban; *Nat. Prod. Commun.*, **2009**, *4*(7), 959-964. <https://doi.org/10.1177/1934578X0900400717>
49. D. Gandhi; K. Umamahesh; S. Sathiyaraj; G. Suriyakala; R. Velmurugan; D.A. Al Farraj; et al., *J. Infect. Public Health*, **2022**, *15*(4), 491-497. <https://doi.org/10.1016/j.jiph.2021.10.014>
50. V.L. Singleton; J.A. Rossi; *AJEV*, **1965**, *16*(3), 144-158. <http://doi.org/citeulike-article-id:7170825>
51. M. Marcucci; R. Woisky; A. Salatino; *Mensagem Doce*, **1998**, *46*, 3-9.

52. N. Farajzadeh; N.G. Kuşçulu; H.Y. Yenilmez; D. Bahar; Z.A. Bayır; *New J. Chem.*, **2022a**, *46*, 19863-19873. <https://doi.org/10.1039/D2NJ02891C>
53. N. Farajzadeh; N.G. Kuşçulu; H.Y. Yenilmez; D. Bahar; Z. Altuntaş Bayır; *Dalton Trans.*, **2022b**, *51*, 7539-7550. <https://doi.org/10.1039/D2DT01033J>
54. N. Farajzadeh; H.Y. Yenilmez; D. Bahar; N. Güler Kuşçulu; E. Kılıçkaya Selvi; Z. Altuntaş Bayır; *Dalton Trans.*, **2023**, *52*, 7009-7020. <https://doi.org/10.1039/D3DT00615H>
55. E. Yabaş; S. Şahin-Bölükbaşı; Z.D. Şahin-İnan; *J. Porphyr. Phthalocyanines*, **2022**, *26*, 65–77.

ANTIOXIDANT POTENTIAL OF CHERRY STALK EXTRACTS

Dejan PRVULOVIĆ^a , Radenka KOLAROV^a ,
Mirjana LJUBOJEVIĆ^a , Goran BARAĆ^a ,
Marijana PEIĆ TUKULJAC^{a,*} 

ABSTRACT. Cherry stalks, as primary by-products of sour cherry (*Prunus cerasus* L.) and sweet cherry (*Prunus avium* L.) harvesting, are often considered agricultural and industrial waste. However, cherry stalks are recognized in traditional and ethno medicine for their therapeutic properties, due to their high content of natural antioxidants. In this study, the concentrations of total phenolic and total flavonoid compounds, as well as antioxidant activity, were evaluated in different cherry stalk extracts (aqueous, methanol, ethanol, and acetone) obtained from sweet cherry cultivars, sour cherry cultivars, and a wild cherry sample. The results depended on the cultivar and the solvent used for extraction. The highest concentrations of total phenolic and total flavonoid compounds were observed in acetone extracts. In various antioxidant tests, the antioxidant activity varied depending on the genotype.

Keywords: antioxidant capacity, cherry, extraction solvent, *Prunus avium* L., *Prunus cerasus* L., phenolics, stalks

INTRODUCTION

Reduction of carbon footprint in sustainable agriculture is one of the main goals of modern humanity. Action plan established by European Union involves reducing, recovering, reusing, and recycling materials and energy through circular economy. By-products originated from different agricultural and food processing operations are rich sources of bioactive and nutritional

^a University of Novi Sad, Faculty of Agriculture, Trg Dositeja Obradovića 8, 21000, Novi Sad, Serbia

* Corresponding author: marijana.peic@polj.uns.ac.rs



compounds and could be used for development of new and innovative food products [1]. Most widespread compounds in agro-food by-products are dietary fibers, carotenoids, and different polyphenolic molecules produced from primary and secondary metabolism of plants [2]. By-products of fruits and vegetables are the most abundant waste, with a percentage of the residues around 40–50% of the total discards and it could be in form of pulp, seeds, pomace or in other forms [3]. Phytochemical valorisation of agro-food by-products is one of the first steps for identification of bioactive compounds with health-related properties.

Cherry stalks (or stems) are, together with cherry stones, one of the main by-products obtained after the harvesting and processing of sour cherries (*Prunus cerasus* L.) and sweet cherries (*Prunus avium* L.). Although stalks are generally recognised as a waste from agriculture and food industry, the traditional and ethno medicine use them as a herbal remedy for some disorders [4]. In Romania, Bosnia and Herzegovina, Turkey, Iran and other countries infusion (herbal tea) or decoction is used for treatment of different kidney disorders, to relief of renal stones, increase urine output, and mild urinary tract infections [4,5,6,7]. The cherry stalks are also used for its sedative properties, to reduce inflammation, treat obesity, positive effect on cardiovascular system and smooth muscle [4,8]. Cherry stalk's extracts possess strong antimicrobial activity and proved to be effective against some pathogenic bacteria that are resistant to the tested antibiotic [9]. Sour and sweet cherry stalks extracts also exhibited anticancer properties *in vitro* conditions [10].

It is assumed that health beneficial properties (anti-inflammatory and diuretic) are results of presence of high concentration of natural antioxidants (primarily flavonoids) present in the stalks [7,11]. Major phenolic compounds present in sweet cherry stems are mostly different hydroxycinnamic acids: *p*-coumaric, ferulic, caffeic, chlorogenic and neochlorogenic acid [8].

For many years, natural sources of antioxidants have attracted considerable attention in scientific research, with increasing focus on the potential use of various agricultural by-products, such as cherry stalks. Although previous research has examined the antioxidant properties of various parts of the cherry plant, it has mostly focused on the fruits, while the stalks have been significantly less studied. This study aims to provide a detailed evaluation of the total phenolic content and antioxidant potential of extracts from the stalks of thirteen sweet cherry cultivars, three sour cherry cultivars, and one wild cherry sample, using four different solvents. The novelty of this work lies in its systematic comparison of various cherry types and extraction solvents, which has not been previously addressed in such depth, highlighting the potential of cherry stalks as valuable bioactive by-products.

RESULTS AND DISCUSSION

The total phenolic content in cherry stalk extracts is presented in Table 1. The total phenolic content ranged from 9.98 to 30.91 mg GAE/g DW in aqueous extracts, from 13.13 to 39 mg GAE/g DW in methanolic extracts, from 13.54 to 34.89 mg GAE/g DW in ethanolic extracts, and from 18.58 to 52.29 mg GAE/g DW in acetone extracts. The highest content of phenolic compounds was found in the acetone extract of sour cherry cultivar Érdi bőtermő.

Table 1. Content of total phenolics in cherry stalk extracts

	Cultivar	Extraction solvent			
		Water	70% methanol	70% ethanol	70% acetone
Sweet cherry	Alex	9.98 ^{bB} ± 0.16	13.67 ^{bcB} ± 1.02	16.63 ^{cdB} ± 1.27	18.58 ^{ba} ± 0.66
	Bigarreau Burlat	17.73 ^{eD} ± 2.43	27.28 ^{bcB} ± 0.37	23.75 ^{deC} ± 0.18	35.85 ^{eA} ± 0.05
	Carmen	14.15 ^{cdD} ± 1.09	19.83 ^{dc} ± 0.66	21.11 ^{bb} ± 0.94	30.04 ^{da} ± 0.54
	Germersdorfer	12.11 ^{cC} ± 0.79	16.21 ^{bb} ± 1.71	17.01 ^{cb} ± 1.11	23.01 ^{ca} ± 0.65
	Hedelfinger	21.68 ^{eD} ± 1.03	24.73 ^{efC} ± 0.88	29.04 ^{eb} ± 1.14	37.95 ^{fgA} ± 1.00
	Katalin	17.54 ^{id} ± 0.42	20.54 ^{jc} ± 0.54	23.76 ^{jkB} ± 1.26	33.07 ^{ia} ± 2.59
	Linda	15.66 ^{hd} ± 0.37	17.36 ^{ic} ± 1.45	17.14 ^{hib} ± 1.43	27.99 ^{ka} ± 1.26
	New Star	10.57 ^{jd} ± 3.86	18.09 ^{ghB} ± 0.29	16.70 ^{ijC} ± 1.19	23.86 ^{ia} ± 2.24
	Peter	13.88 ^{ghC} ± 0.43	20.17 ^{fgB} ± 1.05	19.61 ^{fgB} ± 0.77	29.83 ^{fgA} ± 1.83
	Sandor	19.98 ^{dd} ± 0.35	26.86 ^{cdB} ± 1.22	23.99 ^{deC} ± 0.49	38.25 ^{da} ± 0.67
	Solomary gomboly	27.85 ^{eb} ± 1.28	26.45 ^{ijC} ± 0.80	25.60 ^{kc} ± 2.77	42.98 ^{ka} ± 1.53
	Summit	13.20 ^{fgHc} ± 1.07	17.64 ^{kgB} ± 1.63	15.73 ^{ijBC} ± 0.70	27.93 ^{ha} ± 1.07
	Valery Chkalov	22.48 ^{fgC} ± 0.41	27.78 ^{efB} ± 0.58	28.56 ^{fgB} ± 2.67	40.84 ^{ga} ± 1.08
Sour cherry	Érdi bőtermő	30.91 ^{ad} ± 0.44	39.00 ^{ab} ± 1.93	34.89 ^{ac} ± 2.23	52.29 ^{aa} ± 0.91
	Kantor-jánosi	12.52 ^{hc} ± 0.34	13.13 ^{ijB} ± 0.82	14.32 ^{jkB} ± 1.42	24.04 ^{ja} ± 0.47
	Oblačinska	17.67 ^{ed} ± 0.40	21.67 ^{eb} ± 0.43	20.82 ^{ic} ± 1.46	31.93 ^{fa} ± 1.26
Wild cherry	21.50 ^{ic} ± 2.27	14.11 ^{hBC} ± 1.10	13.54 ^{ghB} ± 0.81	21.61 ^{ha} ± 1.02	

Expressed as mg gallic acid equivalents (GAE)/g dry weight; Values are means ± SD; values preceded by the same lowercase letter in the column do not differ significantly according to the Duncan's multiple range test ($p < 0.05$)

Moreover, the total phenolic content in all extracts of the *Érdi bőtermő* cultivar was significantly higher than that of the other tested cultivars. In the aqueous extracts of the stalks cultivar Alex (sweet cherry), the lowest concentration of phenolic compounds was observed.

Phenolic compounds are important secondary metabolites in plants due to their significant antioxidant activity, which includes free radical-scavenging, hydrogen donation, singlet oxygen quenching, metal ion chelation, and also acting as a substrate for radicals such as hydroxyl and superoxide [12]. The phenolic content depends on cultivar, growing conditions as well as the solvent used for extraction [13,14]. The content of total phenols compounds in methanolic extracts of sweet cherry stalks was in accordance with the study of Afonso et al. (from 23.59 to 32.49 mg GAE/g) [15]. On the other hand, total phenolic content in ethanolic and aqueous extracts of wild cherry was lower than those reported by Ademović et al. (121.3 and 74.1 mg GAE/g, respectively) [16].

According to earlier research, acetone is a suitable solvent for extracting polyphenols, especially those with higher molecular weights [14]. In this study, it has been observed that acetone extracts contain the highest amount of total phenolic compounds compared to extracts obtained using other solvents. The total phenol content of acetone extracts differed significantly among all cultivars when compared to other extracts. The amounts of total phenols in the acetone extracts were comparable to the results in our previous study [17].

In Table 2 are presented the results of total flavonoids content in cherry stalk extracts.

Flavonoids are the most widespread class of phenolic compounds in plants where play a role in various cellular activities like as signalling, pigmentation and plant protection against different stressors [18]. The total flavonoids content was ranged from 8.31 to 23.17 mg QE/g DW in water extracts, from 9.71 to 21.33 mg QE/ g DW in methanolic extracts, from 11.74 to 28.07 mg QE/ g DW in ethanolic extracts, as well as from 18.24 to 33.90 mg QE/ g DW in acetone extracts. The acetone extract of the sour cherry stalks cultivar *Érdi bőtermő* contained the highest amount of flavonoids, while the lowest content was found in the aqueous extracts of the sweet cherry cultivar Alex.

In *P. avium* by-products, such as stalk, pulp, seed, and leaf the highest concentration of total flavonoids was found in the extracts obtained using a solvent of moderate polarity [19]. The highest concentration of total flavonoids was found in acetone extracts. The studies of Do et al. and Xiong et al., also showed higher amount of total phenolic compounds as well as total flavonoids compounds in acetone extracts of *Osmanthus fragrans*' seed and *Limnophila aromatica* than ethanol and methanol extracts. In recent researches, it has

ANTIOXIDANT POTENTIAL OF CHERRY STALK EXTRACTS

been observed that acetone extracts (50-80%) contained higher amount of total phenols and total flavonoids in compared to their corresponding alcoholic-water mixtures [20].

Table 2. Content of total flavonoids

	Cultivar	Extraction solvent			
		Water	70% methanol	70% ethanol	70% acetone
Sweet cherry	Alex	8.31 ^{gC} ±	10.17 ^{iC} ±	11.74 ^{gB} ±	19.60 ^{ghA} ±
		0.63	0.74	2.43	0.71
	Bigarreau Burlat	9.45 ^{efgC} ±	14.44 ^{fgB} ±	20.76 ^{fgB} ±	23.84 ^{bcdA} ±
		0.52	0.23	3.81	0.52
	Carmen	10.24 ^{defC} ±	15.41 ^{efB} ±	17.26 ^{cdeA} ±	21.81 ^{deA} ±
		0.61	0.76	3.50	1.00
	Germersdorfer	10.28 ^{deC} ±	14.85 ^{fB} ±	14.38 ^{fgB} ±	18.24 ^{fA} ±
		1.50	0.83	0.84	1.07
	Hedelfinger	11.70 ^{cdB} ±	14.90 ^{fgB} ±	19.73 ^{bcA} ±	24.14 ^{bcA} ±
		0.66	1.11	4.80	2.01
	Katalin	12.74 ^{cd} ±	17.34 ^{cdC} ±	21.09 ^{cdB} ±	24.92 ^{bcA} ±
		1.04	1.10	2.54	1.43
	Linda	12.56 ^{cdB} ±	12.86 ^{ghB} ±	16.56 ^{defA} ±	18.26 ^{fA} ±
		1.91	1.43	2.22	0.95
New Star	8.83 ^{efgD} ±	12.3 ^{hiC5} ±	15.85 ^{fgB} ±	19.4 ^{efA2} ±	
	0.90	0.10	1.13	1.91	
Peter	7.74 ^{hD} ±	17.54 ^{bcdAB} ±	14.62 ^{fgB} ±	20.82 ^{efA} ±	
	1.96	1.01	2.34	1.34	
Sandor	12.61 ^{cC} ±	18.94 ^{bB} ±	16.31 ^{efgB} ±	23.76 ^{cdA} ±	
	1.00	1.62	1.29	1.53	
Solomary gomboly	23.17 ^{aB} ±	16.33 ^{deC} ±	20.94 ^{bcdB} ±	25.84 ^{bA} ±	
	1.56	0.10	0.62	2.11	
Summit	8.42 ^{fghB} ±	11.62 ^{iB} ±	14.11 ^{fgB} ±	22.30 ^{cdA} ±	
	1.53	0.48	4.37	2.34	
Valery Chkalov	16.57 ^{bB} ±	17.87 ^{bcB} ±	24.55 ^{abA} ±	25.27 ^{bcA} ±	
	1.11	1.62	3.52	0.36	
Sour cherry	Érdi Bötermő	22.39 ^{aC} ±	21.33 ^{aC} ±	28.07 ^{aB} ±	33.90 ^{aA} ±
		0.75	0.72	1.14	2.44
	Kántor-jánosi	9.64 ^{efgB} ±	11.67 ^{iB} ±	17.07 ^{defA} ±	18.87 ^{fA} ±
		0.70	0.55	1.73	0.54
Oblačinska	12.08 ^{cdD} ±	18.26 ^{bB} ±	20.38 ^{cdeB} ±	25.33 ^{bA} ±	
	0.33	0.74	1.32	1.90	
Wild cherry	10.40 ^{defC} ±	9.71 ^{iC} ±	14.16 ^{fgB} ±	19.00 ^{efA} ±	
	1.92	0.58	1.45	0.68	

Expressed as mg quercetin equivalents (QE)/g dry weight; Values are means ± SD; values preceded by the same lowercase letter in the column do not differ significantly according to the t-test ($p < 0.05$); Values preceded by the same capital letters in a row do not differ significantly according to Duncan's multiple range test ($p < 0.05$)

In addition, the total phenolic and total flavonoid content in cherry stalk extracts are presented in the heatmap (Figure 1). The variation in the content of these compounds is represented by a color gradient, ranging

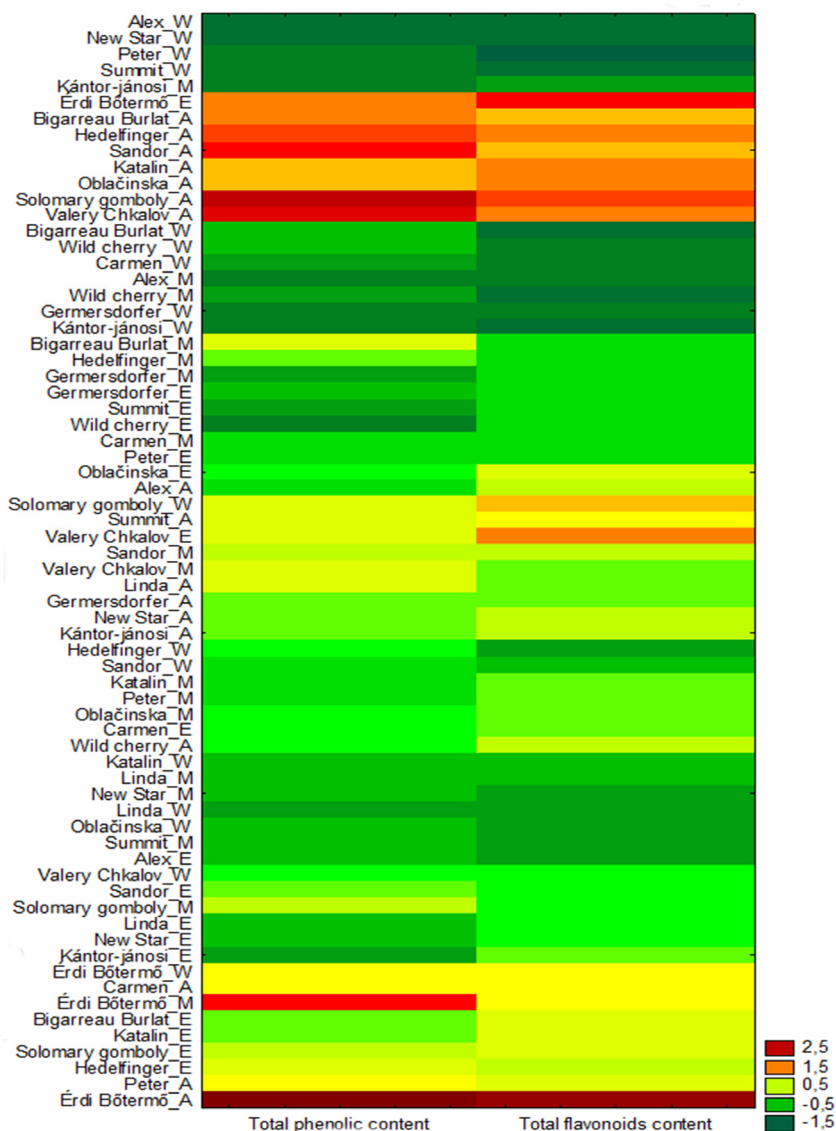


Figure 1. Heat map representation of the total phenolic and total flavonoid contents in different cultivars of cherry stalk extracts prepared using different extraction solutions (W-water, M-methanol, E-ethanol, A- acetone)

from dark green (indicating the lowest concentration) to dark red (indicating the highest concentration). The heatmap clearly confirmed the effect of the extraction solvent on the total phenolic and flavonoid contents. However, differences between varieties (sweet, sour, and wild) are also noticeable, as some cultivars consistently exhibit high phenolic content regardless of the solvent used, highlighting their abundant phenolic composition. Comparing cherry varieties (sweet, sour, and wild), sour cherry cultivars generally exhibited higher levels of total phenolics and flavonoids than sweet and wild cherry samples. Wild cherry showed relatively low phenolic and flavonoid content regardless of the solvent used. Additionally, differences are observed among cultivars within each cherry variety. The cultivars Érdi bőtermő, Valery Chkalov, Sandor and Solomary Gomboly exhibited a color range corresponding to high levels of total phenolics and flavonoids, especially in acetone extracts. On the other side, cultivars New Star and Kántor-jánosi, even in acetone, showed lower content, which may indicate varietal variability in phenolic composition.

In order to evaluate antioxidant activity, five antioxidant tests with different reaction principles were applied. The values of DPPH (2,2-diphenyl-1-picrylhydrazyl) assay were ranged from 3.68 to 25.10 mg Trolox/g DW in aqueous extracts, from 11.39 to 42.93 mg Trolox/g DW, from 7.19 to 27.45 mg Trolox/g DW in ethanolic extracts and from 14.04 to 52.02 mg Trolox/g DW in acetone extracts (Figure 2).

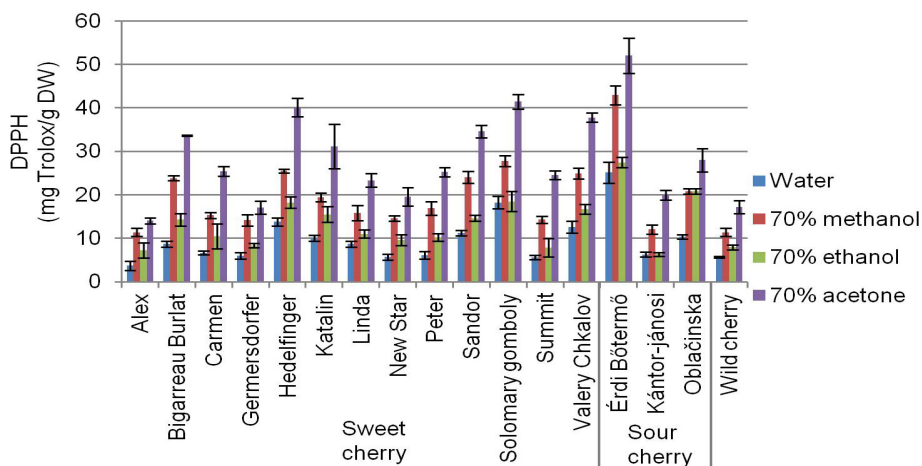


Figure 2. Antioxidant activity measured by DPPH assay

The results of FRAP (Ferric Reducing Antioxidant Power) assay are presented in Figure 3. In aqueous extracts FRAP values varied between 4.12

and 16.73 mg Trolox/g DW, in methanolic extracts between 7.93 and 31.44 mg Trolox/g DW, in ethanolic extracts between 4.13 and 18.07 mg Trolox/g DW and in acetone extracts between 14.92 and 46.62 mg Trolox/g DW.

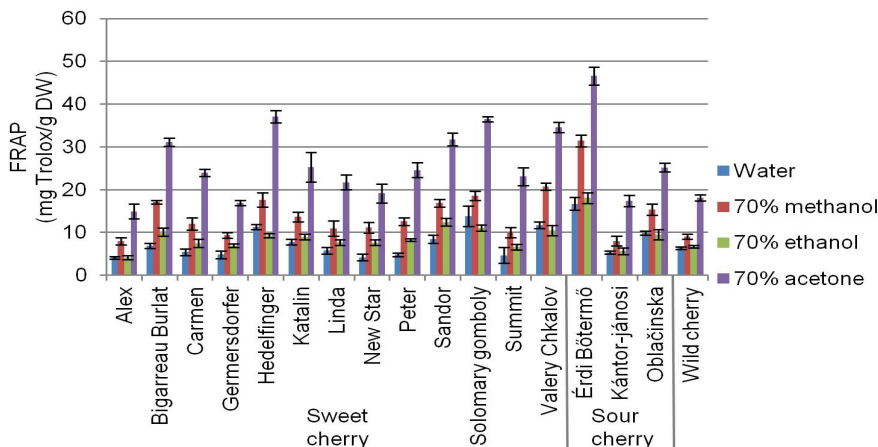


Figure 3. Antioxidant activity in cherry stalk extracts measured by FRAP assay

In aqueous extracts ABTS (2,2'-azino-bis(3-ethylbenzothiazoline-6-sulfonic acid)) values ranged from 12.73 to 68.34 mg Trolox/g DW, in methanolic extracts from 9.41 to 52.86 mg Trolox/g DW, in ethanolic extracts from 18.67 to 69.33 mg Trolox/g DW and in acetone extracts from 19.12 to 62.03 mg Trolox/g DW (Figure 4).

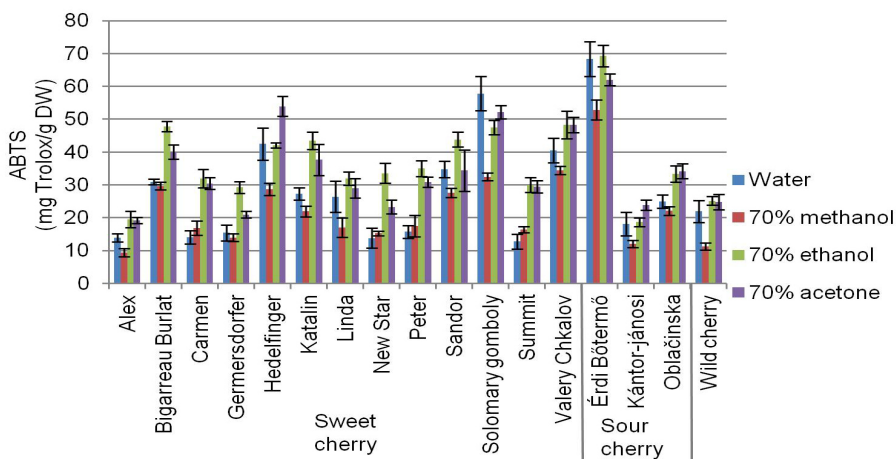


Figure 4. Antioxidant activity in cherry stalk extracts measured by ABTS assay

ANTIOXIDANT POTENTIAL OF CHERRY STALK EXTRACTS

The TAA (total antioxidant activity) in cherry stalks are shown in Figure 5. The value of TAA ranged from 7.33 to 26.84 mgAA/g DW in aqueous extracts, from 13.46 to 37.81 mgAA/g DW in methanolic extracts, from 13.57 to 32.15 mgAA/g DW in ethanolic extracts, from 16.22 to 38.67 mgAA/g DW.

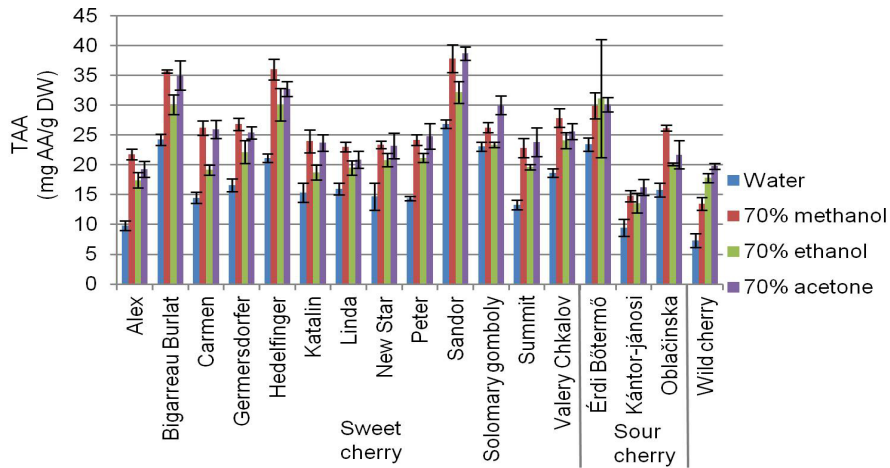


Figure 5. Total antioxidant activity (TAA) in cherry stalk extracts

The values of NBT (Nitroblue tetrazolium) assay were ranged from 0.65 to 1.42% in the aqueous extracts, from 0.84 to 2.17 % in methanolic extracts, from 1.58 to 2.74% in ethanolic extracts and from 1.41 to 2.60 % in acetone extracts (Figure 6).

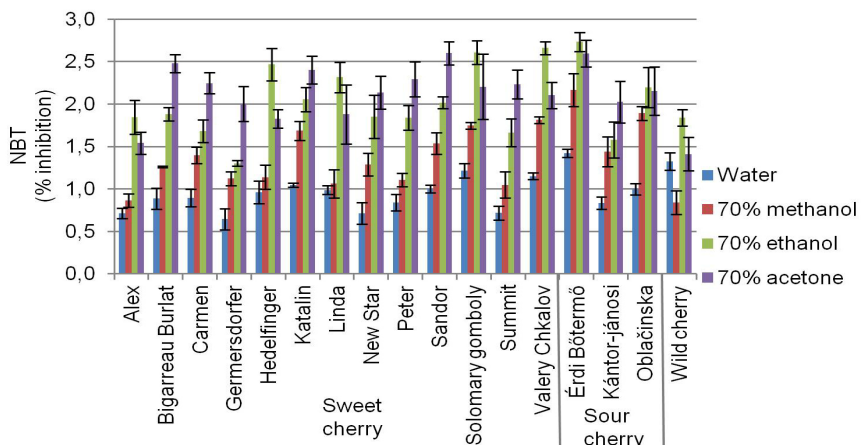


Figure 6. NBT test in cherry stalk extracts

Based on the obtained results of the antioxidant tests, the antioxidant activity is influenced by the extraction solvents. Beyond solvent effects, antioxidant activity also varied significantly among cherry types (sweet, sour, and wild) and also among cultivars within each type. Sour cherries consistently demonstrated stronger activity, likely due to their higher content of phenolic compounds. The variation in the results of antioxidant tests can be explained by the fact that the same antioxidant compounds can act differently when scavenging various types of radicals [21]. The extracts of all tested genotypes increased the capability of scavenging DPPH[•] radicals in the following order: water < methanol < ethanol < acetone, which is in line with the research of Cisowska et al. in mulberry extracts [22]. Cisowska et al. [22] reported the same results for ABTS as for DPPH, which is not in agreement with the current study. In accordance with our findings, Dailey and Vuong [20] observed differences in antioxidant activity measured by DPPH, ABTS, and the FRAP test, explaining this variation by the different chemical properties of phenolic compounds. The correlation analyses between total phenols, total flavonoids and antioxidant activity is presented in Table 3. The strong positive correlations were observed among total phenols, DPPH and FRAP tests ($r>0,9$; $p<0.05$). These results indicate that phenolic compounds are the primary antioxidants in cherry stalks extracts.

Table 3. The correlation between total phenolics, total flavonoids and antioxidant activity

	DPPH	FRAP	ABTS	TAA	NBT
Total phenolics	0.956	0.921	0.769	0.677	0.705
Total flavonoids	0.782	0.751	0.742	0.539	0.795

Correlation at $p<0.05$

CONCLUSIONS

Based on the results, it can be concluded that the cherry stalks extracts contain a significant amounts of total phenolics and total flavonoids, as well as exhibit high antioxidant activity. Statistical analysis confirmed that wild cherry samples had significantly lower total phenolic and flavonoid contents, as well as antioxidant activity, compared to cultivated sweet and sour cherry cultivars. Although sour cherry cultivars generally exhibited higher levels of total phenolics, flavonoids, and antioxidant activity than sweet and wild cherry samples, notable differences were also observed among cultivars within each cherry type. These findings emphasize that both cherry type and individual cultivar, along with the extraction solvent, significantly influence

the antioxidant potential of cherry stalk extracts. When comparing extracts prepared with the same solvent, the highest values of total phenolic and total flavonoids were found in sour cherry cultivar *Ěrdi Bőtermő*. In the aqueous extracts of the sour cherry stalks from the cultivar *Alex*, the lowest amount of total phenols and total flavonoids was determined. Among the tested solvents, acetone extracts consistently showed the highest concentrations of total phenolics and flavonoids across all cultivars. Antioxidant activity measured by FRAP and DPPH assays showed the highest values for acetone extracts, regardless of cultivar. In contrast, the results of the NBT, ABTS, and TAA assays showed variation depending on genotype and solvent extraction.

EXPERIMENTAL SECTION

Plant material and extracts preparation

Fruits and stalks of sweet and sour cherry from different cultivars were harvested at commercial maturity from the productive orchard "Sloga" in Kać in vicinity of Novi Sad, Serbia. Wild cherry fruits and stalks were collected in the vicinity of Fruška Gora, in the village Rivica. The stalks were subsequently air-dried at ambient temperature until they reached a constant weight.

After drying, the plant material was ground into a fine powder, and extracts of cherry stem from each tested cultivar were prepared using four different extraction solutions: distilled water, 70% aqueous methanol solution, 70% aqueous ethanol solution, and 70% aqueous acetone solution. The extraction was carried out by mixing 1 g of plant material with 50 mL of the respective solvent (1:50, m/v), based on the ratio used in our previous study [23]. Extraction was performed using sonication for 20 minutes in an ultrasonic bath at room temperature. Then, the extracts were rapidly vacuum-filtered through a sintered glass funnel and stored in cold conditions until further analysis.

Determination of total phenols and total flavonoids

The total phenolic content in all examined extracts of cherry stalk was determined spectrophotometrically with Folin-Ciocalteu reagent as described by Kroyer [24]. The extracts (50 μ L) were mixed with 2.5 mL of Folin-Ciocalteu reagent and incubated for 5 minutes. Then, 2 mL of saturated sodium carbonate solution was added, and the absorbance of the solutions were measured at 730 nm after 45 min. Gallic acid was used as standard and the results was expressed as mg gallic acid equivalents per gram of dry weight (mg GAE/g DW).

The total flavonoids content was determined following the method described by Saha et al [25]. The extracts (200 μ L) were mixed with 2% AlCl_3 solution (3ml), and the solutions were incubated for 15min at room temperature. After that, the absorbance was read at 430 nm. The results were expressed as quercetin equivalents in mg per gram of dry weight (mg QE/g DW).

Determination of antioxidant activity

Antioxidant activity in cherry stalk extracts was determined using DPPH (2,2-diphenyl-1-picrylhydrazyl), FRAP (ferric reducing antioxidant power), ABTS (2,2'-azinobis-(3-ethylbenzothiazoline-6-sulphonic acid), TAA (total antioxidant activity) and NBT (nitroblue tetrazolium) assays.

The DPPH test in cherry stalk extracts was assayed according to procedure reported by Lai and Lim [26] with slight modifications. DPPH reagent was dissolved in methanol until the absorbance of working solution approached ~ 0.7 . DPPH reagent solution (1.5 ml) was mixed with 20 μ l of extracts. After 30 min incubation, absorbance was read at 517nm.

The FRAP test was determined by the method reported by Valentão et al. [27] with modifications. FRAP reagent was prepared by mixing acetate buffer pH 3.6 (300 mmol/dm³) with a solution of 2,4,6-tris(2-pyridyl)-s-triazine (TPTZ; 10 mmol/dm³) in HCl (40 mmol/dm³) and $\text{FeCl}_3 \times 6\text{H}_2\text{O}$ in ration 10:1:1. In 1.5 ml FRAP reagent was added 20 μ l of extracts and the absorbance was read at 510 nm after 30 min.

The ABTS test was performed as described by Re et al. [28] with slight modifications. The ABTS reagent was prepared by mixing 7.4 mmol/dm³ ABTS solution (2,2'-azinobis-(3-ethylbenzothiazoline-6 sulfonic acid) with 2.6 mmol/dm³ potassium persulfate solution. The mixture was left in dark for 12 h. The stock solution was diluted until the absorbance of the working solution approached approximately 0.7. In 2 ml of reagent was added 25 μ l of extracts and the absorbance was read at 734 nm after 2 h.

The calibration curve was established using different concentrations of trolox and the results of DPPH, FRAP and ABTS tests were expressed as mg of trolox equivalents per gram of dry weight (mg TE/g DW).

TAA of cherry stalk extracts was assayed according to the phosphomolybdenum method described by Kalaskar and Surana [29] with minor modifications. To the mixture of 0.6 M sulfuric acid, 28 mM sodium phosphate, and 4 mM ammonium molybdate (1 ml), 25 μ l of extracts were added. After incubation in a boiling water bath at 95°C for 90 minutes, the absorbance was measured at 695 nm. Different concentrations of butylated hydroxytoluene were utilized to obtain the calibration curve, and results were expressed as mg of butylated hydroxytoluene equivalents per gram of dry weight (mg BHT/g DW).

The NBT assay was carried out according to the procedure described Mandal et al. [30] with slight modifications. The reaction mixture contained 50 mmol/dm³ phosphate buffer (pH 7.8), 13 mmol/dm³ L-methionine, 75 µmol/dm³ NBT, 0.1 mmol/dm³ EDTA, 2 µmol/dm³ riboflavin and 20 µl of the extract. It was kept under a fluorescent lamp for 10 min, and then the absorbance was read at 560 nm. The results were expressed as percent of inhibition of superoxide anion generated (% inhibition).

Statistical analysis

All results were expressed as the mean of the values obtained for three replications ± standard deviation (SD). Statistical significance was tested using software STATISTICA ver. 13 (StatSoft, Inc., USA). The effect of genotype and extraction solvent on the tested biochemical parameters in cherry stalks extracts was evaluated by two-way analysis of variance (Factorial ANOVA), followed by comparison of means by Duncan's multiple range test ($p < 0.05$). Correlation between the tested biochemical parameters was analyzed using the Pearson correlation coefficient.

ACKNOWLEDGMENTS

This research was supported by the Ministry of Education, Science and Technological Development of the Republic of Serbia, grant number: 451-03-136/2025-03/200117 and grant number: 451-03-137/2025-03/200117. Also, this manuscript presents one of the research topics carried out by the researchers gathered in the Center of excellence Agro-Ur-For at the Faculty of Agriculture in Novi Sad, funded by the Ministry of Science, Technological development and Innovations, contract number: 451-03-4551/2024-04/17.

REFERENCES

1. R. N. Raţu; I. D. Valeşcu; F. Stoica; A. Usturoi; V. N. Arsenoiaia; I. C. Crivei; A. N. Postolache; F. D. Lipşa; F. Filipov; A. M. Florea; M. A. Chiţea; I. S. Brumă; *Agriculture*, **2023**, 13, 1559
2. E. Messinese; O. Pitirolo; M. Grimaldi; D. Milanese; C. Sciancalepore; A. Cavazza; *Food Bioprocess Technol.*, **2024**, 17, 606-627
3. F. Dilucia; V. Lacivita; A. Conte; M. A. Del Nobile; *Foods*, **2020**, 9, 857
4. M. Babotă; O. Voştinaru; R. Păltinean; C. Mihali; M. I. Dias; L. Barros; I. C. F. R. Ferreira; A. Mocan; O. Crişan; C. Nicula; G. Crişan; *Front. Pharmacol.*, **2021**, 12, 647947

5. N. Hooman; F. Mojab; B. Nickavar; P. Pouryousefi-Karmani; *Pak. J. Pharm. Sci.*, **2009**, 22, 381-382
6. E. Bursal; E. Köksal; I. Gülçin; G. Bilsel; A. C. Gören; *Food Res. Int.*, **2013**, 51, 66-74
7. Z. Ademović; S. Hodžić; Z. Halilić Zahirović; D. Husejnagić; J. Džananović; B. Šarić-Kundalić; J. Suljagić; *Acta Period. Technol.*, **2017**, 48, 1-13
8. N. Nastić; J. Lozano-Sánchez; I. Borrás-Linares; J. Švarc-Gajić; A. Segura-Carretero; *Phytochem. Anal.*, **2020**, 31, 119-130
9. S. Afonso; I. V. Oliveira; A. S. Meyer; A. Aires; M. J. Saavedra; B. Gonçalves; *Antioxidants*, **2020**, 9, 1295
10. J. Švarc-Gajić; V. Cerdá; S. Clavijo; R. Suárez; P. Mašković; A. Cvetanović; C. Delerue-Matos; A. P. Carvalho; V. Novakov; *J. Chem. Technol. Biotechnol.*, **2018**, 1627-1635
11. J. Peixoto; G. Álvarez-Rivera; R. C. Alves; A. S. G. Costa; N. Andrade; A. Moreira; A. Cifuentes; F. Martel; M. B. P. P. Oliveria; E. Ibáñez; *Food Funct.*, **2020**, 11, 3471-3482
12. N. Balasundram; K. Sundram; S. Samman; *Food Chem.*, **2006**, 99(1), 191-203
13. J. Klepacka; E. Gujska; J. Michalak; *Plant Foods Hum. Nutr.*, **2011**, 66, 64-69
14. N. T. Bui; T. L. T. Pham; K. T. Nguyen; P. H. Le; K. H. Kim; *Res. Appl. Chem.*, **2021**, 12, 2678-2690
15. S. Afonso; I. V. Oliveira; A. S. Meyer; A. Aires; M. J. Saavedra; B. Gonçalves; *Antioxidants*, **2020**, 9(12), 1295
16. Z. Ademović; S. Hodžić; Z. Halilić-Zahirović; D. Husejnagić; J. Džananović; B. Šarić-Kundalić; J. Suljagić; *Acta Period. Technol.*, **2017**, 48, 1-13
17. D. Prvulović; Đ. Malenčić; M. Ljubojević; G. Barać; V. Ognjanov; *Lucrări Științifice USAMV - Iași Seria Agronomie*, **2016**, 59 (2), 403-408
18. J. Laoué; C. Fernandez; E. Ormeño; *Plants*, **2022**, 11(2), 172
19. A. R. Nunes; A. C. Gonçalves; G. Alves; A. Falcão; C. Garcia-Viguera; D. A. Moreno; L. R. Silva; *Foods (Basel, Switzerland)*, **2021**, 10(6), 1185
20. A. Dailey; Q. V. Vuong; *Cogent Food & Agriculture*, **2015**, 1(1)
21. T. Venkatesan; Y. W. Choi; Y. K. Kim; *Biomed Res. Int.*, **2019**; 3520675
22. J. K. Cisowska; O. Szczepaniak; D. S. Powalowska; J. Piechocka; P. Szulc; M. Dziędziński; *Cienc. rural*, **2020**, 50(1), 17.
23. D. Prvulović; M. Popović; Đ. Malenčić; M. Ljubojević; V. Ognjanov; *Res. J. Agric. Sci.*, **2012**, 43(2), 198-202
24. G. T. Kroyer; *Innov. Food Sci. Emerg. Technol.*, **2004**, 5, 101-105.
25. A. K. Saha; M. D. R. Rahman; M. Shahriar; S.K. Saha; N. Al Azad; D. Das; *J. Pharmacognosy Phytother*, **2013**, 2, 181-188
26. H. Y. Lai; Y. Y. Lim; *Int. J. Environ. Sci. Dev.*, **2011**, 2, 442- 447
27. P. Valentão; E. Fernandes; F. Carvalho; P. B. Andrade; R. M. Seabra; M. L. Bastos; *J. Agric. Food Chem.*, **2002**, 50, 4989-4993
28. R. Re; N. Pellegrini; A. Proteggente; A. Pannala; M. Yang; C. Rice-Evans; *Free Radic. Biol. Med.*, **1999**, 26, 1231-1237
29. M. G. Kalaskar; S. J. Surana; *J. Chil. Chem. Soc.*, **2014**, 59, 2299-2302
30. S. Mandal; A. Mitra; N. Mallick; *Physiol. Mol. Plant. P.*, **2008**, 72(1), 56-61

CHEMOMETRIC-ASSISTED SPECTROPHOTOMETRIC AND HPLC METHODS FOR THE SIMULTANEOUS ANALYSIS OF ATORVASTATIN CALCIUM AND EZETIMIBE

Aysun DİNÇEL^{a*}, Nilüfer Burcu ER^a, Feyyaz ONUR^a

ABSTRACT. This study aimed to develop new analytical strategies for the simultaneous determination of atorvastatin calcium (ATVC) and ezetimibe (EZE) in pharmaceutical formulations. The proposed methods included a chemometric approach using the partial least squares (PLS) technique with spectrophotometric data, first derivative zero-crossing, ratio spectra first derivative, and HPLC-DAD. PLS analysis was conducted using specialized software, with calibration performed in the 223–280 nm range at $\Delta\lambda = 4$ nm intervals. In the first derivative zero-crossing method, absorbance values at 245.2 nm for ATVC and 224.8 nm for EZE were used. The ratio spectra first derivative method quantified ATVC at 232.6 nm and EZE at 223.1 nm. HPLC-DAD analysis was carried out using an XBridge C18 column with a mobile phase of 20 mM NaH_2PO_4 :ACN (50:50 v/v), (240 nm, 1.0 mL/min). The linearity ranges were 1–20 $\mu\text{g/mL}$, 2–10 $\mu\text{g/mL}$, and 0.05–1.0 $\mu\text{g/mL}$, respectively. The methods were validated according to ICH guidelines, with no significant statistical differences observed (ANOVA, $p > 0.05$). Recovery from tablet formulations ranged from 95.43% to 102.28%. The PLS technique was highlighted as an environmentally friendly analytical approach. These validated methods demonstrated high sensitivity, accuracy, and reproducibility for routine pharmaceutical analysis.

Keywords: *Atorvastatin calcium, Ezetimibe, Chemometric, Spectrophotometry, HPLC, Validation, Green Chemistry*

^a Department of Analytical Chemistry, Faculty of Pharmacy, Lokman Hekim University, Ankara, Türkiye

* Corresponding author: aysun.dinzel@lokmanhekim.edu.tr



INTRODUCTION

Atorvastatin (ATV) is a reductase enzyme inhibitor. It is used for the prevention and treatment of cardiovascular disease in people at high risk. In pharmaceutical preparations ATV is usually used as the calcium salt atorvastatin calcium (ATVC). It is an enzyme inhibitor of 3-hydroxy-3 methyl glutaryl-coenzyme A (HMG-CoA) reductase. This enzyme catalyses the conversion of HMG-CoA. ATV has the chemical formula $C_{33}H_{35}FN_2O_5$ (Figure 1) and is called (3R,5R)-7-[2-(4-fluorophenyl)-3-phenyl-4-(phenylcarbamoyl)-5-propan-2-ylpyrrol-1-yl]-3,5-dihydroxyheptanoic acid [1-3].

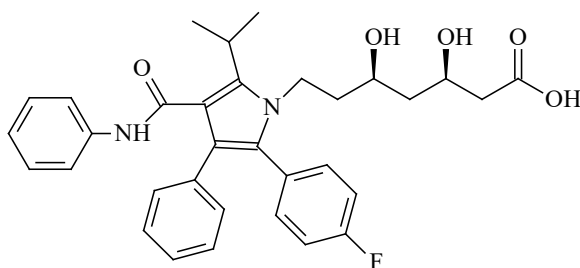


Figure 1. Chemical structure of ATV

Ezetimibe (EZE) is an active substance used to regulate high cholesterol levels in the blood. There are various generic preparations of different companies on the market. EZE has the chemical formula $C_{24}H_{12}F_2NO_3$ and is called 1-(4-fluorophenyl)-3R-[3(S)-(4-fluorophenyl)-3-hydroxy propyl]-4(S)(4 hydroxyphenyl) azetidion-2-one. (Figure 2) [4,5].

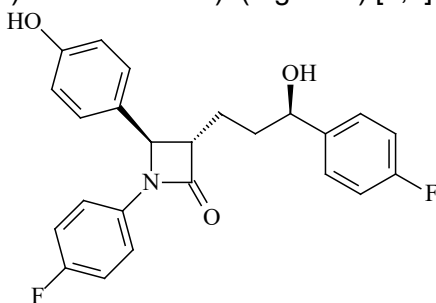


Figure 2. Chemical structure of EZE

Many studies have been conducted on the efficacy and safety of the combined use of ATV and EZE in patients with hyperlipidemia. Clinical studies have shown that the pharmacologic effect of the combined use of

EZE and ATV is more effective than the use of these two drugs alone [4,6]. Studies have also shown that the effect of ATV varies depending on the dose. For this reason, pharmaceutical preparations of ATV at various doses are available in the market [7].

One of the main reasons drugs have different responses in individuals is the genetic factors that affect drug pharmacokinetics. Therefore, drug analysis methods and applications are crucial in terms of drug dosage and the effectiveness of treatment response. ATVC and EZE mixtures have been extensively analyzed using various HPLC and other separation methods. Numerous studies in the literature focus on the determination of ATVC and EZE using UV and first derivative spectrophotometric methods for analyzing ATV and EZE either individually or in combination with other drugs [8-12]. Additionally, several chromatographic methods using HPLC-DAD/UV and LC-MS have been reported, which enable the simultaneous analysis of ATV/ATVC or EZE under different chromatographic conditions [13-18]. These methods not only allow the separation of the two drugs, ATVC and EZE, but in some cases, they achieve the separation of complex multi-component mixtures that include these two drugs. Only a limited number of studies are available for the determination of these two drugs using chemometrics [19]. However, no studies have been reported in the literature on using a chemometric approach with spectrophotometry for the simultaneous separation and quantification of both drugs.

The simplest method for determining the active ingredients in mixtures in pharmaceutical preparation is the chemometric approach. Because the concentration of each component can be calculated in just a few seconds without any separation techniques or other additional operational steps, using only a small number of solutions with varying active substance concentrations. Chemometric methods include mathematical operations that allow the analysis of substances without the use of any chemical reagents other than solvent that used for dissolving the active substance. For this reason, it can allow analysis without the need for solvents or chemicals discharged into the environment. While there are other techniques available for analytical purposes, partial least-squares (PLS) and principal component regression (PCR) are the most widely used methods [20] in chemometric analysis. Comparing two methods to other multicomponent analytes reveals certain advantages. The precise concentration of the preparation's active components can be ascertained by building matrices using variables like absorbance values and concentrations.

An extremely helpful analytical technique for qualitative and quantitative analysis from spectra made up of unresolved bands is derivative spectrophotometry. The zero-crossing approach involves measuring the

peak-to-peak distance from the x-axis, parallel to the ordinate. In this method, the absorbance of one drug is measured at the wavelength where the absorbance of the other drug crosses zero, allowing for the identification of a wavelength that provides a linear response with respect to concentration.

In the ratio spectra first derivative method, each spectrum is divided by the stored standard spectrum of either ATVC or EZE, and then the first derivative of the resulting ratio spectra is calculated. The ratio spectra of the solutions at various concentrations were generated using different mixtures of solutions that contain ATVC and EZE. The first derivative of these spectra is then identified. Chosen wavelength gives the linear relationship against the analyte concentration. Analyte concentrations that are unknown can be determined by analyzing the analytical responses at different intervals within the chosen wavelength range.

In this study, it was aimed to develop new four method for the analysis of ATVC, a cholesterol and triglyceride lowering agent, and EZE, another cholesterol and triglyceride lowering active substance, by a chemometric technique (PLS), first derivative zero-crossing, ratio spectra first derivative spectrophotometry, and HPLC methods and to apply the developed methods to the analysis of ATVC and EZE in Pharmaceutical formulations as tablets. Furthermore, to the best of our knowledge, no study in the literature has developed and compared four different analytical methods for the simultaneous determination of both drugs. Additionally, a comparative evaluation of these four techniques based on green analytical chemistry principles has not yet been conducted.

RESULTS AND DISCUSSION

For validation studies, specificity, limits of detection (LOD) and quantification (LOQ), selectivity, linearity, accuracy, sensitivity, intra-day and inter-day precision were investigated for developed methods. The developed methods were put to the test using the validation parameters for the purpose to demonstrate their validity. The accuracy of the procedure was evaluated by comparing the measured values with the actual values, while precision was assessed by analyzing three different concentration levels in six replicates each.

The first derivative zero-crossing method was found to be linear in the range 1 - 20 $\mu\text{g/mL}$ for ATVC and EZE. With this method, quantification was performed at wavelength values of 245.2 nm for ATVC and 224.8 nm for EZE (Figure 3).

CHEMOMETRIC-ASSISTED SPECTROPHOTOMETRIC AND HPLC METHODS FOR THE SIMULTANEOUS ANALYSIS OF ATORVASTATIN CALCIUM AND EZETIMIBE

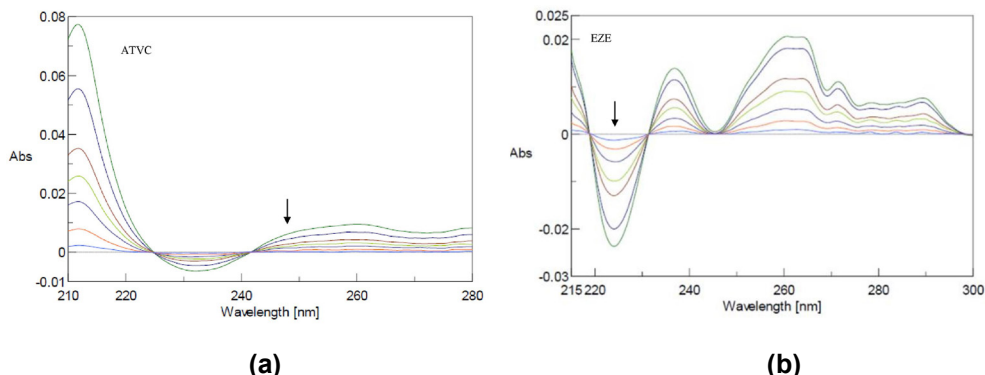


Figure 3. First derivative zero-crossing spectrums for (a) ATVC and (b) EZE in ethanol:water (1:1 v/v).

The ratio spectra first derivative method was found to be linear in the range 2 - 15 $\mu\text{g/mL}$ for ATVC and EZE. In this method, for the quantification of ATVC in mixed solutions, the concentration of ATVC was gradually increased while the concentration of EZE was kept constant at 2 $\mu\text{g/mL}$. Each spectrum was then divided by a fixed ATVC concentration (5 $\mu\text{g/mL}$), and the first-order derivative of the resulting absorbance spectra was calculated and used for quantification through spectral analysis. ATVC quantification was performed at a wavelength of 232.6 nm. Similarly, for EZE quantification, ATVC (2 $\mu\text{g/mL}$) concentration was kept constant and EZE concentration was increased and divided by a constant EZE (5 $\mu\text{g/mL}$) concentration value and the first order derivative of the absorbance spectra were obtained and quantified by using these spectra. EZE quantification was performed at a wavelength of 223.1 nm (Figure 4).

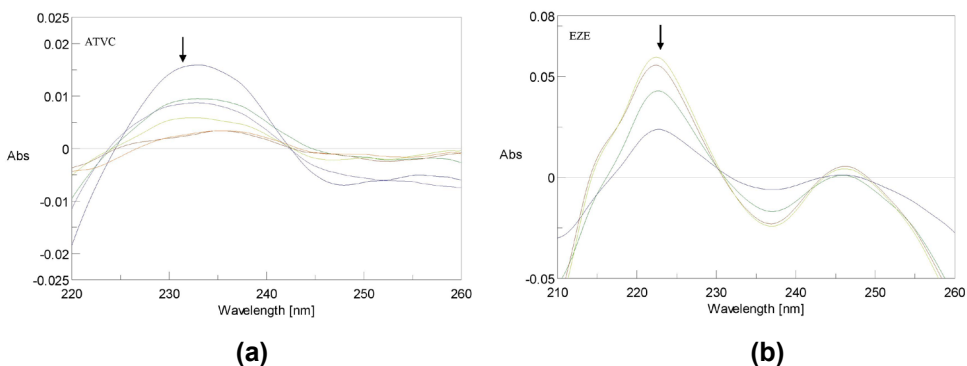


Figure 4. Ratio spectra first derivative absorption spectrums obtained increasing concentrations (a) ATVC and (b) EZE in ethanol:water (1:1 v/v).

In the PLS method, the absorbance values of the calibration data set and the unknown samples were taken in the wavelength range 220-270 nm at the spectral conditions determined and the concentration of the unknown solution was calculated using the vectorial measurements of the absorbance values in the wavelength range 223-280 nm in the chemometric calibrations (Table 6).

In the developed HPLC-DAD method, method was found linear in the range 0.1-1.2 $\mu\text{g/mL}$ for ATVC and EZE. The system suitability test for the standard solution containing 1 $\mu\text{g/mL}$ ATVC, EZE and Q; internal standard (IS) was evaluated, and parameters were accepted in terms of retention times, capacity factor (k'), tailing factor and theoretical number of plates (N) (Table 1). The tailing factor was found to be <2 , capacity factor values in the range $1 < k' < 10$ and $N > 2000$.

Table 1. System suitability parameters

	Retention Time* (Min)	Capacity Factor (k')	Tailing Factor	Theoretical Number of Plates
IS	3.64 \pm 0.01	2.65	1.93 \pm 0.02	10438.08
ATVC	6.13 \pm 0.01	5.11	1.17 \pm 0.01	8620.80
EZE	8.80 \pm 0.01	7.82	1.17 \pm 0.01	11938.96

*n=6, mean \pm standard deviation

The LOD and LOQ values for ATVC and EZE were found as 0.05 $\mu\text{g/mL}$ and 0.15 $\mu\text{g/mL}$, respectively for first derivative spectra zero-crossing, ratio spectra first derivative spectrophotometric methods and PLS technique. For HPLC-DAD method LOD and LOQ values for ATVC and EZE were found as 0.01 $\mu\text{g/mL}$ and 0.03 $\mu\text{g/mL}$, respectively. The calibration curve parameters generated from the data obtained from the methods are given in Table 2. The r^2 ; regression coefficient values from the curve equations were very close to 1.

Table 2. Calibration curve parameters (n=6)

Parameters	First derivative zero-crossing		Ratio spectra first derivative		HPLC	
	ATVC	EZE	ATVC	EZE	ATVC	EZE
λ (nm)	245.2	224.8	232.6	213.8	240.0	240.0
Linear range ($\mu\text{g/mL}$)	1.0-20.0	1.0-20.0	2.0-10.0	2.0-10.0	0.05-1.0	0.05-1.0
($y=mx+n$) Slope (m) \pm SE ^a	0.0002 \pm 0.00	0.0012 \pm 0.00	-0.0008 \pm 0.00	-0.0034 \pm 0.00	0.831 \pm 0.00	0.925 \pm 0.00
($y=mx+n$) intercept (n) \pm SE ^a	0.0001 \pm 0.00	0.0005 \pm 0.00	0.0104 \pm 0.00	0.0027 \pm 0.00	-0.0137 \pm 0.00	0.0014 \pm 0.00
r^2	0.9991	0.9961	0.9987	0.9969	0.9985	0.9996

SE^a: Standard error

Precision studies were performed for each method according to the linear range. Intra-day and inter-day (n=6) evaluation results are given in Table 3. Figure 5 shows the representative chromatogram obtained for the standard solution containing 1 µg/mL ATVC, EZE and Q (IS) under the selected analysis conditions. The retention times (mean ± standard deviation, n=6) for Q, ATVC and EZE were found to be 3.644 ± 0.005, 6.128 ± 0.008 and 8.796 ± 0.013 min. respectively.

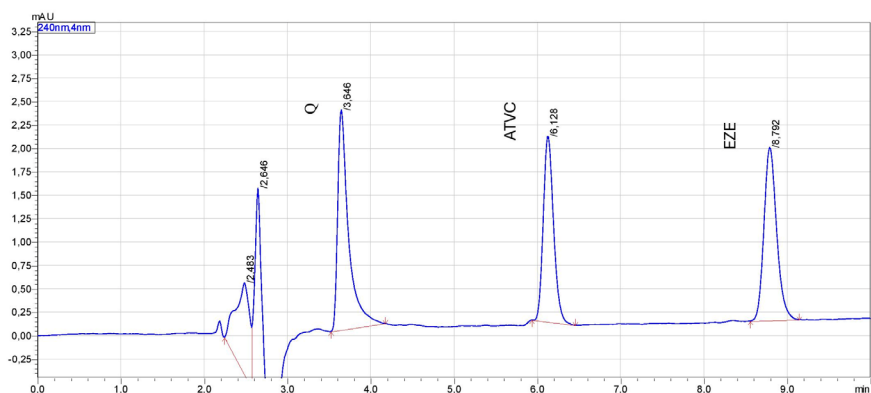


Figure 5. Chromatogram of standard containing 1.0 µg/mL ATVC, EZE, and Q (IS)

Table 3. Precision and accuracy results for inter-day and intra-day (n=6)

Added (µg/mL)	Inter-day			Intra-day		
	Found ^a \bar{x} (µg/mL)	Precision ^b RSD (%)	Accuracy ^c Bias (%)	Found ^a \bar{x} (µg/mL)	Precision ^b RSD (%)	Accuracy ^c Bias (%)
First derivative zero-crossing (EZE)						
2.5	2.48 ± 0.03	1.19	-0.58	2.49 ± 0.04	1.43	-0.41
7.5	7.52 ± 0.06	0.76	0.29	7.60 ± 0.04	0.55	1.38
10.0	9.99 ± 0.82	1.12	-0.09	9.95 ± 0.01	0.13	-0.44
First derivative zero-crossing (ATVC)						
2.5	2.54 ± 0.01	0.28	1.97	2.54 ± 0.03	1.10	1.59
7.5	7.44 ± 0.01	0.18	-0.74	7.45 ± 0.07	0.88	-0.67
10.0	10.00 ± 0.01	0.07	0.07	10.16 ± 0.09	0.90	1.61
Ratio spectra first derivative (EZE)						
2.0	1.99 ± 0.02	1.07	-0.11	1.99 ± 0.01	0.36	-0.49
5.0	5.08 ± 0.01	0.07	1.68	5.06 ± 0.02	0.38	1.23
10.0	9.99 ± 0.13	1.34	-0.02	10.02 ± 0.04	0.43	0.29
Ratio spectra first derivative (ATVC)						
2.0	1.99 ± 0.05	2.31	-0.08	1.99 ± 0.05	2.31	-0.08
5.0	5.07 ± 0.12	2.32	1.43	5.03 ± 0.04	0.82	0.63
10.0	9.97 ± 0.09	0.90	-0.29	10.01 ± 0.08	0.76	0.17

Added (µg/mL)	Inter-day			Intra-day		
	Found ^a \bar{x} (µg/mL)	Precision ^b RSD (%)	Accuracy ^c Bias (%)	Found ^a \bar{x} (µg/mL)	Precision ^b RSD (%)	Accuracy ^c Bias (%)
HPLC (EZE)						
0.1	0.101±0.02	1.22	-0.12	0.097±0.06	0.75	-1.50
0.4	0.405±0.06	1.10	1.14	4.201±0.02	0.88	1.08
0.8	0.799±0.07	0.84	-0.06	0.816±0.03	1.03	2.00
HPLC (ATVC)						
0.1	0.097±0.01	0.71	-1.27	0.10 ± 0.01	0.76	0.92
0.4	0.383±0.04	0.46	-2.17	0.388±0.03	0.94	-1.09
0.8	0.807±0.09	0.73	0.89	0.796±0.03	0.95	-0.54
PLS (EZE)						
2.5	2.53 ± 0.01	1.19	1.02	2.55 ± 0.00	0.05	1.60
7.5	7.58 ± 0.01	0.16	1.00	7.60 ± 0.01	0.17	1.32
10.0	10.15±0.02	0.37	0.51	10.06±0.01	1.46	0.58
PLS (ATVC)						
2.5	2.54 ± 0.00	0.19	1.71	2.54± 0.01	0.68	1.65
7.5	7.58 ± 0.00	0.09	1.08	7.60 ± 0.00	0.06	1.25
10.0	10.09±0.04	1.00	0.98	10.10±0.03	0.60	1.01

^a \bar{x} : Mean value, ^bRSD: Relative Standard Deviation,

^cBias: ((amount found - amount added)/amount found) x100

The developed methods were applied to the analysis of ATVC and EZE in pharmaceutical preparation. For this purpose, three different tablet formulations, Ezetec Plus 10/10, 10/20 and 10/40, were analyzed. The recovery values of ATVC and EZE were found to be in the range of 95.43% to 102.28% (mean) (Table 4). It was determined that the excipients did not interfere with the methods developed. In all recovery studies conducted using the PLS technique, the calculated standard error of prediction (SEP) values were found to be <0.8.

Table 4. Recovery values (%) obtained for Ezetec Plus 10/10, Ezetec Plus 10/20 and Ezetec Plus 10/40 preparations (mean values for n=6)

	First derivative zero-crossing		Ratio spectra first derivative		PLS		HPLC	
	EZE	ATVC	EZE	ATVC	EZE	ATVC	EZE	ATVC
10/10	98.9	100.2	102.0	98.5	101.7	101.6	99.0	99.6
10/20	100.1	99.8	99.1	101.9	98.8	101.7	99.7	100.8
10/40	98.1	101.8	95.4	100.4	99.7	99.2	99.1	102.3

A representative chromatogram obtained after the injection of Ezetec Plus 10/10 into the HPLC-DAD system is shown in Fig. 6. The ATVC, EZE, and IS peaks were well resolved, with no interfering peaks from the tablet observed, ensuring good separation.

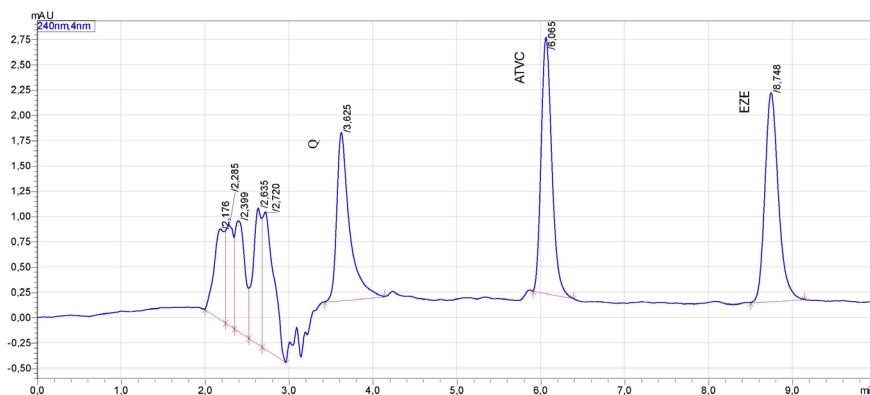


Figure 6. Chromatogram obtained for Ezetec Plus 10/10 tablet and spiked Q (IS)

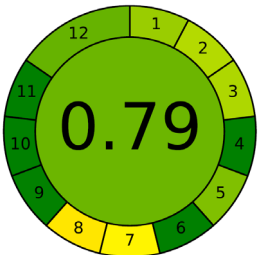
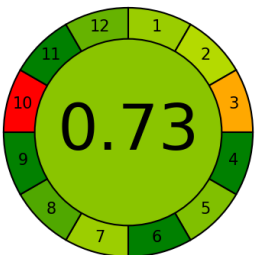
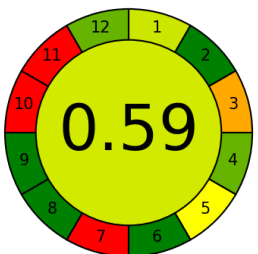
ANOVA was used to test whether there was a statistical difference between the developed methods and the results obtained after tablet analysis and no significant difference was observed ($p > 0.05$).

The first derivative zero-crossing and ratio spectra first derivative spectrophotometric methods, commonly used as spectrophotometric analysis methods, is a practical and preferred analysis method that allows the separation of substances in a mixture without chemical pretreatment and separation procedure.

The selection of the appropriate wavelength for the derivative spectra of the active substances being spectrum scanned, especially for the analysis of substances in mixtures, is of great importance in quantitative calculations. As a chemometric approach, the PLS technique is more practical and environmentally friendly than many analytical methods in that it does not require excessive time for sample preparation, does not require complex liquid-liquid extraction processes, and does not require pre-treatment or any consuming process. There are various spectrophotometric methods for the analysis of ATVC and EZE in the literature. However, no studies have been conducted on the simultaneous analysis of ATVC and EZE in their binary mixtures using chemometric techniques with spectrophotometric data. Therefore, after the developed spectrophotometric methods, a quantification study was carried out with PLS, as a chemometric multicomponent technique. According to the Green Analytical Procedure Index (GAPI), the PLS technique

was evaluated based on the 12 criteria [26-28]. These criteria were listed in Table 5. By using these parameters, the Analytical Greenness Calculator (AGREE) metric and score were calculated. According to the metric results, the PLS technique (0.79 score) qualifies as a green chemistry technique, with all criteria classified as green. When other methods are evaluated using the AGREE metric, the chemometric-spectrophotometric approach emerges as the most environmentally friendly option (Table 5).

Table 5. AGREE Scores for methods

Score of AGREE Metric	Method Criteria
<p style="text-align: center;">For PLS method</p> 	<ol style="list-style-type: none"> 1. Sample treatment 2. Sample amount 3. Device positioning 4. Sample pretreatment stages 5. Automation, miniaturization 6. Derivatization 7. Waste 8. Analysis throughput 9. Energy consumption 10. Source of reagent 11. Toxicity 12. Operator's safety
<p style="text-align: center;">For Spectrophotometric methods</p> 	
<p style="text-align: center;">For HPLC method</p> 	

Compared to previous studies, the developed HPLC method achieved nearly the same AGREE metric score of approximately 0.6 in terms of the organic component used in the mobile phase. However, the score obtained through the chemometric approach demonstrates a higher value, classifying it as green analytical chemistry. Thus, green analytical chemistry emphasizes analytical practices that reduce or eliminate the use or generation of substrates, solvents, or by-products that pose risks to the ecosystem or human health. One approach to minimizing the environmental impact of analytical procedures is the development of alternative direct analysis techniques that do not rely on organic solvents or substrates.

Within the scope of the studies to establish a new HPLC-DAD method, a simple and selective chromatographic method was developed for the simultaneous analysis of ATVC and EZE. The results obtained from other methods were then statistically compared with each other and with our newly developed HPLC-DAD method. Validation studies of the developed methods were performed according to ICH requirements; selectivity, sensitivity, linearity, accuracy, precision, recovery and reproducibility parameters were examined, and statistical evaluations were made. When the obtained LOD and LOQ values and working ranges for the developed methods are compared with previous studies, it can be said that the proposed methods are more precise and sensitive. In previous studies, for instance, the LOQ value for EZE using spectrophotometric methods was reported as 2 µg/mL [11]. In another study employing FTIR, the LOQ values for EZE and ATVC were found to be 1.839 µg/mL and 0.942 µg/mL, respectively [12]. An HPLC-based study reported the LOQ value for EZE as 0.19 µg/mL [14]. In the analysis of ATVC from pharmaceutical preparations, the LOD and LOQ values of the developed method were reported as 0.013 and 0.13 µg/mL, respectively [15]. In a method developed for the determination of ATVC in plasma, the LOQ values for ATVC and EZE were found to be 1.294 µg/mL and 1.384 µg/mL, respectively [16]. In another HPLC-based ATVC analysis, the LOD and LOQ values were found to be 0.31 µg/mL and 0.95 µg/mL, respectively [17]. Similarly, another HPLC method for ATVC reported LOD and LOQ values of 1 µg/mL and 3 µg/mL, respectively [18]. In our current study, the developed HPLC method achieved LOD and LOQ values of 0.01 and 0.03 µg/mL for ATVC and EZE, respectively, while the spectrophotometric methods yielded 0.05 and 0.15 µg/mL, indicating a higher sensitivity compared to those in the literature.

CONCLUSION

In this study, new easy, simple, selective, and validated first derivative zero-crossing and ratio spectra first derivative spectrophotometric, chemometric approach (PLS technique with spectrophotometry) and HPLC-DAD methods were developed for the simultaneous analysis of atorvastatin calcium (ATVC) and ezetimibe (EZE) in their binary mixture. All developed methods evaluated using the AGREEMENT metric and PLS technique can be recognized as a green analytical technique in comparison to others. As a new method, it provides an innovative approach by being feasible, simple, and practical. First derivative zero-crossing, ratio spectra first derivative spectrophotometric, PLS (partial least squares regression), and HPLC-DAD methods were successfully applied for the analysis of ATVC and EZE in three commercially available tablets in Türkiye, yielding good recovery values. Additionally, in this study, four different methods were developed, and these methods were evaluated and compared in terms of active ingredient analysis from pharmaceutical preparations and their green analytical applications.

EXPERIMENTAL SECTION

Chemicals and reagents

Analytical standards of ATVC (USP standard) and EZE, (USP standard) kindly gifted from Neutec, Pharmaceutical Industries Inc, Quercetin (Q; internal standard, IS) was purchased from Merck, (Darmstadt, Germany). Acetonitrile (HPLC grade, CARLO ERBA, Italy), methanol (HPLC grade, CARLO ERBA, Italy), ethanol (analytical grade, CARLO ERBA, Italy), NaH₂PO₄, NaOH were purchased from Sigma-Aldrich (USA). ATVC, EZE and Q (IS) stock solutions were prepared with ethanol at 1 mg/mL and the solutions to be used in the analysis were prepared daily by diluting the stock solutions with ethanol:water (1:1, v/v) mixture to the desired concentrations.

Instrumentation and chromatographic conditions

For chemometric calculations, multivariate chemometric analysis was performed by using R.G. Brereton program. The current program was obtained directly from its developer R.G. Brereton and Multivariate analysis Add-in for Excel v1.3 software [21].

Spectrophotometric analyses were performed by spectrophotometer (Jasco, V-730, C246261798). Used chromatographic system consisted of a Shimadzu liquid chromatography (LC-2030C 3D Plus) that was equipped with

a pump, a controller connected to a computer using a software, an autosampler, 10 μL injection loop and Diode Array Detector (DAD). In the HPLC system, the DAD detector allows for simultaneous analysis of drugs at different wavelengths, enabling analytical measurements at multiple wavelengths at once. This feature offers numerous advantages in analytical applications, making the DAD detector highly beneficial. The system was controlled through a system controller a personal computer workstation with a data processing system (Shimadzu, Kyoto, Japan) installed on it. The separation was performed on a XBridge, C18 (250 x 4.6 mm, particle size 5 μm) analytical columns (Waters, Milford, MA, USA). The column temperature was set to 24 $^{\circ}\text{C}$. The mobile was phase composed of 20 mM NaH_2PO_4 (pH adjusted to 5.17 with NaOH):acetonitrile (50:50, v/v) at 1.0 mL/min. in isocratic mode and DAD detector wavelength was set to 240 nm. ATVC has a pKa value of 4.46 and the estimated pKa of ezetimibe is 9.7 [3,6]. Knowing the pKa of analytes allows for an effective selection of the mobile phase pH. The selection of mobile phase and pH has been adjusted to ensure optimal separation based on the pKa values of the analytes to be analyzed. 10 μL of sample solutions were injected into the HPLC. Quercetin was chosen as an internal standard (IS) because its peak was well separated from the peaks of the two drugs, with no interfering peaks observed. Type 1 water (Simplicity 185 Water System, Millipore Corp., Bedford, MA, USA) was used for all analytical applications. Before using of the mobile phase, it was filtered through a membrane filter with a pore diameter of 0.45 μm and kept in an ultrasonic bath for 15 min. After each analysis procedure analytical column was flushed with approximately 20 times of column volume of a mixture with HPLC grade water and methanol (50:50, v/v).

Analysis with PLS technique

For the chemometric approach, PLS technique was chosen, twenty different mixtures were prepared for calibration or regression matrix. These mixtures contain different amounts of ATVC and EZE (between 2 and 15 $\mu\text{g}/\text{mL}$ concentration range). Zero-order absorbance values were recorded between 223 and 280 nm in the 4 nm wavelengths intervals. Matrix (20 concentration x 20 wavelength) (Table 6) was used as training set for prediction of unknown concentration. A matrix was prepared by recording absorbance values for 20 different solutions. Using this matrix, the active ingredient concentration in an unknown solution, for which 20 different absorbance values were similarly entered, and then it was estimated. For the prediction step, the prediction ability of this technique can be expressed in terms of the standard error of prediction (SEP) [20] (Brereton, 2003). Equation (1) defines the SEP equation. Where n is the total number of samples and C_i^{added} is the concentration of drug added.

$$SEP = \sqrt{\frac{\sum_{i=1}^n (C_i^{added} - C_i^{found})^2}{n}} \quad (1)$$

Table 6. Training set used in PLS technique for ATVC and EZE

Mixture No	ATVC ($\mu\text{g/mL}$)	EZE ($\mu\text{g/mL}$)
1	2	2
2	2	5
3	2	8
4	2	10
5	5	2
6	5	5
7	5	8
8	5	10
9	8	2
10	8	5
11	8	8
12	10	2
13	10	5
14	10	8
15	13	2
16	13	5
17	13	8
18	15	2
19	15	5
20	15	8

First derivative zero-crossing method

For the First Derivative zero-crossing method, the spectra analysis of 10 $\mu\text{g/mL}$ containing standard solutions were recorded in the range of 200-600 nm. The first derivatives of the obtained spectrum graphs were taken and quantified by zero-crossing method in the range of 220-320 nm. Instrument parameters for the first derivative zero-crossing method: Response time: 0.015 s, scan rate: 1000 nm/min, spectral slit width: 1 nm, data spacing: 0.2 nm and $\Delta\lambda = 4$ nm.

Ratio spectra first derivative method

For the ratio spectra first derivative method, zero-order spectrums of the solutions that contain ATVC and EZE at various concentrations in ethanol:water (1:1, v/v) were recorded in the range of 200-600 nm. The

spectrums ratioed to the spectra of standard solutions of ATVC and EZE at various concentrations. The concentration of the solution of division spectra is very important and various concentrations of ATVC and EZE were tried as divisor for finding the optimum value. For this purpose, 5 µg/mL EZE solution was used as divisor for ATVC analysis and 5 µg/mL ATVC solution was used as divisor for EZE analysis. The first derivatives of these spectra were then recorded.

The results obtained by our new developed HPLC method were compared with the results obtained by chemometric technique and derivative spectrophotometric methods. In addition, ANOVA was used to compare the methods statistically with each other.

Method validation

The developed methods were validated according to International Conference on Harmonization (ICH) requirements (“Validation of Analytical Procedures:Text and Methodology Q2 (R1)”, 2014; “validation of analytical procedures Q2(R2)”, 2022). For validation, the data gathered from the HPLC method was used to determine the retention time, capacity factor, tailing factor, and theoretical number of plates for each active ingredient. Specificity, linearity, accuracy, limit of quantification (LOQ), limit of detection (LOD), and intra-day and inter-day precision parameters were investigated for spectrophotometric, chemometric, and HPLC techniques for validation studies [22-24].

The system suitability test of chromatographic method was performed with six repeated analyses of the standard solution (containing 1 µg/mL). Calibration curve was plotted against the ratio of the peak area under the analyte peak to the peak area under the IS peak against the concentration value of each drug. The r^2 values from the acquired curves were examined for the purpose of figuring out the linearity of the methods. Accuracy, sensitivity, selectivity, recovery values from tablets and precision studies were performed at three different concentration values (n=6). The limit of detection (LOD) was taken as the signal-to-noise (S/N) value equal to 3 and the limit of quantification (LOQ) value was taken as the signal-to-noise (S/N) value equal to 10 for repeated (n=6) different standard solution analyses [24,25].

ACKNOWLEDGMENTS

The authors wish to send their gratitude to the Richard G. Brereton and Neutec, Pharmaceutical Industries Inc (Sakarya, Türkiye). This study was supported by Lokman Hekim University BAP Project (TYL-2024-76).

REFERENCES

1. A. Endo; *Journal of Lipid Research* **1992**, 33(11), 1569-1582
2. A. Endo; *Proceedings of the Japan Academy Series B: Physical and Biological Sciences* **2010**, 86(5), 484–493
3. M.S. Vishal; L. Kumar; C.L. Meena; G. Kohli; V. Puri; R. Jain; A.K. Bansal; H.G. Brittain; Chapter 1-Atorvastatin Calcium, *Profiles of Drug Substances, Excipients and Related Methodology*, Academic Press, **2010**, Vol.35
4. C.M. Ballantyne; J. Hourii; A. Notarbartolo; L. Melani; L.J. Lipka; R. Suresh; S. Sun; A.P. LeBeaut; P.T. Sager; E.P. Veltri; and Ezetimibe Study Group; *Circulation* **2003**,107(19), 2409–2415
5. National Center for Biotechnology Information, 2024. PubChem Compound Summary for CID 150311, Ezetimibe.
<https://pubchem.ncbi.nlm.nih.gov/compound/Ezetimibe>
(accessed 30 January 2025)
6. O. Ben-Yehuda; N.K. Wenger; C. Constance; F. Zieve; M.E. Hanson; J.X. Lin, A.K. Shah, C. Jones-Burton; A.M. Tershakovec; *Journal of geriatric cardiology: JGC* **2011**, 8(1), 1–11
7. A. Tello; F. Marín; V. Roldán; A. García-Herola; S. Lorenzo; V.E. Climent; L. de Teresa; F. Sogorb; *Revista española de cardiología* **2005**, 58(8), 934–940
8. N.S. Abdelwahab; B.A. El-Zeiny; S.I. Tohamy; *Journal of pharmaceutical analysis* **2012**, 2(4), 279–284
9. R.G. Balda; B. Patel Vandana; M. Bapna; *International Journal of ChemTech Research* **2009**, 1 (2), 233-236
10. K.S. Brar; *Medical journal, Armed Forces India* **2004** 60(4), 388–389
11. P. Lakshmi; B. Sudha; D. Ramchandran; C. Rambabu; *Journal of Chemistry*, 7, 238140, 101–104
12. J.J.M. Nasr; N.H. Al-Shaalan; S.M. Shalan; *Spectrochimica acta. Part A, Molecular and biomolecular spectroscopy* **2020**, 237, 118332
13. A.L. Assassi; C-E. Roy; P. Perovitch; J. Auzerie; T. Hamon; K. Gaudin; *Journal of Chromatography A* **2015**, 1380, 104-111
14. M. Ashfaq; I. Ullahkhan; S.S. Qutab; S. Naeemrazzaq; *Journal of the Chilean Chemical Society* **2007**, 52(3), 1220-1223
15. S. Ertürk; E.S. Aktaş; L. Ersoy; S. Fiçicioğlu; *Journal of Pharmaceutical and Biomedical Analysis* **2003**, 33(5), 1017–1023
16. S.A. Kumar; M. Debnath; J.V. Rao; D.G. Sankar; *Advanced Pharmaceutical Bulletin* **2015**, 5(3), 385-91
17. K.S. Kokilambigai; K.S. Lakshmi; *Journal of Chromatography Open* **2022**, 2, 100052
18. B. Yilmaz; S. Kaban; *Journal of Advanced Pharmacy Research* **2018**, 2(2), 89-94
19. V.S. Janardhanan; R. Manavalan; K. Valliappan; *Arabian Journal of Chemistry* **2016**, 9(Supp.2), S1378-S1387

CHEMOMETRIC-ASSISTED SPECTROPHOTOMETRIC AND HPLC METHODS FOR
THE SIMULTANEOUS ANALYSIS OF ATORVASTATIN CALCIUM AND EZETIMIBE

20. R. G. Brereton; *Chemometrics: Data Analysis for the Laboratory and Chemical Plant*, John Wiley & Sons, New York, U.S.A., **2003**, pp 297–338
21. R. G. Brereton; *Chemometrics, Data Analysis for the Laboratory and Chemical Plant*, John Wiley & Sons, New York, U.S.A., **2002** (computer program)
22. ICH, **2014**. Harmonized Tripartite Guideline, Validation of analytical procedures: Text and Methodology Q2(R1), ICH Steering Committee, <https://database.ich.org/sites/default/files/Q2%28R1%29%20Guideline.pdf>. (accessed 30 January 2025)
23. ICH, **2022**. Harmonized Tripartite Guideline, on validation of analytical procedures Q2(R2), ICH Steering Committee, https://database.ich.org/sites/default/files/ICH_Q2-R2_Document_Step2_Guideline_2022_0324.pdf. (accessed 30 January 2025)
24. D.R. Jenke; *Journal of Liquid Chromatography & Related Technologies* **1996**, *19*(5), 737–757
25. D.R. Jenke; *Journal of Liquid Chromatography and Related Technologies* **1996**, *19* (12), 1873-1891
26. F. Pena-Pereira; W. Wojnowski, M. Tobiszewski; *Analytical Chemistry*, **2020**, *92*(14), 10076–10082
27. M. Sajid; J. Płotka-Wasyłka; *Talanta*, **2022**, *238*(Pt 2), 123046
28. J.A. Płotka-Wasyłka; *Talanta*, **2018**, *181*, 204–209

THE INFLUENCE OF SOME POWDERS ON THE ANTIMICROBIAL ACTIVITY OF PLA PACKAGING WITH OREGANO OIL ADDITIVES

Andreea Cătălina JOE^a, Ion ONUȚU^{a,*},
Dorin BOMBOȘ^{a,f}, Gabriel VASILIEVICI^b, Abeer BAIOUN^c,
Laura SILAGHI-DUMITRESCU^d, Ioan PETEAN^{d,e}

ABSTRACT. This study investigates the antimicrobial potential and physicochemical performance of PLA-based biocomposite films incorporated with bioglass, oregano essential oil, and diacetin as a green plasticizer. Designed for use in food packaging applications, the films aim to serve as biodegradable, active barriers against microbial contamination while ensuring environmental compatibility and material safety. Initial microbiological screening identified the PB2 formulation comprising 70% PLA, 25% diacetin, 3% bioglass, and 2% oregano oil as the most effective antimicrobial composition. PB2 achieved a 79% inhibition of bacterial growth after two days and maintained 65% suppression after 14 days, confirming its long-term antimicrobial efficacy. To gain a comprehensive understanding of PB2's behavior, extensive characterization was performed. FTIR spectroscopy confirmed the successful incorporation of functional groups from both PLA and active additives. TGA and DSC analyses revealed enhanced thermal stability and a delayed glass transition ($T_g > 83\text{ }^\circ\text{C}$), attributed to the stiffening effect of bioglass. SEM and AFM investigations demonstrated uniform nanoparticle dispersion and low

^a Department of Petroleum Refining Engineering and Environmental Protection, Petroleum-Gas University of Ploiesti, 39 Bucharest Blvd., 100680 Ploiesti, Romania

^b National Institute for Research Development for Chemistry and Petrochemistry-ICECHIM-București, 202 Spl. Independenței, 060021 Bucharest, Romania

^c Chemistry Department, Faculty of Science, University of Damascus, Damascus, Syria

^d Babes-Bolyai University, "Raluca Ripan" Institute for Research in Chemistry, 30 Fântânele Str., 400294 Cluj-Napoca, Romania

^e Faculty of Chemistry and Chemical Engineering, Babes-Bolyai University, 11 Arany János Str., 400028 Cluj-Napoca, Romania

^f S.C. Medacril S.R.L., 8 Carpați Street, 551022 Mediaș, Romania

* Corresponding author: ionutu@upg-ploiesti.ro



surface roughness ($R_a=30.1$ nm), ensuring good structural homogeneity. Mechanical testing showed reduced tensile strength but significantly increased elongation at break, indicating greater ductility due to matrix amorphization promoted by diacetin. Altogether, the results support the potential of PB2 as a multifunctional, antimicrobial biocomposite film suitable for food-grade and biomedical applications.

Keywords: *diacetin, oregano oil, bioglass, antimicrobial barrier, active food packaging*

INTRODUCTION

Driven by the increasing urgency of climate change, the European Union has implemented strategies aimed at reducing environmental pollution by encouraging recycling, minimizing the consumption of conventional plastic materials, and replacing them with biodegradable alternatives. These policies not only address sustainability concerns but also promote public health [1]. A major challenge lies in the insufficient infrastructure for the collection, sorting, and recycling of plastic waste. Moreover, accidental incineration of such materials continues to undermine the enforcement of EU Directive 2019/909 [2].

Within this context, the role of food packaging has gained increasing attention, particularly in light of microbial risks associated with surface contamination [3,4]. Ensuring food safety requires controlling microbial growth and mitigating environmentally driven pathogenic risks caused by pollution and improper waste management practices [5,6]. One promising approach involves the development of bioactive packaging that can act as a functional barrier against microbial colonization and proliferation [7-9].

Oregano essential oil has shown potent antifungal activity, effectively inhibiting the growth of hyphae, spores, filamentous fungi, and molds [10-12]. It is also important to consider how solvents affect membrane properties, especially in terms of selectivity and mechanical strength [13]. In this regard, polylactic acid (PLA) has emerged as a suitable biodegradable polymer offering both structural stability and environmental compatibility [14,15].

The shift from petrochemical plastics and toxic solvents traditionally used in membrane manufacturing toward sustainable, eco-friendly membrane technologies stems from the growing recognition of their reduced ecological footprint. Researchers have highlighted the need to adopt green solvents and biodegradable polymers, leading to a redefinition of membrane fabrication protocols aligned with environmental sustainability [16].

Most synthetic polymers used in food packaging are petroleum-based, raising significant ecological concerns and prompting global efforts to phase them out [17,18]. In contrast, biopolymer-based films such as those derived from PLA not only extend food shelf life but are also safe for direct food contact. Essential oils have emerged as natural alternatives to synthetic preservatives, offering both antimicrobial and antioxidant functionalities. Despite the European recycling rate of plastic standing at only 7%, global demand for plastic remains the third highest after steel and cement. Thus, the gradual shift toward biodegradable food packaging is accelerating. Notably, multilayered systems combining polar and nonpolar biodegradable polymers have demonstrated efficacy in limiting gas exchange between packaged food and the surrounding atmosphere [19].

The effectiveness of active packaging films is governed by multiple factors, including the type of structural biopolymer used, the nature and dosage of active compounds, the retention and release kinetics of these agents, storage conditions, and the specific microbial strains tested. Studies have shown that oregano essential oil can be successfully dispersed in biocomposite matrices such as carboxymethyl cellulose (CMC) and agar without inducing surface defects like pores or cracks [9]. This phenomenon has been attributed to the enhanced compatibility between the essential oil and the biopolymer network. Although PLA is inherently brittle, its functionality in this context was preserved. Diacetins were employed as green plasticizers to improve the flexibility and processability of PLA [8,20], while the antimicrobial efficacy of oregano oil vapors at low concentrations further justified their incorporation into packaging systems [21]. In animal feed applications, oregano oil has demonstrated antimicrobial action against *Escherichia coli* and *Salmonella*, further supporting its versatility as a functional additive [22,23].

Various *in vitro* assays have been developed to assess the antimicrobial performance of polymer matrices loaded with essential oils. The oil–matrix interaction may influence the diffusion of active agents into the surrounding environment, thus modulating antimicrobial efficiency. Commonly used methods include disc diffusion, agar well diffusion, and agar dilution techniques. Nanocomposite films incorporating essential oils such as clove, coriander, cumin, marjoram, cinnamon, and caraway have been shown to inhibit *E. coli*, *S. aureus*, and *L. monocytogenes* using agar diffusion protocols [9].

Over the past five decades, bioactive glass has emerged as a multifunctional material widely employed in medical fields, particularly for its antibacterial properties and applications in tissue engineering. When combined with natural polymers, it has proven effective in biological and biomedical contexts [24]. Studies indicate that gelatin–bioactive glass composites offer enhanced mechanical performance and biocompatibility. Reduced inflammatory

response has also been observed in glycerin bioglass systems. Moreover, lyophilized composites of chitosan and bioglass have shown potential in bone tissue engineering [1]. Bioactive glass continues to be regarded as a third-generation material for soft tissue regeneration although skin regeneration remains challenging due to the lack of a universally effective wound-healing formulation [24].

In this study, we aimed to develop a fully biodegradable packaging film composed of polylactic acid (PLA), an eco-friendly plasticizer (diacetins), and oregano essential oil. The antibacterial performance of the essential oil was evaluated under in situ release conditions, in the presence of various powders with distinct textures. Microbiological tests were conducted to assess the antimicrobial effectiveness of the developed formulations. Building upon this foundation, this manuscript presents a novel approach in the development of biodegradable active packaging films by integrating bioglass and oregano essential oil into a PLA matrix plasticized with diacetin. Unlike previous studies that focused solely on antimicrobial efficacy, this research offers a comprehensive characterization combining microbiological testing with advanced thermal, mechanical, and morphological analysis. The long-term antimicrobial stability and enhanced ductility of the PB2 formulation highlight its promising potential for both food-grade and biomedical applications, marking a significant advancement in the design of multifunctional biocomposite materials.

RESULTS AND DISCUSSION

Evolution of the inhibition zone on solid media

Following microbiological testing, the evaluation of microbial growth in the presence of PLA-based films with varying chemical compositions revealed that the PD3 formulation comprising 73.0% PLA, 25% diacetin, and 2.0% oregano essential oil exhibited the largest inhibition zones on both culture media types: MB (bacterial) and MA (algal) (Figure 1). These media were specifically designed to promote microbial proliferation, thus providing a robust environment for testing the films' antimicrobial efficacy.

The pronounced inhibition effect observed around PD3 samples suggests that the higher concentration of the active compound (oregano oil at 2.0%) successfully created a localized antimicrobial buffer zone, preventing the proliferation of *Bacillus subtilis* as well as the seeded *Chlorella* sp. culture on the Petri dishes.

THE INFLUENCE OF SOME POWDERS ON THE ANTIMICROBIAL ACTIVITY OF
PLA PACKAGING WITH OREGANO OIL ADDITIVES

This clear suppression of cellular development near the PD3 film confirms the superior antimicrobial performance of this specific formulation. The results support the hypothesis that increasing the concentration of natural active agents in biodegradable films can significantly enhance their protective role, making them promising candidates for active food packaging applications.

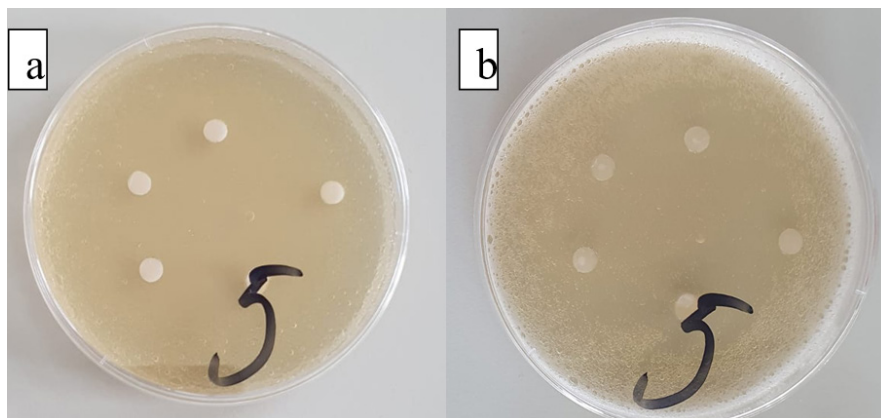


Figure 1. Presentation of the antimicrobial effect of sample PD3 in MB medium:
(a) appearance of the culture medium on the second day of monitoring;
(b) evolution of the antimicrobial effect of the PD3 film component
on the 14th day of monitoring

Based on these promising results, six additional active film formulations were developed. Each of these samples contained 25% diacetin and 2.0% oregano oil, and were supplemented with one of three functional additives activated carbon, Aerosil, or Bioglass at two concentrations (2% and 3%). The detailed compositions of these six samples are summarized in Table 1, highlighting their potential for enhanced antimicrobial performance through synergistic effects between the matrix and active fillers.

To evaluate the antimicrobial inhibition potential of PLA films containing different functional additives alongside the reference sample PD3 a nutrient-rich liquid medium was prepared using the following composition: 0.5 g yeast extract, 7 g casein, 3 g glucose, 0.25 g L-cysteine, 1.25 g sodium chloride, and 0.25 g sodium thioglycolate, with distilled water added to a final volume of 500 mL [25].

The components were dissolved in a water bath at 60 °C for 15 minutes to ensure complete homogenization. After cooling the medium to 35 °C, 50 mL of a *Bacillus subtilis* suspension (10^{-4} cells/mL) was added. The resulting biological mixture was stirred at 200 rpm for 30 minutes to ensure uniform distribution of bacterial cells.

The medium was then distributed into eight sterile test tubes labeled I through VIII. Each tube contained 10 mL of the inoculated medium and was supplemented with two circular PLA discs (7 mm in diameter) from one of the following samples: PD3, PC1, PC2, PS1, PS2, PB1 and PB2. The eighth tube served as the control (blank), containing only the medium and bacterial suspension without any film sample.

All test tubes were incubated at 35 °C for 14 days under sterile conditions. Bacterial growth was monitored throughout the incubation period to assess the inhibitory effect of each formulation and compare their relative antimicrobial efficiencies.

Optical density measurement (OD₅₀₀)

Cell growth within the biological suspension was assessed spectrophotometrically by measuring the optical density at a wavelength of 500 nm (OD₅₀₀). To monitor the dynamics of bacterial proliferation in the culture medium [26-29], daily measurements were performed over a 14-day incubation period.

For each measurement, a 1 mL aliquot was withdrawn from each test tube and analyzed using a UV-Vis spectrophotometer (model T85+, PG Instruments).

The optical density data revealed that the active compounds incorporated into the film samples functioned as effective bacterial growth inhibitors (Figure 2). Among all tested formulations, PB2 demonstrated the highest inhibitory performance: bacterial growth was suppressed by 79% relative to the blank after 2 days, and by 65% after 14 days. These findings highlight the long-term antimicrobial potential of Bioglass-based PLA films.

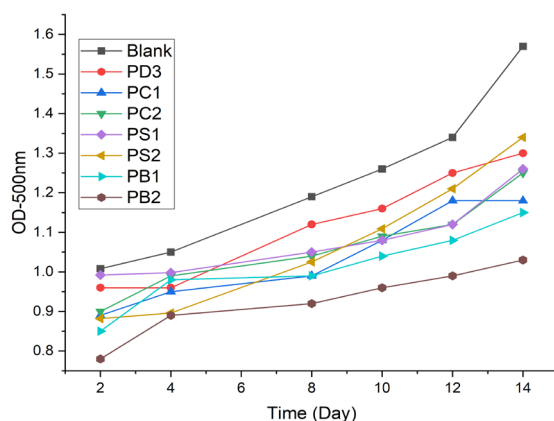


Figure 2. Optical Density Analysis of Samples PD3, PC1, PC2, PS1, PS2, PB1, and PB2 Over a 14-Day Period

Based on these promising results, the PB2 sample underwent comprehensive characterization using scanning electron microscopy (SEM), Fourier-transform infrared spectroscopy (FTIR), atomic force microscopy (AFM), thermal analysis (TGA and DSC), and tensile strength testing. These analyses aim to provide an integrated evaluation of the sample's microstructural, thermal, surface, and mechanical properties to support its suitability for biomedical and dermato-cosmetic applications.

FT-IR analysis

The FTIR spectrum of PB2 sample presented in the figure 3 confirms the characteristic absorption bands of PLA, indicating its presence in the composite material. A strong peak at 1753 cm^{-1} is attributed to the stretching vibrations of the C=O bond found in carboxylic or ester functional groups. This observation is reinforced by intense absorption bands in the $1100\text{-}1200\text{ cm}^{-1}$ range, which are characteristic of the stretching vibrations of the C-O bonds in carboxylic acids and esters. Additionally, specific to PLA, the presence of saturated linear structures, particularly the $-\text{CH}_3$ asymmetric and $-\text{CH}_3$ symmetric types, is indicated by a weak band at 2947 cm^{-1} . The bending frequencies for the $-\text{CH}_3$ asymmetric and $-\text{CH}_3$ symmetric groups have been identified at 1446 and 1369 cm^{-1} , respectively [30-32] The incorporation of diacetin notably enhances the absorption band observed at 1741 cm^{-1} . This enhancement can be attributed to the supplementary contributions from distinct carbonyl functional groups present within the molecular structure.

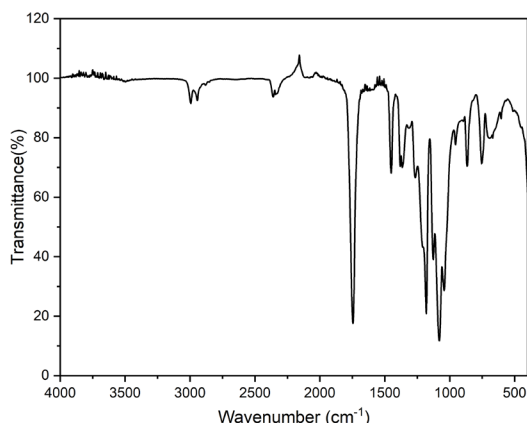


Figure 3. FTIR spectrum of sample PB2

The FTIR spectrum analysis, following the addition of oregano oil, reveals a peak at 858 cm^{-1} . This peak can be attributed to the C–H out-of-plane bending associated with the structure of β -caryophyllene, a natural compound belonging to the sesquiterpene class known for its antibacterial and anti-inflammatory properties [33-35].

Thermal properties

The thermogravimetric analysis (TGA) reveals a clear sequence of mass loss events, as shown in Figure 4, characteristic of the thermal behavior of the analyzed material. In the temperature range of 20–120 °C, the mass losses are negligible, indicating a low residual moisture content and good thermal stability in this lower region. A slight increase in mass loss is observed between 120–280 °C, which is attributed to the volatilization of low molecular weight organic compounds, such as oregano oil and the diacetin-type plasticizer. These compounds are not strongly bound within the polymeric matrix and are gradually eliminated through evaporation. The most significant mass loss, approximately 70%, occurs in the range of 280–350 °C and corresponds to the thermal degradation of polylactic acid (PLA). During this stage, chain scission and thermal decomposition of the base polymer take place, reflecting the thermal stability limits of the polymeric matrix under elevated temperature conditions.

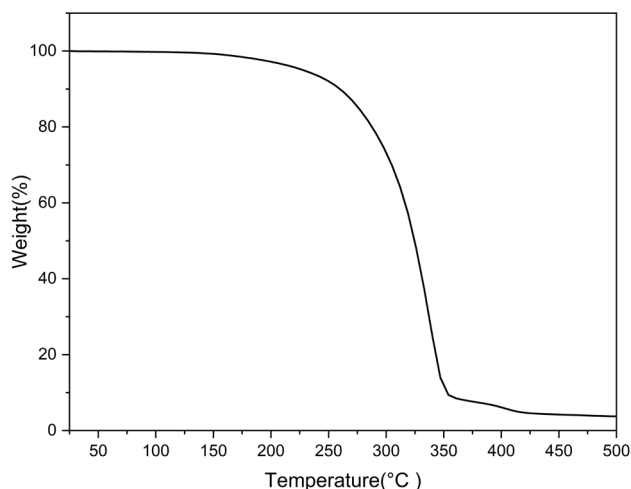


Figure 4. TGA curve of sample PB2

The effect of bioglass on the thermal transitions of PB2 sample composites is shown in the DSC thermogram (Figure 5). As can be seen, the addition of bioglass to PLA has a positive effect on the T_g temperature, increasing it to above 83 °C. This behavior is attributed to the hindered mobility of the PLA segment due to the addition of bioglass which stiffens the PLA and delays the glass transition. The sample showed two endothermic peaks at 175 and 317 °C, probably caused by the melting of the amorphous structures, the size of the peaks being proportional to their concentration.

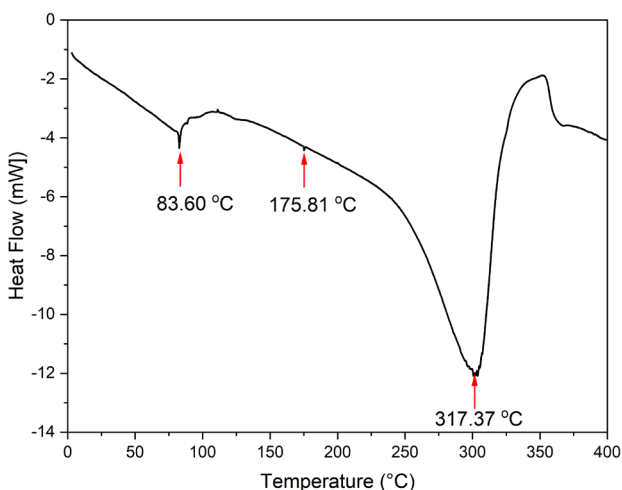


Figure 5. DSC thermogram of sample PB2

Surface analysis

Scanning electron microscopy (SEM) analysis of the bioglass-reinforced PLA-Oregano oil (2%) film (PB2), shown at different magnifications (10 μm , 50 μm , and 200 μm) in Figure 6, reveals important insights into the morphology and dispersion behavior of the composite system. The relatively uniform distribution of bioglass particles throughout the polymer matrix indicates an effective dispersion, which is likely facilitated by the chemical compatibility between the diacetin plasticizer and the bioglass surface. This compatibility attributed to their close polarity enhances interfacial interactions, thereby promoting the formation of a more homogeneous and cohesive polymeric structure. Despite the generally smooth surface morphology observed across all magnifications, the presence of localized micro-aggregates of bioglass is evident, especially at higher resolutions. These micro-clusters

may result from areas with a locally insufficient concentration of diacetin, which limits its plasticizing and dispersive effect. Such aggregates, although minor, suggest that further optimization of the bioglass-to-diacetin ratio could improve the uniformity of dispersion and the overall microstructural integrity of the composite film. Overall, the SEM micrographs support the conclusion that the incorporation of bioglass into the PLA matrix was successful and reasonably well-distributed, with minimal surface defects, making the material potentially suitable for packaging applications.

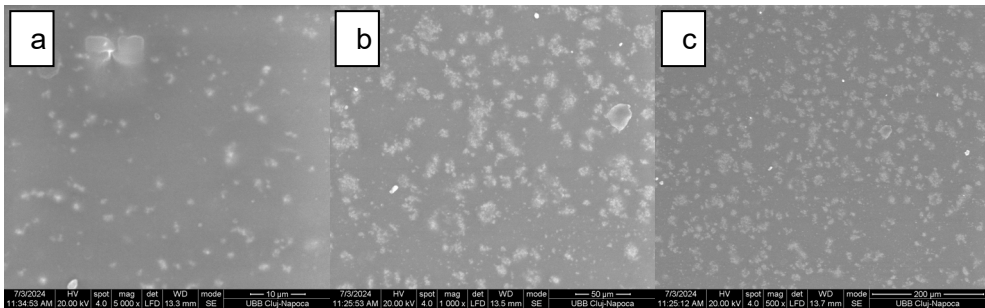


Figure 6. SEM micrographs of the PB2 sample reinforced with bioglass at different magnifications: (a) 10 μm , (b) 50 μm , and (c) 200 μm

Analysis of the PLA film surface by atomic force microscopy (AFM) provided a more detailed image of the microstructural units and topographic features, highlighting an advanced dispersion of bioglass nanoparticles as well as variations in the film thickness (Figure 7). The topographic image reveals uniformly distributed clusters of bioglass, suggesting good compatibility between the filler and the PLA matrix, This arrangement is caused by the composite flow during molding [36]. From the three-dimensional surface profile, a relatively homogeneous texture with similar topographic irregularities is observed. The calculated surface roughness parameters an average roughness (Ra) of 30.1 nm and a root mean square roughness (Rq) of 39.9 nm indicate a low to moderate roughness level, which may contribute positively to interfacial interactions in biomedical or dermato-cosmetic applications. These results confirm the successful incorporation of bioglass into the PLA matrix and support the morphological stability and uniformity of the composite surface.

THE INFLUENCE OF SOME POWDERS ON THE ANTIMICROBIAL ACTIVITY OF
PLA PACKAGING WITH OREGANO OIL ADDITIVES

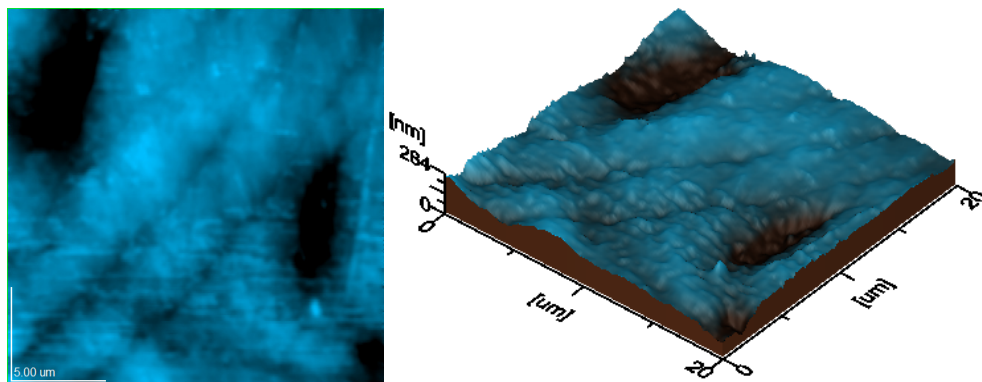


Figure 7. Topographic characteristics of the PB2 sample (a) topographic image; 3D image (scanned area 20 μm x 20 μm, Ra area 30.1 nm; Rq area 39.9 nm)

Tensile test results

The mechanical performance of the bioglass-reinforced PLA composite containing oregano oil, plasticized with diacetin (PB2), reveals a noticeable alteration in tensile behavior compared to neat PLA. As shown in Table 1, the sample exhibited a maximum tensile strength of 25.91 MPa, with a maximum load of 305.39 N, and an elongation at break of 61.08 mm, while the Young’s modulus was 2118.48 MPa. The stress at yield was recorded at 4.87 MPa.

Table 1. Mechanical parameters obtained from the tensile test of the PB2

Tensile strength (MPa)	Maximum load (N)	Elongation at break (mm)	Young’s modulus (MPa)	Stress at yield (MPa)	Tensile strength (MPa)
25.912	305.3945	61.079	4.871	2118.479	5.182

Figure 8 illustrates the stress–strain curve, highlighting the characteristic deformation profile of the material. A distinct yield point is followed by a plastic deformation region, indicating ductile behavior prior to final rupture. The decrease in tensile strength and modulus, when compared to pure PLA, reflects a reduction in rigidity and load-bearing capacity. This can be attributed to the action of the diacetin-type plasticizer, which disrupts the crystalline domains of PLA and promotes the formation of a more amorphous structure. In turn, this facilitates chain mobility and leads to a marked increase in elongation

at break, enhancing the flexibility of the material. Such modifications confirm the role of diacetin in softening the PLA matrix and enabling better energy dissipation under stress, albeit at the expense of reduced mechanical strength. These properties may be favorable for applications requiring enhanced ductility and toughness, such as packaging applications.

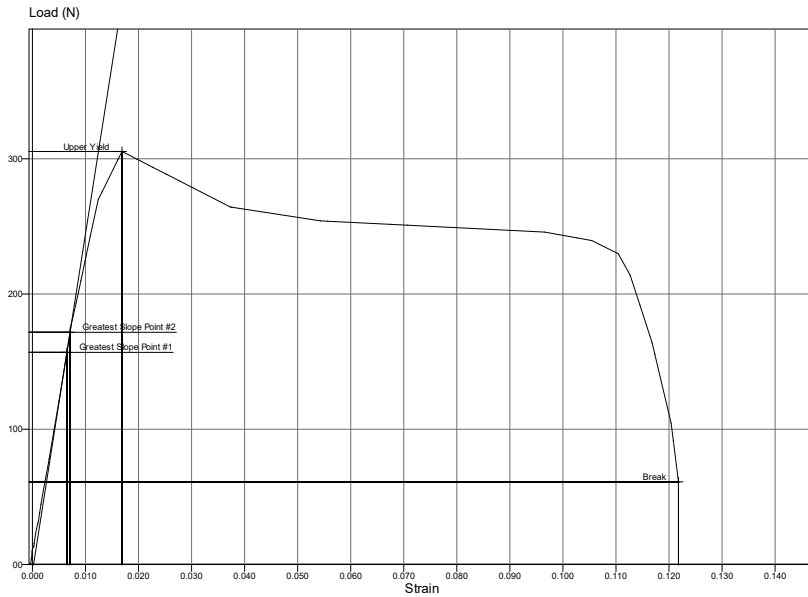


Figure 8. Stress–Strain Curve of PB2 sample

CONCLUSIONS

The research aimed to evaluate the influence of some powders, such as activated carbon, aerosilica and bioglass, on the bactericidal efficiency of PLA-based food packaging plasticized with diacetins and added with oregano oil. The effectiveness over time of bactericidal compounds such as oregano oil can be improved by controlled release from the powders present in the composition of the active food packaging. Thus, in the first part of the research, the oregano oil content of the PLA films was optimized to ensure their efficient bactericidal activity. The optimization of the type of powder and the powder content of the composite were evaluated through microbiological

studies. Following these studies, a bactericidal activity of oregano oil in the presence of bioglass at a concentration of 3% was highlighted. In the second part of the study, the thermal and mechanical characteristics of the PLA composite based on bioglass plasticized with diacetins and added with oregano oil were determined. Experimental data revealed the decrease in mechanical properties of PLA and the improvement of elongation after plasticization with diacetin of PLA composite. Also, the T_g temperature increased and surface examination indicated the presence of smooth samples with small micro-clusters of bioglass aggregates.

EXPERIMENTAL SECTION

Materials and Methods

Polylactic acid (PLA, Ingeo® brand, NatureWorks LLC, Tokyo, Japan), diacetin (used as a plasticizer, purchased from Sigma-Aldrich), and oregano essential oil (sourced from a local natural products supplier) were utilized for the preparation of biodegradable films. The components were dissolved in chloroform under constant stirring at 60 rpm and 50 °C for 30 minutes to ensure homogeneity. After complete solubilization, different powders activated carbon (Merck), Aerosil® 200 (Evonik Operations GmbH), or Bioglass® powder (NovaMin, Schott, USA) were incorporated into the polymer solution.

Preparation of food packaging films

The solubilization process of polylactic acid (PLA) was carried out at a controlled temperature of 50 °C for 1 hour, using a stirring speed of 1400 rpm. Once complete dissolution of the PLA was achieved, the remaining components of each formulation were sequentially added to the solution. The resulting homogeneous mixture was then cast into sterile Petri dishes for film formation via solvent evaporation.

Three active food packaging formulations based on PLA were prepared, as summarized in Table 2. From each of the three films designated PD1, PD2, and PD3 twenty identical circular samples (disc-shaped) were punched, each with a diameter of 7 mm. These test specimens were individually transferred into sterile, sealed vials to prevent external humidity and preserve their structural and microbial integrity prior to testing.

Table 2. Composition of PLA-based film formulations

Sample	PLA (% w/w)	Diacetin (% w/w)	Powder (type and % w/w)	Oregano oil (% w/w)
PD1	74.0	25	–	1.0
PD2	73.5	25	–	1.5
PD3	73.0	25	–	2.0
PC1	71.0	25	Activated carbon: 2.0	2.0
PC2	70.0	25	Activated carbon: 3.0	2.0
PS1	71.0	25	Aerosil 200: 2.0	2.0
PS2	70.0	25	Aerosil 200: 3.0	2.0
PB1	71.0	25	Bioglass: 2.0	2.0
PB2	70.0	25	Bioglass: 3.0	2.0

Biological Culture Preparation and Microbiological Setup

The biological materials used in this study included *Bacillus subtilis* bacterial cultures and *Chlorella* sp. algal cultures, both of which were supplied by the Microbiological Studies Laboratory at the Petroleum-Gas University of Ploiești, Romania [37]. All microbiological tests were conducted in accordance with the OECD Guidelines for the Testing of Chemicals issued by the Organisation for Economic Co-operation and Development (OECD), and in compliance with the standards outlined in USP 35-NF 30 (Pharmacopeial Convention): Microbiological Enumeration of Non-Sterile Products – Tests for Specified Microorganisms.

To support experimental determinations, several analytical instruments were employed. Monitoring of microbial viability during the test period was conducted using a CELESTRON digital microscope, model 4434. Gravimetric measurements were performed using an OHAUS analytical balance, model AX224M. Physicochemical parameters of the culture media such as pH, conductivity, and dissolved oxygen content were recorded using a WTW Inolab Multi 9630 IDS multiparameter meter. This advanced instrument features three galvanically isolated measurement channels, enabling simultaneous and accurate tracking of all relevant parameters critical for evaluating biological responses.

The biological materials used in this study included *Bacillus subtilis* bacterial cultures and *Chlorella* sp. algal cultures, both of which were supplied by the Microbiological Studies Laboratory at the Petroleum-Gas University of Ploiești, Romania [26]. All microbiological tests were conducted in accordance with the OECD Guidelines for the Testing of Chemicals issued by the Organisation for Economic Co-operation and Development (OECD), and in compliance with the standards outlined in USP 35-NF 30 (Pharmacopeial

Convention): Microbiological Enumeration of Non-Sterile Products – Tests for Specified Microorganisms.

To support experimental determinations, several analytical instruments were employed. Monitoring of microbial viability during the test period was conducted using a CELESTRON digital microscope, model 4434. Gravimetric measurements were performed using an OHAUS analytical balance, model AX224M. Physicochemical parameters of the culture media such as pH, conductivity, and dissolved oxygen content were recorded using a WTW Inolab Multi 9630 IDS multiparameter meter. This advanced instrument features three galvanically isolated measurement channels, enabling simultaneous and accurate tracking of all relevant parameters critical for evaluating biological responses.

To evaluate the antimicrobial and algal inhibitory activity of the PLA-based films, two specific growth media were prepared: one for bacterial cultivation and one for algal propagation.

The bacterial growth medium (MB) was composed of: bacto-peptone (10 g), sodium chloride (5 g), agar (20 g), meat extract (10 g), and distilled water up to 1000 mL. The pH was adjusted to 7.5.

The algal growth medium (MA) contained: agar (20 g), magnesium sulfate heptahydrate ($\text{MgSO}_4 \cdot 7\text{H}_2\text{O}$, 1.2 g), potassium nitrate (KNO_3 , 1.2 g), calcium chloride (CaCl_2 , 1.6 g), sodium phosphate monobasic dihydrate ($\text{NaH}_2\text{PO}_4 \cdot 2\text{H}_2\text{O}$, 1.2 g), ferrous sulfate heptahydrate ($\text{FeSO}_4 \cdot 7\text{H}_2\text{O}$, 0.08 g), sodium nitrate (NaNO_3 , 1.2 g), and ammonium chloride (NH_4Cl , 0.8 g), dissolved in distilled water to 1000 mL. The pH was adjusted to 6.5.

Both media types were sterilized in an autoclave at 121 °C for 15 minutes prior to inoculation and pouring.

Following sterilization, the media were poured into sterile Petri dishes in two parallel experimental series:

Series A – targeting bacterial growth promotion (*Bacillus subtilis*)

Series B – targeting algal growth promotion (*Chlorella* sp.)

Each experimental series was tested on three types of PLA-based films (PD1, PD2, and PD3), and each sample was evaluated in triplicate.

For Series A, nine Petri dishes were filled with 25 mL of MB medium cooled to approximately 40 °C and inoculated with 2 mL of *Bacillus subtilis* bacterial suspension at a concentration of 10^{-4} cells/mL. After solidification, the plates were labeled 1–9 (Figure 9).

Plates 1–3 received five circular film samples from PD1

Plates 4–6 received five discs from PD2

Plates 7–9 were loaded with PD3 samples

All dishes were sealed and incubated at 30 °C for 14 days to monitor bacterial growth or inhibition zones.

For Series B, the same protocol was applied, except that the MA medium (algal-specific) was used and the plates were inoculated with *Chlorella* sp. cultures at the same concentration (10^{-4} cells/mL). As with the bacterial series, nine Petri dishes were used to evaluate the three film types in triplicate (PD1, PD2, PD3). These plates were maintained at 24 °C under controlled light conditions using a 12-hour light/dark photoperiod to simulate natural algal growth conditions.

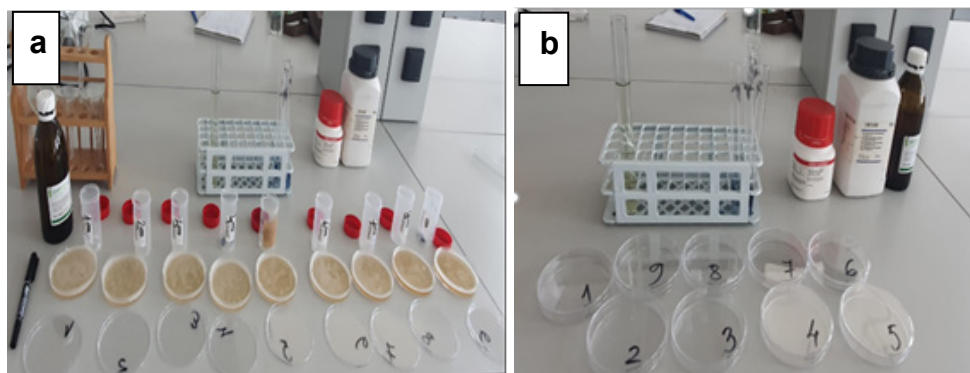


Figure 9. Workflow representation of the experimental stages for the evaluation of PD1, PD2, and PD3 films in the MB series: (a) Arrangement of perforated PLA film discs (7 mm diameter) into groups according to sample type (PD1, PD2, PD3); (b) Labeling of sterile Petri dishes containing MB culture media inoculated with *Bacillus subtilis* for microbiological testing

Characterization of PLA-Based Food Packaging Films

To gain a comprehensive understanding of the physicochemical and mechanical behavior of the developed PLA-based composite films, a series of structural, thermal, mechanical, and surface analyses were carried out using state-of-the-art techniques. These characterizations aimed to evaluate the impact of active additives such as Bioglass®, oregano oil, and various powders on the overall performance and functionality of the films.

Fourier Transform Infrared Spectroscopy (FTIR): was employed to investigate the molecular structure and the specific functional groups present in the PLA matrix and its composite formulations. The analysis was conducted using a Shimadzu IRTracer-100 spectrometer (Kyoto, Japan), operating in the $4000\text{--}500\text{ cm}^{-1}$ spectral range with a resolution of 4 cm^{-1} . The recorded spectra revealed characteristic absorption bands associated with the PLA backbone as well as distinct peaks indicating the successful incorporation of bioactive and inorganic additives.

Thermal Properties Analysis (TGA/DSC): The thermal behavior and stability of the PLA–Bioglass® composites were assessed via thermogravimetric analysis (TGA) and differential scanning calorimetry (DSC). TGA and DTG measurements were performed using the TGA 2 Star System (Mettler Toledo, Zurich, Switzerland) under a nitrogen atmosphere, with a temperature ramp from 25 °C to 500 °C at a controlled rate of 5 °C/min. These analyses provided detailed insights into thermal degradation patterns and mass loss events.

Complementary DSC measurements were carried out using a DSC 3+ Star System (Mettler Toledo, Leicester, UK), under nitrogen, with a heating rate of 10 °C/min across a range of 25–400 °C. The thermal transitions including glass transition temperature (T_g), crystallization, and melting points were evaluated to determine the influence of bioglass and essential oil components on the thermal profile and phase behavior of the PLA matrix.

The mechanical performance of the composite films was investigated using a Lloyds Instron Universal Testing Machine (Lloyd Instruments, AmetekIns, West Sussex, UK), controlled by Nexygen software version 4.0. Tensile tests followed the EN ISO 527-3:201 standard and were performed on rectangular film specimens measuring 3 mm in thickness, 4 mm in width, and 40 mm in length, with a calibrated gauge area of 25 × 25 mm. A constant axial force of 5 N was applied at ambient temperature until sample failure. From the resulting stress–strain curves, key mechanical parameters were extracted, including: Ultimate Tensile Strength (UTS), Elongation at Break (ϵ), Young’s Modulus (E). These parameters provided critical information regarding the tensile behavior, ductility, and stiffness of the different formulations, directly influencing their suitability for food packaging applications.

Surface Morphology and Microstructural Analysis: The surface features and microstructure of the PLA composites were examined using high-resolution imaging techniques, including scanning electron microscopy (SEM) and atomic force microscopy (AFM) [38]. SEM images were acquired using an Inspect™ microscope (FEI, Hillsboro, OR, USA) operated under high vacuum at an accelerating voltage of 30 kV. This method enabled detailed visualization of the dispersion of fillers, phase separation, and surface homogeneity. AFM investigations were carried out using a JEOL JSPM-4210 instrument (JEOL, Tokyo, Japan), scanning a surface area of 20 μm × 20 μm . The resulting three-dimensional surface maps were analyzed with JEOL WIN SPM 2.0 software to assess nanoscale roughness, uniformity, and potential interactions between the polymer matrix and the incorporated additives. Together, SEM and AFM analyses provided complementary insights into the morphological and interfacial properties of the films.

Acknowledgments: “Development of innovative food packaging without negative impact on the environment (AMBAL-INOV)”, My SMIS: 120994, contract: 375/390051/30.09.2021, Competition: 63/POC/163/1/3/LDR.

REFERENCES

1. Y. A. Hamdan; H. Oudadesse; S. Elouali; N. Eladlani; B. Lefeuvre; M. Rhazi; *International Journal of Biological Macromolecules*, **2024**, 278, 134909.
2. C. G. Gheorghe; O. Pantea; V. Matei; D. Bombos; A.C. Borcea; *Revista de Chimie*, 2011, 62, 707-711.
3. M. Ferdes; F. Al Juhaimi; M.M. Özcan; K. Ghafoor; *South African Journal of Botany* **2017**, 113, 457-460.
4. T. Marino; E. Blasi; S. Tornaghi; E. Di Nicolò; A. Figoli; *Journal of Membrane Science*, **2018**, 549, 192-204.
5. C. G. Gheorghe; O. Pantea; V. Matei; D. Bombos, A. C. Borcea; *Revista de Chimie*, **2011**, 62, 926-929.
6. M.A. Elsayy; K.H. Kim; J.W. Park; A. Deep; *Renewable and Sustainable Energy Reviews*, **2017**, 79, 1346-1352.
7. T.A. Otitoju; C. H. Kim; M. Ryu; J. Par; T. K. Kim; Y. Yoo; H. Park; J.H. Lee; Y.H. Cho; *Journal of Cleaner Production*, **2024**, 467, 142905.
8. C. G. Gheorghe, C; O. Pantea; V. Matei; D. Bombos; A. F. Borcea; *Revista de Chimie*, **2011**, 62, 1023-1026.
9. S.A. Varghese; S. Siengchin; J. Parameswaranpillai; *Food Bioscience*, **2020**, 38, 100785.
10. T. R. Putri; A. Adhitasari; V. Paramita; M. E. Yulianto, H.D. Ariyanto; *Materials Today: Proceedings*, **2023**, 87, 192-199.
11. H.C. dos Santos; B. E. Stutz; A.F. Young; *Renewable Energy*, **2024**, 237, 121943.
12. C. G. Gheorghe; O. Pantea; V. Matei; D. Bombos; A.C. Borcea; *Revista de Chimie*; **2011**, 62, 582-584.
13. M. Johar; A. Rusli; *Materials Today: Proceedings*; **2022**, 66, 2957-2961.
14. A.K. Tyagi; A. Malik; *International Journal of Food Microbiology*; **2010**, 143, 205-210.
15. D.R. Popovici; C. G. Gheorghe; C.M. Dușescu-Vasile; *Bioengineering*; **2024**, 11, 1306.
16. K. Abouelezz; M. Abou-Hadied; J. Yuan; A. A. Elokil; G. Wang; S. Wang; Wang; G. Bian; *Animal*; **2019**, 13, 2216-2222.
17. L. Krishnan; P. Chakrabarty; K. Govarthan; S. Rao; T.S; *International Journal of Biological Macromolecules*; **2024**, 277, 133073.
18. V Gheorghe; C.G. Gheorghe; A. Bondarev; V. Matei; M. Bombos; *Revista de Chimie*; **2019**, 70, 2996-2999.

THE INFLUENCE OF SOME POWDERS ON THE ANTIMICROBIAL ACTIVITY OF
PLA PACKAGING WITH OREGANO OIL ADDITIVES

19. N. M. Nasir; A. Jusoh; H. Manan; N.A. Kasan; A. S. Kamaruzzan; W. A. W. A. K. Ghani; S. B. Kurniawan; F. Lananan; *Biocatalysis and Agricultural Biotechnology*; **2023**, *47*, 102596.
20. Y. Su; Z. Cheng; Y. Hou; S. Lin; L. Gao; Z. Wang; R. Bao; L. Peng; *Aquatic Toxicology*; **2022**, *244*, 106097.
21. P. Parmar; R. Kumar; Y. Neha; V. Srivatsan; *Frontiers in Plant Science*; **2023**, *14*, 1073546.
22. C. G. Gheorghe, C. Dutescu; M. Carbureanu; *Revista de Chimie*; **2016**, *67*, 2106-2110.
23. G. M. Vingiani; P. De Luca; A. Ianora; A.D.W. Dobson; C. Lauritano; *Marine Drugs*; **2019**, *17*, 459.
24. A. A. Singh; S. Sharma; M. Srivastava; A. Majumdar; *International Journal of Biological Macromolecules*; **2020**, *153*, 1165-1175.
25. OECD. Test No. 201: Freshwater Alga and Cyanobacteria, Growth Inhibition Test, OECD Guidelines for the Testing of Chemicals, Section 2. 2011.
26. M. Roszak; J. Jabłońska; X. Stachurska; K. Dubrowska; J. Kajdanowicz; M. Gołębiewska; A. Kiepas-Kokot; B. Osińska; A. Augustyniak; J. Karakulka; *International Journal of Molecular Sciences*; **2021**, *22*, 13469.
27. A. Silva; S. A. Figueiredo; M.G. Sales; C. Delerue-Matos; *Journal of Hazardous Materials*; **2009**, *167*, 179-185.
28. C. G. Gheorghe; C. M. Dutescu-Vasile; D. R. Popovici; D. Bombos; R. E. Dragomir; F. M. Dima; M. Bajan; G. Vasilievici; *Toxics*; **2025**, *13*, 368.;
29. V. Gheorghe; C. G. Gheorghe; D. R. Popovici; S. Mihai; R. E. Dragomir; R. Somoghi; *Bioengineering*; **2024**, *11*, 623.
30. C.-S. Wu.; H.-T. Liao; *Polymer*; **2005**, *46*, 10017.
31. B.W. Chieng; N.A. Ibrahim; W.M. Yunus; M.Z. Hussein; *Polymers*; **2014**, *6*, 93
32. P. Singla; M. Rajeev; B. Dusan; S.N. Upadhyay; *Journal of Macromolecular Science*; **2012**, *49*, 963
33. C. Kamaraj; G. Balasubramani; C. Siva; M. Raja; V. Balasubramanian; R.K. Raja; S. Tamilselvan; G. Benelli; P. Perumal; *Journal of Cluster Science*; **2017**, *28*, 1667
34. D. Vârban; M. Zăhan; I. Crișan; C.R. Pop; E. Gál; R. Ștefan; AM. Rotar; A.S. Muscă; S.D. Meseșan; V. Horga; I. Lados; O. Loredana; A. Stoie; R. Vârban; *Plants*, **2023**, *12*, 4017.
35. F. Francomano; A. Caruso; A. Barbarossa; A. Fazio; C. La. Torre; j. Ceramella; R. Mallamaci; C. Saturnino; D. Iacopetta; M.S. Sinicropi; *Applied Sciences*; **2019**, *9*, 5420.
36. A. Moldovan, S Cuc, D. Prodan, M. Rusu, D. Popa, I. Petean, D. Bomboș; O. Nemes; *Polymers*; **2023** *15*, 2855.
37. V. Gheorghe; C. G. Gheorghe; A. Bondarev; R. Somoghi; *Toxics*; **2023**, *11*, 285.
38. A. Moldovan; I. Sarosi; S. Cuc; D. Prodan; A.C. Taut; I. Petean; D. Bombos; R. Doukeh; S.C. Man; *Journal of Thermal Analysis and Calorimetry*; **2024**, *150*, 2469–2481.

GOLD-DECORATED TITANIA NANOTUBES WITH GRAPHENE FOR VISIBLE LIGHT-MEDIATED AMOXICILLIN PHOTODEGRADATION

Alexandra URDA^{a,b} , Diana LAZAR^a , Dragos COSMA^a ,
Ion GROSU^{b,*} , Crina SOCACI^{a,*} 

ABSTRACT. The degradation of amoxicillin was accomplished using TiO₂ nanotubes photocatalysts decorated with Au nanoparticles and containing reduced graphene or nitrogen-doped graphene under visible light exposure. The structural and morphological characterization confirmed the presence of gold nanoparticles and graphene, and the optical properties showed light absorption into visible region. The best results in the degradation of amoxicillin (up to 60%) were reached in the presence of the photocatalyst with nitrogen-doped graphene. A basics kinetic study showed a physical adsorption of the amoxicillin on the catalyst surface, and that the photodegradation step followed the pseudo-first kinetic model with the apparent kinetic constant of 0.0039 min⁻¹.

Keywords: amoxicillin, titania nanotubes, reduced graphene, nitrogen-doped graphene, photodegradation

INTRODUCTION

The development of chemical and pharmaceutical industries led to a large release of industrial wastewaters into the environment, resulting in a growing deterioration of overall water. In an effort to reduce the chemical impact on public health and environmental quality, a wide range of technologies

^a National Institute for Research and Development of Isotopic and Molecular Technologies (INCDTIM), Donat 67-103 str., Cluj-Napoca, Romania.

^b Babeş-Bolyai University, Faculty of Chemistry and Chemical Engineering, 11 Arany Janos str., RO-400028, Cluj-Napoca, Romania.

* Corresponding authors: crina.socaci@itim-cj.ro; ion.grosu@ubbcluj.ro



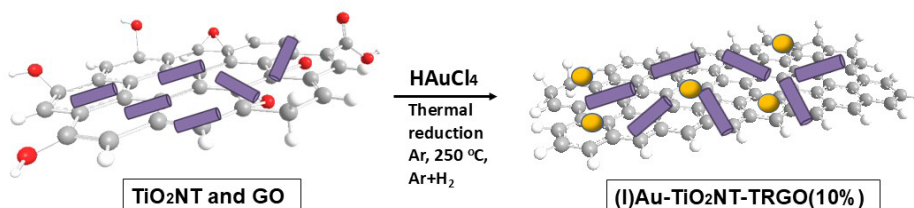
are being employed based on *physical* (filtration, sorption techniques); *chemical* (precipitation, oxidation, irradiation, electrochemical processes) or *biological* (microbial degradation, enzymatic treatment) methods. However, these conventional wastewater treatment technologies still have some limitations (e.g. high operation costs, energy consumption, or reduce efficiency due to the chemical stability of reluctant pollutants [1]). In this context, photocatalysis is becoming a promising oxidation technique for an effective water and wastewater treatment, capable of degrading contaminants using UV and visible light exposure [2]. Even though a great amount of work has been performed in order to understand the mechanisms and improve the photodegradation efficiency of TiO₂-based nanomaterials [3], this oxide with semiconductive properties continue to be interesting for further development due to its low cost, high stability, availability and biocompatibility. Compared to nanoparticles, TiO₂ nanotubes (TiO₂NTs) are suggested to be superior in chemical and optoelectronic performance due to its one-dimensional channel for carrier transportation, in which the recombination of photogenerated e⁻/h⁺ is expected to be reduced.

Because the photonic efficiency of titanium dioxide is under 10% for majority of degradation processes [4] due to its restricted sensitivity to UV light [4-6], several methods for improvement has been proposed and developed: doping with 3d transition metals like Co, Ni, Mn, Fe [7] or noble metals, mainly silver or gold [8]; dye anchoring [9]; surface modifications [10]; and, in the last decade, the preparation of hybrids nanomaterials [11]. As part of our scientific interest, graphene showed their potential as electron co-catalyst to enhance the photocatalytic efficiency of semiconductors [12-18]. There is a common agreement regarding the positive impact of the graphene-based material [19,20], mainly based on their electron trapping properties or enhanced absorption capabilities. Further improvement in the photocatalytic activity has been demonstrated by the introduction of the heteroatoms (e.g. nitrogen) into the graphene sheet with altering the electronic structure thus shifting the photocatalytic response in the visible-light domain [21,22]. Previously, we investigated gold nanoparticles-decorated titania nanotubes photocatalysts with 10wt.% graphene oxide (GO) or reduced graphene oxide (TRGO), for the removal of β -estradiol under visible-light exposure [17].

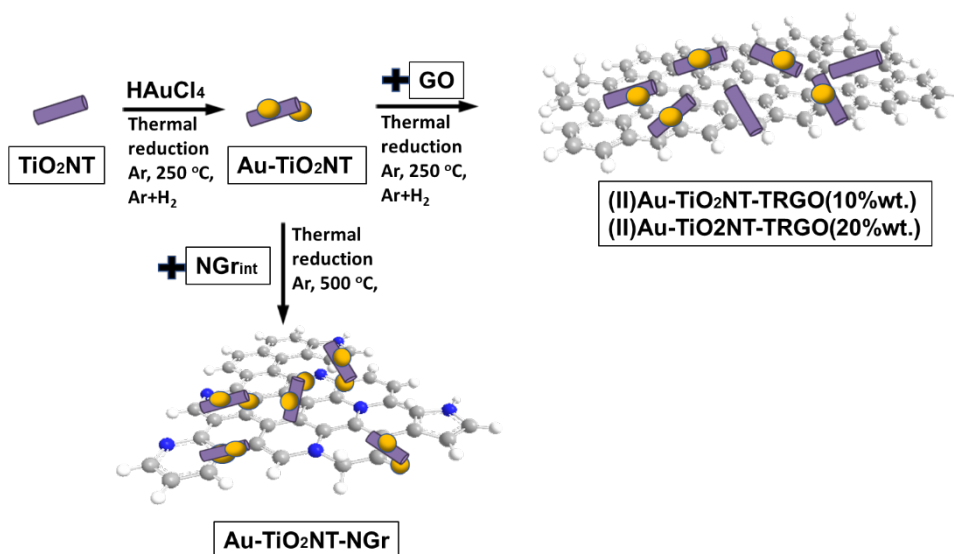
Herein, we considered of interest to continue the investigations and prepare gold-decorated titania nanotubes (Au-TiO₂NT) with 10 wt.% and 20wt.% thermally reduced graphene oxide (TRGO) or nitrogen-doped graphene (NGr) and compare their visible-light-mediated photodegradation efficiency of amoxicillin as model pollutant. Amoxicillin is an antibiotic from the β -lactam family and was categorized in the emerging pollutant family due to its deleterious effects to the environment and human health, even at low concentrations [23,24].

RESULTS AND DISCUSSION

For the preparation of Au-TiO₂NT-TRGO/NGr we started with TiO₂ nanotubes obtained by hydrothermal treatment in an aqueous environment. The preparation of gold nanoparticles-containing titania nanotubes with reduced graphene oxide was employed by two methods and the structural features of the resulted composites were compared. In the first method, a mixture of TiO₂NT and graphene oxide (GO) was impregnated with the gold precursor, followed by a simultaneous thermal reduction of the metal and GO (Scheme 1). The second method was first decorating the TiO₂NT with Au nanoparticles, mixing with graphene oxide (GO), followed by graphene reduction (Scheme 2).



Scheme 1. Preparation method I for Au-TiO₂NT-TRGO composite (Au – gold nanoparticles; TiO₂NT - titania nanotubes; GO – graphene oxide; TRGO – thermally reduced graphene oxide)



Scheme 2. Preparation method II for Au-TiO₂NT-TRGO composite and for Au-TiO₂NT-NGr (Au – gold nanoparticles; TiO₂NT - titania nanotubes; GO – graphene oxide; TRGO – thermally reduced graphene oxide; NGr – nitrogen doped graphene)

The nitrogen-doped graphene containing composite was obtained starting with the same titania nanotubes decorated with gold nanoparticles and mixing with a nitrogen-modified graphene oxide (NGr_{int.}) [18], followed by thermal annealing.

Structural and morphological characterization

Comparative X-Ray diffraction analysis showed that the TiO₂NTs are present only in the anatase form of titania in all the investigated nanomaterials (Figure 1). The comparison of the XRD spectra of Au(2.5wt.%)–TiO₂NT-TRGO catalysts prepared by the two methods (I or II) showed no significant differences. TRGO and NGr could not be observed in XRD patterns being covered by the intense reflection of anatase situated at 25.2°, so the general aspect of XRD patterns of Au(2.5wt.%)–TiO₂NT-graphene catalysts and of the corresponding Au–TiO₂NT are very similar. The three main reflections of metallic Au (30.1°, 44.3° and 64.4°) are well observed and suggest the presence of well crystallized metal with relatively large Au crystallites: 36 nm diameter for the first preparation method, and 16-20 nm for the second method.

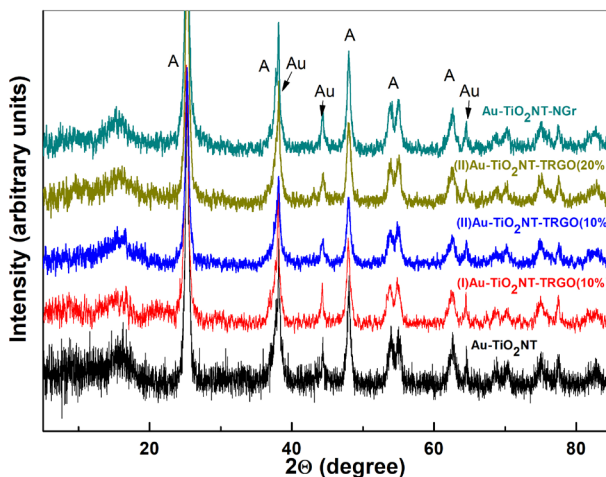


Figure 1. X-Ray diffractograms of the prepared photocatalysts powders (A – anatase)

The electronic microscopy (TEM) investigation confirms the presence of well dispersed large AuNPs (Figure 2) in the Au(2.5wt.%)–TiO₂NT-graphene catalysts prepared by all three methods. The TEM images show large Au nanoparticles of about 15-20 nm for the second method, confirming the calculated dimensions of the Au nanoparticles from XRD data.

GOLD-DECORATED TITANIA NANOTUBES WITH GRAPHENE FOR VISIBLE LIGHT-MEDIATED AMOXICILLIN PHOTODEGRADATION

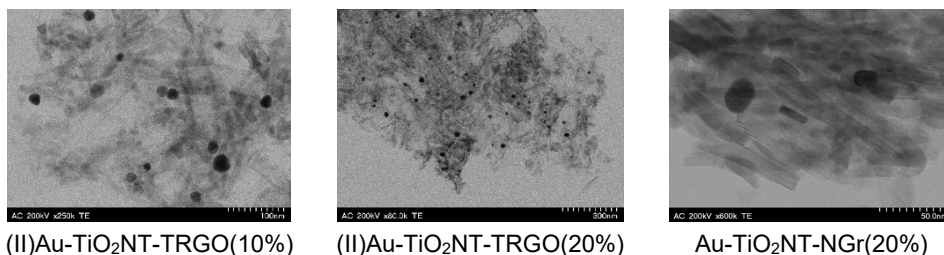


Figure 2. TEM micrographs of selected photocatalysts decorated with Au NPs.

To conclude, the XRD and TEM characterization of materials showed no significant differences between these materials and the metal/TiO₂NTs catalysts, showing that graphene derivatives are not affecting the crystalline structure of gold-decorated titania nanotubes.

Optical properties of the prepared photocatalysts

UV–Vis reflectance spectra of the investigated Au-TiO₂NT-TRGO/NGr photocatalysts (Figure 3a) present the strong light absorption of TiO₂NT in the UV region due to the electron transfer from the valence band O2p to the conduction band Ti3d. The presence of reduced graphene or nitrogen-doped graphene is shifting the optical absorption edge towards the visible region. Additionally, a minimum reflectance level was obtained in the visible region for composites containing the graphene, the 20wt.% thermally reduced graphene having the largest impact. The catalyst with 10wt.% TRGO obtained by the first method has a lower absorption at 550 nm than the one obtained by the second method, showing a less efficient utilization of light by the present gold nanoparticles. Consequently, the 20wt% TRGO catalyst was prepared exclusively by the second method.

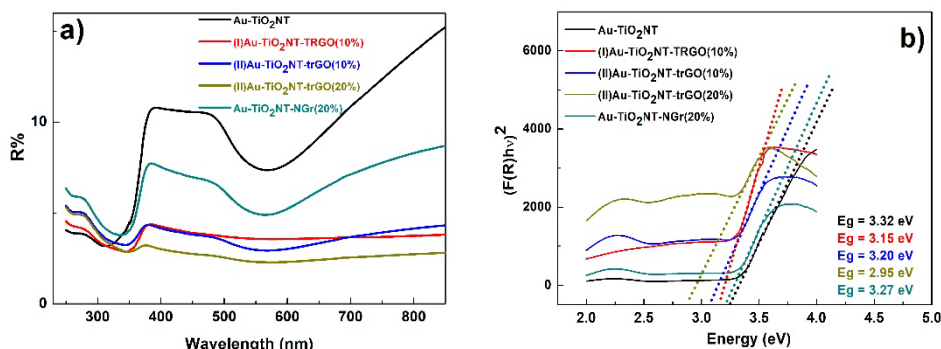


Figure 3. a). DR-UV–Vis spectra of Au-TiO₂NT-TRGO/NGr powders. b). The optical band gap estimation for Au-TiO₂NT-TRGO/NGr composites.

The diffuse reflectance (DRS) spectra were used to estimate the band gap (E_g) of the investigated photocatalysts, using Kubelka-Munk equation (Eq. 1) and the Tauc plot by representing the $[F(R)hv]^n$ vs. hv , where hv is the light energy ($1240/\lambda$), and n is the composite transition (direct transition, $n = 1/2$) [26].

$$F(R) = (1 - R_\infty)^2 / (2R_\infty) \quad (1),$$

where R_∞ represents the reflectance of the composite and $F(R)$ is the absorbance.

The calculated band gap of each composite is presented in the Figure 3b. The bandgap of the starting TiO_2NTs was found to be 3.37 eV. A bandgap narrowing induced by the interfacial interaction among components was obtained for Au- TiO_2NT -TRGO/NGr composites. In accordance with previous studies [27, 28], these results proved that a more efficient utilization of light could be obtained and the Au- TiO_2NT -TRGO/NGr composites should possess higher photocatalytic efficiency than undecorated titania nanotubes for the degradation of organic pollutants, in the visible region.

Visible light photodegradation of amoxicillin

The composites containing gold nanoparticles and titania nanotubes prepared by the second method were tested for the influence of reduced graphene or nitrogen-doped graphene on the visible light-mediated photodegradation of amoxicillin, using white LED lamps in the domain 420 – 800 nm. For this, the adsorption and photocatalytic degradation processes were simultaneously studied. The adsorption equilibrium was set at one hour. The overall results of amoxicillin decrease (C/C_0), working with 1 mg/L amoxicillin and 0.5 mg/mL catalyst dose in a buffer phosphate at pH = 7 are shown in Figure 4. The presence of 10wt.% reduced graphene oxide in the Au- TiO_2NT composite is not improving the photocatalytic behaviour. The decrease in amoxicillin concentration over exposure time was very similar (Figure 4, black and blue lines). The 20%wt. ratio of reduced graphene oxide or nitrogen-doped graphene is clearly enhancing the photocatalytic activity of Au- TiO_2NT composite. As expected, an even better response was measured for the nitrogen-doped graphene-containing composite (Figure 4, dark cyan line), most probably due to the presence of the free electrons of nitrogen atoms that are improving electronic transfer towards or from titania.

The adsorption stage is crucial for heterogeneous catalysis, as reactions are happening on the photocatalyst surface. Besides lowering the bandgap energy and enhancing the light absorption capability of the catalysts, the presence of 20% wt. of graphene (simple or nitrogen doped) in the composites is leading to a larger amount of adsorbed amoxicillin, before exposure to light (Figure 4, dark cyan and dark yellow lines). In order to deepen the processes understanding, we performed a small study on the decrease

of amoxicillin concentrations versus time during the adsorption process alone over a period of 120 minutes. Two starting concentrations of amoxicillin were employed: 1 mg/L and 1.5 mg/L. Data showed that an increase in the initial amoxicillin concentration is enhancing the adsorption (Figure 5). The initial adsorption rate is very rapid, then a bit slower and was not completely reaching the equilibrium, probably because the working concentrations were low and the maximum loading capacity of the photocatalysts cannot be achieved.

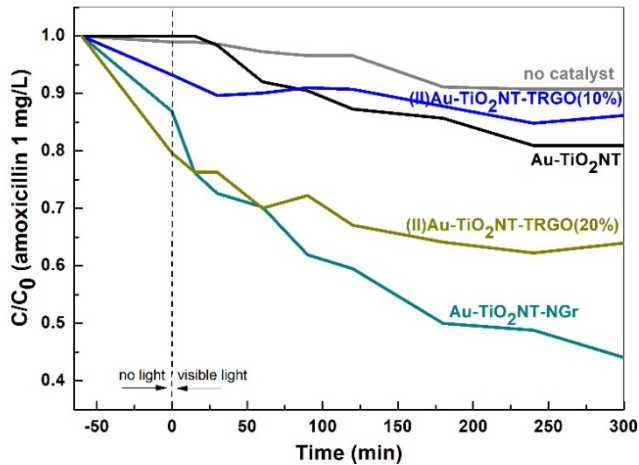


Figure 4. The decrease in amoxicillin ratio under visible light exposure using photocatalysts

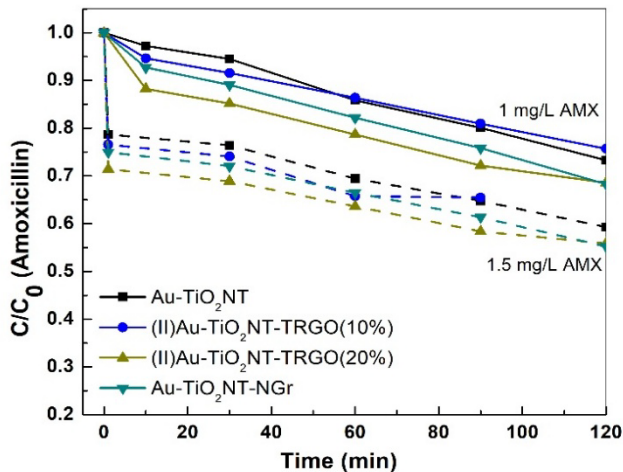


Figure 5. The decrease in amoxicillin ratio during adsorption stage on the selected photocatalysts

The kinetic study was performed by the linearization of the pseudo-first order, pseudo-second order and Elovich kinetic mathematical models of the obtained experimental data. The kinetic equations and parameters of the three models are described below:

$$\ln(q_e - q_t) = \ln q_e - k_1 t \text{ (pseudo-first order model)} \quad (2)$$

$$t/q_t = 1/k_2 q_e^2 + t/q_e \text{ (second order model)} \quad (3)$$

$$q_t = \frac{1}{\beta} \ln(\alpha\beta) + \frac{1}{\beta} \ln t \text{ (Elovich model)} \quad (4)$$

where k_1 and k_2 are the corresponding rate constants, β is the desorption constant (g/mg) and α is the initial adsorption rate (mg/g min).

The calculated constants for the first two models are comparatively presented and the R-squared value are presented in Table 1 (the Elovich model fitting gave inconsistent results and are not presented here). The results show that the adsorption kinetic is dependent on the starting concentration. For all photocatalysts, the higher R^2 and the very close q_e experimental values show that the best describing model at 1 mg/L concentration is the pseudo-first order, while for a starting concentration of 1.5 mg/L the best describing model is the second order. This suggested that physical adsorption was the main process. The mechanism was similar for all the four measured photocatalysts, at small initial concentrations of amoxicillin. As expected, the concentration of graphene is influencing the adsorption. Reduced graphene is a known adsorbent and the catalyst with 20wt.% TRGO showed clearly the best adsorption of amoxicillin.

Table 1. Adsorption kinetics parameters for two concentrations of amoxicillin on the four selected photocatalysts

Composite	Initial AMX conc. (mg/L)	q_e exp. (mg/g)	Pseudo-first order model			Second order model		
			q_e (mg/g)	k_1 (min^{-1})	R^2	q_e (mg/g)	K_2 (mg/(g . min))	R^2
Au-TiO ₂ NT	1	0.55	0.59	0.015	0.9680	0.93	0.0092	0.2978
	1.5	1.03	-	-	0.5620	1.01	0.1212	0.9590
(II)Au-TiO ₂ NT-TRGO(10%)	1	0.50	0.50	0.016	0.9729	0.57	0.0459	0.7648
	1.5	1.26	-	-	0.6762	0.91	0.2385	0.9847
(II)Au-TiO ₂ NT-TRGO(20%)	1	0.64	0.61	0.022	0.9558	0.694	0.0726	0.9112
	1.5	1.12	-	-	0.4980	1.157	0.1049	0.9825
Au-TiO ₂ NT-NGr	1	0.66	0.65	0.014	0.9810	0.742	0.0356	0.7568
	1.5	1.12	-	-	0.5770	1.163	0.0715	0.9591

Further on, the photodegradation step of amoxicillin, under visible light irradiation, was also evaluated from the kinetic point of view in order to evaluate the amoxicillin removal in time. It is generally accepted that photocatalytic reactions are following the simplified Langmuir-Hinshelwood model of pseudo-first order kinetics described by equation (5) [29].

$$r = -\ln\left(\frac{C}{C_0}\right) = k_{obs}t \quad (5)$$

where r is the reaction rate, C is the amoxicillin concentration and k_{obs} the observed first order rate constant.

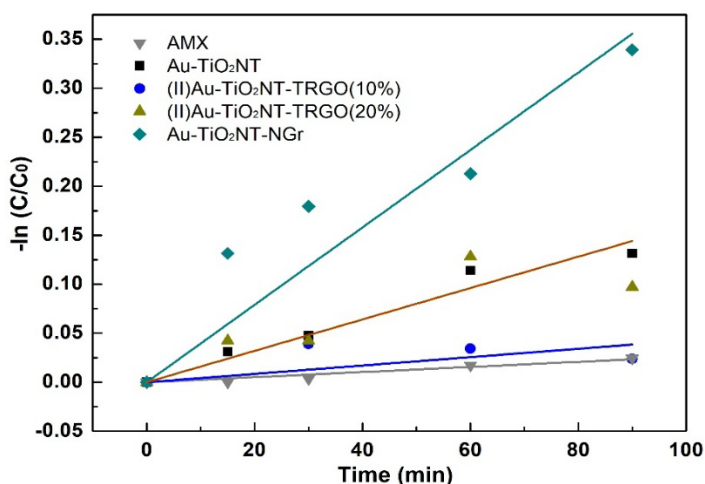


Figure 6. Linearization of amoxicillin photodegradation following the 1st order kinetics model

Figure 6 presents the linear fitting of the representation of $-\ln(C/C_0)$ as a function of time for the four selected photocatalysts, on the time interval up to 90 minutes. The obtained values for the apparent velocity constant (k_{obs}) of 0.00042 min^{-1} (for (II)Au-TiO₂NT-TRGO(10%)), 0.0016 min^{-1} (for Au-TiO₂NT and (II)Au-TiO₂NT-TRGO(20%)) and 0.0039 min^{-1} (for Au-TiO₂NT-NGr) show that Au-TiO₂NT-NGr composite was photodegrading the amoxicillin the fastest. This observation is in contradiction with the observed modifications in the optical properties of the investigated materials, that measured narrower bandgaps for the catalysts bearing reduced graphene oxide instead of nitrogen-doped graphene. The larger reaction rate associated with the nitrogen-doped can only be explained by the reported enhanced electronic mobility between TiO₂ and graphene [21,22].

CONCLUSIONS

This work demonstrated the efficient decoration of titania nanotubes with gold nanoparticles (around 20 nm) and introduction of reduced graphene oxide (up to 20%wt.) or nitrogen-doped graphene, by two preparation methods. These improved the optical properties of the photocatalyst by narrowing the band gap energy value and enlarging the visible light absorption capabilities. The combined effects led to better photocatalytic performances in the removal of amoxicillin (up to 60%) under visible light irradiation, mediated by the nitrogen-doped containing photocatalyst. This is probably due to the electron mediator role of nitrogen-doped graphene, providing an efficient separation between the photogenerated electrons in TiO₂ and photogenerated holes in Au. This study confirms the importance of the graphene presence in the composition of photocatalysts for the visible-light mediated processes, leading to a more efficient use of solar light for environmental applications.

EXPERIMENTAL SECTION

Materials and methods

The starting TiO₂ nanotubes were received from USN, Norway and were prepared by hydrothermal method. Graphene oxide was prepared according to the reported literature procedure [19]. The NGr_{int} was prepared according to the reported literature procedure [18]. Au(2.5%)-TiO₂NT were prepared according to the reported literature protocol [17]. Amoxicillin and HPLC-grade formic acid were purchased from Sigma-Aldrich.

Scanning/Transmission Electron Microscopy (STEM) was employed to investigate the morphology of the composites (at 200 kV and 10 μA) using an H-7650 120 kV Automatic Microscope (Hitachi, Japan). The samples were prepared by dropping a few μL of diluted ethanol suspension of the composites on the copper grid.

The diffuse reflectance UV–Vis spectra of Au-TiO₂NT-containing composites were recorded on a V-570 JASCO Spectrophotometer using solid powders. X-Ray powder Diffraction (XRD) measurements were performed on a Bruker D8 Advance diffractometer, using CuKα1 radiation (λ = 1.5406 Å), with 0.02 grade 2θ/second.

Preparation of (I)Au(2.5%)-TiO₂NT-TRGO(10%)

TiO₂NT, together with the appropriate amount of graphene oxide (GO) were impregnated with an appropriate volume of 0.076 M HAuCl₄ solution to result into a 2.5%wt. gold(0). The slurry was dried under normal

conditions and the resulted solid was heated up to 250°C under argon flow, and then the gas flow was switched to a mixture of H₂ in Ar (10 vol.% H₂) in order to pursue the reduction of graphene oxide (250°C, 10 minutes), resulting into Au-TiO₂NT with thermally reduced graphene oxide, denoted as (I)Au(2.5%)-TiO₂NT-TRGO(10%).

Preparation of (II)Au(2.5%)-TiO₂NT-TRGO

Au(2.5%)-TiO₂NT was sonicated with the appropriate amount of graphene oxide (GO) followed by lyophilization. The resulted composite was seated in a quartz boat into a temperature-programmed furnace. The furnace was heated up to 250°C under argon flow, and then the gas flow was switched to a mixture of H₂ in Ar (10 vol.% H₂) in order to pursue the reduction of graphene oxide (250°C, 10 minutes), resulting into Au-TiO₂NT with thermally reduced graphene oxide, denoted as (II)Au(2.5%)-TiO₂NT-TRGO(10%) and (II)Au(2.5%)-TiO₂NT-TRGO(20%).

Preparation of Au(2.5%)-TiO₂NT-NGr

Au(2.5%)-TiO₂NT was sonicated with the appropriate amount of NGr_{int}, followed by lyophilization. The resulted solid was heated up to 500°C under argon flow, resulting into Au-TiO₂NT with nitrogen-doped graphene, denoted as Au(2.5%)-TiO₂NT-NGr(20%).

Adsorption and photocatalytic degradation of amoxicillin

The photocatalytic degradation tests were carried out in a Photoreactor Luzchem LZC-4V (Canada) equipped with 12 white LEDs (8 W) that emits in the visible domain 420 – 800 nm, the light intensity being 241.000 lx (lumen/m²). The batch equilibrium experiments (adsorption/desorption) were performed in the dark over the described period of time (60 minutes or 120 minutes). After adsorption, the visible light was turned on and 150 µL aliquots were withdrawn from the solutions at various time intervals under well-mixing conditions and transferred to an inset in a two-mL HPLC vial and the aqueous concentration of amoxicillin was determined by a high-performance liquid chromatograph (HPLC) equipped on a UHPLC Restek Pinnacle C18 column (5 × 2.1 mm; 1.9 µm particle size) at room temperature, isocratic elution acetonitrile: water (0.3% formic acid) = 95:5 at a flow rate of 0.25 mL/min, and the UV detector set at 230 nm. Amoxicillin concentrations were calculated on the basis of a calibration curve.

The residual ration (C/C₀) were calculated with the following formula:

$$\frac{C}{C_0} = \frac{C_t}{C_i} \quad (6)$$

ACKNOWLEDGMENTS

This work was supported through the “Nucleu” Program within the National Research Development and Innovation Plan 2022–2027, Romania, carried out with the support of MEC, project no. 27N/03.01.2023, component project code PN 23 24 01 01.

REFERENCES

1. A. Malik, E. Grohmann, *Environmental Protection Strategies for Sustainable Development*, Springer Netherlands, 2012, p. 12
2. S.C. Ameta, R. Ameta, *Advanced oxidation processes for waste water treatment-emerging green chemical technology, Chapter 6 – Photocatalysis*, Academic Press, 2018, 135-175
3. N. Farooq, P. Kallem, Z. ur Rehman, M. I. Khan, R. K. Gupta, T. Tahseen, Z. Mushtaq, N. Ejaz, A. Shanableh, Recent trends of titania (TiO₂) based materials: A review on synthetic approaches and potential applications, *Journal of King Saud University – Science* **2024**, *36*, 103210.
4. O. Carp, C.L. Huisman, A. Reller, *Prog Solid State Ch* **2004**, *32*, 33–177
5. M. Pelaez, N.T. Nolan, S.C. Pillai, M.K. Seery, P. Falaras, A.G. Kontos, P.S.M. Dunlop, Jeremy, W.J. Hamilton, J.A. Byrne, K. O’Shea, M.H. Entezari, D.D. Dionysiou, *Appl Catal B* **2012**, *125*, 331-349
6. M.J. Wu, T. Bak, P.J. O’Doherty, M.C. Moffitt, J. Nowotny, T.D. Bailey, C. Kersaitis, *Int J Photochem* **2014**, 1-9
7. T. Umebayashi, T. Yamaki, H. Itoh, K. Asai, *J Phys Chem Solids* **2002**, *63*, 10, 1909-1920
8. S. Linic, P. Christopher, D.B. Ingram, *Nat Mater* **2011**, *10*, 12, 911-921
9. E. Bae, W. Choi, J. Park, H.S. Shin, S. Bin Kim, J.S. Lee, *J Phys Chem B* **2004**, *108*, 37, 14093-14101
10. H. Park, Y. Park, W. Kim, W. Choi, *J Photochem Photobiol C: Photochem Rev* **2013**, *15*, 1-20
11. M. Minella, D. Fabbri, P. Calza and C. Minero, *Curr Opin Green Sust Chem* **2017**, *6*, 11–17
12. S.D. Perera, R.G. Mariano, K. Vu, N. Nour, O. Seitz, Y. Chabal Jr, K.J. Balkus, *Catalysis* **2012**, *2*, 949–956
13. J. Liu, H. Bai, Y. Wang, Z. Liu, X. Zhang, D.D. Sun, *Adv Funct Mater* **2010**, *20*, 23, 4175–4181
14. A. Trapalis, N. Todorova, T. Giannakopoulou, N. Boukos, T. Speliotis, D. Dimotikali, J. Yu, *Appl Catal B* **2016**, *180*, 637–647
15. A. Urda, T. Radu, C. Socaci, V. Floare-Avram, D. Cosma, M. C. Rosu, M. Coros, S. Pruneanu, F. Pogacean, *J. Photochem. Photobiol. A* **2022**, *425*, 113701.
16. D. Cosma, A. Urda, T. Radu, M.C. Rosu, M. Mihet, C. Socaci, *Molecules* **2022**, *27*, 18, 5803.

17. D. Cosma, M.-C. Roșu, C. Socaci, A. Urda, T. Radu, A. Turza, M. Dan, R. M. Costescu, K. R. Gustavsen, O. Dobroliubov, K. Wang, *Journal of Environmental Chemical Engineering* **2024**, 12, 3, 112885.
18. A. Urda, T. Radu, K. R. Gustavsen, D. Cosma, M. Mihet, M. C. Rosu, A. Ciorîța, A. Vulcu, K. Wang, C. Socaci, How is graphene influencing the electronic properties of NiO-TiO₂ heterojunction?, *Journal of Physics D: Applied Physics* **2025**, 58, 015103.
19. A.T. Kuvarega, B.B. Mamba, *Crit Rev Solid State Mater Sci* **2016**, 295-346
20. P. Huo, P. Zhao, Y. Wang, B. Liu, M. Dong, *Energies* **2018**, 11, 630
21. H. Pan, X. Zhao, Z. Fu, W. Tu, P. Fang, H. Zhang, *Appl Surf Sci* **2018**, 442, 547–555
22. H. Xu, M. Ding, W. Chen, Y. Li, K. Wang, *Sep Purif Technol* **2018**, 195, 70–82
23. D. Ding, B. Wang, X. Zhang, J. Zhang, H. Zhang, X. Liu, Z. Gao, Z. Yu, *Ecotoxicol. Environ. Saf.* **2023**, 254.
24. S.M. Al-Jubouri, H.A. Sabbar, E.M. Khudhair, S.H. Ammar, S. Al Batty, S. Yas Khudhair, A.S. Mahdi, *J. Photochem. Photobiol. A Chem.* 2023, 442.
25. J. Liu, K.Y. Chen, J. Wang, M. Du, Z.Y. Gao, C.X. Song, *Journal of Chemistry* **2020**, 2928189.
26. P. Martins, S. Kappert, H.N. Le, V. Sebastian, K. Kühn, M. Alves, L. Pereira, G. Cuniberti, M. Melle-Franco, S. Lanceros-Méndez, *Catalysts* **2020**, 10, 234.
27. N. Liu, X. Chen, J. Zhang, J.W. Schwank, *Catalysis Today* **2014**, 225, 34– 514.
28. D. Chen L. Zou, S. Li, F. Zheng, *Scientific Reports* **2016**, 6, 20335.
29. C. Turchi, D.F. Ollis *J. Catal.* **1990**, 122, 178–192.

APPLICATION OF BANANA BASED AGRO-WASTE AS A PRECURSOR OF HETEROGENEOUS CATALYST FOR BIODIESEL PRODUCTION

Santhosh VISWANATHAN^{a*}, Siva PERIYASAMY^b,
Senthilkumar KANDASAMY^c

ABSTRACT. In the recent decades, the exploration of agro-wastes and other renewable biomass wastes as a precursor of heterogeneous catalysts for transesterification has become more fascinating in contrast to the conventional homogeneous catalysts. This is mainly attributed by its peculiar characteristics such as easy separation, reusability, cost effectiveness, eco friendliness, etc. Hence, the potential of banana inflorescence (BI), a byproduct of banana cultivation with less economic value was investigated herein, for the development of a competent heterogeneous catalyst for profitable biodiesel production from Used cooking oil (UCO). The transformation in porosity, surface area and chemical composition of banana inflorescence, brought about by calcination was examined by Scanning electron microscopy (SEM), Brunauer–Emmett–Teller (BET), Powder X-ray diffractogram (XRD), Fourier transform infrared spectroscopy (FTIR) and Energy Dispersive X-ray Spectroscopy (EDS) analysis. The conversion was enumerated by Nuclear magnetic resonance (¹H NMR) spectroscopy and it was observed that transesterification using 2 wt% catalyst, 9:1 methanol to oil molar ratio for a reaction time of 75 min at 65 °C showed a fatty acid methyl ester (FAME) conversion of 98.62%.

Keywords: *Banana inflorescence; Used cooking oil; Calcination; Biodiesel*

^a Department of Chemical Engineering, Erode Sengunthar Engineering College, Perundurai, Tamilnadu-638057, India

^b Department of Mechanical Engineering, Government College of Technology, Coimbatore, Tamilnadu, India

^c Department of Food Technology, Kongu Engineering College, Erode, Tamilnadu, India

* Corresponding author: vsanthoshchemical@gmail.com



INTRODUCTION

Renewable energy resources are basic requisites for developing as well as developed nations and are the base for economic growth which in turn triggers the energy demand. Almost 80% of world's energy needs are met by fossil fuels, a primary energy source [1]. In today's world, where fuel prices are hiking due to spiraling demand and diminishing supply, the fuels are getting exploited in a rate faster than what nature can replenish. This is precisely evident from the statistics that points out the crude oil production of 36,468.97 ktoe (kilo tonne of oil equivalent) and import of 2,25,282.02 ktoe (kilo tonne of oil equivalent) by India in 2017-18 [2]. In India, 72% of transportation fuel is diesel, followed by 23% of petrol, 5% of CNG, LPG, etc. of which 80% of oil needs is dependent on imports [3]. Diesel plays a major role in transportation, agriculture, power generation, industries, mining, quarrying and private imports [2]. This precisely implicates a critical need for providing alternate energy sources in a sustainable manner, especially at a relatively affordable cost.

Besides the accelerated exploitation, the byproducts of the fossil fuel combustion has been imposing threat to health and climate mitigation. Concomitant with the growth of global energy consumption by 2.9 % in 2018, CO₂ emission grew up by 2% and share of non-fossil fuels has increased to 15.3%, a highest record in recent history [4]. Biodiesel is one such non fossil fuel that has a considerable heating value of 39–41 MJ/kg like fossil based gasoline (46 MJ/kg), petrodiesel (43 MJ/kg), petroleum (42 MJ/kg) and coal (32–37 MJ/kg). It is noteworthy that higher heating value (HHV) makes the fuel more economic and the fuel can be used without any modification in the diesel engine [5]. The physical properties of biodiesel are similar to that of fossil based diesel and are entirely dependent on the nature of feedstock. Furthermore, biodiesel emission is devoid of sulfur and aromatic compounds and has reduced emission of CO₂, CO, NO_x and other particulate matters [6]. Along with this, renewability, high flash point and biodegradability has made biodiesel as a promising fuel to either blend with diesel or as a complete substitute [7,8]. Hence, biodiesel has become an attractive alternate for mineral diesel in spite of the diminishing petroleum reserves and increasing environmental crisis.

Biodiesel is a mixture of mono alkyl esters of fatty acids that can be produced from various types of vegetable oils, animal fats, microbial oil, algal oil and waste oil by transesterification with methanol or ethanol using nucleophilic homogeneous or heterogeneous catalyst [9]. Biodiesel can be produced by various methods such as pyrolysis, micro-emulsion, dilution, microwave technology, reactive distillation, catalytic distillation, super fluid method and

transesterification. But transesterification is preferred over other techniques due to its ease of operation, suitability for large scale production and fuel properties [10]. Selection of a feedstock is a key factor as it affects the cost, yield, physicochemical properties and purity of biodiesel and it should be easily procurable [11]. It has been reported that the physico-chemical properties vary with sources of collection which owes to the varying optimum conditions obtained for biodiesel production using similar catalyst [12]. UCO is of 2 types: first used cooking oil that is collected from restaurants and second used cooking which is generally dumped into landfills by street food sellers [13]. Hence the conversion of used cooking oil into biodiesel is environment friendly, economically feasible, sustainable and reduces the risk of disorders. Niju et al employed UCO as a feedstock for biodiesel production using different calcium based heterogeneous catalysts and reported a high biodiesel conversion [14-17].

Nowadays, heterogeneous catalysts seeks more attention due to easy catalyst separation and reusability [18]. Several agro-waste biomasses have been explored as precursor of catalyst for biodiesel production in the last few decades which includes *Musa balbisiana* trunk [19], *Musa balbisiana* underground stem [20] and *Musa balbisiana* peels [21], *Musa paradisiacal* peels [22], *Musa acuminata* peels [23], *Musa acuminata* peduncle [24] and *Musa sp.* "Pisang Awak" peduncle [25], etc. India being the largest producer of banana (25.7 % globally) [26], generates a huge amount of banana inflorescence, that has quite low value due to its inconsistent demand, less shelf life and limited acceptance [27]. Banana inflorescence (botanical term-thryse) has a complex structure consisting of female flowers at proximal end followed by a male bud at the distal end which comprises of bracts enclosing male flowers [28]. While female flowers give rise to edible and economically valuable bananas, male buds are considered as waste during crop production with less economic value and are thrown away after harvesting leading to a huge post harvest waste, most of which are discarded in water bodies that increase the biological oxygen demand and affects the aquatic life [29]. Banana inflorescence can be used to treat dysentery, diabetes, ulcers, bronchitis, etc [30] and it is rich in polyphenols, dietary fibres and antioxidants [31]. Also, it is consumed as vegetable in many regions, particularly in India and Malaysia [29]. Eventhough it has tremendous nutritional and medicinal values, the tedious preparation process and less shelf life limits its consumption [32].

Hence the objective of the present work is to prepare a highly active heterogeneous catalyst from banana inflorescence (BI) and to test the catalytic activity for transesterification of UCO into biodiesel. The prepared catalyst was characterized using SEM, EDS, FTIR, XRD and BET techniques. Further, the biodiesel conversion was estimated by ^1H NMR analysis.

RESULTS AND DISCUSSION

Catalyst Characterization

Sem analysis

The surface morphology and particle size distribution of **CBIA (calcined banana inflorescence ash)** and **UBIP (uncalcined banana inflorescence peel)** was compared by means of Scanning electron microscopy (SEM) analysis and presented in Figure 1(a,b,c,d). UBIP (Figure 1(a,b)) has a rugged surface that is devoid of pores but has crevices whereas the CBIA (Figure 1(c,d)) has become relatively smoother and porous upon calcination.

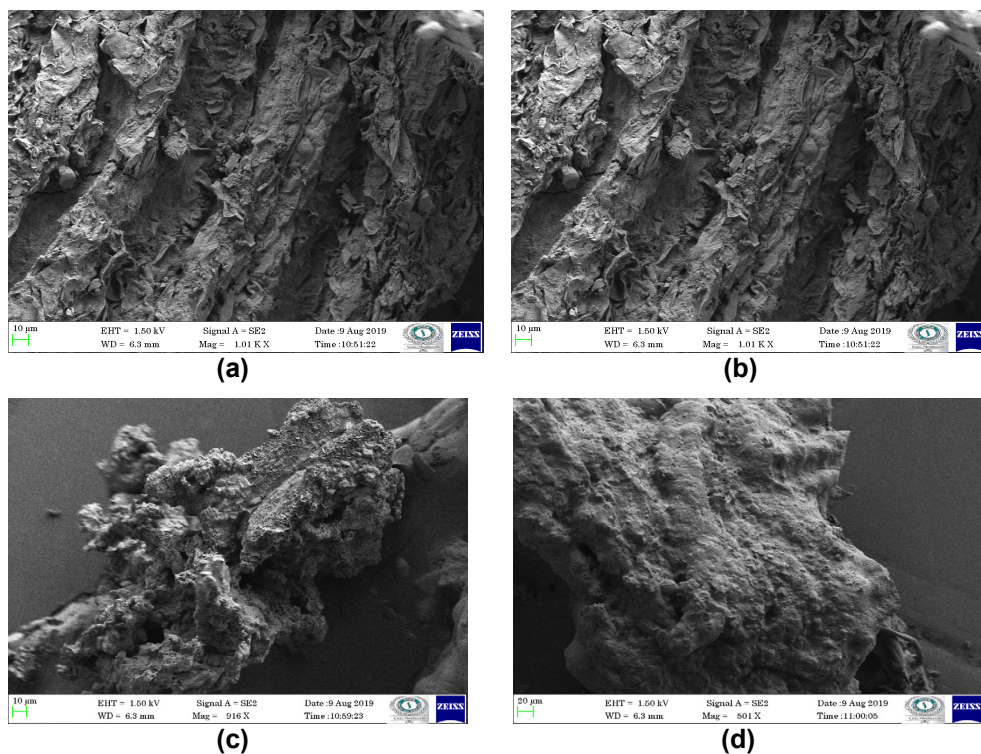


Figure 1. SEM images of UBIP (a and b) and CBIA (c and d)

The pores are formed due to the degradation of volatile organic compounds (VOCs) in the biomass to CO_2 , CO , NO_2 , etc [34]. Thus the calcination process increases the surface area in the form of porous structures for enhanced catalytic activity. This is evident through BET analysis which showed the

increase in surface area from 0.879 m²/g to 2.002 m²/g. This is advantageous because a comparatively less amount of catalyst is sufficient which in turn increases the ratio of catalyst surface area to reactant volume, a crucial factor to increase collision rate and hence the reaction rate. Moreover the calcination process removes the undesired organic compounds in the form of gases leaving behind the minerals that are nonvolatile. Pathak et al (2018) reported similar observation of aggregates with mesopores and micropores after calcination of *Musa acuminata* peel for biodiesel production [22]. Balaji and Niju (2019) tested the potential of *Musa acuminata* peduncle as catalyst for biodiesel production wherein they reported the transformation of irregularly distorted particles into highly ordered porous particles upon calcination [24].

BET analysis

In order to substantiate the increase in surface area upon calcination, BET analysis was performed with UBIP and CBIA. Before calcination, surface area was 0.877 m²/g which increased to 2.002 m²/g after calcination. As expected, there was more than two fold increase in the surface area upon calcination. Also, there was an increase in pore volume and diameter from 0.002 cc/g, 2.103 nm to 0.003 cc/g, 2.463 nm respectively. Pathak et al (2018) had performed similar studies with *Musa acuminata* peel and reported the increase in surface area to 1.4546 m²/g upon calcination [23]. These findings illustrate the improvement of biomass surface area upon calcination which makes it effective as a catalyst in transesterification reaction.

FTIR analysis

FTIR spectroscopy is an analytical technique that identifies the organic, polymeric and in some cases inorganic compounds. It makes use of infrared rays (10,000 to 100 cm⁻¹) to irradiate the sample which absorbs a part and others get passed through i.e., transmitted. The absorbed radiation brings about rotational and/or vibrational energy to the sample molecules. Depending on the chemical structure, a unique spectral fingerprint is produced for each molecule [35]. Hence, in order to determine the changes in the chemical composition of banana inflorescent powder brought about by calcination, UBIP and CBIA were analysed by FTIR (Figure 2) and the corresponding functional groups were presented in Table 1. Before calcination, i.e., in UBIP, OH stretching is stronger due to the presence of moisture [21,23,25], C=O and C-H stretching is prominent, indicating the presence of aldehyde and ketones [36,37]. All these corresponding peaks are absent after calcination, i.e. in CBIA indicating its degradation. Instead the peaks C-O stretching of K₂CO₃ has become more prominent [21,25,32,50].

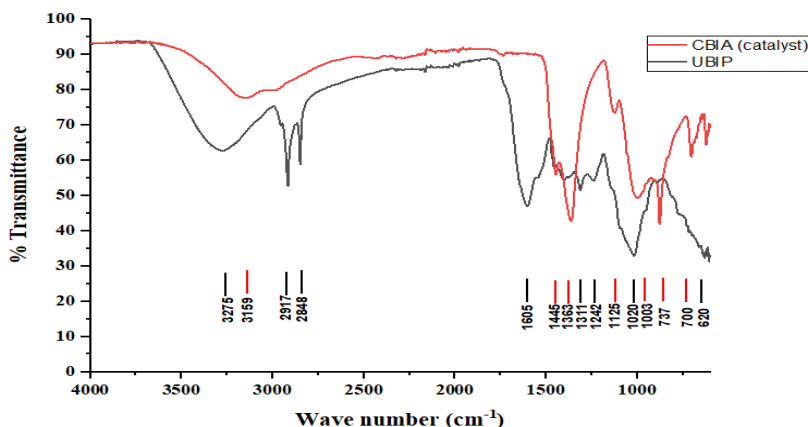


Figure 2. FTIR spectra of UBIP and CBIA

From the extent of transmittance, it is obscure that C=O stretching of K_2CO_3 has high absorbance which implies that potassium is present predominantly in the form of carbonates rather than oxides. OH stretching of $K_2CO_3 \cdot 1.5 H_2O$ denotes the association of small fraction of potassium carbonate with water molecules [25]. This may be due to the absorbance of CO_2 and moisture in atmosphere. Peaks for Si-O-Si stretching bands [33] and $CaCO_3$ was also observed but not as prominent as K [34]. These results are in concordance with the findings of Gohain et al (2017) [21], Pathak et al (2018) [23], and Balaji and Niju (2019, 2020) [24,25].

Table 1. Functional groups present in UBIP and CBIA detected from FTIR spectra

Wave number (cm ⁻¹)	CBIA	UBIP
700	CO ₃ ²⁻ in metal carbonates	-
1003	Si-O-Si stretching bands	-
1020	-	C-O-C stretching at β(1→4)-glycosidic linkage of cellulose
1242	-	O-H Deformation
1311	-	C-N stretching of primary and secondary amines
1445	OH stretching in $K_2CO_3 \cdot 1.5H_2O$	-
1605	K_2CO_3	C=O stretching
2848, 2917	-	Aliphatic C-H stretching
3159	K_2CO_3	-
3275	-	OH stretching NH in amine

EDS analysis

EDS is used for qualitative and quantitative analysis of chemical composition of any matter. It makes use of the unique atomic structure to differentiate the elements present in the sample that is irradiated with the beam of X-rays. The energy of emitted x-rays from the sample is a characteristic of the elements present in it [34]. The area of the peak indicates its abundance. Before calcination, only a fraction of metal ions are detected as most of them are bound to organic biomolecules [35]. After calcination, an obscure dominance of potassium was observed along with traces of Ca, Mg, Si, P, S, Cl, Br and Al. Calcination has enhanced the potassium content from 20.2 to 35.81 wt%, which is more than a two-fold increase. The detection of negligible amount of Br and S after calcination, is due to the removal of volatile organic compounds which in turn has increased its accessibility.

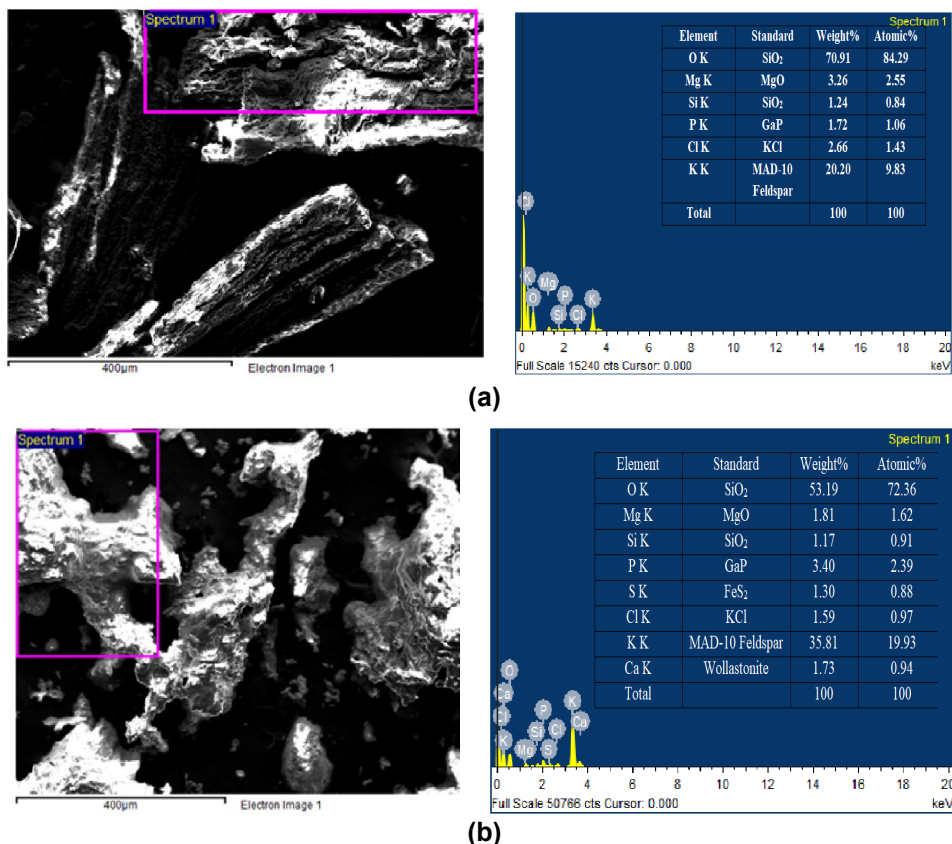


Figure 3. Elemental composition of UBIP (a) and CBIA (b) from EDS analysis

This implies the significance of calcination process. The prevalence of oxygen and absence of carbon indicates the presence of minerals in the form of oxides rather than carbonates. Balaji and Niju (2019) examined *Musa acuminata* peduncle for biodiesel production wherein they reported an increase in K content from 25.63 wt% to 42.23 wt% upon calcination [24]. The previous works on agrowaste derived heterogeneous catalysts for transesterification were reported with abundance of K that contributed for its catalytic activity [20,21], [23,24].

XRD analysis

The presence of crystalline compounds in the UBIP and CBIA were detected by XRD analysis. In UBIP (Figure 4a), strong peaks corresponding to cellulose, a monoclinic crystal were observed between angles 2θ between 15.16° to 24.6° . Strong peaks corresponding to 2θ at 21.77° , 19.63° implies the presence of cellulose II whereas the peaks corresponding to 2θ at 15.16° , 14.54° implies the presence of cellulose I [36,37]. Cellulose I and Cellulose II are major plant cell wall components and the latter was detected predominantly in UBIP due to its thermodynamically stable crystalline nature [38]. After calcination i.e., in CBIA (Figure 4b), those peaks were absent indicating the combustion of cellulose and other volatile organic compounds (VOC) [34].

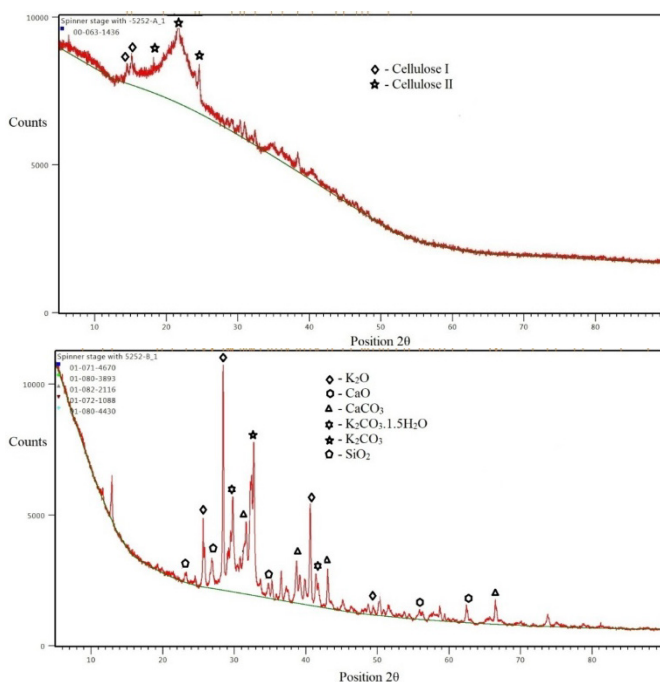


Figure 4. XRD spectra of UBIP (a) and CBIA (b)

Thus calcination reduces the background of organic compounds, allowing the trace minerals to be detected at high intensity. Strong characteristic peaks at angles 2θ of 25.66° , 25.86° , 40.62° , 41.4° , 28.45° , 33° , 30.5° , 42° were observed, indicating the predominance of K_2O , K_2CO_3 and $K_2CO_3 \cdot 1.5H_2O$ [23,39]. Small peaks at angles 2θ of 30.85° , 39.19° , 43° , 67° indicates the presence of CaO and $CaCO_3$ [23,39]. Peaks corresponding to 24° , 28.5° , 34.5° indicates the presence of SiO_2 [23,39]. This clearly indicates the random distribution of several minerals in the form of oxides and carbonates. Moreover, Potassium was predominant among the minerals that is present in the CBA. These results are in accordance with the findings of Gohain et al (2017) [21], Pathak et al (2018) [23], and Balaji and Niju (2019, 2020) [23,24].

Biodiesel characterization by 1H -NMR analysis

Transesterification reaction was performed using 2 wt% CBA catalyst with methanol to oil ratio of 9:1 at $65^\circ C$ for a reaction time of 75 min. 1H -NMR analysis was performed for quantitative estimation of FAME in the biodiesel. A characteristic peak of methyl group at 3.66 ppm that is prominent for a typical FAME is abundant, confirming the presence of biodiesel [35]. This is due to the substitution of glycerol part of glycerides with methoxy group. A triplet peak at 2.75-2.79 ppm indicates the presence of α -methylene group nearby to methoxy ester. Peak corresponding to 5.28-5.41 ppm denotes the presence of olefinic protons that is peculiar for unsaturated hydrocarbon chains. Peaks between 1.25-1.30 ppm represents the backbone CH_2 of the hydrocarbon chains.

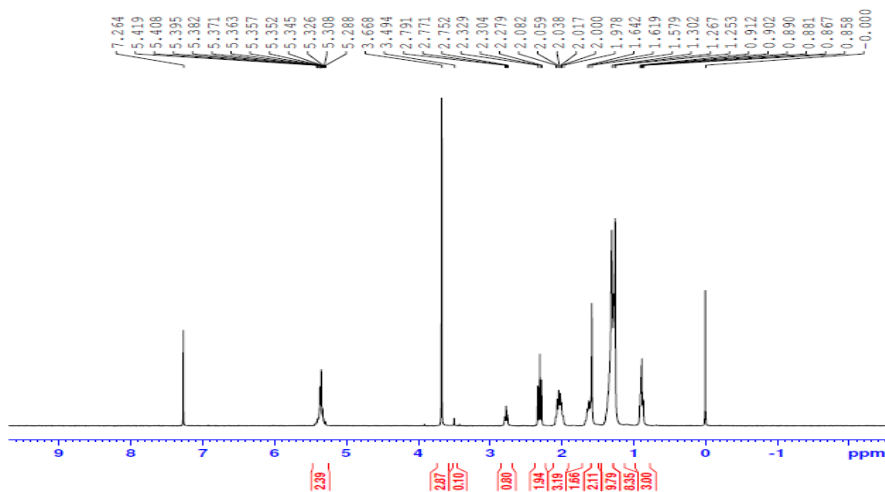


Figure 5. 1H NMR spectrum of Biodiesel

Peaks between 0.85-0.91 ppm corresponds to the terminal methyl group. Presence of fatty acids were also detected by the peaks between 1.57-1.64 ppm [36,37]. Absence of peaks between 3.73 to 5.27 ppm denotes the absence of mono, di and triglycerides [38]. The percentage conversion of UCO to biodiesel was found to be 98.62 % using Eq.(1). This indicates the potential of CBIA as a catalyst for biodiesel production from UCO.

Comparison of different agro-residue based heterogeneous catalysts for biodiesel production

Potential of different biomass derived heterogeneous catalysts for biodiesel production was discussed. The catalytic activity of CBIA was compared with the state of the art in the literature and presented in Table 2. Deka and Basumatary (2011) investigated the transesterification of *Thevetia peruviana* oil using calcined *Musa balbisiana* trunk as a heterogeneous catalyst and reported 96% biodiesel conversion using 20 wt% catalyst, 10:1 methanol to oil ratio for a reaction time of 3 h [19]. Pathak et al (2018) made a similar study on transesterification of soybean oil with *Musa acuminata* peel at room temperature wherein they obtained 98.95% of biodiesel with 0.7 wt% catalyst, 6:1 methanol to oil ratio in 4 h [23]. Aslam et al (2014) examined the potential of *Musa balbisiana* underground stem for transesterification of *Jatropha curcas* into biodiesel but the high acidic value of the oil required transesterification at a high temperature (275 °C) and pressure (4.2 Mpa) [20]. This shows the impact of physicochemical properties of the feedstock on FAME conversion. Betiku and Ajala (2014) reported a two step biodiesel synthesis from *Thevetia peruviana* oil to decrease the acid value by esterification and utilized *Musa paradisiacal* peel as a catalyst in transesterification process. The authors reported 95% yield of biodiesel by means of transesterification using 3 wt% catalyst, 3:0.9 methanol to oil ratio at 60 °C for a reaction time of 75 min [22]. Balaji and Niju (2020) tested the catalytic activity of *Musa sp.* "Pisang Awak" peduncle for transesterification of esterified *Ceiba pentandra* oil into biodiesel wherein they reported an yield of 98.69±0.18% with 1.978 wt% catalyst loading, 9.20:1 methanol to oil ratio at 65 °C for 60 min [25]. They have also reported the potential of *Musa acuminata* peduncle for transesterification of esterified *Ceiba pentandra* oil into biodiesel. However this process required 11.46:1 methanol to oil ratio with 2.68 wt% catalyst for 106 min at 65 °C for a similar conversion of 98.73±0.5% [25]. Gohain et al (2017) had reported complete conversion of used cooking oil into biodiesel with 2 wt% calcined *Musa balbisiana peel*, 6:1 methanol to oil ratio at 60 °C. Eventhough used cooking oil does not require esterification this took a quite

APPLICATION OF BANANA BASED AGRO-WASTE AS A PRECURSOR OF
HETEROGENEOUS CATALYST FOR BIODIESEL PRODUCTION

longer reaction time of 180 min [21]. In the present work, 98.62% of conversion of used cooking oil into biodiesel was achieved in 75 min with a single step transesterification using 2 wt% CBIA, 9:1 methanol to oil molar ratio at 65 °C.

Table 2. Summary of potential of different agrowastes as precursor of catalyst for biodiesel production

Feedstock	Precursor of catalyst	Calcination conditions	Surface area (m ² /g)	Catalyst concentration (wt %)	Methanol to oil ratio	Time (min)	Temperature (°C)	Yield / Conversion (%)	Reference
<i>Thevetia peruviana</i> oil	<i>Musa balbisiana</i> Colla trunk	Burnt in air	1.487	20	10:1	180	32	96	[19]
<i>Jatropha curcas</i> oil	<i>Musa balbisiana</i> Colla underground stem	550 °C, 2 h	38.71	5	9:1	60	275	98	[20]
Used cooking oil	<i>Musa balbisiana</i> peel	700°C, 4 h	10.176	2	6:1	180	60	100	[21]
<i>Thevetia peruviana</i> oil	<i>Musa paradisiacal</i> peel	500°C, 3.5 h	-	3	3:0.9	90	60	95	[22]
Soybean oil	<i>Musa acuminata</i> peel	Burnt in air	1.4546	0.7	6:1	240	Room temperature	98.95	[23]
<i>Ceiba Pentandra</i> oil	<i>Musa acuminata</i> peduncle	700°C, 4 h	45.99	2.68	11.46:1	106	65	98.73	[24]
<i>Ceiba Pentandra</i> oil	<i>Musa sp.</i> "Pisang Awak" peduncle	700°C, 4 h	-	1.978	9.20:1	60	65	98.69	[25]
Used cooking oil	Banana inflorescence	700°C, 4 h	2.002	2	9:1	75	65	98.62	Present study

CONCLUSION

The present work elucidates the competency of CBIA in catalyzing the transesterification of used cooking oil into biodiesel. Morphological changes and improvement in the catalyst surface area from 0.877 mm²/g to 2.002 mm²/g upon calcination was evident from SEM and BET analyses. FTIR and XRD analyses confirmed the enrichment of potassium in the form of oxides and carbonates after calcination. EDS analysis unveiled a drastic increase of potassium from 20.20 to 36.22 wt% upon calcination. These data, altogether supports the theoretical basis of potential of banana inflorescence calcine as a heterogeneous catalyst. Thereby, an attempt was made to bringforth CBIA as a catalyst for an efficient biodiesel production. Further, transesterification with a catalyst loading of 2 wt % and methanol to oil ratio of 9:1, for a reaction time of 75 min at 65 °C has yielded a FAME conversion of 98.62%.

EXPERIMENTAL SECTION

Materials and Chemicals

BI was collected from a Plantation field in Erode (Tamil Nadu, India). Analytical grade methanol (CH_3OH , 99.8%) was purchased from Hi Media Laboratories Pvt. Ltd., Mumbai. UCO was collected from a local restaurant near Erode (Tamil Nadu, India). It was filtered to remove the unwanted food particles and residues, followed by preheating at 105°C in hot air oven to remove the moisture content.

Catalyst Preparation

BI was washed with deionised water twice to remove the dust particles. In order to remove the moisture content, it was dried at 65°C in hot air oven for 24 h. It was then made into a fine powder using a mixer grinder and sieved using ASTM 18 mesh size sieve (≤ 0.425 mm). The banana inflorescence powder (BIP) was calcined at 700°C separately for 4 h in muffle furnace to concentrate the minerals in the form of ash. Muffle furnace can be manually programmed for gradual increase, hold on and gradual decrease of temperature at a rate of $5^\circ\text{C}/\text{min}$ to maintain the consistency and reliability. The calcined banana inflorescence ash (CBIA) catalyst was further stored in an air tight container.

Characterization of Catalyst

The surface morphology of uncalcined banana inflorescence peel (UBIP) and calcined banana inflorescence ash (CBIA) was explored by CARLZEISS SIGMA V model Scanning electron microscopy (SEM). The functional groups present in the UBIP and CBIA were detected by Fourier transform infrared spectroscopy (FTIR) using Thermo Scientific Ltd., spectrometer. X-ray diffraction (XRD) analysis was performed on both UBIP and CBIA to detect the crystalline components in the UBIP and CBIA using PANalytical X'Pert3 powder diffractometer.

The XRD Characterization was carried out using a Cu K α radiation, 40 Kv and 30 Ma with over a 2θ range of 2 to 100° with a step size of 2° per minute. Energy dispersive X-ray spectroscopy (EDS) was performed to ascertain the elemental composition of both UBIP and CBIA. The Brunauer-Emmett-Teller (BET) analysis was performed by Quantachrome NovaWin (version 11.05) in order to identify the surface area, pore volume and pore diameter of both UBIP and CBIA.

Transesterification

The schematic representation of the workflow is presented in Figure 6. Transesterification of UCO with methanol using CBIA catalyst was performed in a 250 ml three neck round bottomed flask placed in the water bath which was set at 65 °C. Middle neck was connected to a mechanical stirrer and one of the side necks was connected to a condenser and the other to temperature indicator. Transesterification reaction was performed at 65 °C using 9:1 methanol to oil molar ratio, 2 wt% catalyst loading for a reaction time of 75 min. After the completion of reaction, the excess methanol was separated by rotary evaporator. The catalyst was then filtered by No.1 Whatman filter paper and the filtrate was transferred to a separating funnel. The phases were allowed to separate overnight. The top layer, biodiesel was separated and stored in a separate air tight container for further analysis. The bottom layer, glycerol which is a byproduct in transesterification process was collected and stored separately.

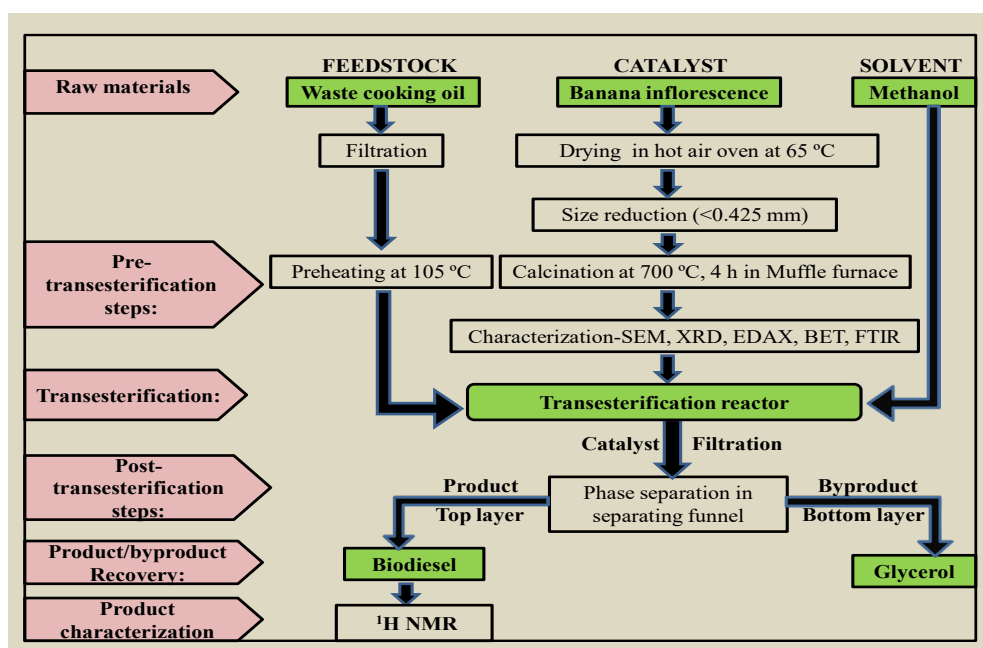


Figure 6. Schematic representation of workflow involved in biodiesel production

Biodiesel Characterization by NMR

The structural elucidation of fatty compounds present in the biodiesel was analysed by proton nuclear magnetic resonance (^1H NMR) using Bruker biospin. This aids in the quantitative determination of fatty acid methyl esters in the biodiesel in terms of % conversion.

The % conversion was calculated by the following formula (Eq.1) [33],

$$\% \text{ Conversion} = \frac{2A_{\text{ME}}}{3A_{\alpha\text{-CH}_2}} \times 100 \quad (1)$$

where,

% conversion = % FAME in Biodiesel,

A_{ME} = Area of peak at 3.7 ppm corresponding to methyl group of FAME,

$A_{\alpha\text{-CH}_2}$ = Area of peak corresponding to 2.3 ppm α -methylene group of FAME.

ACKNOWLEDGEMENTS

There are no acknowledgements.

REFERENCES

- 1 D. Huang; H. Zhou; L. Lin; *Energ Procedia.*, **2012**, *16*, 1874-1875.
- 2 G.S. Lakshmi; S. Bhawna; K. Amit; S.V.K. Shobha; *Energy statistics*, **2019**.
- 3 M.R. Nouni; P. Jha; R. Sarkhel; C. Banerjee; A.K.Tripathi; *J. Manna Fuel*; **2021**, *305*, 121583.
- 4 U.K. Pata; A.Kumar; *Water*; **2021**, *13(10)*, 1387.
- 5 A. Demirbas; *Energ. Policy*, **2007**, *35*, 4661-4670
- 6 S. Basumatary; B. Nath; P. Kalita; *J. Renew. Sust. Energ.*, **2018**, *10*, 043105.
- 7 P.A. Handayani; A. Abdullah; H. Hadiyanto; *Period. Polytech. Chem. Engi.*, **2019**, *63*, 406-413.
- 8 W. Shi; J.Li; B. He; F. Yan; Z. Cui; K. Wu; L. Lin; X. Qian; Y. Cheng; *Biores. Tech.*, **2013**, *139*, 316-322.
- 9 M. Kaur; A. Ali; *Renew. Ener.*, **2011**, *36*, 2866-2871.
- 10 E. Bet-Moushoul; K. Farhadi; Y. Mansourpanah; A.M. Nikbakht; R. Molaei; M. Forough; *Fuel.*, **2016**, *164*, 119-127.
- 11 A. Demirbas; *Biomass and Bioenerg.*, **2009**, *33*, 113-118.
- 12 A.N. Phan; T.M. Phan; *Fuel.*, **2008**, *87*, 3490-3496.
- 13 W. Asri; A. Budiman; *Phy. Procedia*, **2013**, *32*, 190-199.
- 14 S.Niju; K.M.M Sheriffa Begum; N. Anantharaman; *Env. Prog. Sust. Ener.*, **2015**,

- 34, 248-254.
- 15 S.Niju; K.M.S Begum; N.Anantharaman; *Int. J. Green Energ.*, **2016**, 13, 1314-1319.
- 16 S. Niju; R. Rabia; K.S Devi; M.N. Kumar; M. Balaji; *Waste and Biomass Valorization*, **2018**, 11, 793-806. <https://doi.org/10.1007/s12649-018-0520-6>
- 17 S. Niju; M. Kirthikaa; S. Arrthi; P. Dharani; S. Ramya; M. Balaji; *J. Inst. Eng. India*, **2019**, 101, 53-60.
- 18 I. Ambat; V. Srivastava; M. Sillanpa; *Renew. Sust. Ener. Rev.*, **2018**, 90, 356-369.
- 19 D.C. Deka; S. Basumatary; *Biomass and Bioener.*, **2011**, 35, 1797-1803.
- 20 A. Kumar; S. Prashant; *Cat let.*, **2014**, 144, 1344-1353.
- 21 M. Gohain; A. Devi; D. Deka; *Ind. Cro. Prod.*, **2017**, 109, 8-18.
- 22 E. Betiku; S.O. Ajala; *Ind. Cro. Prod.*, **2014**, 53, 314-322.
- 23 G. Pathak; D. Das; K. Rajkumari; L. Rokhum; *Green Chem.*, **2018**, 20, 2365-2373.
- 24 M. Balaji; S. Niju; *Ene. Conv. Manag.*, **2019**, 189, 118-131.
- 25 M. Balaji; S. Niju; *Ren. Ener.*, **2020**, 146, 2255-2269.
- 26 P.R. Sudha; Vidyadhar; S. Mamta; R. Rajesh; K. Pankaj; B. Hemanga; T. Bhawna; Ministry of Agriculture and Farmers' Welfare, New Delhi, India.
- 27 B.S. Padam; H.S. Tin; F.Y. Chye; M.I. Abdullah; *J. Food. Sci. Tech.*, **2014**, 51, 3527-3545.
- 28 B.F.Lau; K.W. Kong; K.H. Leong; J. Sun; X. He; Z. Wang; M.R. Mustafa; T.C. Ling; A. Ismail; *Trends in Food Science and Technology*, **2020**, 97, 14-28.
- 29 P.F. Zehla; D. Vijayalakshmi; V.C. Suvarna; S.Yatnatti; *Int. J. Curr. Micro. and App. Sci.*, **2018**, 7,1243-1250.
- 30 K.S. Kumar; D. Bhowmik; S. Duraivel; M. Umadevi; *J. Pharm and Phytochem.*, **2012**, 1, 51-63.
- 31 J.J Bhaskar; N.D. Chikunda; P.V.Salimath; *J. Agri. and Food Chem.*, **2011**, 60(1), 427-432.
- 32 A. Krishnan; V.R. Sinija; *Int. J. Agri. and Food Sci Tech.*, **2016**, 7, 13-22.
- 33 G. Gelbard; O. Bres; R.M. Vargas; F. Vielfaure; U.E. Schuchard; *J. Amer. Oil Chem. Soc.*, **1995**, 72, 1239-1245.
- 34 L. Gustavsson; M.L. Karlsson; *Adv. in Therm. Bio. Conv.*, **1993**, 1522-1532.
- 35 R.M. Silverstein; X.F. Webster; J.D. Kiemi; John Wiley & Sons., Inc., USA, **2005**.
- 36 Y. Inbar; Y. Chen; Y. Hadar; *Soil Sci.*, **1991**, 152, 272-282.
- 37 I.M. Mendonca; Paes, A.R.L. Orlando; Maia; J.S. Paulo; M.P. Souza; C. Silva; *Renew. Ene.*, **2019**, 130, 103-110.
- 38 F.A. Miller; C.H. Wilkins; *Anal. Chem.*, **1952**, 24(8), 1253-1294.
- 39 E. Betiku; A.M. Akintunde; T.V. Ojum; *Energy*, **2016**, 103, 797-806.
- 40 D. Shindo; T. Oikawa; *Anal. Elec. Micro. for Mat. Sci.*, **2002**, 81-102.
- 41 D. Fancello; J. Scalco; D. Medas; E. Rodeghero; A. Martucci; C. Meneghini; G.D.Giudici; *Int. J. Env. Pub. Hea.*, **2019**, 16(11), <https://doi.org/10.3390/ijerph16111976>
- 42 A.D. Frenc; *Cellulose*, **2014**, 21, 885-896.

- 43 J. Gong; J. Li; J. Xu; *RSC Advances*, **2017**, 7, 33486-33493.
- 44 S. Kumar; R. Gupta; Y.Y. Lee; R.B. Gupta; *Biores. Tech.*, **2010**, 101, 1337-1347.
- 45 M. Sharm; A. Ali; S.K. Puri; D.K. Tuli; *Biomass and Bioenerg.*, **2012**, 41, 94-106.
- 46 V.M. Mello; F.C.C. Oliveira; W.G. Fraga; J.S. Claudia; A.Z. Paulo; *Mag. Res. Chem.*, **2008**, 46, 1051-1054.
- 47 F. Faraguna; M. Racar; Z. Glasovac; A. Jukic; *Energ. and Fuels*, **2017**, 31, 3943-3948.
- 48 J.K. Satyarthi; D. Srinivas; P. Ratnasamy; *Energ. and Fuels*, **2009**, 23, 2273-2277.
- 49 B. Nieva-Echevarría; E. Goicoechea; M.J.G Manzanos; *Food Res. Int.*, **2014**, 66, 379-387.
- 50 Y. Zhou; M. Chen; X. Dong; D. Yang; *Molecules*, **2024**, 29(17), <https://doi.org/10.3390/molecules29174113>

THE EFFECT OF SYNTHESIS PROCESS PARAMETERS ON THE PHYSICO-CHEMICAL PROPERTIES AND PHOTOCATALYTIC ACTIVITY OF PRISTINE AND ZrO₂-DOPED TiO₂ CATALYSTS

Marija VASIĆ JOVEV^{a,*} , Radomir LJUPKOVIĆ^a ,
Katarina STEPIĆ^a , Marjan RANDELOVIĆ^a ,
Miloš MARINKOVIĆ^b , Aleksandra ZARUBICA^{a,*} 

ABSTRACT. In this study, TiO₂-based catalysts were synthesized using a modified sol-gel method. The catalysts were prepared at two different pH values (10 and 13) and were subsequently doped with zirconia to improve their photocatalytic performance. The physico-chemical properties of the catalysts, including structural, textural, morphological, and thermal properties, were studied using XRD, BET, SEM, and TG/DTA methods, respectively. The photocatalytic activity of the synthesized catalysts was tested in the degradation/decolorization reaction of methylene blue dye. The results indicated that the synthesis parameters and zirconia doping had a significant impact on the catalysts' physico-chemical characteristics and, therefore, their activity. It can be pointed out that catalysts with improved properties and enhanced photocatalytic activity can be obtained by carefully selecting and optimizing synthesis conditions, as well as by modifying or doping them with a suitable dopant.

Keywords: TiO₂, ZrO₂-doping, Photocatalysis

INTRODUCTION

One of the major challenges confronting modern society and a significant issue for researchers is water pollution [1]. Organic pollutants, such as dyes commonly used in industry, can lead to severe environmental problems [1, 2, 3].

^a Department of Chemistry, Faculty of Science and Mathematics, University of Niš, Serbia

^b Institute of General and Physical Chemistry, University of Belgrade, Belgrade, Serbia

* Corresponding authors: marija.vasic@pmf.edu.rs, marijavasic84@gmail.com; zarubica2000@yahoo.com



Many of these pollutants are toxic and carcinogenic [3, 4]. They can reduce sunlight penetration in water, disrupt photosynthesis [1, 4], and harm aquatic life and marine organisms [1]. Therefore, it is crucial to remove these pollutants from wastewater before discharging it into the environment [1, 2, 3]. Organic dyes are commonly used in various industries, including textiles, paper, printing, and paint [1, 2], with methylene blue (MB) dye being frequently studied in research [1, 2, 3]. Over the years, numerous methods and techniques have been studied to remove organic pollutants from water and wastewater [3, 4].

One often-tested method is heterogeneous catalysis, with TiO₂-based materials being extensively researched. TiO₂ is a semiconductor that generates electrons and electron holes in its conduction and valence bands, respectively, when exposed to UV light [2]. Despite its numerous advantages and exceptional photocatalytic properties [2], TiO₂ has certain limitations. Due to its wide band gap, TiO₂ can only be activated by UV radiation and has a rapid recombination of electron charge carriers [2]. To overcome these limitations, numerous methods and techniques have been studied, including doping or modifying with different metals such as noble metals (Ag, Au, Pt, Pd, etc.) [4-8], alkaline-earth metals (such as Mg) [9], or transition metals (Fe, Cu, Mo, W, Zr, etc.) [1, 10-14].

Moreover, various process parameters during catalyst synthesis (such as the pH of the preparation solution, the applied calcination temperature, etc.) can significantly influence the catalyst's structural, textural, morphological, and other properties [10, 15-19]. These parameters can be adjusted to design materials with preferable physico-chemical properties, thus influencing their photocatalytic activity.

In this study, two different TiO₂-based catalysts were prepared using the sol-gel method, with two pH values (10 and 13) adjusted during the preparation process as parameters that can affect the physico-chemical properties and photocatalytic activity of the TiO₂-based samples. The resulting catalysts were subsequently modified/doped with zirconia as a dopant [10]. Zirconium was selected as a dopant because its ionic radius (Zr⁴⁺) is similar to the ionic radius of Ti⁴⁺. This similarity suggests the potential for the substitution and/or deformation of Ti with Zr in the crystal lattice of TiO₂. Additionally, the formation of crystal defects could occur, promoting better and prolonged separation of charge carriers (electrons and holes) and enhancing photocatalytic efficiency [10, 20-22].

In this study, we investigated the physico-chemical characteristics, crystal structure, morphology, textural, and thermal properties of the prepared catalysts using various techniques. Additionally, we examined the photocatalytic activity of all synthesized catalysts in the photocatalytic reaction of methylene blue dye decolorization/degradation under relatively mild reaction conditions (low-energy UV irradiation and the original pH value of the model solution).

The results presented in this paper indicate that different process parameters during material synthesis, as well as the doping with the selected dopant, significantly influenced the physico-chemical characteristics and photocatalytic activity of the prepared catalysts.

As previously mentioned, this study employed sol-gel and wet impregnation methods to synthesize pristine TiO₂ and zirconia-doped TiO₂-based catalysts with optimized physico-chemical properties. To the best of our knowledge, no prior research has addressed the identical synthesis and modification methods for preparing pristine and zirconia-doped TiO₂-based catalysts using the same mass ratio, synthesis conditions, and precursors, while specifically focusing on the influence of the same synthesis process parameters, such as varying selected pH levels, on the properties and activity of the catalysts. Additionally, this study investigates the decolorization of MB dye under specific, relatively mild (low-energy) conditions using the prepared catalysts.

RESULTS AND DISCUSSION

Structural properties

The structural properties of the prepared TiO₂-based and ZrO₂-doped TiO₂ catalysts are shown in Figure 1 [10].

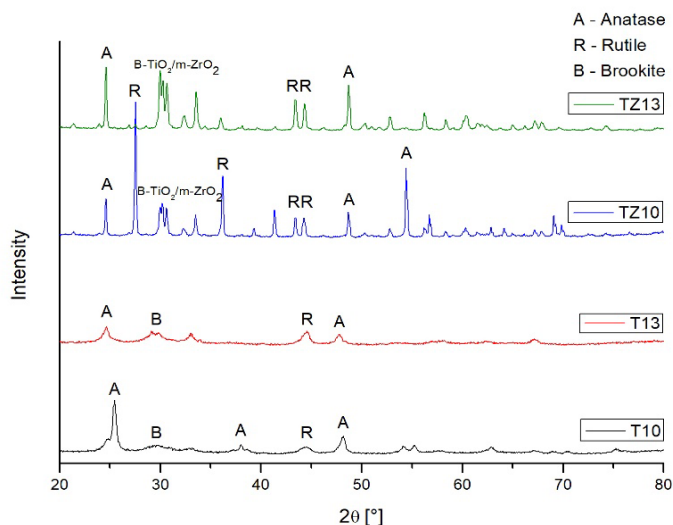


Figure 1. XRD patterns of: T10, T13, TZ10, and TZ13 catalysts (A - Anatase, B - Brookite, R - Rutile)

The results presented in Figure 1 indicate that the T10 catalyst is predominantly characterized by an anatase (A) crystalline phase, with the highest intensity peak at around 25.5° (JCPDS Card No. 21-1272) [10, 23, 24]. Additionally, the initial formation of the rutile (R) crystalline phases has been detected (JCPDS 21-1276) [10, 24, 25], (and/or brookite (B)), indicating that the transformation from the anatase to rutile phase began at the applied calcination temperature of 550°C [10].

Sample T13, synthesized at pH 13 and calcined at the same temperature, has a smaller proportion/volume of the anatase crystal phase compared to sample T10 (Figure 1). However, sample T13 shows an increased volume of the rutile crystal phase and a noticeable presence of the brookite crystal phase, which is present in a much smaller amount in sample T10. Additionally, the increase in pH from 10 to 13 resulted in a decrease in crystallite grain size. Namely, the estimated anatase crystal grain size for the T10 sample, calculated by Scherrer's equation, was approximately 20 nm, while the grain size for the T13 sample was around 15 nm [10]. Furthermore, sample T13 exhibited poorly defined low-intensity peaks, while sample T10 is characterized by well-defined intense peaks, indicating that the T10 catalyst has a more favorable crystal structure. Overall, the variation in pH during the synthesis process significantly influenced the structural properties of the prepared catalysts.

After doping with zirconia and calcination at 800°C , the samples are characterized by sharper, stronger, and better-defined diffraction peaks. This indicates an increase in the crystallinity degree and an improved crystal structure. Furthermore, doping has resulted in increased crystallite sizes for both doped samples, measuring around 40 nm for the anatase crystal phase, compared to the pristine TiO_2 samples [10].

The sample TZ10 is characterized by a dominant crystalline phase of rutile (approximately 60%). This is expected at higher calcination temperatures, indicating that the phase transformation from anatase to rutile has occurred. In contrast, the doped TZ13 catalyst shows an increased presence of the anatase phase, which may be due to the presence of the dopant that can inhibit the anatase to rutile phase transformation. Additionally, the diffraction peak at 30° Bragg's angle is much more noticeable in TZ13 than in TZ10. This peak is believed to correspond to the brookite titania and/or monoclinic zirconia phase [10].

Textural properties

Nitrogen adsorption-desorption isotherm and pore size distribution curve for the modified TZ13 catalyst are presented in Figure 2 [10].

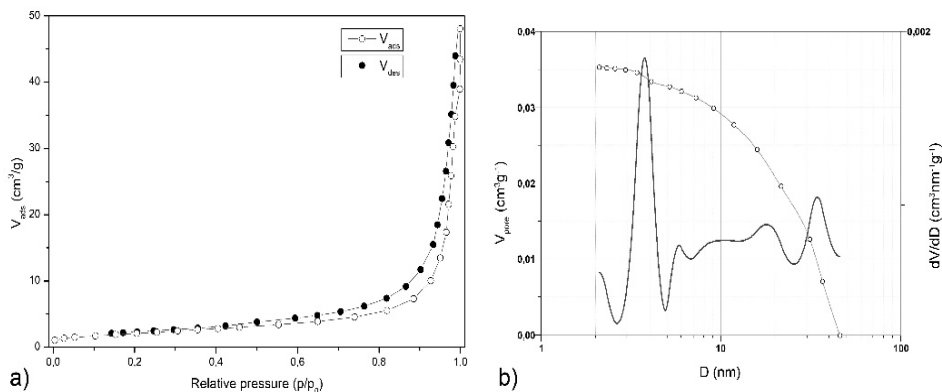


Figure 2. a) Nitrogen adsorption-desorption isotherm and b) pore size distribution curve for modified TZ13 catalyst [10]

Table 1. Textural properties of TZ13 catalyst [10]

Sample	S _{bet} (m ² /g)	Median pore size (nm)	Pore volume (cm ³ /g)
TZ13	7.8	29.0	0.044

The nitrogen adsorption/desorption isotherm for catalyst TZ13, shown in Figure 2 a) [10], indicates the presence of mesopores. This sample is characterized by a type IV sorption isotherm with an H3 hysteresis type [10], according to the IUPAC classification of isotherms and hysteresis loops [26, 27]. The type of hysteresis observed suggests that the catalyst contains crack-shaped pores. Additionally, the relatively small specific surface area of the catalyst TZ13 (Table 1) aligns with the characteristics of the adsorption isotherms and the type of hysteresis loop. This may further affect the activity of the catalyst in photocatalytic reactions [10].

The results of the pore size distribution, as shown in Figure 2 b) [10], indicate that the catalyst TZ13 shows a non-standard bimodal, i.e., multimodal distribution of pores ranging between 3 and 40 nm. This confirms that TZ13 is mostly a mesoporous material. Most pores are near the micro-mesopore boundary (3-4 nm). Additionally, there is a noticeable presence of mesopores with a medium pore diameter of approximately 35 nm, although they are present in a somewhat smaller quantity/amount [10].

Morphological properties

The results of the morphological properties of the prepared TiO₂-based and ZrO₂-doped TiO₂ catalysts are shown in Figure 3 [10].

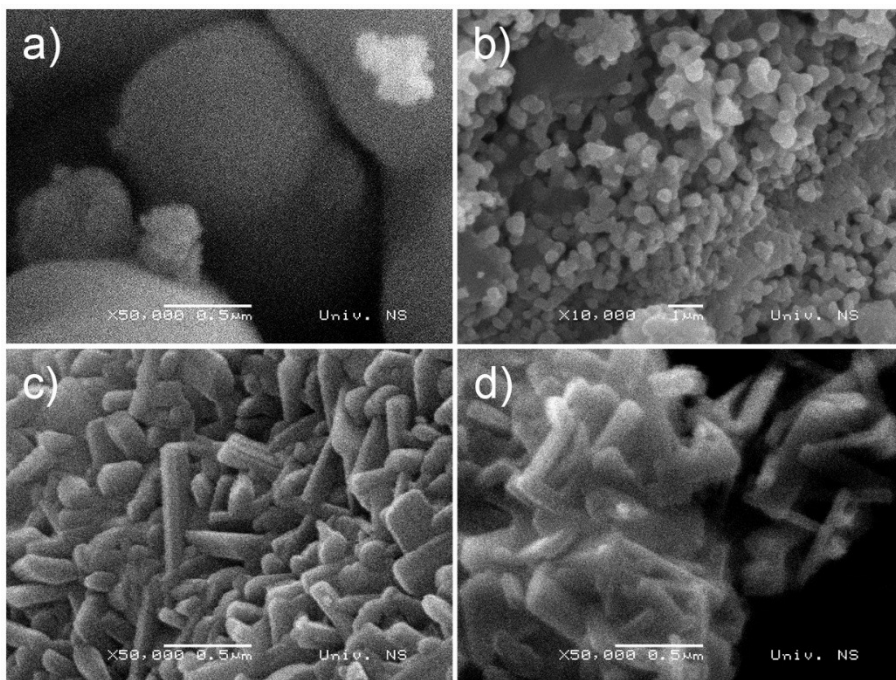


Figure 3. SEM micrographs of a) T10 (at x 50000 magnification), b) T13 (at x 10000 magnification), c) TZ10 (at x 50000 magnification), and d) TZ13 (at x 50000 magnification) [10]

The morphology of the T10 catalyst is characterized by agglomerated secondary particles that are around 100 nm in size and spherical in shape, along with inter-agglomerate pores. Some primary particles can also be observed, either in spherical or irregular shapes [10].

The high pH value of the medium used during the synthesis of catalyst T13 resulted in a significant change in the system's porosity and morphology. Namely, catalyst T13 displayed the formation of agglomerates or aggregates larger than 100 nm in size, and a decreased porosity, indicating a less favorable morphology for the material [10].

Based on the SEM results presented in Figures 3 c) and d), the doping process and the application of relatively high temperatures led to a significant change in the surface morphology of the doped catalysts, TZ10 and TZ13, compared to the pristine TiO_2 -based catalysts. It can be noted that agglomerated secondary particles were formed in both doped samples due to the sintering process at the elevated calcination temperature. These agglomerates consist of irregular or rod-shaped primary particles that are larger than those in the pristine TiO_2 -based catalysts, which aligns with the XRD results [10].

Thermal properties

The thermal properties of the prepared TiO₂-based and ZrO₂-doped TiO₂ catalysts are presented in Figure 4, which includes both DTA and TG analyses [10].

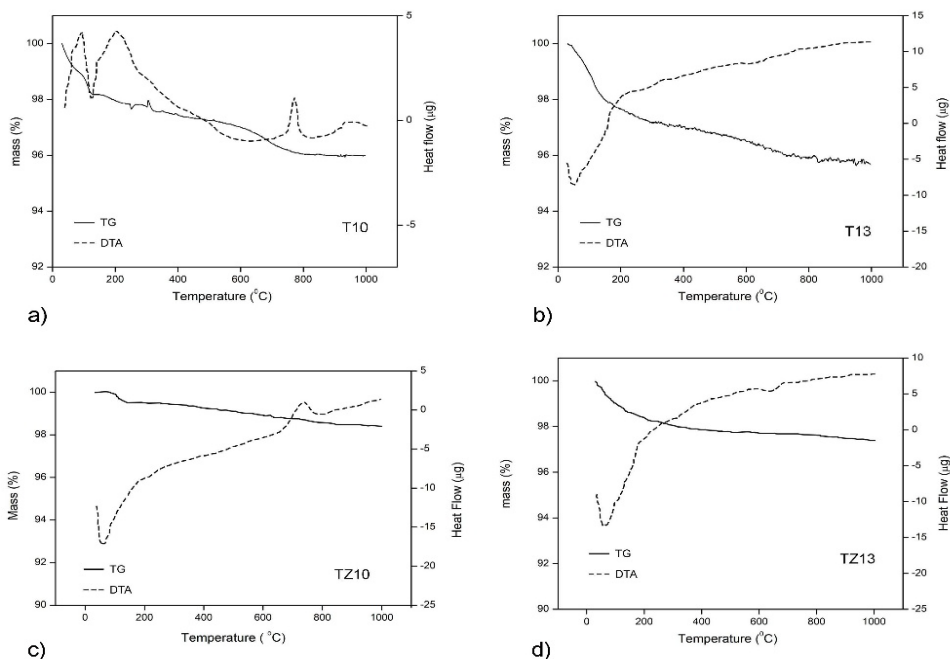


Figure 4. Thermal analysis of: a) T10, b) T13, c) TZ10, and d) TZ13 catalysts

The DTA curve for the T10 sample (Figure 4 a)) displays an endothermic effect occurring at around 120 °C. This effect correlates with a mass loss of up to 4%, as confirmed on the TG curve. This mass/weight reduction is ascribed to the removal of surface physisorbed water molecules or the evaporation of residual organic solvents during the drying process of catalyst preparation. Additionally, an exothermic peak observed at a temperature of 750°C indicates that the phase transformation from anatase to rutile shift towards higher temperatures, which aligns with the obtained results for structural properties. The DTA results for the T13 sample also showed an endothermic effect at approximately 100°C, followed by a mass loss of 4-5%, as shown in the TG curve (Figure 4 b)) [10].

Based on the results shown in Figures 4 c) and d), DTA curves indicate that both doped samples, TZ10 and TZ13, show an endothermic peak at approximately 100°C. This is followed by a mass loss of around 2-3%, as observed

in the TG curves. This peak is attributed to dehydration, the removal of physisorbed water, and/or the evaporation of solvent and other remaining organic compounds present during the gel formation process in the synthesis of the catalysts. Additionally, the DTA curve for TZ10 shows an exothermic peak at approximately 750°C, which is most probably due to the presence and removal of constitutional water from residual hydroxide and/or phase transformation.

Photocatalytic activity

The photocatalytic activity of all the prepared catalysts in the degradation/ decolorization of methylene blue dye is shown in Figure 5. It is important to note that the use of different pH values during the synthesis process, along with the addition of a dopant, significantly influences the physico-chemical properties of the catalysts, which subsequently affects their photocatalytic activity.

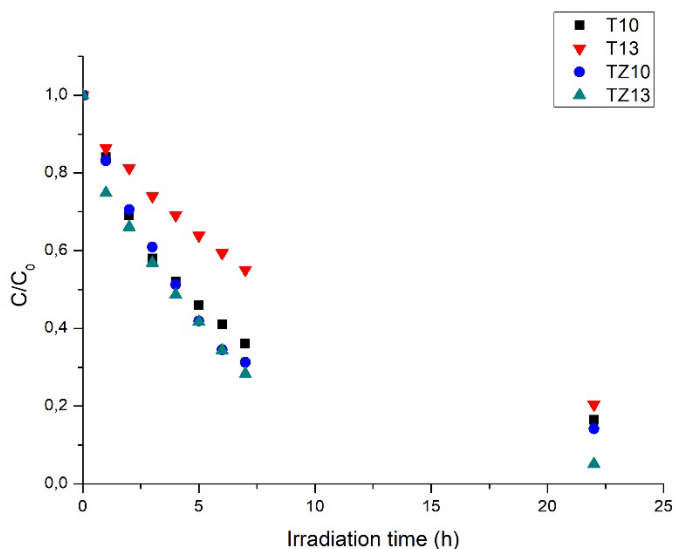


Figure 5. Photocatalytic degradation/decolorization of methylene blue dye with the use of T10, T13, TZ10, and TZ13 catalysts

When examining the pristine TiO₂-based samples, the T10 sample showed good activity in the photocatalytic reaction. Notably, the T10 sample exhibited a higher degradation rate than the T13 sample. This can be attributed to the more favorable structural (including better crystallinity, a dominant anatase crystalline phase, and an appropriate crystal grain size) and morphological properties of the T10 catalyst compared to the T13 sample.

Additionally, it is notable that doped sample TZ13 exhibited the highest photocatalytic activity among all the prepared samples. Despite having a relatively small specific surface area, this sample has a favorable mesoporosity, beneficial structural properties, and suitable morphology. As discussed earlier, sample TZ13 is characterized by good crystallinity and a dominant presence of the highly active anatase crystal phase, which is important for photocatalytic activity.

CONCLUSIONS

The modified sol-gel method was selected as a relatively simple method for preparing pristine and ZrO₂-doped TiO₂ catalysts. This study focuses on the influence of the synthesis process parameters (the use of two different pH values) on the physico-chemical properties and photocatalytic activity of the pristine and zirconia-doped TiO₂-based catalysts. The degradation/decolorization of methylene blue, carried out under relatively mild experimental conditions, was chosen to test the activity of all prepared samples. The results showed that both the pH during synthesis and the use of zirconia as a dopant significantly influenced the physico-chemical properties of the catalysts. As a result, both doped samples showed higher photocatalytic activity in the methylene blue degradation reaction compared to the pristine TiO₂ catalysts.

The TZ13 catalyst demonstrated the highest rate of degradation/decolorization of methylene blue dye. This improved performance can be attributed to the dominant presence of the highly active anatase phase, along with an improved crystalline structure and the presence of mixed crystal phases (anatase, rutile, brookite titania, and/or monoclinic zirconia). Furthermore, the catalyst is characterized by beneficial mesoporosity, featuring bimodal or multimodal pore distribution and an appropriate surface morphology.

Overall, the findings in this paper highlight the importance of optimizing synthesis conditions and investigating suitable dopants to obtain efficient photocatalytic materials for future research focused on removing organic pollutants from water.

EXPERIMENTAL SECTION

In this study, four different catalysts were prepared: two catalysts based on pristine TiO₂ and two based on ZrO₂-doped TiO₂ catalysts. Firstly, TiO₂-based catalysts were synthesized using a modified sol-gel method, with Titanium isopropoxide as a precursor and a mixture of water and 2-Propanol for precipitation

purposes. During the synthesis process, the pH value was varied and adjusted to 10 and/or 13 to obtain the two different catalysts. After precipitation, the samples were filtered and rinsed with deionized water and then with an alcohol/water mixture. Both TiO₂ samples were then dried at 105-110 °C for three hours. After drying, they were annealed at a temperature of 550 °C for three hours, with a heating rate of 10 °C per minute [10]. Samples prepared in this way were denoted as TX, where T stands for TiO₂ and X stands for the pH value used during the synthesis process (T10 and T13).

Subsequently, the prepared pristine TiO₂-based samples, T10 and T13, were modified/doped using the wet impregnation method. Both samples were doped using the same amount of ZrOCl₂·8H₂O to obtain a mass ratio of 2.5 mass.% of zirconia. After doping, both doped samples were dried at 105 °C for three hours and then calcined at a temperature of 800 °C for three hours, with a heating rate of 10 °C per minute [10]. Catalyst samples obtained in this way were denoted as TZX (TZ10 and TZ13), where T stands for TiO₂, Z stands for dopant ZrO₂, and X stands for used pH value used during the synthesis procedure, 10 or 13.

To determine the physico-chemical properties of the prepared catalysts, structural (XRD), textural (BET), morphological (SEM), and thermal (TG/DTA) analyses were performed [10]. Structural analysis (XRD) was performed on a Philips APD-1700 diffractometer in the 2θ range of 20-80° under the CuKα radiation source. The operation mode was set to 40 kV and 55 mA [10].

The average crystallite size (d) was calculated using the Scherrer equation (1) where k is the Scherrer constant, λ is the X-ray wavelength, β represents the peak at half maximum, and θ denotes the Bragg angle [10, 28]:

$$d = \frac{k\lambda}{\beta \cos\theta} \quad (1)$$

The weight percentages of anatase and rutile were determined using the following equation by Spurr and Myers [29, 30]:

$$W_A = \frac{1}{1 + 1.265 \frac{I_R}{I_A}} \quad (2)$$

where I_A and I_R are the intensities of the most intense peaks for anatase [101] and rutile [110] crystal phases, respectively.

Textural (BET) measurements were conducted using a Micromeritics ASAP 2010, based on the adsorption and desorption of liquid nitrogen, with helium as the carrier gas. Before measurements, all catalyst samples were degassed [10].

The morphology of the prepared catalysts was analyzed using a SEM JEOL JSM-6460LV scanning electron microscope (SEM) [10].

Thermal properties were determined using a Derivatograph MOM, M-1000 under static conditions, with temperatures ranging from 20 to 1000 °C. A heating rate of 10 °C/min and a cooling rate of 20 °C/min were applied [10].

The activity of the prepared TiO₂ and ZrO₂-doped TiO₂ catalysts was tested for the photocatalytic degradation/decolorization of methylene blue (MB) dye solution. To separate the adsorption process from photocatalysis, the prepared catalysts were placed in the dark with continuous stirring in the MB test solution for 24 hours. After the adsorption process was completed and the adsorption/desorption equilibrium was established, the photocatalytic reaction was carried out under UV illumination (using a UV lamp with a maximum emission at the wavelength 366 nm, 16W). Changes in the concentration of MB during both the adsorption and photocatalytic tests were monitored using a UV/VIS spectrophotometer.

ACKNOWLEDGMENTS

The work was supported by the Ministry of Science, Technological Development and Innovation of the Republic of Serbia (Contract numbers: 451-03-136/2025-03/200124, 451-03-137/2025-03/200124 and 451-03-136/2025-03/200051) and by the Ministry of Education, Science and Technological Development of the Republic of Serbia (Project number: ON 172061).

REFERENCES

1. H. Liyanaarachchi; C. Thambiliyagodage; C. Liyanaarachchi; U. Samarakoon; *Arab. J. Chem.*, **2023**, *16*, 104749.
2. L. Liu; Y. Liu; X. Wang; N. Hu; Y. Li; C. Li; Y. Meng; Y. An; *Appl. Surf. Sci.*, **2021**, *561*, 149969.
3. E. Basturk; M. Işık; M. Karatas; *Desalin. Water Treat.*, **2019**, *143*, 306-313.
4. C. H. Nguyen; C.-C. Fu; R.-S. Juang; *J. Clean. Prod.*, **2018**, *202*, 413-427.
5. D. Georgescu; Z. Pap; M. Baia; C.I. Fort; V. Danciu; G. Melinte; L. Baia; S. Simon; *Studia Universitatis Babeş-Bolyai Chemia*, **2011**, *LVI*, *3*, 51-58.
6. A. Peter; M. Baia; F. Toderas; M. Lazar; L.B. Tudoran; V. Danciu; *Studia Universitatis Babeş-Bolyai Chemia*, **2009**, *LIV*, *3*, 161-171.
7. R. Kumar; J. Rashid; M.A. Barakat; *Colloid. Interfac. Sci.*, **2015**, *5*, 1-4.
8. M. Khairy; E.M. Kamar; M.A. Mousa; *Mater. Sci. Eng. B-Adv.*, **2022**, *286*, 116023.
9. M. Giahi; D. Pathania; S. Agarwal; G.A.M. Ali; K.F. Chong; V.K. Gupta; *Studia Universitatis Babeş-Bolyai Chemia*, **2019**, *LXIV*, *1*, 7-18.

10. M. Vasić; *Optimisation and photocatalytic application of nanostructured TiO₂*, Doctoral Dissertation, Faculty of Sciences and Mathematics, University of Niš, Niš, **2017**.
11. C. Bathula; A. S Nissimagoudar; S. Kumar; A. Jana; S. Sekar; S. Lee; H.-S. Kim; *Inorg. Chem. Commun.*, **2024**, *164*, 112442.
12. A. Mishra; V. Verma; A. Khan; D. Kumar; T. S. Khan; V. Amoli; A. K. Sinha; *J. Environ. Chem. Eng.*, **2023**, *11*, 110319.
13. S. Bibi; S. S. Shah; F. Muhammad; M. Siddiq; L. Kiran; S. A. Aldossari; M. S. S. Mushab; S. Sarwar; *Chemosphere*, **2023**, *339*, 139583.
14. A. Khlyustova; N. Sirotkin; T. Kusova; A. Kraev; V. Titov; A. Agafonov; *Mater. Adv.*, **2020**, *1*, 1193.
15. M. Yalcin; *J. Cryst. Growth*, **2022**, *585*, 126603.
16. R. Vasanthapriya; N. Neelakandeswari; K. Uthayarania; M. Chitra; *Dig. J. Nanomater. Bios.*, **2023**, *18*, 2, 767-771, <https://doi.org/10.15251/DJNB.2023.182.767>
17. A. Molea; V. Popescu; N. A. Rowson; A. M. Dinescu; *Powder Technol.*, **2014**, *253*, 22-28.
18. M. Lal; P. Sharma; C. Ram; *Optik*, **2021**, *241*, 166934.
19. N.C. Horti; M.D. Kamatagi; N.R. Patil; S.K. Nataraj; M.S. Sannaikar; S.R. Inamdar; *Optik*, **2019**, *194*, 163070.
20. J. Lukáč; M. Klementová; P. Bezdička; S. Bakardjieva; J. Šubrt; L. Szatmáry; Z. Bastl; J. Jirkovský; *Appl. Catal. B-Environ.*, **2007**, *74*, 83-91.
21. D. Kapusuz; J. Park; A. Ozturk; *J. Phys. Chem. Solids*, **2013**, *74*, 1026-1031.
22. M. Vasić; M. Randjelović; M. Momčilović; B. Matović; A. Zarubica; *Process. Appl. Ceram.*, **2016**, *10*, 189-198.
23. S.S. Arbuj; R.R. Hawaldar; U.P. Mulik; B.N. Wani; D.P. Amalnerkar; S.B. Waghmode; *Materials Science and Engineering B*, **2010**, *168*, 90-94.
24. W. Li; R. Liang; A. Hu; Z. Huang; Y.N. Zhou; *RSC Adv.*, **2014**, *4*, 36959.
25. R. Gao; Z. Jiao; Y. Wang; L. Xu; S. Xia; H. Zhang; *Chemical Engineering Journal*, **2016**, *304*, 156-164.
26. K. Sing; D. Everett; R. Haul; L. Moscou; R. Pierotti; J. Rouquerol; T. Siemineiewska; *Pure Appl. Chem.*, **1985**, *57*, 603-619.
27. M. Thommes; K. Kaneko; A. V. Neimark; J. P. Olivier; F. Rodriguez-Reinoso; J. Rouquerol; K. S. W. Sing; *Pure Appl. Chem.*, **2015**, *87*, 1051-1069.
28. S.A. Hassanzadeh-Tabrizi; *J. Alloy. Compd.*, **2023**, *968*, 171914.
29. R. Spurr; H. Myers; *Analytical Chemistry*, **1957**, *29*, 760-762.
30. D. Mardare; A. Manole; A. Yildiz; D. Luca; *Chem. Eng. Comm.*, **2011**, *198*, 530-540.

EXPERIMENTAL STUDY ON THE CRYSTALLIZATION FORMATION MECHANISM OF BLIND PIPE IN WUJIAYUAN TUNNEL

Haiting WANG^{a,c}, Haifeng XU^a, Pengfei HUO^a,
Zhuangzhuang WANG^a, Jiqiang YUE^b, Zheng WANG^b,
Di ZHANG^c, Tianzhi YU^{c,*}

ABSTRACT. In the construction of high-speed railway tunnels, when passing through different geological areas, the groundwater flowing through the drainage blind pipe is easy to produce crystals to block the drainage pipe. These crystal blockages are mainly produced by the dissolution of the concrete material of the initial support of the tunnel, which leads to the accumulation of precipitates in the drainage system and affects the tunnel structure safety. Based on the study of crystals and water samples in the blind pipe of Wujiayuan Tunnel, this paper discusses the relationship between the crystals in the blind pipe and the ion concentration, pH value, carbon dioxide concentration and partial pressure and temperature in groundwater. Combined with the environmental water chemical equilibrium software Visual MINTEQ 3.1, the influence of the above conditions on the formation of crystallization was simulated and the formation mechanism of Wujiayuan tunnel blind tube crystallization was proposed.

Keywords: *tunnel blind pipe, crystals, water samples, Visual MINTEQ 3.1, precipitation formation mechanism*

INTRODUCTION

With the rapid development of high-speed railroad projects in China, tunnel blind crystallization has become a major challenge for Chinese engineers

^a The 6th Engineering Co., Ltd. of China Railway, 3th Bureau Group, 710000, China.

^b Xi'an Chengdu Railway Passenger Dedicated Line Shaanxi Co., Ltd, Xi'an, 710000, China.

^c Lanzhou Jiaotong University, Lanzhou 730070, China.

* Corresponding author: yutzh@mail.lzjtu.cn



during tunnel construction. The Wujiayuan Tunnel is located in the northern part of China's Shanxi Province, where the terrain is complex and varied. The local water is rich in calcium ions (Ca^{2+}), which tend to crystallize and deposit on the tunnel walls. This deposition usually leads to blockage and jeopardizes the load-bearing capacity of the tunnel; therefore, it is crucial to study the formation mechanism of tunnel crystallites.^[1-4]

The crystallization process of groundwater is a series of complex chemical reactions. The main components of the crystalline substances in the tunnel groundwater are insoluble carbonates and calcium salts mainly composed of calcium carbonate. The key to solving the problem of calcium carbonate crystallization blocking the pipeline is to clarify the mechanism of calcium blocking. Studies have shown that calcium carbonate crystals are solid substances arranged continuously in space according to a certain regularity, and the crystallization process is carried out in stages, and the crystallization morphology is different at different stages^[5]. Bobet et al.,^[6] investigated and quantified the crystallization blockage in the drainage system of Nanla Tunnel, revealed its formation mechanism, and explored the effectiveness and applicability of coatings in preventing crystallization blockage. Jiang et al.^[7] investigated the crystallization of the Nanla Tunnel drainage system, the crystalline clogging in the drainage system, of Nanla tunnel and found that the crystalline clogging was mainly composed of calcium carbonate and a small amount of sediment and cement hydration products, and the formation of crystals was a result of the corrosive effect of the groundwater on the shotcrete. Yan et al^[8] investigated the mixing of calcium carbonate and calcium sulphate in the scaling precipitation, which was frequently observed in the extracted water supply due to the treatment process. The results of co-precipitation were compared with the experimental results of single salt crystallization, and several parameters, such as conductivity, pH, crystal morphology and crystal shape, were carefully monitored to study the crystallization mechanism. Liu et al^[9] used mathematical modeling to synthesize and analyze the mechanism of flocking and anti-clogging of drainage pipes. Zhou et al^[1] measured the flow rate of a calcium carbonate crystal tunnel in a southwestern mountainous area. Numerical simulation was combined with finite element software (ANSYS Fluent) based on the actual flow results. The crystallization of calcium carbonate near the interface of the tunnel drain and the formation mechanism were analyzed. Feng et al^[10] investigated calcium ion deposition in the presence of different sources of PCC to reveal the influencing factors and mechanisms of CaCO_3 nucleation and crystal growth. Chen et al^[11] examined the crystals by using EDS, Scanning Electron Microscope (SEM), and XRD^[12-18] to analyze the elemental compositions, material composition and microstructure. Finally, a measure to remove crystals from tunnel drains using ultrasound was proposed.

Groundwater seepage through the initial support concrete is alkaline environment, which provides the basis for the formation of crystals, and CO_2 is dissolved in groundwater, which is easy to react with Ca^{2+} to form precipitates under alkaline environment. This paper analyzes the relationship between the crystals in the blind pipe and the ion concentration, pH value, CO_2 concentration and partial pressure and temperature in the groundwater, and summarizes and researches the formation mechanism of the crystals in the blind pipe by using Visual MINTEQ 3.1, which can be used to analyze the relationship between the crystals in the blind pipe and the ion concentration and partial pressure and temperature in the groundwater.

RESULTS AND DISCUSSION

Analysis of Ion Concentration in Water Seepage from the Wujiayuan Tunnel

The groundwater in the tunnel area exhibits a diverse array of ions, including Ca^{2+} , Mg^{2+} , Ba^{2+} , CO_3^{2-} , HCO_3^- , OH^- , and SO_4^{2-} . These ions significantly influence the crystallization processes within the tunnel's groundwater. Additionally, ions such as Cl^- and Na^+ play a role as well. The introduction of NaCl into carbonate solutions induces an ionic strength effect, resulting in an influx of Na^+ ions due to NaCl 's high solubility, the increase of ionic strength has an effect on the solubility of carbonate.

To investigate the ion concentrations in the seepage water from the Wujiayuan Tunnel, we collected samples from various locations: the outer layer of the exit shotcrete, the outer layer of shotcrete from Well 3, drainage water from Well 3, and water samples from different positions within the surrounding rock of the inclined Well 3, as well as leachate from the sprayed concrete. A total of eight samples were obtained. Additionally, we conducted ion concentration tests on the leachates from the construction materials used in the Wujiayuan Tunnel, such as cement and fly ash ^[11]. The specific data for the leachate from the shotcrete at the tunnel exit is illustrated in the figure below ^[12].

Through the analysis of the data presented, it is evident that two samples were taken from the leachate of the shotcrete outer layer at the exit of the Wujiayuan Tunnel. Additionally, one sample was collected from the drainage pipe of shotcrete at Shafts No.3, and one sample each from the surrounding rock water at Shaft No.3, tunnel exit surrounding rock water, and leachate from the shotcrete. The second sampling of the leachate from the shotcrete outer layer at the tunnel exit occurred post-application. The provided

data indicates that the Na^+ concentration remained relatively stable, while the Ca^{2+} concentration increased by approximately threefold. Furthermore, the Mg^{2+} content surged by 30 mins. The cause may be linked to water flowing along the outer perimeter of the tunnel after passing through the shotcrete, which leads to the leaching of significant amounts of Ca^{2+} and Mg^{2+} from the surface of the shotcrete. The concentrations of sodium ions in the leachate from the three batches of fly ash, the shotcrete leachate from Wujiayuan, and the surrounding rock water at the tunnel exit showed fluctuations between 2 to 10 times compared to other samples. Given that the sodium ion concentration in the three batches of fly ash leachate reached 159 mg/L, it is reasonable to deduce that the increase in sodium ion concentration in the shotcrete leachate and the surrounding rock water at the tunnel exit is associated with the fly ash used in the construction process.

Table 1. The water seepage and ion concentration of various sections of Wujiayuan Tunnel

Sample name	Ion content mg/L					
	Na^+	Ca^{2+}	Mg^{2+}	CO_3^{2-}	HCO_3^-	SO_4^{2-}
Water seepage through the concrete outer layer at the tunnel exit of the Wujiayuan tunnel	42.3	6.34	0.185	no detection	176.6	71.6
Two samples of the Wujiayuan tunnel	44.1	19	31.5	8.8	211.9	99.2
No. 3 inclined shaft blowout concrete outer drainage pipe leaching water	47.5	5.74	1.37	no detection	118.4	99.4
No. 3 Shakai Rock Water	54.6	15.3	19.8	6.8	214.3	69.5
Wujiayuan exit tunnel surrounding rock water	760	5.12	1.61	110.0	594.2	237
Three rounds of cement leaching water	71	409	0.484	no detection	140.6	1.62×10^3
Three rounds of fly ash leaching water	159	465	0.588	no detection	130.2	1.23×10^3
Wujiayuan shotcrete leaching water	183	28.5	0.682	3.2	65.8	509

The data from the table 1 indicates that the Ca^{2+} concentration in the first sampling was relatively low. In contrast, the concentrations of Ca^{2+} and Mg^{2+} in the second sampling exhibited a significant increase compared to the first. This difference may stem from the initial stage of groundwater seepage,

where the water had insufficient contact with the concrete, resulting in minimal transport of calcium and magnesium. As the duration of groundwater seepage increased, the interaction between groundwater and concrete intensified, leading to a greater release of cations.

In the leachate tests of cement and fly ash construction materials, significant levels of calcium ions were detected, with concentrations reaching 409 mg/L and 465 mg/L. However, the absence of CO_3^{2-} ions suggests that the primary source of anions in carbonate crystals relates to CO_2 . This observation confirms that groundwater flowing through tunnel surrounding rock layers leads to the formation of substantial crystalline structures upon discharge from blind pipes. Notably, the concentrations of HCO_3^- and SO_4^{2-} ions were higher than those of other ions, which likely explains why carbonate and sulfate dominated in the formed crystals.

Analyzing the first three sets of provided data reveals that sodium ion concentrations remained relatively constant. However, the leachates from the fly ash and pumped concrete, as well as the surrounding water at the tunnel exit, exhibited sodium ion concentrations that were 2 to 10 times higher than those of other samples. Given that the sodium ion concentration in the fly ash leachate reached 159 mg/L, and the sample sourced from the surrounding rock utilized fly ash that was sprayed during construction, it is reasonable to associate the elevated sodium ion concentrations in the sprayed concrete leachate and tunnel exit water with the presence of fly ash.

The primary cause of crystal formation in blind pipes stems from the significant interaction between abundant calcium ions in groundwater and construction materials like cement and fly ash, along with CO_2 from water and air. The accumulation of crystals within blind pipes poses a threat to tunnel lining structures and drainage systems. A prominent issue arising from this is crystallization, which obstructs the drainage systems, leading to drainage failure. This results in the lining structures experiencing elevated external water pressure, thereby jeopardizing the structural integrity of the tunnel. Consequently, this may lead to cracks and subsequent leaks, severely affecting the safe operation of the tunnel.

XRD analysis of crystallites in Wujiayuan tunnel

In order to further explore the chemical composition of the crystalline substance of the tunnel blind tube, water samples were collected at the tunnel construction site, and the crystalline substance of the blind tube was tested and analyzed by XRD (as shown in Figure 1~2). It can be seen from Figure 2(a) that the horizontal coordinate is the Angle formed between the direction of the reflected diffraction beam at the crystalline edge of Wujiayuan

Tunnel and the direction of the incident beam, and the vertical coordinate represents the crystallization peak intensity of Wujiayuan tunnel. The location of the main peak of tunnel crystallization is the same as that of JCPDS file 97-001-6710 in the crystal Structure and diffraction database. The X-ray diffraction spectra show different diffraction peaks, angular positions and relative intensity changes, indicating that the composition elements of the crystal materials are different. Based on equations (1) ~ (2), the mass fraction of each phase within the substance was calculated.

$$\frac{\omega_i}{\omega_j} = \frac{I_i K_{Al_2O_3}^i}{I_j K_{Al_2O_3}^j} \quad (1)$$

$$\omega_i + \omega_j = 1 \quad (2)$$

According to the XRD fitting curve shown in Figure 1, the maximum diffraction peak is located at $2\theta = 29.178^\circ$, and the crystal face index is (104) corresponding to the #86-2341 calcite standard card, whose content accounts for 82% of the crystallite mass ratio in Wujiayuan Tunnel. The maximum diffraction peak is located at $2\theta = 29.499^\circ$, the crystal surface index is (104) corresponding to the #89-1304 high magnesium calcite standard card, and its content accounts for 18% of the mass ratio of crystallites in Wujiayuan Tunnel. The standard XRD spectra of the two crystal types are shown in Figure 2(b).

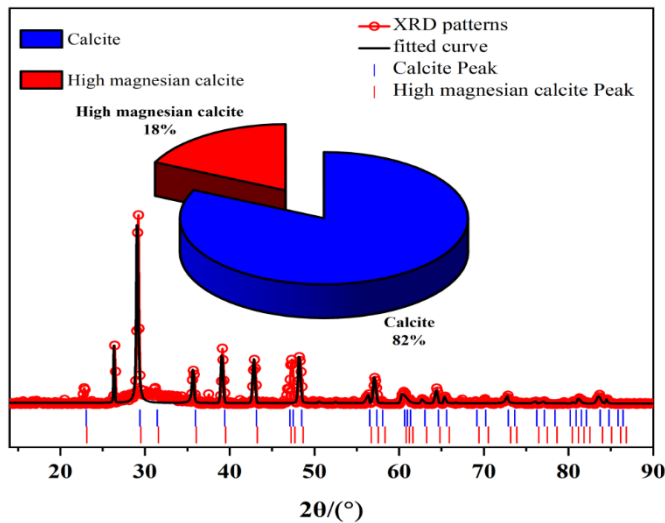


Figure 1. XRD pattern fitting analysis

EXPERIMENTAL STUDY ON THE CRYSTALLIZATION FORMATION MECHANISM
OF BLIND PIPE IN WUJIAYUAN TUNNEL

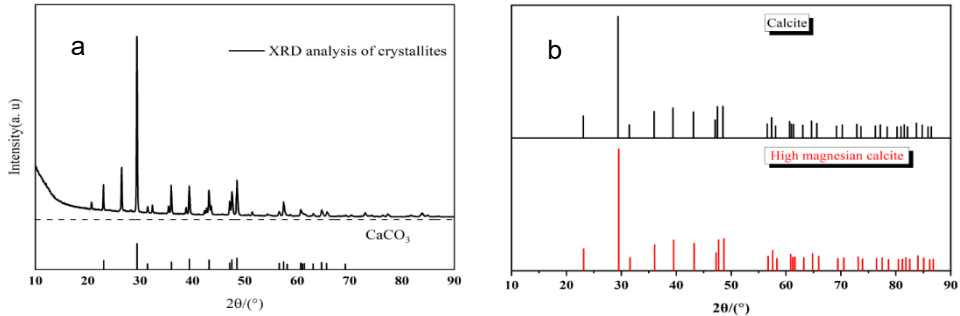


Figure 2. Tunnel XRD pattern and standard XRD diffraction spectrum of each crystal type

Calculation and simulation of the effect of pH on precipitation saturation index

In order to clarify the cause and mechanism of crystal formation in tunnel drainage system, the influence factors of crystal formation and precipitation equilibrium process in tunnel were simulated by simulation software Visua I MINTEQ (Figure 3). The mathematical expression of SI is:

$$SI = \lg(IAP/K_{sp}) \quad (3)$$

In the formula, IAP (ion activity product) is the product of ion activity in solution, that is, ion product; K_{sp} is the activity product constant (solubility product constant) of insoluble compounds at a specific temperature, which is a function of temperature and has nothing to do with the initial ion concentration. When $IAP > K_{sp}$, $SI > 0$, the substance is supersaturated, it will precipitate; The ion concentration has a direct and significant effect on the precipitation saturation index of calcium carbonate. As shown in Figure 3, firstly, the calcium ion distributions containing carbonates under different pH are calculated (Figure 3a). It can be seen that the contribution of carbonate to precipitation is greater, which is consistent with the test results of crystalline precipitation samples. The main precipitate component is calcium carbonate. Due to the high solubility of calcium ions, it forms mixed precipitation with $CaCO_3$ when it is supersaturated. The ion concentration in the surrounding rock water of the tunnel is $HCO_3^- > Ca^{2+} > CO_3^{2-}$ from high to low. Among them, the content of HCO_3^- is higher, which is 214.3 mg/L. The concentration of calcium ion is high, and the concentration of CO_3^{2-} ion does not reach the detection limit, indicating that the crystals precipitated in the karst tunnel

drainage pipe are mainly produced by chemical reaction under the condition of solubility change. In the range of low pH, there is only HCO_3^- and CO_2 in water. There are only CO_3^{2-} ions in the higher pH range. HCO_3^- dominates in the range of medium pH values. Therefore, when the pH of water is high, the precipitation amount of calcium carbonate increases; on the contrary, when the pH value of water is low, calcium carbonate is not easy to precipitate (Figure 3b). When the pH is 0-10, the precipitation formation rate continues to increase, but when the pH is more than 10, the precipitation formation rate tends to slow down. At room temperature, the higher the pH, the greater the saturation index of CaCO_3 . When $\text{pH} > 8.1$, CaCO_3 precipitates gradually. This is due to the fact that the concentration of Ca^{2+} in the open system increases with the increase of pH, which makes the ion product of CaCO_3 increase gradually. This is due to the fact that the concentration of Ca^{2+} in the open system increases with the increase of pH, which makes the ion product of CaCO_3 increase gradually. The trend curve of the saturation index of CaCO_3 in the open system with temperature change in the temperature range of 20.0 - 26.0 °C at $\text{pH} = 8.1$ was drawn according to the convergence data (Figure 3c). With the increase of temperature, the saturation index of CaCO_3 increases, and the critical temperature of CaCO_3 precipitation is about 25.0 °C. This is because the solubility of CaCO_3 in the solution decreases with the increase of temperature, that is, more CaCO_3 will be precipitated when the water temperature increases. According to the simulation data, the pH when the saturation index was reached at 1 times carbon dioxide partial pressure, 1.5 times carbon dioxide partial pressure, and 2 times carbon dioxide partial pressure was summarized. As shown in Figure 3d, it can be found from the figure that as the partial pressure of CO_2 increases, the content of CO_2 in the gas phase gradually increases. According to Henry's law, the content of CO_2 in the liquid phase will also increase accordingly, resulting in more carbonic acid. The pH value of the solution is reduced, and the calcium carbonate precipitation is easily dissolved under acidic conditions, thus reducing the deposition rate of calcium carbonate. From the diagram, it can also be found that the critical pH of calcium carbonate precipitation is 8.1 under the condition of 1 times the partial pressure of carbon dioxide. Under the condition of 1.5 times of carbon dioxide partial pressure, the critical pH of calcium carbonate production precipitation is 7.9 ; under the condition of 2 times carbon dioxide partial pressure, the critical pH of calcium carbonate production precipitation is 7.8.

EXPERIMENTAL STUDY ON THE CRYSTALLIZATION FORMATION MECHANISM OF BLIND PIPE IN WUJIAYUAN TUNNEL

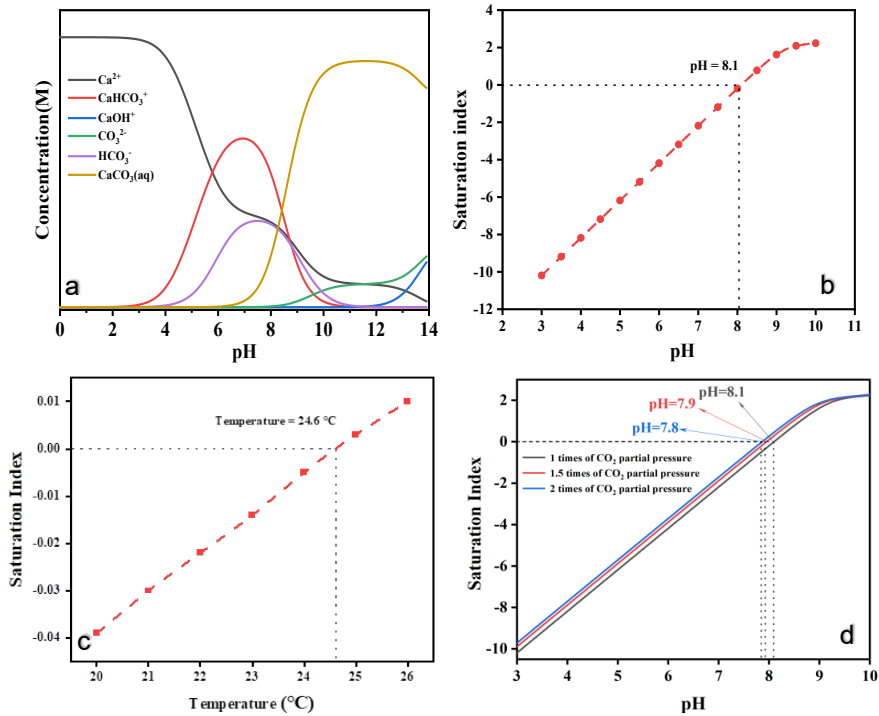


Figure 3. The influence of various factors on the saturation index is calculated and simulated (a. The precipitation mechanism of Ca^{2+} in water as the pH changes. b. Effect of pH on saturation Index of calcium Carbonate. c. Saturation index of CaCO_3 changing with temperature. d. Effect of pH on the saturation index of calcium carbonate.)

pH influence experiment analysis

While keeping other factors the same and unchanged, we set different pH gradients, observed and recorded the crystallization of the experimental solution under different pH environments, studied and analysed the effect of pH on the crystallization blockage of tunnel blind pipes, and provided guidance for the control of environmental pH during tunnel maintenance. The crystallization quality of experimental water samples under different pH conditions is shown in the figure below.

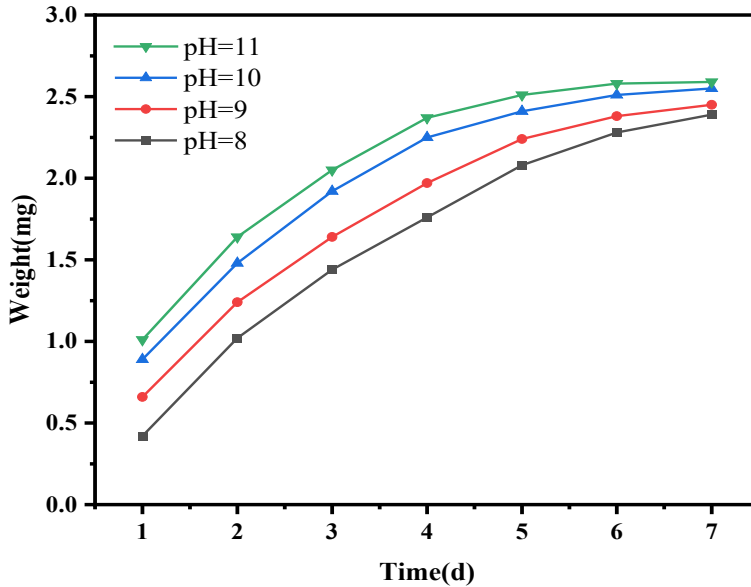


Figure 4. Relationship between time and crystal quality in different pH environments

It can be seen from Figure 4 that the reaction rates of the experimental solutions are different in different pH environments after a complete experiment lasting about one week. Taking pH equal to 8 as the research point, in the environment of high pH, the crystal formation rate is faster in the early stage, and tends to be slower in the middle and later stage, while in the alkaline environment with lower pH, the reaction rate of the experimental solution is relatively small, and the crystal quality increases slowly, but in the later stage, the solution is faster in the pH environment with higher crystal formation rate. The reason for the analysis may be that there is little difference in the content of Ca^{2+} and Mg^{2+} in the whole experimental solution and there is no follow-up supplement with the experimental reaction, which leads to the relatively large pH value of the experimental environment in the middle and later stage, but the ion concentration is low, so the reaction rate becomes slower. At the end of the experiment, the quality of crystals formed in different pH solutions is about the same, indicating that Ca^{2+} and Mg^{2+} in the experimental solution react with CO_3^{2-} and SO_4^{2-} to form carbonates and sulfates.

It can be seen that the pH value has a great influence on the solubility of calcium carbonate precipitates. When the pH is closer to 8, the crystallization rate is slower, and when the pH is further increased, the crystallization rate becomes faster, so in the actual tunneling operation, the solution pH should be kept near 8 as far as possible.

Experimental study on the effect of different ionic strength on the crystallization of tunnel blind tube

Referring to the on-site water sample analysis report and various literature data, the initial concentrations of Ca^{2+} ions and HCO_3^- should be set at higher levels to prevent excessive experimental error due to low initial concentrations. The production of crystallization in weakly alkaline solutions relates to the concentrations of Ca^{2+} and HCO_3^- . However, calcium bicarbonate easily decomposes into CaCO_3 , and a single reagent cannot adjust the concentrations of different ions. Therefore, it is not feasible to directly prepare a solution using solid calcium bicarbonate; instead, CaCl_2 and NaHCO_3 are used to prepare the experimental solution. The experimental results and analysis are as follows, with specific experimental procedures detailed in the section on factors influencing calcium carbonate crystallization.

The reaction temperature is 25 °C, the pH is adjusted to 8.1 with borax solution, the beaker is open, the initial concentration of bicarbonate is 50 mg/L, and the initial concentration of Ca^{2+} ion is changed. The experimental results are shown in Figure 5.

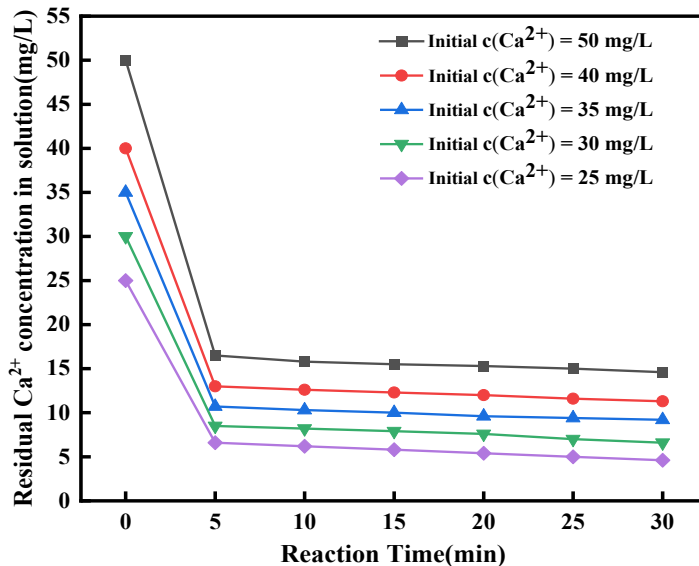


Figure 5. Variation of Ca^{2+} ion concentration with reaction time under different initial Ca^{2+} ion concentration

It can be seen from Figure 5 that with the increase of the initial Ca^{2+} ion concentration, the slope of the Ca^{2+} ion concentration curve of 5 min before the reaction also increases, from 3.68 mg/ (L·min) when the initial

Ca²⁺ ion concentration is 25 mg/L to 5.40 mg/ (L·min) when the initial Ca²⁺ ion concentration is 50 mg/L. The curve fluctuates slowly within 25 min after the reaction, because the formation and dissolution of CaCO₃ is a slow and reversible process with the participation of CO₂ and H₂O.

Bicarbonate first dissociates, and the resulting CO₃²⁻ reacts with Ca²⁺ in the solution to form CaCO₃ crystals. The HCO₃⁻ produced by hydrolysis is unstable and is easily decomposed into CO₂ and H₂O, the reaction of CaCO₃, CO₂ and H₂O to form water-soluble Ca(HCO₃)₂. When the initial Ca²⁺ ion concentration is not high, the Brownian motion of the particles in the solution is slow and the reaction rate is slow. Increasing the initial Ca²⁺ ion concentration increases the collision probability between particles and increases the reaction rate. It can be seen from the reaction formula that increasing the initial Ca²⁺ ion concentration can promote the reaction equilibrium to shift to the right and increase the overall reaction rate.

Table 2. Crystallization rate after reaction for 30 min at different initial Ca²⁺ concentrations

Initial Ca ²⁺ concentration (mg/L)	50	40	35	30	25
Crystallization rate W (%)	4.00	4.05	3.05	2.39	0.31

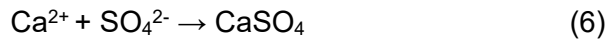
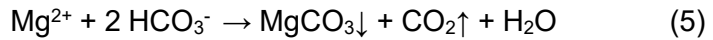
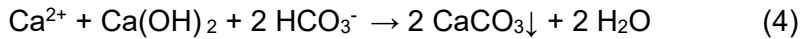
Table 2 shows the crystallization rate (W) after the reaction of 30 min with different initial Ca²⁺ ion concentrations. The formula for calculating the crystallization rate is as follow: $W = \frac{\Delta m}{A} \times \Delta t$. In the equation, Δm refers to the mass of crystals formed during the crystallization process. A denotes the surface area available for crystal growth, which typically depends on the shape and size of the crystals. Δt indicates the duration from the onset of nucleation to the point at which the crystals reach a specified size. The crystallization rate increases with the increase of the initial Ca²⁺ ion concentration. It can be seen from the reaction formula that the increase of Ca²⁺ ion concentration can make the reaction proceed to the left and inhibit the dissolution of calcium carbonate.

The effect of CO₂ on the formation of tunnel crystals

CO₂ plays a vital role in the formation of precipitated crystals in the tunnel drainage pipe. CO₂ dissolves in water to form carbonic acid (H₂CO₃), and carbonic acid can be ionized in water. The ionization equation is shown in Equation (3):



When $[\text{H}^+] = 3 \times 10^{-7} \text{ mol / L}$, the concentration of H_2CO_3 is equal to the concentration of HCO_3^- , and the aqueous solution is in equilibrium, that is, there is neither precipitation crystallization nor dissolution. When $[\text{H}^+] > 3 \times 10^{-7} \text{ mol / L}$, the precipitation and crystallization of calcium carbonate and magnesium carbonate will occur. The precipitated crystals in the tunnel drainage pipe are mainly precipitated by the precipitated crystals formed and dissolved by the chemical reaction in the case of solubility changes. The chemical equation for the precipitate crystals formed by the chemical reaction is as follows:



By observing the above chemical reaction equations, it is not difficult to find that CO_2 plays a very important role in the formation of precipitated crystals in the tunnel drainage pipe. When the tunnel is excavated, the gas partial pressure of CO_2 in the groundwater will decrease, resulting in a decrease in the solubility of CO_2 in the groundwater. The dissolved CO_2 escapes from the groundwater solution, resulting in a chemical reaction in the direction of the formation of precipitated crystals. The dissolved Ca^{2+} and Mg^{2+} in the aqueous solution are precipitated in the form of insoluble carbonates, and the crystalline precipitates in the groundwater solution tend to be saturated. The carbonates precipitated from the aqueous solution will adhere to the wall of the tunnel drainage pipe, resulting in an increase in the wall friction of the tunnel drainage pipe. The movement of the groundwater flow becomes more and more significant, which ultimately leads to the weakening of the water conveyance capacity of the tunnel drainage pipe.

Experiment on the effect of CO_2 on tunnel crystallization

The experimental part of the effect of CO_2 on tunnel crystallization is presented in the following sections. Analysis of comparative experimental results of sealed and unsealed under indoor conditions. The crystallization quality of the solution under different CO_2 contact modes is shown in Table 3.

Table 3. Experimental results of the effect of CO₂ on crystallization

Time (d)	Quality of unsealed crystalline water sample (mg)	Quality of sealed crystalline water sample (mg)
1	0.0500	0.0169
2	0.1025	0.0206
3	0.1427	0.0241
4	0.1762	0.0263
5	0.2049	0.0282
6	0.2336	0.0300
7	0.2581	0.0314

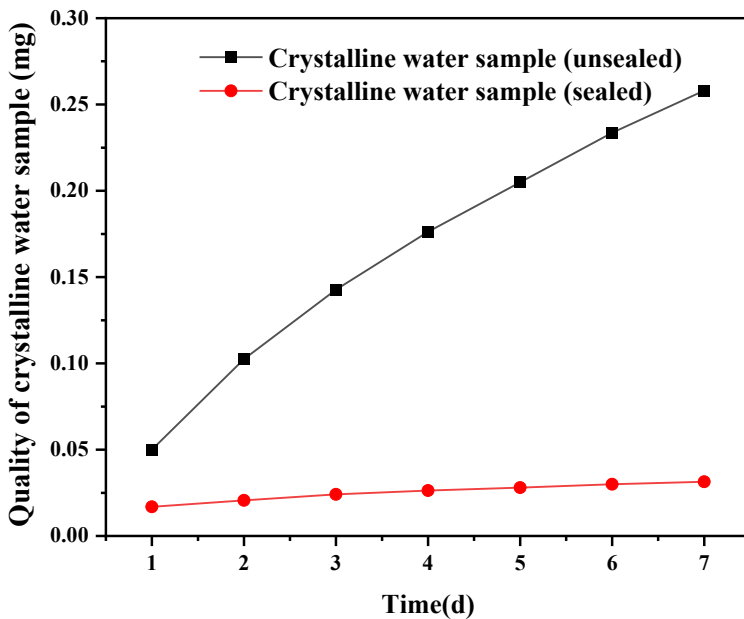


Figure 6. The effect of CO₂ on the crystallization of water samples in tunnel site under indoor conditions

Figure 6 shows the effect of CO₂ on the crystallization of water samples in the tunnel site under sealed and unsealed conditions under indoor conditions. It can be seen from the figure that the crystal quality generated when the experimental water sample in the beaker is in full contact with the air is larger than that when the seal is not in contact with the air, and the amount of crystallization gradually increases. With the increase of CO₂ contact time, the deposition rate of calcium carbonate gradually decreases. The reason is that with the increase of CO₂ contact time, CO₂ in the gas

phase is continuously supplemented, and the content of CO_2 in the liquid phase will increase accordingly, resulting in more carbonate ions and the formation of calcium carbonate precipitation. At the same time, with the increase of calcium carbonate deposition, the concentration of Ca^{2+} ions gradually decreases, so that the deposition rate of calcium carbonate gradually decreases.

The experimental results show that CO_2 has a great effect on the crystallization of tunnel water samples, as shown in Table 3 and Figure 6. In the beaker in contact with air, the maximum crystallization amount was 0.258 mg after 7 days, while in the sealed tunnel water sample, the maximum crystallization amount was only 0.031 mg after 7 days. At the same time, according to the image, the effect of CO_2 on the amount of crystallization is a significant trend in the early stage and a gentle trend in the later stage. That is, in the first 5 days of the experiment, the amount of crystallization increases rapidly, while in the 6-7 days, the amount of crystallization increases slowly. The reason may be that the corresponding Ca^{2+} and Mg^{2+} are consumed during the crystallization process, resulting in insufficient ion concentration in the later stage and a decrease in the crystallization rate, which is in line with the deposition rate of CaCO_3 .

Effect of temperature on the formation of tunnel crystals

The effect of temperature on the formation of precipitated crystals in the tunnel drainage pipe is also very significant. According to statistics, under normal atmospheric pressure, when the water temperature is $5\text{ }^\circ\text{C}$, the solubility of CaCO_3 is 86 ppm; when the temperature is increased by $10\text{ }^\circ\text{C}$, the solubility of CaCO_3 is reduced to 75 ppm. This indicates that CaCO_3 is more likely to approach supersaturation as the temperature of water increases. When the temperature increases, the reaction proceeds in the direction of positive reaction, which is beneficial to the formation of precipitated crystals in the tunnel drainage pipe.

The results of crystallization kinetics study on CaCO_3 precipitation crystallization show that the precipitation crystallization process of CaCO_3 conforms to the general law of crystallization kinetics, which can be divided into the formation of crystal nucleus and the growth stage of crystal grains. Among them, the solute crystallizes from the solution and needs to go through two stages: in the aqueous solution, tiny particles are first produced as the core of the crystallization, which is called the crystal nucleus, and then the crystal nucleus gradually grows into a visible crystal. The process of nucleation is called nucleation (or nucleation formation). Then, the nucleus gradually grows into micro-grains, which are called grain growth due to the process of continuous contact, collision and growth of micro-grains in solution due to thermal motion (Brownian motion).

The change of temperature conditions will not only lead to the change of the hydrodynamic properties of the aqueous solution and the balance of $\text{CO}_2 - \text{CaCO}_3$, which will promote the escape of CO_2 dissolved in the aqueous solution, resulting in the acceleration of the precipitation crystallization rate of carbonate rocks, but also directly affect the volume and concentration of the solution. For example, when the temperature increases, the liquid surface of the aqueous solution evaporates, resulting in an increase in the concentration of Ca^{2+} ions in the solution.

Effect of temperature on the formation of calcium carbonate precipitation

Table 4. Crystallization of saturated / unsaturated water samples with temperature

	20 °C	25 °C	30 °C	35 °C
Tunnel saturated water sample	Crystal did not form	White crystals are formed	Suspended liquid appears	The solution becomes clear
Tunnel supersaturated water sample	There is slight crystallization formation.	White crystals are formed	Suspended liquid appears	The solution becomes clear

The specific operation and related conditions of the experiment have been described in detail in the experimental section. It can be seen from the data in the Table 4 that the temperature has an important influence on the crystallization of the tunnel blind tube. In the Wujiayuan tunnel, the temperature has obvious crystallization at 25 °C. As the temperature increases, the solubility of the crystal increases. At 35 °C, the crystal dissolves and the solution is clarified. Therefore, increasing the temperature to about 30 °C can effectively reduce the crystallization of the tunnel blind tube. In the process of dealing with blind tube crystals, it can be considered to increase the temperature to inhibit blind tube crystallization.

Analysis of the formation mechanism of crystals in Wujiayuan tunnel

Combined with the calculation and simulation process of crystals, it can be seen that the crystallization and precipitation of tunnel blind tube are related to the saturation, pH value, temperature, pressure and solution properties of the solution, and the crystallization process is the combined effect of several factors. Changes in ambient temperature, pressure, evaporation, concentration of impurities or any other component in the solution may cause the equilibrium system to be readjusted.

The scaling ions also mainly come from two aspects, one is the groundwater itself (with the rock, etc.), and the other is the dissolution of concrete. There are many kinds of soluble salts in the groundwater of tunnel surrounding rock, such as bicarbonate, sulfate, phosphate, chloride, soluble carbonate and silicate. At the same time, the tunnel shotcrete is rich in calcium salts, and the groundwater seepage brings calcium ions into the tunnel blind tube through shotcrete. When in contact with the air, a large amount of CO_2 is dissolved in water, so that the groundwater contains a large amount of CO_3^{2-} , HCO_3^- , etc., HCO_3^- is unstable and easy to decompose to form CO_3^{2-} . The combination of Ca^{2+} and CO_3^{2-} is easy to form insoluble calcium carbonate. Calcium carbonate crystals are precipitated from water and grow slowly on the inner wall of the blind tube. At the same time, cement and fly ash contain a large amount of silicon dioxide, and the multiple effects of the above situation eventually form blind tube crystallization.

Temperature is another important factor affecting crystal precipitation. The solubility of most salts in water increases with the increase of temperature, but the solubility of the tunnel crystal is abnormal. When the temperature increases, the solubility decreases, that is, more crystals will be precipitated when the water temperature increases. Fig.7 shows the solubility curve of calcium carbonate crystals with temperature. With the increase of temperature, the saturation index of the crystal becomes larger, and the critical temperature for the formation of the tunnel crystal is about 25.0 °C.

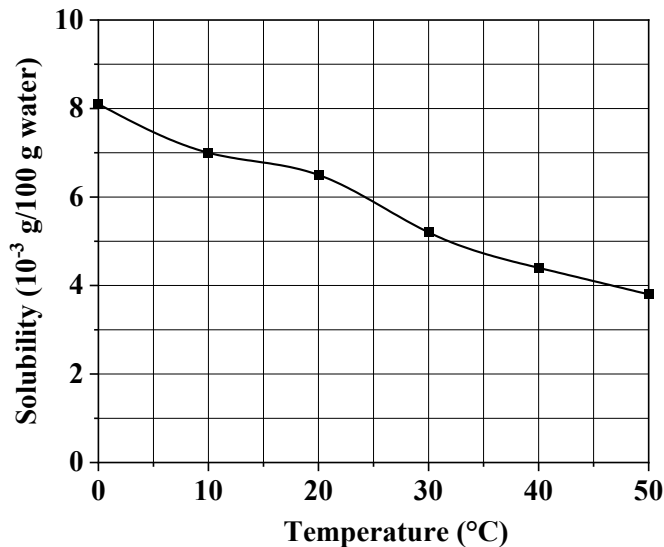


Figure 7. The solubility curve of calcium carbonate crystal changing with temperature

Different pH environments will significantly affect the formation of tunnel fissure water crystals, and change the balance of HCO_3^- , CO_3^{2-} , OH^- , and H^+ in the original solution. Under alkaline conditions, HCO_3^- will be more easily converted into CO_3^{2-} , and then react with Ca^{2+} to form insoluble crystals. The formation mechanism of crystals is shown in Figure 8. In the low pH range, only bicarbonate and carbon dioxide exist in the water. HCO_3^- is dominant in the medium pH range. Only CO_3^{2-} ions are present in the higher pH range. At room temperature, the higher the pH, the greater the saturation index of CaCO_3 . When $\text{pH} > 8.1$, CaCO_3 precipitate gradually. This is because the concentration of CO_3^{2-} in the open system increases with the increase of pH, which makes the ion product of CaCO_3 gradually increase. High pH water is easy to absorb carbon dioxide and react with calcium ions in the drainage solution, which is the main reason for the scaling of calcium carbonate, calcite and aragonite. There are two main reasons for the high pH value in water. One is the increase of pH value caused by concrete reaction. Second, part of the groundwater itself has a high pH. At the same time, the main cations in the tunnel blind pipe water are Ca^{2+} , Mg^{2+} and Na^+ ions. In this alkaline environment rich in calcium and magnesium ions, Mg^{2+} has a stronger affinity for some sites on the surface of the mineral, so it can replace part of Ca^{2+} into the lattice and eventually form high magnesium calcite. In summary, the crystallization mechanism of the tunnel drainage system is shown in the figure, and the reaction mechanism is summarized as follows:

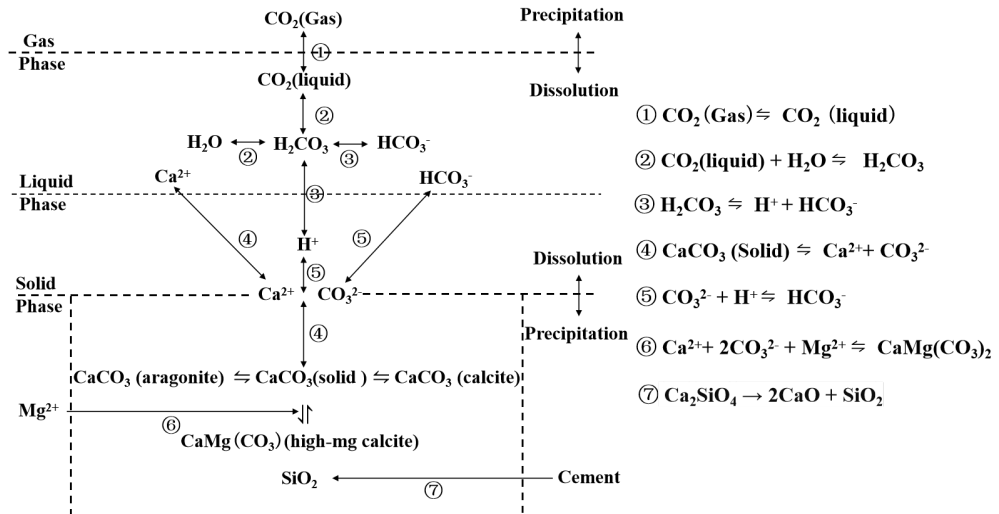


Figure 8. Formation mechanism of calcium carbonate crystallization in tunnel

The fissure water in the surrounding rock of the tunnel penetrates through the shotcrete of the initial support, which will take away a large amount of alkaline substances such as $\text{Ca}(\text{OH})_2$, making the water body strongly alkaline. The changes of high temperature, high humidity environment conditions and CO_2 partial pressure in the drainage system lead to the destruction of chemical equilibrium and the rapid crystallization of carbonate. In addition, at present, there are no requirements for the smoothness, smoothness and pollution resistance of the inner wall of the drainage component. Crystals are concentrated on the inner wall surface of the drainage system, and long-term crystallization precipitation blocks the drainage system. Especially when the water flow rate is low, the crystallization time is sufficient, and the drainage system is more likely to be blocked. The crystal of the drainage blind pipe is white and light yellow. In the drainage blind pipe, a uniform deposition layer is formed and deposited on the blind pipe wall at a relatively uniform density. These crystals may gradually increase density under the erosion of water flow. With the passage of time, the sediment will lead to the decrease of the inner diameter of the drainage blind pipe, and poor drainage will occur when the deposition is serious. The deposition of crystals may cause uneven water flow, forming rapid and slow changes in water flow. Turbulence may be more pronounced in the area where crystals accumulate. The bottom or side wall of the drainage ditch is a crystal deposition area, which may visually appear as a granular or uniform crystal layer. Crystals may form granular, massive or aggregated structures on the surface of the drain, and different surface textures may be felt during observation. Many tunnels still produce crystals after 5 years or even 10 years of operation, because cement hydration is a long-term continuous process, and the flowing water has a great influence on the concrete. Under the action of continuous groundwater erosion, the calcium substances in the concrete are continuously dissolved and brought out, so the tunnel faces the potential harm of drainage pipe crystallization blockage for a long time, which is a long and lasting process.

CONCLUSION

In this paper, the water treatment analysis is carried out according to the crystals sampled in the Wujiayuan tunnel. The relationship between the crystal in the blind tube and the ion concentration, pH value, CO_2 concentration and partial pressure, temperature in the groundwater was explored. The effect of pH on the precipitation saturation index, the effect of carbon dioxide partial pressure on the precipitation saturation index, the effect of temperature on the precipitation saturation index, and the effect of ionic strength on the

precipitation saturation index were simulated by using the environmental water chemical equilibrium software Visual MINTEQ 3.1. The formation mechanism of blind tube crystallization in Wujiayuan tunnel is summarized.

EXPERIMENTAL SECTION

For details of the experimental part, please refer to the Supporting Information.

REFERENCES

1. C. Chen; J. Rao; Y. Tao; C. Nie; P. Xiong; Y. Xue; X. Peng; *Asia-Pacific Journal of Chemical Engineering*, **2023**, *18*, e2897.
2. Y. Zhou; X. Zhang; L. Wei; S. Liu; B. Zhang; C. Zhou; *Advances in Civil Engineering*, **2018**, *2018*, 9430517.
3. T. Chai; *Gansu Science and Technology*, **2020**, *36*, 90-92.
4. H.-S. Jung; Y.-S Han; S.-R. Chung; B.-S. Chun; Y.-J. Lee; *Tunnelling and Underground Space Technology*, **2013**, *38*, 476-486.
5. G. Atkinson; K. Raju; R. D. Howell; *SPE International Symposium on Oilfield Chemistry*, **1991**, *85*:1778.
6. Y. B. Zeng, H. M. Li; Q. H. Niu; *Journal of Jianghan Petroleum Institute*, **2001**, *23* (2): 56-57
7. H. R. Song; S. Y. Huang; *Carsologica Sinica*, **1990**, *9* (2): 105-188.
8. J. Mi; Y. G. Tang; *Resources and Environmental Engineering*, **2010**, *24* (5): 589-592.
9. G. P. Lu. *Journal of Mineralogy and Petrology*, **1994**, *14*, 73-78.
10. H. M. Li; S. Y. Liu; S. Xiong; H. Leng; H. Q. Chen; B. Zhang; Z. Liu. *Coatings*, **2021**, *11*, 1493.
11. X. F. Zhang; Y. F. Zhou; B. Zhang; Y. J. Zhou; S. Y. Liu. *Advances in Materials Science and Engineering*, **2018**, *2018*, 1-6.
12. R. Jain. *Conference Series*, **2022**, *35*, 1033-1047.
13. Y. Otsuka; D. Sasaki; K. Kusamori; M. Nishikawa; B. Ben-Nissan. *Coatings*, **2023**, *56*, 1373-1380.
14. K. A. Shadi; B. T. Bennett; J. P. Beck; S. Jeyapalina; T. D. Sparks. *Journal of Materials Research*, **2023**, *38*, 2287-2301.
15. V. Glauco; P. Bezerra; S. Leyliane. *Journal of Non-Crystalline Solids*, **2023**, *617*, 122494.
16. A. S. Abyzov, V. M. Fokin, E. D. Zanotto. Predicting homogeneous nucleation rates in silicate glass-formers[J]. *Journal of Non-Crystalline Solids*, **2018**, *500*: 231-234.
17. M.F. Vladimir, S.A. Alexander, S.Y. Nikolay, et al. Effect of structural relaxation on crystal nucleation in glasses[J]. *Journal of Materials Research*, **2021**, *203*: 116472.
18. T. S. Abu Haimed, S. J. Alzahrani, E. A. Attar, L. Al-Turki. Effect of Repressing Lithium Disilicate Glass Ceramics on The Shear Bond Strength of Resin Cements. *Materials*, **2023**, *16*: 6148.

BEHAVIOR OF NEWTONIAN AND NON-NEWTONIAN FLUIDS IN PUMPING AND TRANSPORT PROCESSES

Andra-Camelia PAVEL^a , Elena-Mihaela NAGY^b ,
Teodor Gabriel FODOREAN^b and Adina MICLĂUȘ^{a*} 

ABSTRACT. The present study investigates the behavior of Newtonian and non-Newtonian fluids in pumping and transport processes, using a laboratory facility. The rheological behavior of the selected fluids were determined by a rotational viscometer with concentric cylinders. The effect of pressure difference on pumping of selected fluids in the laboratory circuit showed a linear decrease of effective/delivered volumetric flow rate for the Newtonian fluid, glycerin/water 80%, and a non-linear decrease for non-Newtonian fluid, Separan AP 30E, 2g/l.

Keywords: *Newtonian, non-Newtonian fluids, apparent viscosity, material consistency, flow behavior index, volumetric flow rate, pressure difference, pumping and transport.*

INTRODUCTION

Fluid flow in pipelines and pumps is a fundamental topic and a crucial aspect of practical engineering that can affect a broad range of operations in industries such as chemical, pharmaceutical, food and agriculture, oil and gas [1-4]. The correlation between rheological properties, flow rate and pump selection, based on modelling, simulation and experimental validation, can be challenging for ensuring efficient transport, especially for fluids with non-Newtonian behavior [5-8].

^a Babeş-Bolyai University, Faculty of Chemistry and Chemical Engineering, 11 Arany Janos Str., 400028 Cluj-Napoca, Romania

^b National Institute of Research-Development for Machines and Installations Designed to Agriculture and Food Industry, B-dul Ion Ionescu de la Brad nr.6, Bucharest, Romania

* Corresponding author: adina.miclaus@ubbcluj.ro



The fluids used in the present application have Newtonian or non-Newtonian behavior, shear-thinning or pseudoplastic behavior, each exhibiting distinct flow properties [9]. Newtonian fluids, such as water, or simple liquids such as alcohol, gasoline, diesel or mineral oils, under low to moderate flow rates, have a constant viscosity regardless of the applied rheological parameters, shear stress, τ , or the shear rate, $\dot{\gamma}$. With a linear relationship between these two parameters, the flow behavior is predictable, and engineers can easily calculate flow rates and pressures.

The study of Newtonian fluids is foundational in fluid mechanics, and it is a pivot when compared to non-Newtonian fluids [10].

Described by Isaac Newton's law of viscosity around 1687, the equation (1) is still groundbreaking and establishes the fundamental proportional relationship between shear stress and shear rate.

$$\tau = \eta \cdot \dot{\gamma} \quad (1)$$

where: τ is the shear stress, force per unit area exerted by the fluid (Pa), η - the dynamic viscosity, the constant value for Newtonian fluids at constant thermodynamic conditions (Pa·s), $\dot{\gamma}$ - the shear rate, rate at which the fluid layers move relatively to each other (1/s).

Non-Newtonian fluids are fluids whose viscosity changes with the rheological parameters shear rate, or shear stress, meaning their behavior is not anymore constant [9, 10]. Shear-thinning fluid are non-Newtonian fluids that exhibit a decrease in viscosity as the shear rate increases. This means that when these fluids are subjected to stress or deformation, they become less viscous, making them easier to flow. Examples of materials that exhibit shear-thinning behaviors are blood, paints and coatings, ketchup, polymer melts or gels, lotions and creams, muds and slurries.

The flow behavior of shear-thinning fluids is essential in medicine for designing specific medical devices like blood pumps, industrial and agricultural manufacturing, oil and gas field or wastewater management for choose pumps and pipes. The non-Newtonian behavior adds a layer of complexity to fluid dynamics and necessitates models that are more sophisticated to predict flow properties.

The power law model, also known as the Ostwald-de Waele model, equation (2), was first proposed by Ostwald in the late 19th century (around 1895) and later refined by de Waele in the early 20th century (around 1923) and describes the non-linear relationship between shear stress, τ , and the shear rate, $\dot{\gamma}$.

$$\tau = K \cdot \dot{\gamma}^n \quad (2)$$

where: τ is the shear stress (Pa), $\dot{\gamma}$ - the shear rate (1/s), K – material consistency, a material constant that indicates the fluid's flow resistance ($\text{Pa} \cdot \text{s}^n$), and n – flow behavior index (-), with the value: $n < 1$ for shear-thinning or pseudoplastic fluids, $n = 1$ for Newtonian fluids, and $n > 1$ for shear-thickening or dilatant fluids.

The Hagen-Poiseuille equation (3) describes the flow of an incompressible, Newtonian fluid through a uniform cross-section along its length, under laminar flow conditions, when the fluid moves in parallel layers [10]. This equation is essential to understand the relationship between pressure drop, volumetric flow rate, the properties of the fluid and dimensions of the flow system.

$$Gv = \frac{\pi \Delta P r^4}{8 \eta L} \quad (3)$$

where: Gv is the volumetric flow rate, the volume of fluid passing through the pipe per unit of time (m^3/s), ΔP - the pressure drop, the difference in pressure between inlet and outlet in the pipe (Pa), r - the radius of the pipe (m), η - the dynamic viscosity of the Newtonian fluid ($\text{Pa} \cdot \text{s}$), L - the length of the pipe (m).

For shear-thinning fluids, the effective viscosity or apparent viscosity is a function of the shear rate, equation (4), and the volumetric flow rate becomes as equation (5) shows [9]:

$$\eta_{eff} = K \cdot \dot{\gamma}^{n-1} \quad (4)$$

$$Gv = \frac{\pi \Delta P r^4}{8 \eta_{eff} L} \quad (5)$$

The objective of the present study was to determine experimentally and understand how two fluids, one Newtonian and the other non-Newtonian, behave under various conditions at pumping and transport. The knowledge of non-Newtonian fluid effects on the pump performance is fundamental in the design process, as well as in the pump choice. In addition, it has significant implications in control of industrial processes, reducing energy consumption, and improving the efficiency of fluid transport and pumping systems.

RESULTS AND DISCUSSION

a. Rheological behavior

The rheological behavior of the chosen samples, glycerin/water mixture as Newtonian fluid and Separan AP 30E as non-Newtonian fluid, evaluated by the viscosity curves, are shown in Figure 1 and 2.

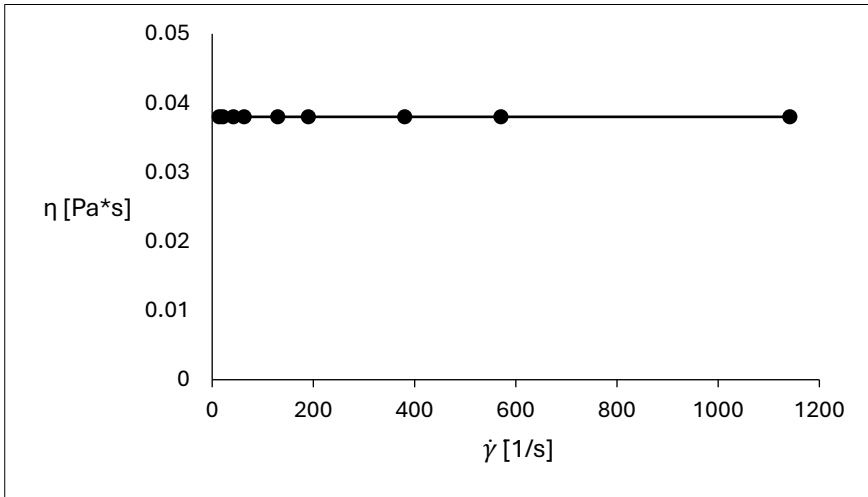


Figure 1. Viscosity curve for the Newtonian fluid: glycerin/water (80 %, vol. %)

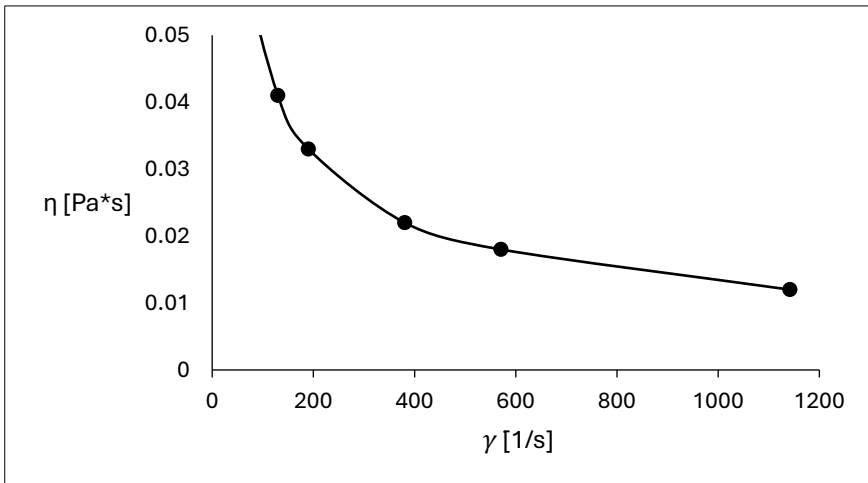


Figure 2. Viscosity curve for the shear-thinning/pseudoplastic solution: Separan AP 30E (2g/l H₂O, 25°C)

The effective viscosity was obtained in accordance with Newton's law, from the ratio between shear stress and shear rate. To determine the material consistency, K , and the flow index, n , the shear stress against shear rate in double logarithmic scale is presented in Figure 3 for Separan sample.

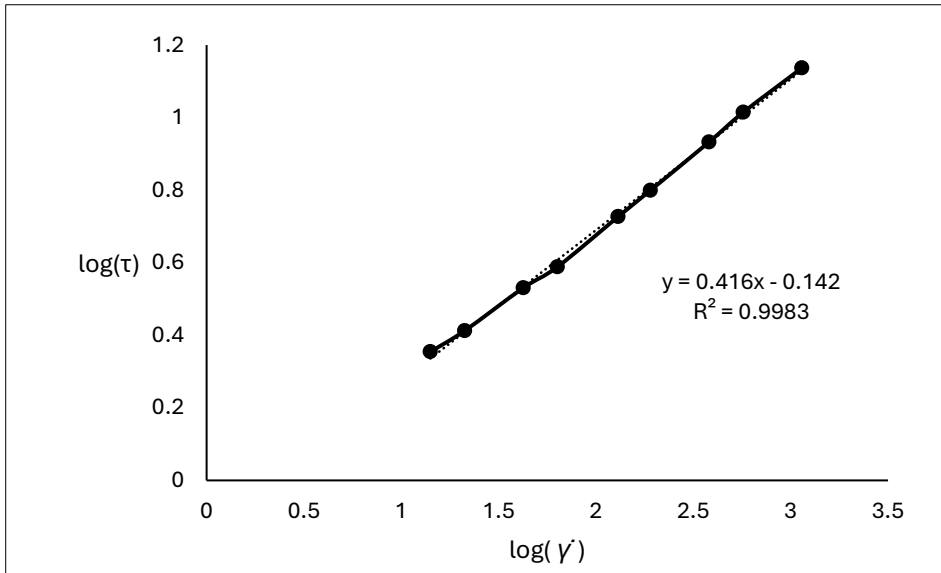


Figure 3. Flow curve in logarithmic scale for the pseudoplastic liquid: Separan AP 30E (2g/l H₂O, 25°C)

The constant viscosity value of 0.038 Pa·s, and the obtained value of flow index, $n = 1$, for glycerin/water mixture confirms the Newtonian behavior.

In the case of Separan AP 30E, the apparent viscosity decreases with the increase of shear rate, and flow behavior index lower than 1, $n = 0.416$, confirms the shear-thinning or pseudoplastic behavior. The material consistency in this case is $K = 0.721 \text{ Pa}\cdot\text{s}^n$.

b. Pumping behavior

Figures 4 and 5 show the effective volumetric flow of glycerin/water and Separan AP 30E as a function of pressure difference between delivery and suction, with the change of the pump's rotation speed.

The obtained curves show a linear decrease of the volumetric flow with the increase of pressure difference in pump for the glycerin/water mixture, a Newtonian fluid, and a non-linear decrease for Separan AP 30E, a shear-thinning fluid.

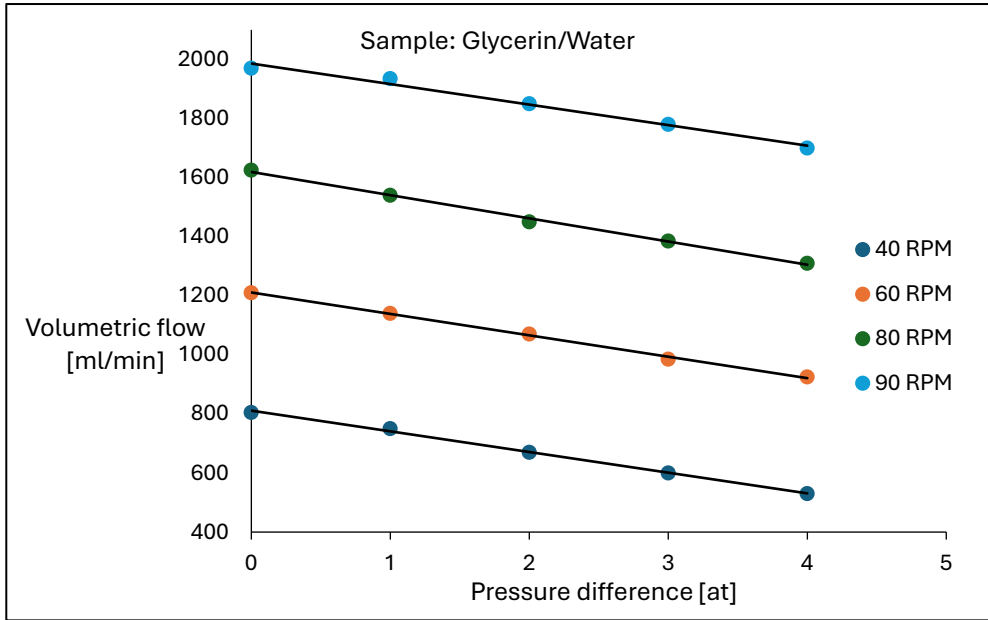


Figure 4. Volumetric flow rate vs. pump's pressure difference for glycerin/water

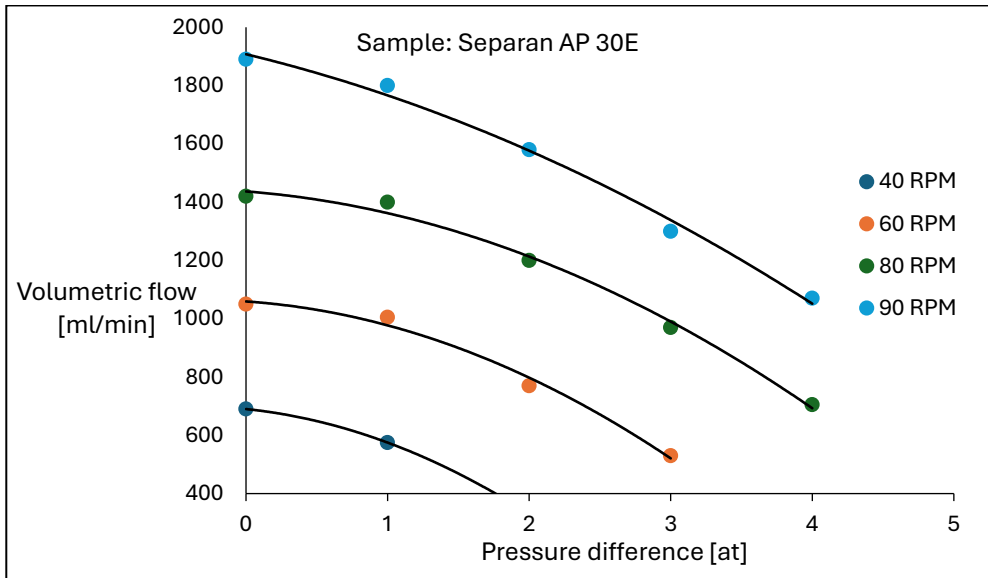


Figure 5. Volumetric flow rate vs. pump's pressure difference for Separan AP 30E solution

In order to explain the decrease of the effective volumetric flow, G_{Veff} , we have to consider that the effective volumetric flow or outflow is the difference between theoretical volumetric flow, G_{Vt} , and the recirculation flow, G_{Vr} , which is proportional with the friction/drop pressure, equation (6).

$$Gv_{eff} = Gv_t - Gv_r \quad (6)$$

$$Gv_r = C \times \frac{\Delta P}{\eta_{eff}} \quad (7)$$

Thus, increasing the pressure difference, the recirculation flow in the system increases and as result, the value of effective/delivered volumetric flow of the pump will decrease. The friction losses in the system increases also due to the decrease of the effective viscosity, for the non-Newtonian fluid, as equation (7) shows.

The constant C contains the numerical constants and the dimensions that characterize the pipeline; ΔP is the pressure drop in the pipeline; n is the flow behavior index. For the viscosity, the effective viscosity or apparent viscosity, corresponding to the respective shear rate must be set.

The results show that the influence of the recirculation is more evident for non-Newtonian fluids than for Newtonian fluids, the effective flow rate decrease is higher for Separan solution comparative with glycerin/water mixture.

Figure 6 shows the influence of rotation speed on the effective volumetric flow rate at different pressure. In the domain of rotation speed used in the present study, the volumetric flow rate increases linearly with the rotation speed at the same pressure difference for both fluids.

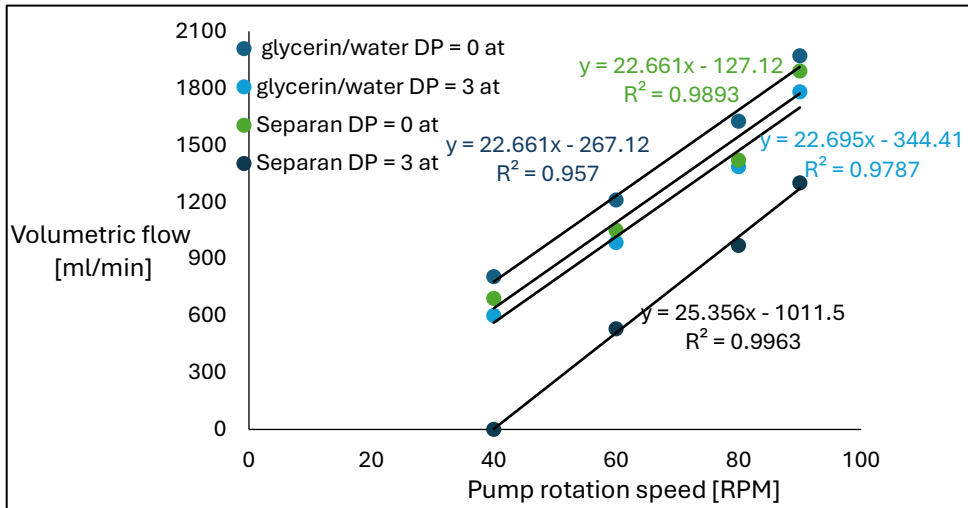


Figure 6. Volumetric flow rate vs. pump's rotation speed for glycerin/water mixture and Separan AP 30E at pressure difference 0 and 3 at

The slope of the linear curves has almost the same value, around 22, for the glycerin/water mixture, a fluid with constant viscosity, but a higher value, around 25, in the case of Separan at higher pressure difference. The result can be explained considering that the decrease of effective/ apparent viscosity is more significant at higher applied shear load.

CONCLUSIONS

The study explores the influence of the rotation speed and pressure difference as operational parameters on the pumping and transport of Newtonian and non-Newtonian fluids.

The rheological behavior of glycerine/water as Newtonian fluid and Separan AP 30E as shear-thinning fluid was experimentally determined using a rotational viscometer with two concentric cylinders.

The effective delivered volumetric flow rate decreased with the pump's pressure difference in accordance with equation (6), the decrease was more obvious for Separan solution than for the glycerin/water mixture.

In the domain of rotation speed used in the present study, the volumetric flow rate increases linearly with the rotation speed at the same pressure difference, for both Newtonian and non-Newtonian fluids.

EXPERIMENTAL SECTION

In this section, there are described the materials, methods, and procedures used for the transport and pumping of the two fluids with different rheological behavior.

Materials: Glycerine/water mixture, 80 vol. % glycerin, as Newtonian fluid, and Separan AP 30E, a polymeric solution with 2g/l H₂O, as non-Newtonian sample. Separan AP 30E is a polymer made by polymerizing acrylamide molecules, commonly used for water treatment, drilling fluids or enhanced oil recovery.

Apparatus: Rotational viscometer Rheotest II for the determination of the rheological measurements; and the laboratory facility, with recirculation loop or bypass, the thermostat T, gear pump P, pressure gauge M, overpressure valve V, control valve R, and the column S, presented schematically in Figure 7.

Experimental conditions: temperature: 25 (°C), rotation speed between: 40 and 90 (RPM), pressure differences between delivery and suction: 0 - 4 (at). The pressure difference 1 (at) is equivalent with 98100 (Pa).

BEHAVIOR OF NEWTONIAN AND NON-NEWTONIAN FLUIDS
IN PUMPING AND TRANSPORT PROCESSES

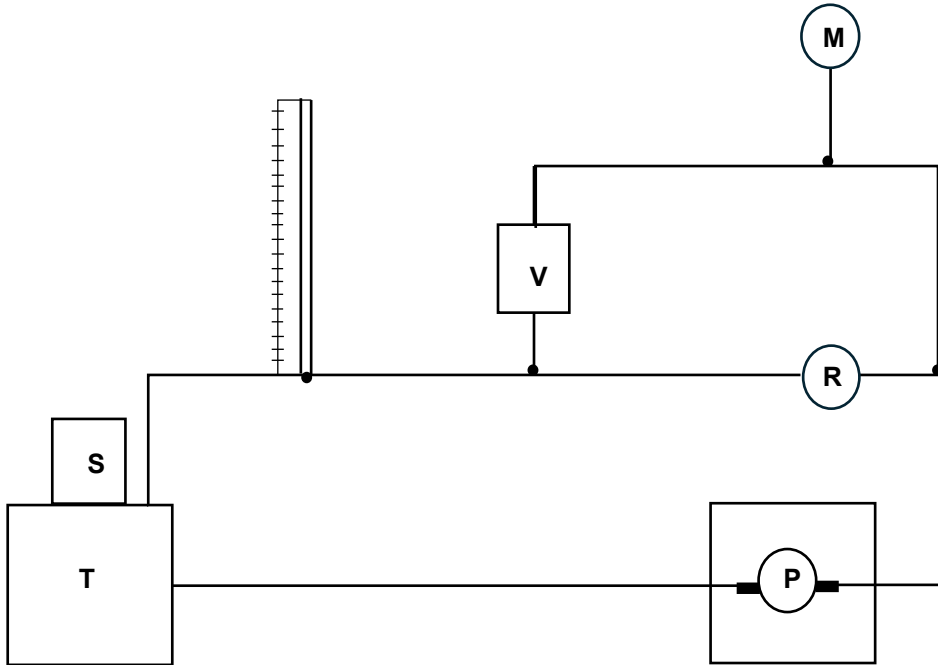


Figure 7. Experimental circuit for pressure difference measurement

The testing method offers the possibility of pumping the fluids at different pressures using magnetically coupled gear pumps with the speed adjusted in stages.

A constant pump rotation speed is set on the gear pump using the specific push button settings, starting with 40 RPM. The control valve R and the measured overpressure M on the bypass line, equipped with a pressure bypass valve V, allow us to determine the discharge pressure.

The height of the liquid column S is measured, and the resulting volumetric flow rate G_v is determined from the corresponding calibration curve (see Table 1).

Minor deviations in the reproducibility of the measurements can be explained by physical structural modifications of the Separan due to mechanical stress (constant pumping in the circuit).

Table 1 shows the results obtained at different pressure between delivery and suction for each tested case.

Table 1. Measurement data for the operating behavior of the gear pump

Sample	Speed rotation of the pump [RPM]	Pressure diff. ΔP (at)	Height of the fluid h (mm)	Volumetric flow G_v (ml/min)
Glycerin/ Water	40	0	120	805
		1	100	750
		2	70	670
		3	45	600
		4	22	530
	60	0	265	1210
		1	240	1140
		2	213	1070
		3	185	985
		4	165	925
	80	0	405	1625
		1	384	1540
		2	352	1450
		3	325	1385
		4	302	1310
	90	0	535	1970
		1	525	1935
		2	495	1850
		3	470	1780
		4	440	1700
Separan AP 30E	40	0	100	690
		1	70	575
		2	10	330
		3	0	-
	60	0	200	1050
		1	180	1005
		2	120	770
		3	60	530
	80	4	0	-
		0	285	1420
		1	280	1400
		2	230	1200
	90	3	170	970
		4	105	705
		0	410	1890
		1	380	1800
		2	325	1580
		3	255	1300
		4	195	1070

REFERENCES

1. G. Towler; R. Sinnott; Piping and instrumentation. In *Principles, Practice and Economics of Plant and Process Design*, 3rd ed.; Butterworth-Heinemann Elsevier, Oxford, UK, **2022**, pp. 235-297.
2. J. F. Steffe; Tube viscometry. In *Rheological Methods in Food Process Engineering*, 2nd ed.; Freeman Press, East Lansing, Michigan, USA, **1992**, pp. 94-157.
3. M. Sabah Kassim; S. A. Sarow; *IOP Conf. Series, Mater. Sci. Eng.*, **2020**, 870(1), (012032), pp.12-32.
4. P. Angeli; G. F. Hewitt; *Int. J. Multiphase Flow*, **2000**, 26, 1117–1140.
5. S. K. Kim; *J. Rheol.*; **2018**, 62, 1397-1407.
6. T. Shende; V. J. Niasar; M. Babaci; *Rheol. Acta.*, **2021**, 60, 11-21.
7. F. Rituraj; A. Vacca; *Mech. Systems and Signal Processing*, **2018**, 106, 284-302.
8. T. Hayase; *Fluid Dyn. Res.*; **2015**, 47(5), (051201), pp. 1-20.
9. T. G. Mezger; Flow curves and viscosity functions. In *The Rheology Handbook: For users of rotational and oscillatory rheometers*, 2nd revised ed.; Vincentz Network GmbH, Hannover, Germany, **2006**, pp. 30-58.
10. A. Miclăuș; V. Pode; Curgerea laminară a fluidelor in conducte (tuburi) cu secțiune circulară. In *Cazuri particulare de curgere a fluidelor ideale si reale. Elemente de reologie*, Casa Cărții de Știință, Cluj-Napoca, Romania, **2018**, pp.81-92.